

TECHNISCHE UNIVERSITÄT MÜNCHEN

Fakultät für Physik

Lehrstuhl für Funktionelle Materialien

**Tailoring titania photoanodes for application  
in solid-state dye-sensitized solar cells and  
hybrid solar cells**

Lin Song

Vollständiger Abdruck der von der Fakultät für Physik der Technischen Universität  
München zur Erlangung des akademischen Grades eines

**Doktors der Naturwissenschaften (Dr. rer. nat.)**

genehmigten Dissertation.

Vorsitzende: Prof. Dr. Martin Zacharias

Prüfer der Dissertation: 1. apl. Prof. Dr. Peter Müller-Buschbaum  
2. Prof. Dr. Friedrich Simmel

Die Dissertation wurde am 22.05.2017 bei der Technischen Universität München  
eingereicht und durch die Fakultät für Physik am 21.06.2017 angenommen.



## **Abstract**

In this thesis mesoporous titania films are investigated with respect to their application as photoanodes in solid-state dye-sensitized solar cells and hybrid solar cells. The main focus lies on the tailoring of nanostructured titania photoanodes and its influence on the device performance. For this, pre-synthesized crystalline titania nanoparticles are added during the block copolymer assisted sol-gel process, which gives precise control over titania nanostructures and enhances the crystallinity of the resulting titania films. Spray coating as a low-cost technique for an scalable production is employed to deposit titania films. A sponge-like morphology is obtained, which is favorable for solar cell application due to its high surface-to-volume ratio and porosity. Moreover, the kinetic processes of spray coating are investigated using in situ grazing incidence small angle x-ray scattering, allowing to determine the structure evolution of the deposited films. The influence of mesopore sizes of titania photoanodes on the crystalline order of backfilled P3HT is studied, which has a direct correlation to the solar cell performance and stability. Furthermore, a low-temperature routine is established to fabricate hierarchically structured titania photoanodes and hybrid solar cells. In addition, the effect of artificial superstructures on the device performance is studied.

## **Zusammenfassung**

In dieser Arbeit werden mesoporöse Titandioxid-Schichten im Hinblick auf ihre Anwendung als Photoanoden in Festkörper-Farbstoffsolarzellen und Hybridsolarzellen untersucht. Das Hauptaugenmerk liegt auf der Veränderung der nanostrukturierten Titandioxid-Photoanoden und deren Einfluss auf die Funktionalität der Solarzellen. Zu diesem Zweck werden vorsynthetisierte kristalline Titandioxid Nanopartikel zum Reaktionsgemisch des Block-Copolymer assistierten Sol-Gel-Prozess hinzugefügt. Dies erlaubt die präzise Kontrolle über die Nanostruktur und verbessert die Kristallinität der entstehenden Titandioxid-Schichten. Sprüh-Beschichtung wird als kostengünstige Methode zur großflächigen Herstellung, von Titandioxid-Schichten auf Substraten verwendet. Man erzielt eine schwammartige Morphologie, welche durch das große Oberflächen-zu-Volumen-Verhältnis und Porosität für Anwendungen in Solarzellen vorteilhaft ist. Weiterhin werden kinetische Prozesse während der Sprüh-Beschichtung mit Röntgenstreuungsmethoden unter streifendem Einfall untersucht, die eine untersuchung von zeitlichen Änderungen in der Struktur der Filme erlauben. Es wird der Einfluss der Mesoporengröße in Titandioxid-Photoanoden in der

Größenordnung von kristallinem P3HT, welches in die Poren eindringt, untersucht, wobei eine direkte Korrelation zur Solarzelleneffizienz und Stabilität besteht. Außerdem wird eine Niedrigtemperaturroute zur Herstellung von hierarchisch strukturierten Titandioxid-Photoanoden und Hybridsolarzellen etabliert. Zudem wird der Einfluss der künstlichen Superstrukturen auf die Effizienz untersucht.



# Contents

<b>Contents</b>	<b>iii</b>
<b>List of abbreviations</b>	<b>vii</b>
<b>1 Introduction</b>	<b>1</b>
<b>2 Theoretical aspects</b>	<b>7</b>
2.1 Polymer basics . . . . .	7
2.1.1 Diblock copolymers . . . . .	11
2.1.2 Conducting polymers . . . . .	13
2.2 Titania and sol-gel synthesis . . . . .	17
2.2.1 Properties of titania . . . . .	17
2.2.2 Principles of sol-gel synthesis . . . . .	19
2.2.3 Structure direction with polymer template . . . . .	20
2.3 Titania based solar cells . . . . .	23
2.3.1 Basic principles . . . . .	23
2.3.2 Solid-state dye-sensitized solar cells . . . . .	25
2.3.3 Hybrid solar cells . . . . .	28
2.4 Scattering methods . . . . .	30
2.4.1 Principles . . . . .	30
2.4.2 X-ray diffraction . . . . .	32
2.4.3 Grazing incidence small angle x-ray scattering . . . . .	34
2.4.4 Grazing incidence wide angle x-ray scattering . . . . .	36
<b>3 Characterization methods</b>	<b>39</b>
3.1 Structural characterizations . . . . .	39
3.1.1 Height profilometry . . . . .	39
3.1.2 Atomic force microscopy . . . . .	40
3.1.3 Scanning electron microscopy . . . . .	42
3.1.4 Nitrogen adsorption–desorption isotherms . . . . .	43
3.1.5 X-ray diffraction . . . . .	44

3.1.6	Grazing incidence scattering . . . . .	45
3.2	Spectroscopic and electronic characterizations . . . . .	48
3.2.1	UV/Vis spectroscopy . . . . .	48
3.2.2	FT-IR spectroscopy . . . . .	49
3.2.3	I-V characterization . . . . .	50
3.2.4	External quantum efficiency . . . . .	51
<b>4</b>	<b>Sample preparation</b>	<b>53</b>
4.1	Materials . . . . .	53
4.2	Processing . . . . .	59
4.2.1	Compact titania layer . . . . .	59
4.2.2	Synthesis of mesoporous titania film . . . . .	59
4.2.3	Deposition methods . . . . .	63
4.2.4	Solar cell assembly . . . . .	67
4.2.5	Imprint master fabrication . . . . .	70
<b>5</b>	<b>Spray deposition of titania films with incorporated crystalline nanoparticles</b>	<b>73</b>
5.1	Titania nanostructures modified with crystalline nanoparticles . . . . .	75
5.1.1	Surface morphology . . . . .	77
5.1.2	Inner morphology . . . . .	78
5.1.3	Crystallinity and conductivity . . . . .	84
5.2	Solar cell performance . . . . .	87
5.2.1	Effect of PEDOT:PSS blocking layer . . . . .	87
5.2.2	Discussion . . . . .	89
5.3	Summary . . . . .	90
<b>6</b>	<b>In situ study of spray-deposited titania films for scalable fabrication of solid-state dye-sensitized solar cells</b>	<b>93</b>
6.1	In situ GISAXS measurements during spray coating . . . . .	95
6.1.1	Setup and protocol . . . . .	95
6.1.2	Morphological evolution during spray coating . . . . .	97
6.2	Morphologies before and after calcination . . . . .	103
6.2.1	Surface morphology . . . . .	104
6.2.2	Inner morphology . . . . .	105
6.2.3	Discussion . . . . .	106
6.3	Solar cell performance . . . . .	108
6.4	Summary . . . . .	110

---

<b>7</b>	<b>In situ study of degradation in P3HT-titania based solid-state dye-sensitized solar cells</b>	<b>113</b>
7.1	Mesoporous titania film with different pore sizes . . . . .	115
7.1.1	Surface Morphology . . . . .	116
7.1.2	Inner Morphology . . . . .	117
7.1.3	Crystallinity of the titania template . . . . .	121
7.2	Dyed titania films backfilled with P3HT . . . . .	121
7.2.1	P3HT crystallization inside the titania mesopores . . . . .	122
7.2.2	Temporal evolution of the P3HT crystalline order . . . . .	126
7.3	Temporal evolution of photovoltaic performance . . . . .	128
7.4	Summary . . . . .	131
<b>8</b>	<b>Low temperature synthesis of hierarchically structured titania films</b>	<b>133</b>
8.1	Film before and after polymer-template extraction . . . . .	135
8.1.1	Fabrication routine of hierarchical titania nanostructures . . . . .	136
8.1.2	Surface morphology . . . . .	138
8.1.3	Inner morphology . . . . .	141
8.1.4	Incorporation of pre-synthesized nanoparticles into titania network at low temperatures . . . . .	144
8.2	P3HT-backfilled titania films . . . . .	147
8.2.1	Active layer morphology . . . . .	148
8.2.2	Optical properties of the active layer . . . . .	149
8.3	Current-voltage characteristic . . . . .	152
8.4	Summary . . . . .	156
<b>9</b>	<b>Conclusion and outlook</b>	<b>159</b>
	<b>Bibliography</b>	<b>163</b>
	<b>List of publications</b>	<b>193</b>
	<b>Acknowledgements</b>	<b>199</b>



**List of abbreviations**

BHJ:	bulk heterojunction
DOS:	density of states
DSSC:	dye-sensitized solar cell
DWBA:	distorted wave Born approximation
FF:	fill factor
FTIR:	Fourier transformed infrared spectroscopy
FTO:	fluorine doped tin oxide
FWHM:	full width at half maximum
GISAXS:	grazing incidence small angle X-ray scattering
GIWAXS:	grazing incidence wide angle X-ray scattering
HOMO:	highest occupied molecular orbital
I/V:	current-voltage characteristics
$J_{SC}$ :	short circuit current
LMA:	local monodisperse approximation
LUMO:	lowest unoccupied molecular orbital
$M_n$ :	number average molecular weight
$M_w$ :	weight average molecular weight
PCE:	power conversion efficiency
PEDOT:PSS:	poly(3,4-ethylenedioxythiophene):poly(styrenesulfonate)
P3HT:	poly(3-hexylthiophene-2,5-diyl)
PS-b-PEO:	poly(styrene-block-ethylene oxide)
SDD:	sample detector distance
SLD:	scattering length density
spiro-OMeTAD:	2,2',7,7'-tetrakis(N,N di-p-methoxyphenyl-amine)9,9'-spiro-bifluorene
ssDSSC:	solid-state dye-sensitized solar cell
TOF-GISANS:	time-of-flight grazing incidence small angle neutron scattering
UV/Vis:	ultraviolet/visible spectroscopy
$V_{OC}$ :	open circuit voltage
XRD:	X-ray diffraction



# 1 Introduction

From the 1950s on, the global energy consumption increased dramatically due to the rapid advance of economy and industrial growth. To date, the main energy sources are still fossil fuels, which account for more than 80 % of the global sources of energy [1]. However, concerns related to environmental pollution and global-temperature increase motivate the use of renewable energies [2]. Solar energy as the most abundant energy source has received great attention and many technologies have been developed to harvest solar energy. Among the different technologies, photovoltaics show a great application potential as it can directly convert light into electricity.

The first practical solar cell (silicon-based) was invented in the Bell Laboratories in 1953, with a power conversion efficiency (*PCE*) of about 6 % [3]. The crystalline and polycrystalline silicon panels are called first generation solar cells, which are still dominating the photovoltaics market today. The so-called second generation solar cells are based on amorphous silicon and III–VI semiconductors such as copper indium gallium selenide (CIGS) and cadmium telluride (CdTe). The typical *PCE* is in the range of 10 % - 15 % [4–6], but the large energy consumption and the rare elements involved in the manufacturing are limiting factors for their market expansion. The third generation devices are organic thin-film solar cells, which have been developed with a target of high *PCE* and low costs. The prologue to thin-film solar cells was the discovery of conductive polymers in 1977 [7]. Since then, polymer-based solar cells have been explored extensively and are by now capable of competing with their inorganic counterparts. Moreover, the intrinsic nature of mechanical flexibility and light weight of the used organic materials offers the possibility to shape and color the organic photovoltaic devices in various forms. However, the stability of polymer-based solar cells is still limited as compared to the first and second generation solar cells. Therefore, besides pure organic solar cells, devices using organic and inorganic materials have recently received great attention due to the combination of merits from both, the organic and inorganic components. In the present thesis, solid-state dye-sensitized solar cells (ssDSSCs) and hybrid solar cells are the main focus. Both types of solar cells evolved from DSSCs which comprise inorganic components as electron conducting materials, dyes as photosensitizers and liquid electrolytes as hole transport materials (HTMs). The *PCE* of DSSCs has been improved to over

12 % in a long going recent using advanced porphyrin-based dyes [8]. Although DSSCs have achieved commercial breakthrough, problems related to liquid electrolytes motivate researchers to develop other solid-state substitutes. As a result, ssDSSCs and hybrid solar cells have been developed in terms of high stability. Recently, a new class of thin film solar cells, organometal halide perovskite solar cells, has been developed from ssDSSCs, which shows a huge potential for the commercial application as the *PCE* has reached values beyond 20 % [9].

In the present thesis, both ssDSSCs and hybrid solar cells are composed of n-type nanostructured titania as electron transport material and p-type organic material as HTM. The interface between titania and organic HTM is of crucial importance as excitons generated in the organics can only be dissociated with the aid of an inner electrical field such as the built in pn-junction. After exciton dissociation, the separated negative charge carriers travel along the titania structure and are collected by the corresponding electrode. Therefore, the film morphology plays an important role in device performance, as it defines the interface area and pathways for electron transport. In order to have sufficient available interface, a high surface-to-volume ratio is favorable. Therefore, titania nanostructures with mesopores are commonly employed as photoanodes in both ssDSSCs and hybrid solar cells. A very promising route for preparing mesoporous titania films is sol-gel chemistry in combination with diblock-copolymer templates. This approach gives control over the size of the titania nanostructures and mesopores, which has also been successfully used for other applications such as photocatalysis, anti-reflection coating and Li-ion battery materials [10–14]. Another important parameter for the titania films is the thickness. As dyes anchor on the surface of the titania, the titania thickness directly relates to the amount of dye loading and correspondingly to the light harvesting. However, the film thickness also decides the pathway lengths for charge carriers. Longer distances lead to an increased probability of charge carrier recombination and thus loss of efficiency. Besides the fabrication of suitable titania films, the subsequent backfilling with HTMs is very important. Here, a model of organic HTMs infiltrating into mesoporous titania films is adopted in this work, which implies that the titania films determine the morphology of the organic HTMs as well. A deciding factor for solar cell performance is the degree of pore filling. It has a strong impact on the solar cell performance [15]. A higher filling degree leads to a larger interface area between donor and acceptor, i.e. more potential sites for exciton dissociation. Additionally, the crystalline order of polymer HTMs is crucial in both ssDSSCs and hybrid solar cells. The mobility of positive charge carriers in the crystalline regions is several orders of magnitude higher than in the amorphous regions, thus a conducting polymer with a high crystallinity is desirable [16, 17]. A large polymer



crystallite is beneficial for high mobility of positive charge carriers and low recombination of charge carriers [18].

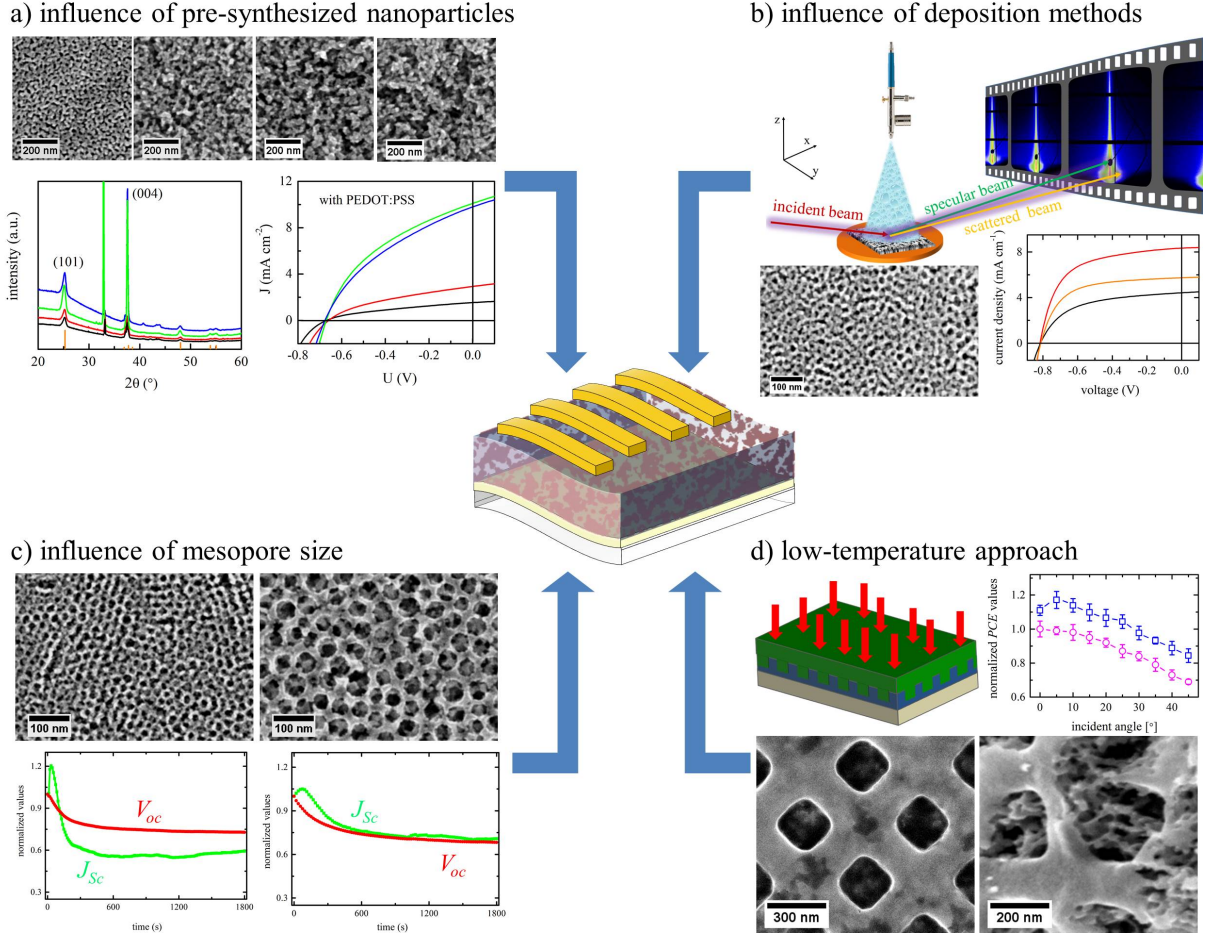


**Figure 1.1:** A schematic illustration of a titania-based thin film solar cell (in the center) along with different research projects included in the present thesis. The topics from (a) to (d) are presented in chapter 5 to chapter 8 correspondingly.

The main target of the present thesis is to address the correlation between morphology and solar cell performance. By tailoring nanostructured titania films, the morphology and crystalline order of titania films and organic HTMs are investigated and the subsequent influence on solar cell performance is studied. To start with, the theoretical background is introduced in chapter 2, including the basics of polymers, titania and sol-gel synthesis, the working principles of solar cells, and the fundamentals of the scattering methods used for probing the film nanostructures. Thereafter, chapter 3 describes the used characterization instruments as well as their operating parameters, followed by the sample preparation methods in chapter 4. Research results as the main part of the present thesis are discussed

from chapter 5 to chapter 8. An overview of different research projects are schematically illustrated in figure 1.1. In more detail the discussed topics are:

Typically, titania films obtained from sol-gel synthesis are amorphous and the degree of crystallinity is still relatively low even after 500 °C calcination. One effective way to improve the crystallinity is to process the amorphous film under much higher temperature, but the high-temperature processing often leads to a great decrease in the specific surface area and thereby a reduced dye loading [19]. Moreover, an increased calcination temperature implies an increased energy consumption. Therefore, the question arises whether the degree of crystallinity can be improved in the sol-gel-synthesized titania films at processing temperatures below 500 °C. In chapter 5, an approach to enhance the film crystallinity by incorporating pre-synthesized crystalline titania nanoparticles into the templated titania network structure is investigated. The influence of nanoparticles on morphology, crystallinity and conductivity of titania films and the final solar cell performance is discussed.

Besides the sol-gel chemistry, the deposition methods also strongly influence the resulting films. Spray coating as a cost-effective technique is selected to deposit titania photoanodes. As known, the spray coating technique contains kinetic processes with great complexity. Therefore, a question is raised: is it possible to monitor these kinetic processes? Chapter 6 gives a view on the structural evolution of titania/PS-b-PEO films (with and without incorporating pre-synthesized crystalline titania nanoparticles) during spray deposition. Also, the different methods to backfill the organic HTM into mesoporous titania films are demonstrated. The combined effect of nanoparticles and deposition method on the solar cell performance is discussed.

As pointed out above, the structure of titania photoanodes is a key point to the device performance. The mesoporous titania films consist of two parts, titania nanostructures and mesopores. The question whether the pore size also has any impact on the solar cell performance is addressed. In chapter 7, two titania films with ordered pore arrays but with different pore sizes are fabricated. The crystalline order and stability of a polymer HTM inside pores with different sizes, which are directly correlated to the performance and stability of the solar cells, are discussed.

For photovoltaic applications, high-temperature treatment is usually required to crystallize the titania film. However, a reduced manufacturing temperature has a high significance regarding energy efficiency and production costs. Is it possible to fabricate mesoporous titania films at low temperatures for solar cell applications? This question is dealt with in chapter 8. A special titania precursor is employed to synthesize mesoporous titania films at low temperatures. Moreover, artificial superstructures are introduced onto the mesoporous titania films at low temperatures to improve the solar cell performance

compared to the non-structured cells. The characterization of the angular dependent absorption and *PCE* of solar cells gives a practical proof of the positive effect of artificial superstructures.

The conclusion of the thesis is given in chapter 9, which systematically summarizes the obtained results based on various investigations. Finally, a brief outlook for further studies on the basis of this thesis is provided.



## 2 Theoretical aspects

The materials, methods and processes used and developed in this thesis are for the study of solid-state dye-sensitized solar cells (ssDSSCs) and hybrid solar cells. In this chapter, the theoretical background for all materials, characterizations and devices is discussed. The basic knowledge of polymer physics is given in section 2.1. Since diblock copolymers and conductive polymers are primarily used in this work, they are discussed in detail individually. Afterwards, titania as electron acceptor in ssDSSCs is discussed in section 2.2, regarding its property and its preparation. An overview about titania-based solar cells is described in section 2.3. Lastly, the basic principles of different x-ray scattering techniques, which were used in the present thesis to probe thin films, are discussed in section 2.4 .

### 2.1 Polymer basics

This section covers a basic introduction to polymers. General properties and definitions of polymers are given, followed by a description of their crystallization behavior. A detailed discussion about diblock copolymers is presented in section 2.1.1, followed by the fundamental aspects of conducting polymers in section 2.1.2.

#### Basic definitions

Polymers, also referred as macromolecules, are made up of a large number of one or more types of repeating subunits. The subunit is called monomer, which are connected to each other by covalent bonds. The number of monomeric units is defined as the degree of polymerization. Knowing the molecular mass of the monomers, the molecular weight of the polymer  $M$  can be calculated. Typically, polymers have a  $M > 10$  kg/mol. The molecules with  $M$  between 1 kg/mol and 10 kg/mol are called oligomers, whereas micromolecules are referred to the molecules which have a  $M$  less than 1 kg/mol.

In order to understand polymer architecture and nomenclature, polyethylene (PE), which has a particularly simple structure, is set as an example for illustration. It is

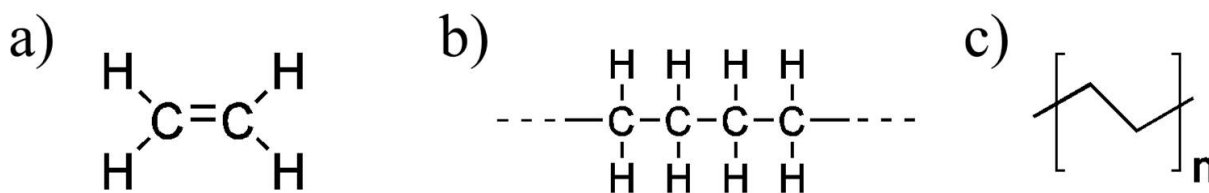


**Figure 2.1:** a) Ethylene monomer, b) Lewis structure formula, and c) skeletal formula. The polymer PE serves in this case as an example for polymers.

depicted in figure 2.1. Ethylene, as shown in figure 2.1a, is the monomer and its number determines the degree of polymerization. Figure 2.1b shows the Lewis structure formula of PE, which gives a detailed description of its architecture, including the composition of atoms and the formation of bonds. A typical way to abbreviate structure formulas of PE is shown in figure 2.1c, denoted as skeletal formula, where  $n$  gives the number of repetitions. Thus, a repeatedly linked monomer A gives a polymer A-A-A-...-A-A-A, which can be named polyA or PA on the monomer-based nomenclature, and its chemical formula can be written like PE.

Rather than a unique degree of polymerization, polymers usually have various chain lengths and thereby various molar masses. Therefore, statistical mean values are required for a full characterization. One of them, the number average molar mass  $M_n$ , is the ordinary arithmetic average of the molecular masses of the individual polymers

$$M_n = \frac{\sum_i n_i M_i}{\sum_i n_i} \quad (2.1)$$

where  $M_i$  and  $n_i$  are the molar mass and chain number of component  $i$ , respectively. Instead of using  $M_n$ , the average molecular weight  $M_w$  is also employed to describe the molar mass distribution in terms of weight fractions.  $M_w$  is described by

$$M_w = \frac{\sum_i n_i M_i^2}{\sum_i n_i M_i}. \quad (2.2)$$

Normally,  $M_w$  is larger than  $M_n$ . The ratio of  $M_w$  to  $M_n$  is called the polydispersity index  $PDI$ .  $PDI$  is given by

$$PDI = \frac{M_w}{M_n} = U + 1 \quad (2.3)$$

where  $U$  is the inconsistency. In the case of  $U = 0$  the polymer shows a uniform molar mass distribution, also known as perfect monodisperse.

Molar mass distributions greatly depend on the methods used in the polymerization synthesis, and most of them can be categorized into two classes. The first class of synthesis methods is called step polymerization, where monomers and polymer fragments can be coupled with each other randomly. This way, the molar mass distribution is very broad, which is often described by the Schulz-Zimm distribution. In the second class, known as chain polymerizations, triggers for polymerization can only react with monomers, called reactive centers. Each time a new monomer is linked to reactive centers, the active site is regenerated, thus the polymer grows only at one end. In this way, a much sharper distribution can be obtained, which is in a good agreement with the Poisson-distribution.

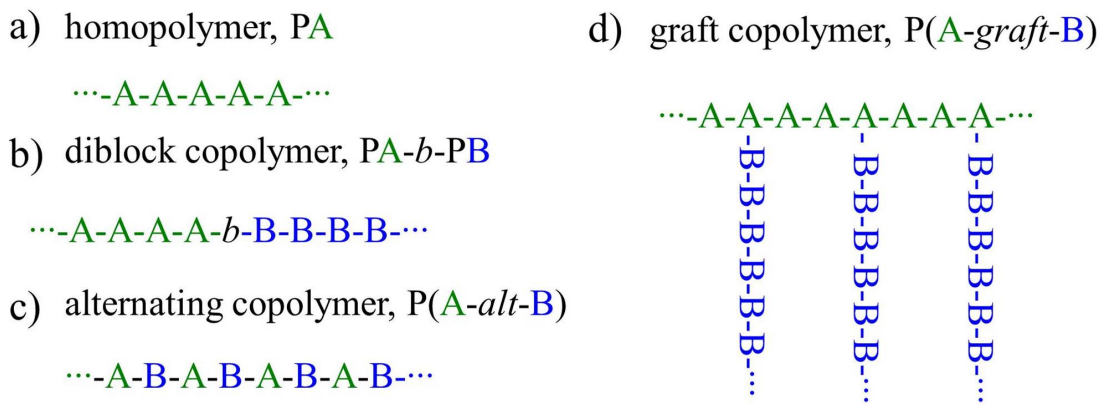


**Figure 2.2:** a) Homopolymer, b) diblock copolymer, c) alternating copolymer and d) graft copolymer.

Depending on the sequence and the type of monomers, various polymer structures are possible. With respect to polymer shapes, the most simple one is the chain-like structure. By substituting the hydrogen atoms with additional side groups, more complex polymer structures can be obtained, such as ring-like structures, brush-like geometries, or star-shaped polymers. Moreover, different types of monomers can be linked together to form a polymer. If the polymer consists of only one type of monomer, it is called homopolymer (figure 2.2a). If more than one type of monomers are involved in the polymer formation, the obtained polymer is named as copolymer. It can be divided into several subspecies based on the arrangement of the different monomers, as shown in figure 2.2. If a homopolymer subunit PA and the other homopolymer subunit PB are linked by covalent bonds, a diblock copolymer PA-*b*-PB is formed (figure 2.2b). If the polymer consists of alternating monomers A and B, it is called alternating copolymer (figure 2.2c). If A and B is not linked in such an order, the polymer is named as random copolymer. The so-called graft copolymer describes a special branched copolymer where some small side groups are replaced by long side chains. Additionally, the side chains are

structurally different from the back bone. Figure 2.2d shows a schematic sketch of a graft copolymer.

## Crystallization

Polymer crystallization describes a process where molecular chains of polymers are partially aligned or folded to form ordered regions. In the crystallization process, temperature plays an important role, since the polymer can change from one state to another along with temperature variation. There are several characteristic temperatures for polymers, which are shortly described in the following.  $T_m$ , the melting point, above this temperature polymers are in the liquid phase, where the polymer chains lose their molecular ordering and become mobile.  $T_g$ , the glass transition temperature, below this temperature polymers are in the glass state, where polymer chains lose their large scale mobility completely and are basically frozen. Between  $T_m$  and  $T_g$ , the polymer chains lose some of long-range mobility. When the temperature decreases from  $T_m$ , amorphous regions can transit into crystalline regions. The temperature, where the crystallization process starts, is called the crystallization temperature  $T_c$ . In general,  $T_c$  lies between  $T_g$  and  $T_m$ . With further decrease of the temperature, more crystalline regions are formed, e.g. the polymer crystallinity increases. Once the temperature reaches  $T_g$ , amorphous regions can no longer transit into crystalline regions due to the motionless polymer chains.

The crystallinity of conducting polymers plays a critical role in photovoltaic applications, as higher crystallinity typically gives higher mobility of positive charge carriers [16, 17]. However, unlike inorganic materials or metals, polymers cannot crystallize completely and crystalline regions are typically separated by amorphous regions. The degree of crystallinity typically ranges between 10 % and 80 % for polymers, thus crystallized polymers are usually referred to the semi-crystalline state. In crystalline regions, polymer chains are folded into layered structures with a thickness of  $d_c$  as shown in figure 2.3a. It is noteworthy that  $d_c$  matters strongly with  $T_c$  rather than the molecular weight of the polymer [20]. The layered structures can grow laterally (perpendicular to the polymer chains) up to micrometers. The growth mechanism of polymer crystals is described by a multi-stage growth model, as schematically illustrated in figure 2.3a. The first step of polymer crystallization is the nucleation. The nuclei can be dust particles, impurities, or defects. The way starting from the pre-existing nuclei is called heterogeneous nucleation. Another type of nucleation is known as homogeneous nucleation. In this case, the thermal fluctuations of the system can result in a ordered arrangement of polymer chains which serves as the nuclei. After the onset of nucleation, a transient state is observed, which is named the formation of a mesomorphic layer. In this phase



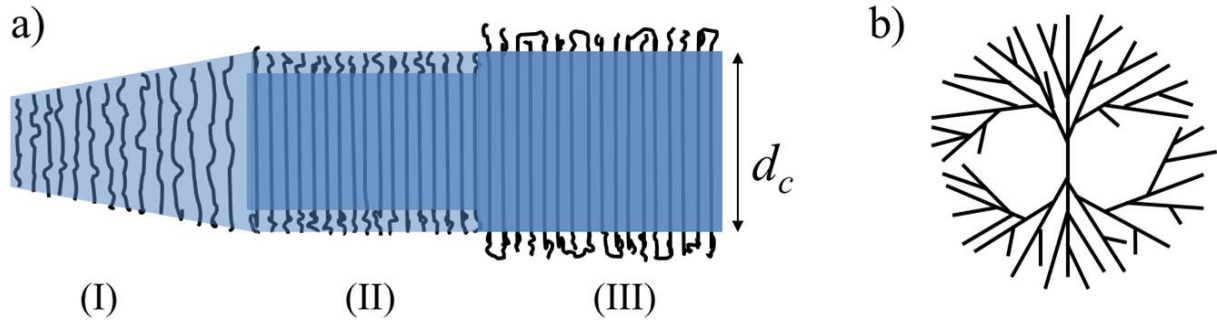


**Figure 2.3:** a) Schematic representation of a crystal growth with a multi-stage growth model: (I) formation of a mesomorphic layer, (II) solidification of the core and (III) stabilization of the crystal via surface ordering.  $d_c$  indicates the thickness of the crystal. b) Schematic model of a spherulite crystal structure.

the polymer chains are aligned by epitaxial forces [21], which can be considered as the formation of preliminary lamellar stacks. Due to high inner mobility more polymer chains are folded into lamellar stacks. When this procedure continues till a certain degree, the growth of lamellar stacks stops and a more regular alignment of the polymer chains occurs. The mesomorphic state solidifies via the core crystallization, which results in the formation of a block, as depicted in the stage II of figure 2.3a. Finally, the ordering of polymer chains on the surface increases for stabilizing the crystal structures. Generally, without a temperature gradient the growth of the polymer crystals occurs radially from a nucleation point, which leads to spherical aggregates (figure 2.3b). This way, the crystal aggregates are called spherulite. Spherulites have semicrystalline structure where the amorphous regions are located in between the highly ordered lamellar stacks. In the case of the diblock copolymer poly(styrene-*b*-ethylene oxide) (PS-*b*-PEO), the spherulite crystallization is frequently observed in the formation of PEO crystal structures [22]. In this thesis PS-*b*-PEO is chosen as the structure-directing agent for the preparation of the mesoporous titania films.

### 2.1.1 Diblock copolymers

As shown in figure 2.2b, the diblock copolymer consists of two different homopolymer blocks which are linked together with a covalent bond. In the case of figure 2.2b, the polymer is termed as polyA-block-polyB, short as PA-*b*-PB. Generally, PA and PB in the diblock copolymer have different degrees of polymerization  $N_A$  and  $N_B$ , from which the so-called block ratio  $f_A$  and  $f_B$  can be calculated:

$$f_A = \frac{N_A}{N_A + N_B} \quad (2.4)$$

$$f_B = \frac{N_B}{N_A + N_B} = 1 - f_A \quad (2.5)$$

Recently, block copolymers have received great attention because a microphase separation can occur between two blocks to form periodic nanostructures when PA and PB are incompatible. To minimize the system energy, each homopolymer block of the copolymers tends to aggregate together and thereby domains are formed. Because PA and PB are covalently linked to each other, they cannot demix macroscopically as in polymer blends. The size of the domains is determined by the chain length  $y$  of each block.

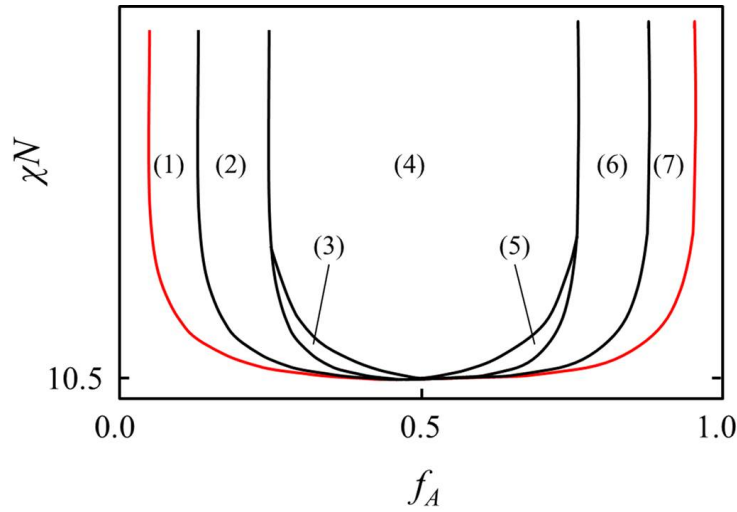


**Figure 2.4:** Typical phase diagram of a diblock copolymer PA-b-PB. With increasing block ratio  $f_A$ , the A domains inside the B matrices undergoes a morphological transition from (1) spheres via (2) hexagonal cylinders to (3) gyroid. When  $f_A = 0.5$ , (4) a lamellar nanostructure is achieved. For  $f_A > 0.5$ , the structure inverts to the scheme that B domains are incorporated in the A matrices and undergoes the same transition with: (5) gyroid, (6) hexagonal cylinders and (7) spheres. The red line indicates the order-disorder transition (ODT) below which the diblock copolymer is a homogeneous melt without ordered nanostructures. The image is adapted from [23].

The interaction parameter  $\chi$  also known as the Flory-Huggins interaction parameter is an important parameter for diblock copolymers, which describes the interaction between two homopolymers PA and PB [24, 25].

$$\chi = \chi_S + \frac{\chi_H}{T} \quad (2.6)$$

where  $\chi_S$  and  $\chi_H$  are the entropic and enthalpic contribution, respectively. Normally, an intermixed phase of the two blocks can be formed when the value of  $\chi$  is sufficient small. Some polymers, for example, can be dissolved in solvents at elevated temperatures rather than room temperature. The reason is that the  $\chi_H$  decreases with increasing temperature. The degree of microphase separation in a diblock copolymer greatly depends on the factor  $\chi N$ . For instance, in case of a symmetric diblock copolymer the critical value of  $\chi N$  is about 10.5. When  $\chi N$  is far smaller than the critical value, an intermixed phase is built when the diblock copolymer has a short chain length. Upon increasing the  $\chi N$  value, compatibility between the two blocks decreases, which leads to a composition fluctuation in the homogeneous melt. When  $\chi N$  reaches the critical value, a so-called weak segregation limit (WSL) is observed. With continuously increasing the  $\chi N$  value, the repulsion between the two blocks enhances and a strong segregation limit (SSL) is reached in the system. Upon this point, a sharp interface between blocks can be observed.

For a symmetric diblock copolymer ( $f_A = 0.5$ ), microphase separation typically gives periodic lamellar nanostructures. Moreover, various ordered nanostructures can be obtained by varying the value of  $f_A$ . In figure 2.4 the possible morphologies for a diblock copolymer PA-b-PB are depicted in a phase diagram. By changing  $f_A$  and  $\chi N$ , the structures which form during the phase separation can be tuned. The red curve in figure 2.4 indicates the order-disorder transition (ODT) below which the diblock copolymer is a homogeneous melt without ordered nanostructures. However, typically asymmetric phase diagrams are reported in literature due to the chemical differences between two blocks A and B [26–28]. Moreover, other factors have an influence such as different conformation of polymer blocks or some specific features of the blocks like crystallization. In addition, confinement effects have a strong impact on the phase behavior. For example, in case of a thin film of a diblock copolymer, interfacial interactions might result in different morphologies than those defined in figure 2.4.

## 2.1.2 Conducting polymers

Conventionally, polymers are considered as good insulators, which are usually used to insulate good electrical conductors such as metals. As research moves along, it was found that the electrical conductivity of polymers can be possibly tuned over a range from insulating to metallic. Conducting polymers have received substantial attention in technological applications. The significant breakthrough in the development of conducting polymers occurs in 1977 when a doping process was applied to an intrinsically insulator, polyacetylene (PA). This polymer has an intrinsic electrical conductivity lower than  $10^{-5} \Omega^{-1} \text{ cm}^{-1}$ . After doping with oxidizing or reducing agents the electrical conductivity

can reach values up to  $10^3 \text{ } \Omega^{-1} \text{ cm}^{-1}$  [7]. Due to this important discovery, the Nobel Prize was awarded to Shirakawa, MacDiarmid and Heeger in 2000. For conducting polymers, a conjugated  $\pi$ -electron system with alternating single and multiple bonds is required. A region of overlapping p-orbitals allows the delocalized  $\pi$  electrons cross all the adjacent aligned p-orbitals. In this way, the  $\pi$ -electrons belong to a group of atoms rather than a single atom. From an energetic perspective, bonding  $\pi$ - and antibonding  $\pi^*$ - bands form as a consequence of the overlap of  $\pi$  orbitals. The  $\pi$ - and  $\pi^*$ - bands are referred as the highest occupied molecular orbital (HOMO) and the lowest unoccupied molecular orbital (LUMO), respectively. If the system is in the ground state, all of the  $\pi$ -electrons are located in the HOMO and leaving the LUMO empty. However, electrons can be excited into higher energetic states and then occupy states in the LUMO.

### Band structure and charge carriers

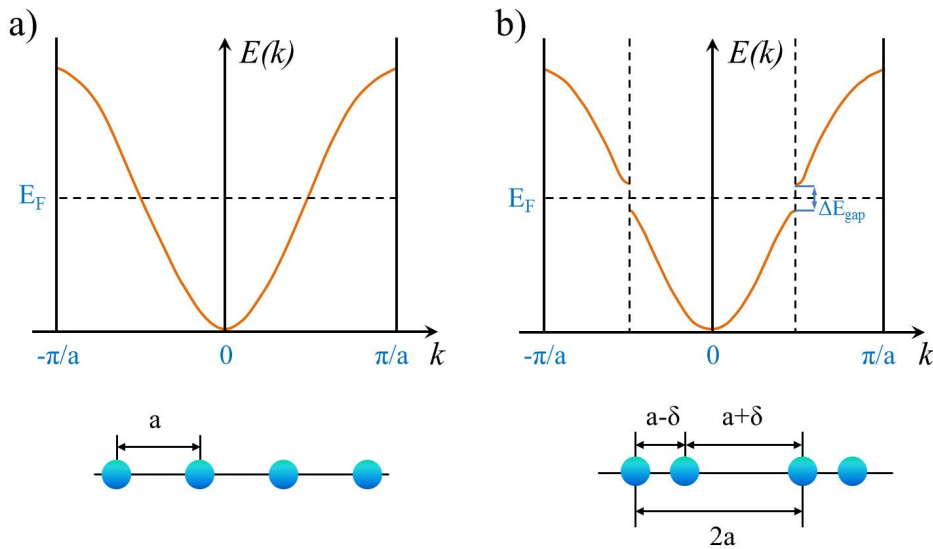


**Figure 2.5:** Schematic illustration of Peierl's instability theorem: band structures and sketches of a) an undistorted 1D lattice with lattice spacing  $a$ , and b) a distorted 1D lattice with distortion of  $\delta$  and periodicity of  $2a$ .

The origin of the band structure of conjugated polymers can be described by Peierl's instability. In this theorem, a one dimensional (1D) crystal with constant lattice spacing  $a$  is assumed. If each atom contributes one electron, the band is half-filled up to the Fermi level  $E_f$  as shown in figure 2.5a. However, in case of conducting polymers such as polyacetylene, the backbone is conjugated, the alternation of sigma and double bonds leads to a new periodicity of the 1D crystal since they differ in length (figure 2.5b). In order to lower the total energy of the system, the Brioullin zone is broken at the position

of  $k = \pm \pi/2a$  in case of the scheme described in figure 2.5b and a new band gap  $\Delta E_{gap}$  is formed. In polymers, the values of  $\Delta E_{gap}$  matters strongly with structure, degree of polymerization and doping. Typically, the Peierl's instability for polymers gives rise to band gaps ranging from 1.5 eV to 3 eV [29]. For example, P3HT is a widely used conducting polymer with a band gap of 1.9 eV - 2 eV.

In conducting polymers, charge carriers are generally generated by doping or by light excitation. Unlike electrons or holes in inorganic systems, charge carriers are transported within polymers by quasiparticles (QPs), which combine the charges and lattice distortion. Three primary quasiparticles, termed as solitons, polarons and bipolarons, are present in systems consisting of degenerate ground states. Taking PA as an example, an overview of these three quasiparticles is schematically described in figure 2.6. Solitons have three

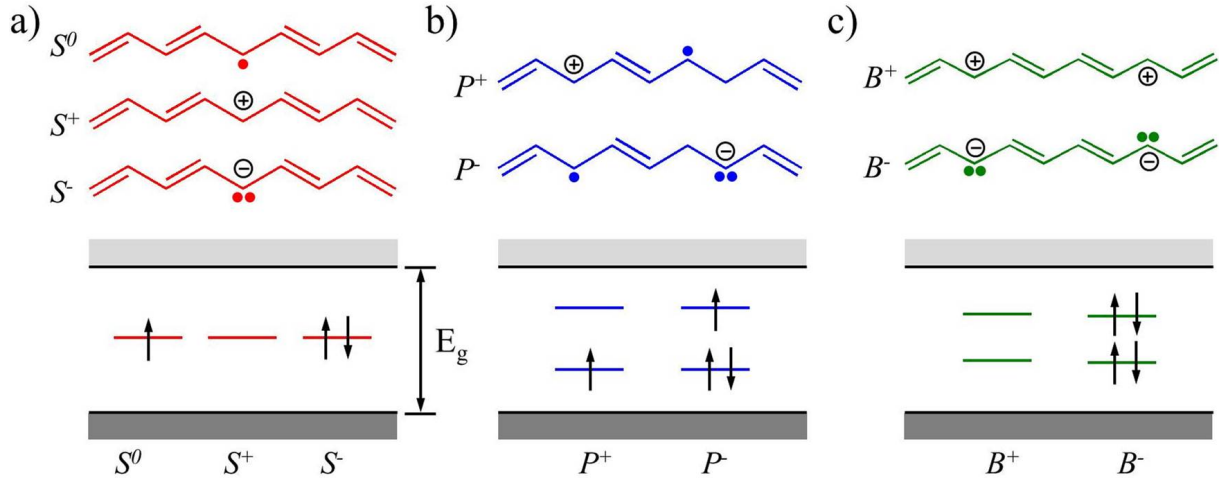


**Figure 2.6:** Schematic illustrations of a) solitons, b) polarons, and c) bipolarons in a conducting polymer PA. Solitons exist in the form of  $S^0$ ,  $S^+$  and  $S^-$ . Positive and negative polarons are represented as  $P^+$  and  $P^-$ . Bipolarons have two positive  $B^+$  or two negative charges  $B^-$ . The three red short lines in a), four blue short lines in b) and four green short lined in c) represent the energetic band states of all quasiparticles which stay within the band gap  $E_g$ .

variation (figure 2.6a). A neutral soliton ( $S^0$ ) with no charge and a spin of  $1/2$  is created when two degenerate ground states meet. When an electron is taken away from the polymer chain, a positive charge is left behind, a positive soliton ( $S^+$ ) with a spin of 0 is generated. Similarly a negative soliton ( $S^-$ ) is produced by donating an electron to the polymer chain. Since no unpaired spins exist, the spin of  $S^-$  is 0. A polaron can be thought as a bound state of a neutral soliton and a charged soliton (figure 2.6b). Therefore, polarons are charged and have a spin of  $1/2$ . While bipolarons are charged and spinless (figure 2.6c). Bipolarons are formed out of 2 polarons.

## Charge transport

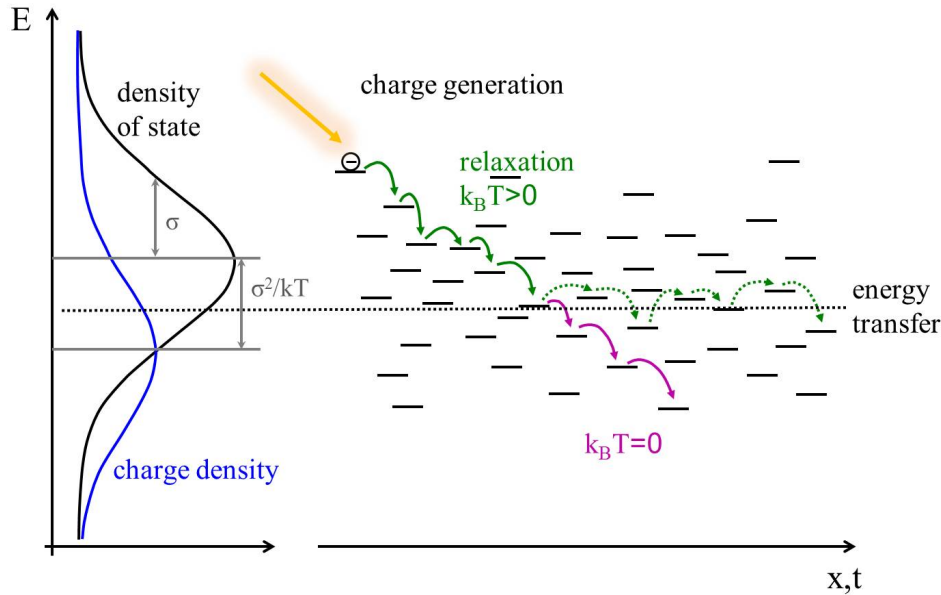


**Figure 2.7:** Schematic illustration of hopping transport of a charge carrier in a conducting polymer. In left, black and blue curves indicate density of states distribution and charge density distribution, respectively. Right, dashed lines represent localized energetic states. A generated charge hops downwards accompanied with relaxation, and hops upwards with prerequisite of obtaining external energy. The middle dotted line indicates the transport energy. Adapted from reference [30].

The transport of charge carriers in polymer systems is distinct from band transport found in inorganic crystalline semiconductors. The aforementioned QPs are able to move freely along the chain backbone due to the existence of a conjugated system of overlapping  $\pi$ -orbitals. However, the so-called hopping transport occurs when the charge carriers transfer to neighboring chains. This is because of spatial and energetic disorders in conducting polymers. The Gaussian disorder model has been developed to illustrate the hopping mechanism, as schematically shown in figure 2.7. A Gaussian density of states with width  $\sigma$  is used to describe the energetic disorder of hopping sites. Under steady-state conditions, the charge density lies below the center of density of states by a thermal activation energy  $-\sigma^2/k_B T$ . A charge is generated at a high energetic site (figure 2.7) and then hops to a neighboring state via tunneling. The neighboring state has a lower energy, thus the hopping process is accompanied with a relaxation. When the charge reaches the area between the centers of the charge density and the density of states, it can potentially be thermalized. If the charge gains the thermal energy from the system, it is able to hop towards energetically higher states. If not, it will hop down until it reaches a trap state.

In the former process, there will be more accessible states for charge carriers if a higher temperature is applied to the system. For the latter case, the trap state makes charge carriers immobile, thereby they do not contribute to the electrical conductivity. It is noteworthy that, the mobility of charge carriers is much higher in crystalline regions than in amorphous regions. For example, the mobility of positive charge carriers in the P3HT crystalline regions can reach  $0.1 \text{ cm}^2/\text{Vs}$ , whereas lower than  $10^{-5} \text{ cm}^2/\text{Vs}$  in amorphous regions [16,17]. But in general, charge carriers travel slower in polymers than in metals.

## 2.2 Titania and sol-gel synthesis

Titania has been widely used as photoanodes in photovoltaic applications due to its long-term stability, non-toxicity and proper valence and conduction band positions. In particular, its anatase phase is more favorable because of the larger specific surface area, longer charge-carrier lifetime and higher charge-carrier mobility [31–33]. The basic properties of titania are discussed in section 2.2.1. For photoanodes, a high surface to volume ration is essential as the interface between titania and p-type semiconductors is the site for current generation. Therefore, mesoporous titania nanostructures are of great interest. In this thesis, a so-called block-copolymer-assisted sol-gel synthesis is applied to manufacture nanostructured titania films. Section 2.2.2 gives an overview about the basics of sol-gel process, and structuring titania films with polymer template is described in section 2.2.3.

### 2.2.1 Properties of titania

In nature, titania ( $\text{TiO}_2$ ) has three crystalline forms: anatase, rutile and brookite [34]. As inorganic crystals, all these three phases display high densities, high refractive indexes and large band gaps. The detailed parameters are listed in table 2.1. However, anatase and brookite are thermodynamically metastable, whereas rutile is a thermodynamically stable phase. Due to the difficulties in synthesis of a pure phase, brookite has been rarely reported in photovoltaic applications [35,36]. Thus, the following discussion is mainly focused on anatase and rutile rather than brookite.

The unit cells of anatase and rutile are depicted in figure 2.8. In both cases, the  $\text{TiO}_6$  octahedron is not exactly regular. A slight orthorhombic distortion is present in rutile, while in anatase a significant distortion leads to a symmetry that is lower than orthorhombic. The different degree of distortion results in different crystal structures. In the rutile phase, the octahedrons connect to each other at opposing edges, which leads to a linear packing of the octahedrons. In the anatase polymorph, the highly distorted octahedrons

	density (g cm <sup>-3</sup> )	refractive index	band gap (eV)
anatase	3.83	2.57	3.2
rutile	4.24	2.95	3.0
brookite	4.17	2.81	3.1-3.4

**Table 2.1:** Crystal phases of titania, with their corresponding refractive index, density, and energy bandgap [35, 37–39].

only link to each other at neighboring edges. As a consequence, a zigzag packing of the octahedrons forms. The closer packing of  $\text{TiO}_6$  octahedron in linear landscape is the reason for the higher density and thermodynamical stability of rutile phase. Moreover, the linear packing leads to shorter Ti-Ti interionic distances in rutile phase (3.57 Å and 2.96 Å) than in anatase phase (3.79 Å and 3.04 Å) [40]. Therefore, the surface area per unit volume is larger for anatase. In contrast, Ti-O interionic distances are slightly longer in rutile (1.94 Å and 1.99 Å) than in anatase (1.91 Å and 1.95 Å) [40].

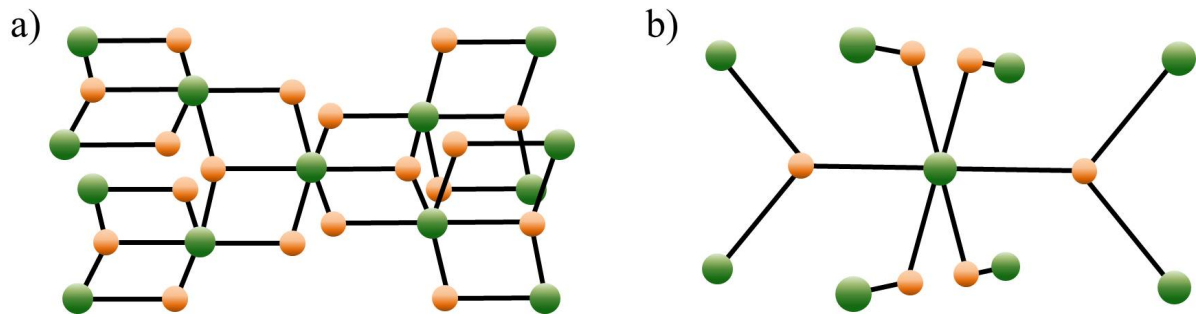


**Figure 2.8:** Unit cell structures of a) anatase and b) rutile. Green and orange spheres represent titania and oxygen atoms, respectively.

Both anatase and rutile are indirect semiconductors with band gaps of 3.0 eV and 3.2 eV, respectively [38, 41]. In both cases, the strong p-d hybridizations between the 2p states of O and a few 3d states of Ti result in the formation of the valence bands. While 3d states of Ti with a few 2p states of O and 3p states of Ti comprise the conduction bands [42]. Due to the structural differences, the width of Ti 3d band and p-d hybridization vary, which is responsible for the difference in the band gap for rutile and anatase. Nevertheless, the large band gaps enable either anatase or rutile to have a great UV absorbing ability. The absorption edges of anatase and rutile occur at a wavelength of 388 nm and 413 nm, respectively. Along with the bio-compatibility, titania is an important ingredient for sun screens to prevent the negative effect of UV irradiation. Regarding organic solar cells, it is a new strategy to apply a compact titania layer as a hole blocking layer. Besides



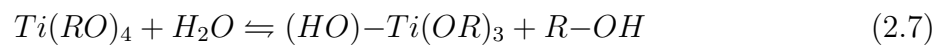
the electronic contribution, the titania layer is potentially able to protect photoactive polymers from UV degradation.

For applications in photocatalysts, self-cleaning materials and photoanodes of solar cells, nanostructured titania always demonstrates high performance levels due to its high surface-to-volume ratio. However, when the titania grain size gets smaller than twice the size of its exciton Bohr radius, quantum confinement occurs as the excitons are squeezed. Under this effect, a decreased titania size usually leads to an increased band gap. The shift of band gap splits the band gap of titania. However, a blue shift of the band gap energy is observed to be only 0.1 eV - 0.6 eV in titania [43]. For a clear observation of band gap shift, the quantum-size of titania is required to be smaller than 2 nm [44]. The quantum-sized objects offers very high ratio of surface area to volume, but on the other hand gives high density of trap states which is detrimental to the device performance [45].

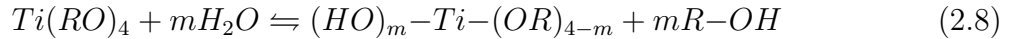
### 2.2.2 Principles of sol-gel synthesis

The sol-gel process is a wet chemical technique. It was firstly developed by Jacques-Joseph Ebelmen in 1846, who synthesized tetraethoxysilane (TEOS) by mixing silicon tetrachloride ( $\text{SiCl}_4$ ) and ethanol. It was found that TEOS could hydrolyze with moisture and further reactions lead to the formation of a network of silica. After over a century of development, the process has been well established for the fabrication of metal-oxide, ceramic, and/or ceramic-organic materials. The sol-gel synthesis is a typical bottom up method where small precursor monomers convert to a colloidal solution (sol) or an integrated network (gel) via chemical reactions. Metal alkoxides are the typical precursors, which typically contain a core of a metal atom and several arms of organic groups 'R'. For titania sol-gel, the precursors can be written as  $\text{Ti}(\text{OR})_4$ . The chemical activity of the titania precursors strongly depends on different types of R.

$\text{Ti}(\text{OR})_4$  is chosen as an example to illustrate the sol-gel process. Firstly,  $\text{Ti}(\text{OR})_4$  is fully dissolved in an organic solvent. It is important to note that, the homogeneous precursor solution is the prerequisite for the following chemical reactions starting at a molecular level. Afterwards, other reactants are added to  $\text{Ti}(\text{OR})_4$ . Take water for example, with addition of water the titania precursor monomers start to react with water molecules steadily in the solution. The reaction with  $\text{H}_2\text{O}$  is called hydrolysis as a OR group is replaced by a hydroxyl group:



$\text{Ti}(\text{OR})_4$  can react with more than one water molecules at the same time as a result of an excess of water and/or the use of a hydrolysis catalyst.



where  $m$  is not larger than 4. When  $m = 4$ , the reaction is called complete hydrolysis. After the generation of hydroxy groups (-OH), a polycondensation process occurs. Two partially hydrolyzed monomers connect via a Ti-O-Ti bond. Oxygen bridges form between two monomers by releasing a  $H_2O$  or  $ROH$  molecule. The oxolation has two mechanisms in terms of by-products.



The continue of the polycondensation process is able to build a large Ti-containing molecule or even an oxide network. The final oxide structure greatly depends on the hydrolysis and polycondensation reactions, which can be controlled by many parameters such as the type of titania precursor, the amount of water, the use and/or the type of catalyst, the ratio of reactants, temperature and aging time. In the present thesis, concentrated HCl is used as the catalyst, which provides a strong acidic environment for the hydrolysis and polycondensation reactions. In this way, the active sites for linkage are preferably located at the end of chains rather than at the center. Moreover, the strong acidic environment promotes the hydrolysis reaction but suppresses the polycondensation reaction, which results in a delayed gelation process [46]. As a consequence, a transparent sol solution is obtained instead of white precipitates when the aging time is not too long.

### 2.2.3 Structure direction with polymer template

Mesoporous titania films are favorable for solid-state dye-sensitized solar cells (ssDSSCs). On one hand, more dye molecules can anchor the titania due to its high specific surface area. On the other hand, mesopores enable solid-state hole transporting materials (ssHTMs) to penetrate the whole titania interconnected network. The usual sol-gel synthesis generally gives rise to compact titania films or films with rare and small pores, which prevent ssHTM infiltration. Moreover, the resulting nanostructures are often ill-defined. In order to meet experimental needs, possibilities for tuning the morphologies and structure sizes are highly demanded. To achieve this target, the use of copolymers is a common way to direct titania nanostructures. In this thesis, a diblock copolymer with amphiphilic nature is selected as the structure-directing agent in combination with the sol-gel process. As the hydrophobic block is covalently linked to the hydrophilic

block, the diblock copolymer tend to undergo microphase separation, as explained in section 2.1.1. Through adjusting  $\chi$  and/or  $N$ , different morphologies are obtained, as shown in figure 2.4. In solution, the copolymer can form micelles with the aid of a "good-poor" solvent pair. The "good" solvent, also termed as non-selective solvent, is used to dissolve both hydrophobic and hydrophilic blocks. While only one block can be dissolved in the "poor" solvent which is also called selective solvent. Given the fixed solvents and external parameters like temperature and humidity, the size and shape of the micelles are determined by the weight ratio and chain length of the two blocks [47]. In order to produce titania nanostructures, the titania precursor is added to the polymer solution. It is important to note that, there is a prerequisite for the polymer template directing titania nanostructures: only one block of the diblock copolymer is allowed to incorporate titania species. In the present thesis, poly(styrene-block-ethylene oxide) (PS-*b*-PEO) is selected as structure-directing agent and the titania species are selectively bound to the hydrophilic PEO chains. The method that combines diblock copolymers with sol-gel process is termed as diblock-copolymer-assisted sol-gel synthesis.

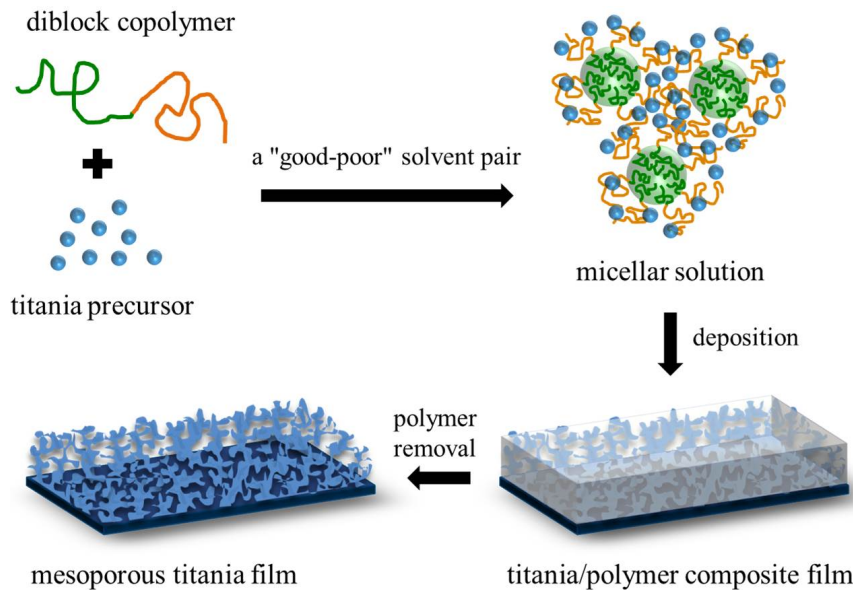


**Figure 2.9:** Schematic illustration of the production of nanostructured titania films using the diblock-copolymer-assisted sol-gel synthesis.

The principle of the diblock-copolymer-assisted sol-gel process is schematically shown in figure 2.9. The block copolymers are dissolved in the good solvent, followed by slow addition of the titania precursor and the poor solvent. Since one block cannot be dissolved in the poor solvent, the interface energy between this block and the good-poor solvent pair increases, which drives the copolymer to form micelles in the solution. It is important to note that, the self-assembly of the diblock copolymer is a dynamic equilibrium where

the fusion and separation of the micelles are reversible. Meanwhile, the hydrolysis and polycondensation processes of titania precursors start and the resulting titania species are incorporated into the hydrophilic PEO domains. Zhao et al. demonstrated that hydrogen bonding bridges were the main reason for PEO chains hosting inorganic species in a strong acid environment [48]. The incorporation process in turn makes the PEO domain an active site for chemical reaction. Moreover, the dynamic equilibrium of micelles is also influenced by the incorporation process, since the size of titania species increases steadily over time. The cross-linking of the inorganic material may connect two or more micelles as illustrated in figure 2.9. The change of the dynamic equilibrium and the cross-linking effect may result in more complicated morphologies in the deposited titania/polymer composite film than the possible morphologies shown in figure 2.4. As discussed in section 2.2.2, water plays a crucial role in the sol-gel process. Also, it has a great impact on the micelle formation since water is a polar solvent and therefore is a common selective solvent for the hydrophobic block. Thus, the atmospheric humidity should be considered as an important factor for the influence of the final film morphology. The complex interplay of the various parameters, including the good-poor solvent pair, the interaction between one block of the copolymer and titania species, the interaction between solvents and titania species and the hydrolysis and polycondensation processes, determine titania-containing micellar solution.

In addition to all influences in the solution, deposition method matters strongly on the final film morphology. Film deposition actually is a process that removes solvents and solidifies samples. Upon drying, there are two major opposing processes impacting the final film morphology [49]. One is that the rearrangement of the block copolymer occurs in the favor of the lower system energy. The other one is that the cross-linking of titania species hampers the rearrangement tendency. If the former process dominates, ordered architectures are usually obtained by the microphase separation of the diblock copolymers. For the latter case, a less ordered morphology is more favorable. Additionally, different deposition methods may have different influences. Some deposition techniques such as spin-coating and spraying are fast and nonequilibrium processes, which can freeze structures within seconds. While other techniques like solution-casting, printing and blade-casting are slow processes for solvent removal, which provide sufficient time for structural rearrangements.

After deposition, the obtained titania/polymer composite films can undergo some post-treatments such as solvent exposure and thermal annealing. In general, these external stimuli are aimed to increase mobility of the polymer chains and therefore to promote structural rearrangements. In addition, a pure nanostructured titania film can be achieved by removing the polymer template. High-temperature combustion such as calcination

in air is a typical route since polymers cannot resist temperatures above 400 °C. For polymeric substrates, the high-temperature combustion is not suitable. Therefore, some low-temperature methods were developed to extract the polymer scaffold, such as UV irradiation, oxygen plasma and solvent extraction [50, 51].

## 2.3 Titania based solar cells

Solar cells are electrical devices that can convert solar energy directly into electricity. There are various different types of solar cells, such as inorganic solar cells, organic solar cells and hybrid solar cells. The solar cells studied in the present thesis are using titania as photoanodes, which therefore are denoted as titania based solar cells. The titania based solar cells in this work are categorized according to their device architecture into solid-state dye-sensitized solar cells (ssDSSCs) and hybrid solar cells. The basic principle of titania based solar cells is described in section 2.3.1. Afterwards, detailed descriptions for ssDSSCs and hybrid solar cells are given in section 2.3.2 and section 2.3.3, respectively.

### 2.3.1 Basic principles

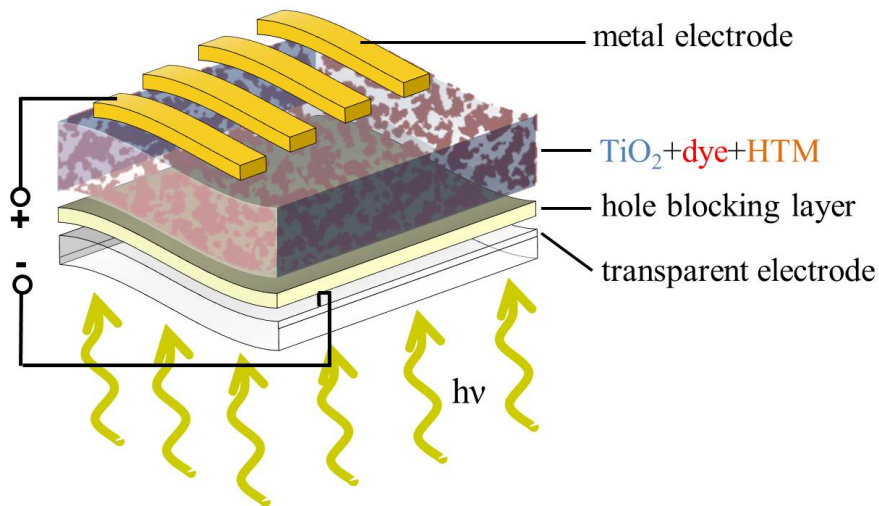


**Figure 2.10:** Schematic architecture of a titania based solar cell under solar illumination.

A basic setup of a titania-based solar cells is shown in figure 2.10. It consists of several layers that have different functionality. The middle layer, consisting of titania, dye and a hole transport layer (HTM), is called active layer, where the light absorption actually takes place, followed by the generation of charge carriers and their transport to their respective electrodes. Titania is a n-type semiconductor, which is used for transporting

the generated electrons to the transparent electrode. The dye is a sensitizer, where the light absorption and exciton creation occurs. It is attached to the titania surface to form a monolayer. This is the reason why a high volume-to-surface ratio is favored for the titania, as more dye molecules can be loaded. For the conventional dye-sensitized solar cells (DSSCs), an iodide/triiodide ( $I/I^-$ ) redox couple is the most common used HTM. Therefore, the working principle of titania-based solar cells is introduced in the present thesis by taking DSSCs with  $I/I^-$  liquid electrolytes as an example.

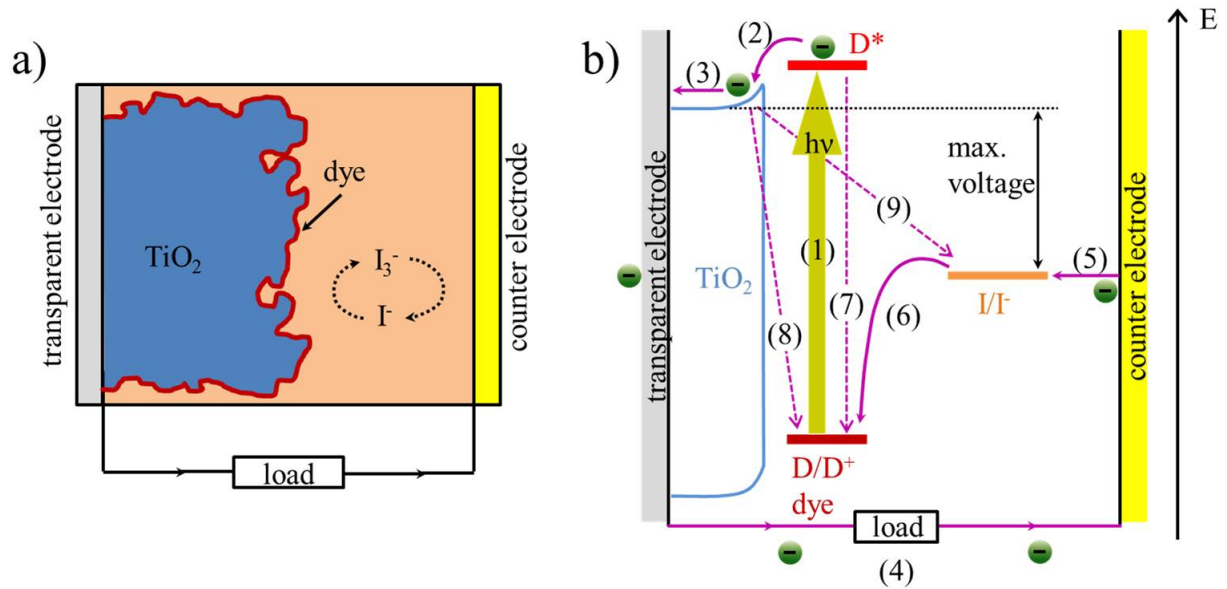


**Figure 2.11:** a) The cross-section of a typical DSSC with  $I/I_3^-$  liquid electrolytes. b) A detailed energy diagram of the electronic processes and main loss mechanisms in the DSSC. Process 1: Photoexcitation of a dye by light absorption. Process 2: The injection of the electron to the conduction band of  $TiO_2$ . Process 3: Electron diffusion to the transparent electrode. Process 4: Through a external circuit, the electron reaches the counter electrode. Process 5: Regeneration of the  $I/I^-$  redox couple. Process 6: Regeneration of the dye. Process 7: Decay of a excited dye. Process 8 and process 9: the injected electron recombines with the oxidized dye and the  $I/I^-$  redox couple, respectively.

A schematic of the working mechanism during device operation is illustrated in figure 2.11. Firstly, a dye molecule absorbs a photon, photoexcitation of the sensitizer occurs (equation 2.11). The Franck Condon principle governs the photoexcitation [52,53]. Afterwards, an electron injects into the conduction band of titania from the excited state of the dye molecule (equation 2.12). An oxidized dye ( $D^+$ ) is generated, which is subsequently reduced by electron donation from the  $I/I^-$  redox couple (equation 2.13). The separated electron is extracted by the transparent electrode. Afterwards, it passes the external external circuit to the counter electrode. At the counter electrode, the  $I/I^-$  redox couple is regenerated by capturing this electron. The whole photovoltaic energy-conversion cycle

is regenerative, thus the DSSCs can generate electricity continuously under sunlight illumination. However, the device efficiency is always lower than the theoretical value due to some undesirable reactions that cause charge recombination.



The dye in the excited state relaxes to the ground state following the fluorescence effect (equation 2.15). After injection, the electron can recombine with the oxidized dye (equation 2.16) or with the oxidized I/I<sup>-</sup> redox couple that are situated in the vicinity of the titania surface (equation 2.17).



### 2.3.2 Solid-state dye-sensitized solar cells

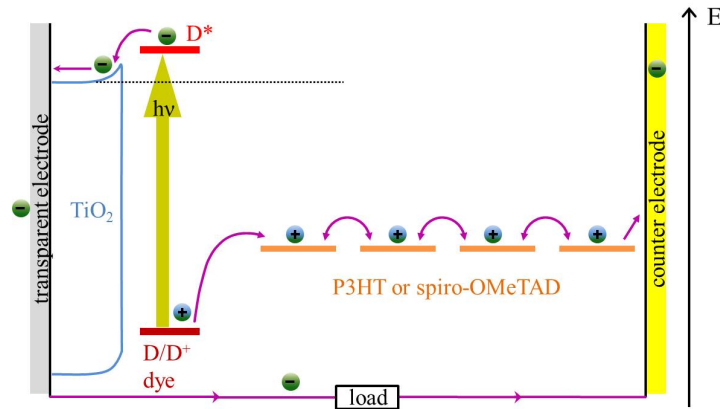


**Figure 2.12:** Schematic illustration of the electronic processes in an ssDSSC. The electronic processes are similar to those shown in figure 2.11, except that the positive charge carriers are transported in the organic HTMs via hopping transport.

Although DSSCs have reached a high power conversion efficiency (*PCE*) of over 12 %, there remain many problems related to liquid-electrolyte leakage and electrode corrosion.

Alternatively, solid-state hole transport materials (ssHTMs) have been developed to replace liquid electrolytes. In this way, the device is termed as solid-state dye-sensitized solar cell (ssDSSC). A schematic illustration of the working mechanism during device operation is shown in figure 2.12. The electronic processes such as dye photoexcitation, electron injection and dye regeneration are the same as shown in figure 2.11, except that the positive charge carriers are transported in the organic HTMs via hopping transport to the counter electrode.

### Photoexcitation and electron injection

Dye molecules adsorbed at the surface of titania photoanodes are an essential part for current generation. The incoming light is absorbed by dye molecules, and thereby photoexcitation of the sensitizers occurs resulting in the generation of an electron-hole pair, known as an exciton. However, this reaction only occurs when the energy of the incident photons is equal or larger than the band gap of the dye.

$$E_{\text{photon}} = \frac{hc}{\nu} \geq \Delta E_{\text{gap}} \quad (2.18)$$

As titania has a high electron affinity, the electrons are injected to the conduction band of titania with the aid of an inner electrical field built by the interface of titania/dye/ssHTM. The electron transfer from the dye to titania can be regarded as a tunneling process described by Gerischer [54]. In Gerischer's model, the energy levels of the ground and excited states of the dye are assumed to have a Gaussian distribution due to thermal fluctuations. For electron injection, it is necessary that the energy states of the excited dye and the conduction band (CB) of titania are overlapping. An optimum electron injection occurs in the case of a complete overlap. In principle, the holes can transfer from the valence band (VB) of titania to the ground state of the dye during the electron injection. However, this process is unfavorable since it would increase the possibility for the recombination of separated charges. Therefore, in the ideal case lies the ground state energy of the dye within the band gap of titania, i.e. does not overlap with the VB of titania.

Up to now, there are many dyes used as sensitizers. Basically, they can mainly be divided into metal complexes and metal-free sensitizers according to structure. Both types are based on three main components: an electron donor moiety (D), a  $\pi$  bridge ( $\pi$ ) and an electron acceptor moiety (A). The dyes typically have molecular structures of D- $\pi$ -A or D-A- $\pi$ -A. The A parts are located in the vicinity of titania, whereas the D parts are situated close to ssHTMs, i.e. far from the titania surface. In this way, rapid electron injection and dye regeneration is facilitated. Moreover, the recombination of the



oxidized dye with the injected electrons is inhibited to a certain degree due to a specific distance between the titania surface and D parts. The metal complexes includes either polypyridyl complexes with metal ions such as Ru, Os, Pt, Re, Cu and Fe, or porphyrins and phthalocyanines complexes with Zn, Ru, Ti, Si, Fe, Hf and Zr [55–64]. The latter class contains functional groups of coumarin, heteroanthracene, perylene or indole [65–68]. The sensitizers used in the present thesis are indoline dyes D149 and D205. The detailed description of both dyes is given in section 4.1.

### **Charge carrier transport**

After exciton dissociation, electrons are transported through mesoporous titania to the transparent electrode. The electron mobility in mesoporous titania films is of several orders of magnitude lower than in a single anatase crystals. The existing sub-band-gap states in the  $\text{TiO}_2$  are significantly influencing the transport rate. Considering electrons that can only be transferred into the conduction band of titania, the probability of electrons present in the conduction band dominates the overall electron mobility. The probability depends on the processes of trapping and detrapping of electrons from the sub-band-gap states, which implies that the exact location of the trap states is of high importance. Kopidakis et al. have reported that the transport-limiting traps are mainly located on the titania surface rather than in the volume of  $\text{TiO}_2$  nanoparticles or at the particle boundaries [69]. This appears to indicate that the traps are proportional to the roughness and porosity of a given titania film. As known, titania films with a high surface-to-volume ratio are beneficial for dye loading. Therefore, the electron mobility in titania and dye adsorption on the titania surface are in contradictory existence. This explains the observation by Yang et al., who demonstrated that a  $\text{TiO}_2$  nanoparticle size of about 25 nm gives rise to a higher power conversion efficiency of solar cells than smaller nanoparticles [70].

The hole transport on the other side happens from the ssHTM to the counter electrode after the injection of electrons. To be a good performing ssHTM in ssDSSCs, on the one hand, the upper edge of the VB of the ssHTM should be located above the ground state of the dye with respect to the energy level. On the other hand, ssHTM should have a good infiltration into mesoporous titania film to form a decent interface area of titania/dye/ssHTM. In the present thesis, spiro-OMeTAD and P3HT are used as organic ssHTMs. These two ssHTMs are described in detail in section 4.1. Positive charge carriers are transported either through spiro-OMeTAD or P3HT via polaron hopping, as explained in section 2.1.2. The mobility of positive charge carriers in the solid films of pristine spiro-MeOTAD is about  $2 \times 10^{-4} \text{ cm}^2 \text{ V}^{-1} \text{ s}^{-1}$ , while in the case of the spiro-MeOTAD inside  $\text{TiO}_2$  network this value is one order of magnitude less, about  $4 \times 10^{-5} \text{ cm}^2 \text{ V}^{-1} \text{ s}^{-1}$  [71,

72]. Many techniques have been developed to increase the mobility of positive charge carriers. The ionic additives Li-TFSI has been found to enhance the positive charge carrier mobility remarkably up to one order of magnitude with a molar ratio of Li salt to spiro-OMeTAD ranging from 0.1 to 0.2 [73]. Chemical p-doping is another strategy to increase the conductivity of spiro-OMeTAD. Burschka et al. have reported that the spiro-OMeTAD conductivity increased from  $4.4 \times 10^{-5} \text{ S cm}^{-1}$  to  $5.3 \times 10^{-4} \text{ S cm}^{-1}$  with 1.0 % p-type dopant [74]. The mobility of positive charge carriers in P3HT is closely related to its crystallinity, orientation and regioregularity. Amorphous regions of P3HT usually hamper the hopping processes, which leads to a low charge carrier mobility of less than  $10^{-5} \text{ cm}^2 \text{ V}^{-1} \text{ s}^{-1}$ . However, the ordered crystalline domains give a much higher charge carrier mobility. With respect to the orientation, the face-on geometry offers a higher mobility than the edge-on geometry by more than a factor of 100 [75,76]. Regarding the regioregularity, the mobility is only  $2 \times 10^{-4} \text{ cm}^2 \text{ V}^{-1} \text{ s}^{-1}$  with P3HT regioregularity of 81 %, while this value jumps to 0.05 - 0.1  $\text{cm}^2 \text{ V}^{-1} \text{ s}^{-1}$  in the crystalline P3HT with 96 % regioregularity [16].

Due to the relatively low charge mobility through organic ssHTMs (compared to liquid electrolytes) and the difficulty for organic ssHTMs being infiltrated into the mesoporous  $\text{TiO}_2$ , an optimum active layer thickness is estimated to be around 2  $\mu\text{m}$  [77,78].

### 2.3.3 Hybrid solar cells

Hybrid solar cells often describe a device where the active layer consists of inorganic and organic components. In this way, hybrid solar cells can employ the advantages of inorganic materials, such as physical and chemical stability, high electron affinity, high charge carrier mobility and controllable nano-morphology, and adopt the merits of organic components, such as low costs, ease of production, facile solution processability, ease of changing molecular structures for tuning the energy bands. In the present thesis, titania and P3HT are used as inorganic and organic components for hybrid solar cells, respectively. In hybrid solar cells, P3HT serves not only as hole-conducting material, but also as light absorber and thereby as the site for exciton generation.

Figure 2.13 shows the working mechanism of a hybrid solar cell by an energy level diagram. The whole process is split into five steps. Firstly, the light reaches the active layer and is absorbed by P3HT in the current case. Many factors such as the absorption spectra of P3HT, the thickness of P3HT and the device architecture can influence efficiency of the light absorption.  $\eta_a$  is used to denote the fraction of incident photons absorbed by P3HT as illustrated in figure 2.13a. The binding energy of exciton is much higher than thermal energy at room temperature, which implies that excitons cannot dissociate to holes and

electrons under natural conditions. They must diffuse towards the interface of a donor and an acceptor, where the potential difference can provide sufficient energy for exciton dissociation (figure 2.13b).  $\eta_{diff}$  describes the ratio of the number of excitons that reach the interface to the number of generated excitons. This efficiency can be improved by increasing the exciton lifetime and/or reducing the P3HT nano-domain size [79,80]. With the aid of an inner electrical field built up by titania and P3HT, the exciton dissociation occurs (figure 2.13c). After dissociation, the separated charges could be weakly bound at the interface or be completely independent. The former case is called charge transfer (CT) states and the latter one is termed as charge separated (CS) states.  $\eta_{diss}$  describes

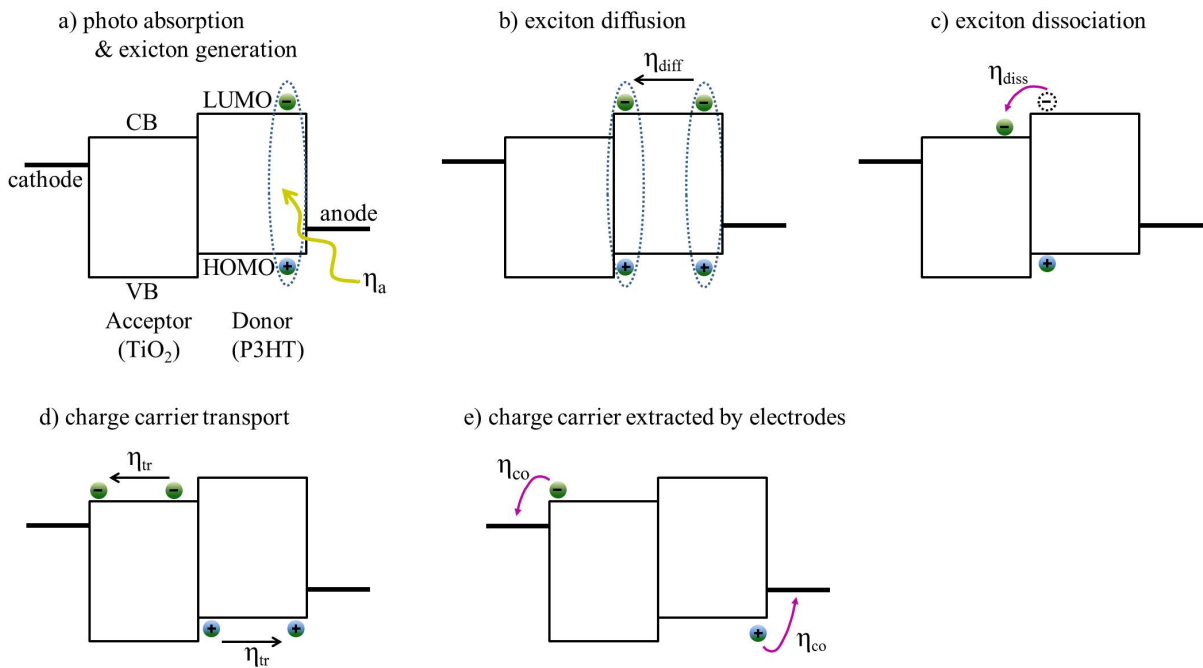


**Figure 2.13:** Schematic illustration for the electronic processes in a hybrid solar cell (from a) to e)). In a), CB and VB representing the conduction band and valence band of titania, respectively. LUMO and HOMO indicating the lowest unoccupied molecular orbital and highest occupied molecular orbital of P3HT, respectively.

the ratio of the number of the separated charges in CS states to the number of excitons at the titania/P3HT interface. Afterwards, the free charge carriers are transported to the electrodes. Structural defects and/or impurities in the donor and acceptor can be the origin for trap states for charge carriers, which increases the possibility for charge recombination.  $\eta_{tr}$  indicates the ratio of the number of free charge carriers that are reaching the electrodes to the number of generated free charge carriers. Finally, the charge carriers are collected by the electrodes.  $\eta_{co}$  describes the ratio of the number of charge carriers collected externally to the number of charge carriers at the electrodes. Therefore, the ef-

efficiency of converting the energy of light into electricity, also known as external quantum efficiency ( $EQE$ , see section 3.2.4), is given by

$$EQE = \eta_a \eta_{diff} \eta_{diss} \eta_{tr} \eta_{co} \quad (2.19)$$

## 2.4 Scattering methods

Some real space measurements such as AFM and SEM can provide structure information on the nanoscale. However, they are restricted to surface structures on a more local scale. In contrast to these techniques, scattering methods using x-rays or neutrons are able to probe the film volume over a macroscopic sample area. In this way, structural information about the inner film morphology can be obtained with a high statistical relevance. The basic principles of scattering techniques are discussed in section 2.4.1, followed by a description about x-ray diffraction in section 2.4.2 and grazing incidence small angle x-ray scattering (GISAXS) in section 2.4.3. For probing crystalline order of thin films, grazing incidence wide angle x-ray scattering (GIWAXS) is employed, which is discussed in section 2.4.4.

### 2.4.1 Principles

X-rays can be regarded as a electromagnetic plane wave with its electric field vector  $\vec{E}(\vec{r}) = \vec{E}_0 \exp(i\vec{k}_i \cdot \vec{r})$ . When it travels through a medium with a refractive index of  $n(\vec{r})$ , the propagation obeys the Helmholtz equation [81].

$$\nabla^2 \vec{E}(\vec{r}) + k^2 n^2(\vec{r}) \vec{E}(\vec{r}) = 0 \quad (2.20)$$

where  $\vec{r}$  is the position of the electromagnetic wave and  $k = 2\pi/\lambda$  is the modulus of the wave vector  $\vec{k}$ . The refractive index for x-rays  $n$  in the investigated material can be described by

$$n(\vec{r}) = 1 - \delta(\vec{r}) + i\beta(\vec{r}) \quad (2.21)$$

depending on the dispersion part  $\delta$  and the absorption part  $\beta$ . Both  $\delta$  and  $\beta$  can be written as a function of the wavelength  $\lambda$  of x-rays

$$\delta = \rho \frac{\lambda^2}{2\pi} = \rho_e r_e \frac{\lambda^2}{2\pi} \quad (2.22)$$

$$\beta = \mu \frac{\lambda}{4\pi} \quad (2.23)$$

where  $\rho$  is the scattering length density (SLD) of the homogeneous medium, which relies on the classical electron radius  $r_e$  ( $2.814 \times 10^{-5}$  Å) and the electron density of the probed sample  $\rho_e$ . Therefore, the SLD of a material is closely correlated to its density and thus the electron density of its elements.  $\mu$  describes the linear absorption coefficient. In general, for x-rays the value of  $\delta$  ranges from  $10^{-5}$  to  $10^{-6}$  and  $\beta$  is of the order of  $10^{-7}$ . Therefore, the refractive index of x-rays is slightly smaller than 1. Different materials usually have different electron densities, which gives rise to different SLDs in the x-ray scattering experiments. This difference is the origin of the scattering contrast between materials.

For thin films, the standard transmission techniques usually give a very weak scattering signal due to the small scattering volume. To overcome this problem, a reflection geometry with grazing incidence conditions is employed as it provides a large footprint of the x-ray beam and thereby increases the probed volume and yields sufficient scattering signal for recording. Specular and diffuse scattering occur in grazing incidence mode and are schematically illustrated in figure 2.14a and 2.14b. For specular scattering, the incident

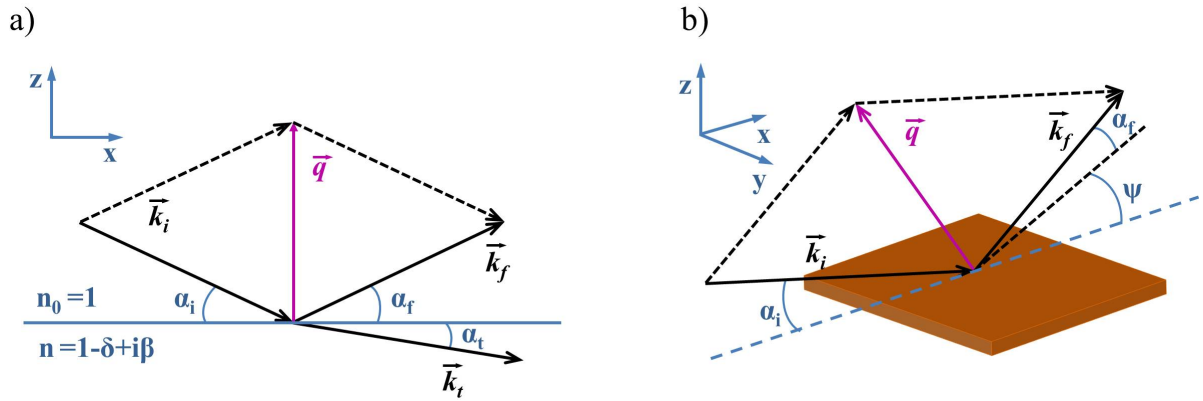


**Figure 2.14:** Schematic geometry of a) specular scattering and b) diffuse scattering with basic definitions of directions and angles.

x-ray beam  $\vec{k}_i$  impinges on a sample with a shallow angle of  $\alpha_i$  and the specular beam exits the sample under an exit angle  $\alpha_f$  which is equal to  $\alpha_i$ . Both incident and specular x-ray beams stay at the same plane as shown in figure 2.14a. The momentum transfer from the incident beam to the exit beam determines the scattering wave vector  $\vec{q}$ , which is given by

$$\vec{q} = \vec{k}_f - \vec{k}_i \quad (2.24)$$

Since elastic scattering is used in the present thesis,  $\vec{q}$  only changes its direction whereas its modulus remains unchanged. Under diffuse conditions, the scattered beam is not confined

only in the xz-plane, but is also present in the xy-plane with an additional scattering angle of  $\psi$ , as shown in figure 2.14b.

At the interface between air and a medium with a refractive index  $n$ , the diffraction of the x-rays beam can be described by Snell's law,

$$n_0 \cos(\alpha_i) = n \cos(\alpha_t) \quad (2.25)$$

where  $n_0$  is 1 for air and  $\alpha_t$  is the exit angle of the transmitted beam  $\vec{k}_t$ . For total reflection (x-rays travel from air to the material)  $\alpha_t$  also possible: is equal to 0. At this point, the incident angle is called the critical angle  $\alpha_c$  of the material. Thus,

$$\cos(\alpha_c) = n \quad (2.26)$$

$$n^2 = \cos^2(\alpha_c) \approx 1 - \alpha_c^2 \quad (2.27)$$

$$\alpha_c \approx \sqrt{2\delta} = \lambda \sqrt{\frac{\rho}{\pi}} \quad (2.28)$$

If  $\alpha_i < \alpha_c$ , total reflection occurs with the formation of the evanescent waves. These waves can penetrate the sample to a certain depth, but their intensity decreases exponentially with the penetrating distance. The depth where the intensity of the evanescent wave decreases to 1/e of its original intensity is termed penetration depth. In addition, the escape depth is proposed in the case that x-rays will get a second damping on the way out of the sample surface. Therefore, the scattering depth depends on the penetration depth and the escape depth and can be regarded as approximately half of the penetration depth [82]. Typically, the scattering depth is of the order of 50 Å. In the case of  $\alpha_i > \alpha_c$ , the x-rays are able to penetrate the whole thin films, which gives also information about the volume of the sample.

### 2.4.2 X-ray diffraction

The crystal structure of the samples can be characterized with x-ray diffraction. Crystals consist of ordered arrays of atoms, which act as periodic gratings for x-rays. Typically, each crystal structure has its own dimension of the lattice as well as the electrons present around the atoms. The electrons are the scatterers for x-rays, which produce spherical waves after the reaction with incoming x-rays. Therefore, every crystal provides a unique scattering pattern which can be used to identify the crystalline phases of the material.

Figure 2.15 graphically shows the x-ray diffraction at two neighboring lattice planes of a crystal. The interference of the scattered x-ray beam gives rise to different intensities. Furthermore, the maximum intensity appears when the Bragg equation is fulfilled. For

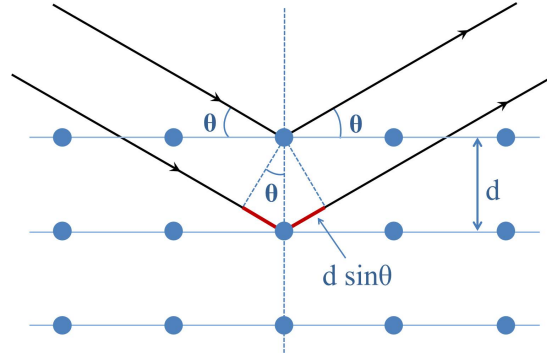


**Figure 2.15:** Schematic illustration of the Bragg equation. The incoming beams (black lines) interact with the scatterers (blue circles) which are located in regular lattice planes. The distance between these planes is described by the lattice spacing  $d$ . The x-ray travels a longer distance when it interacts with the lower lattice plane. The increased path lengths are marked by red lines.

constructive interference, the path difference must be an integer multiple of the x-ray wavelength  $\lambda$ .

$$2d \sin(\theta) = n\lambda \quad (2.29)$$

where  $d$  is the lattice spacing of a crystal and  $\theta$  is the incident angle. Given the  $\lambda$ , the  $\sin(\theta)$  is inverse proportional to the spacing between diffracting planes. Therefore, the  $\theta$  can be used to identify the types of the crystal phase. Conventionally,  $2\theta$ , the angle between the incoming and the scattered x-ray beam, is used as Bragg reflex. However, not all reflexes can be observed in an XRD measurement due to the so-called systematic extinction [83]. Bragg reflexes along with their relative intensities of the rutile and anatase titania crystal phases are listed in table 2.2. The crystallite size  $D_{hkl}$  along  $\langle hkl \rangle$  crystal direction can be estimated from the width of the Bragg reflex using the Scherrer equation,

$$D_{hkl} = \frac{K\lambda}{\Delta(2\theta) \cos(\theta_0)} \quad (2.30)$$

where  $K$  is the Scherrer form factor, which has a typical value of about 0.9 but varies with the crystallite shape.  $\Delta(2\theta)$  is the full width half maximum (FWHM) of the Bragg peak at  $2\theta$ . The position of the Bragg reflexes can also be indicated by  $\vec{q}$  instead of  $\theta$ , then the Scherrer equation can be written by

$$D_{hkl} = \frac{2\pi K}{\Delta q_{hkl}} \quad (2.31)$$

where  $\Delta q_{hkl}$  is the integral line width. The Scherrer equation shows that the crystallite size depends on the FWHM. In reality, the peak width can be broadened by many factors, such as instrumental effects, inhomogeneous strain, lattice imperfections and so on. Therefore,

	crystal order	$2\theta$ ( $\lambda(\text{Cu}_\alpha)$ )	$q$ [ $\text{nm}^{-1}$ ]	rel. intensity
rutile	(110)	$27.45^\circ$	19.35	100
	(101)	$36.098^\circ$	25.26	50
	(200)	$39.19^\circ$	27.35	8
	(111)	$41.23^\circ$	28.72	25
	(210)	$44.05^\circ$	30.59	10
	(211)	$54.32^\circ$	37.24	60
	(220)	$56.64^\circ$	38.70	20
anatase	(101)	$25.28^\circ$	17.85	100
	(103)	$36.95^\circ$	25.85	10
	(004)	$37.80^\circ$	26.42	20
	(112)	$38.58^\circ$	26.94	10
	(200)	$48.05^\circ$	33.21	35
	(105)	$53.89^\circ$	36.96	20
	(211)	$55.06^\circ$	37.70	20

**Table 2.2:** Bragg reflexes of rutile and anatase titania crystal phases, along with their corresponding relative intensities (obtained from JCPDS database).

for an accurate calculation of the crystal size, other contributions of the peak width should be ruled out.

### 2.4.3 Grazing incidence small angle x-ray scattering

The grazing incidence small angle x-ray scattering (GISAXS) technique is able to probe both surface and bulk morphologies of thin films in a large length scale ranging from the nanometer to micrometer size. In order to obtain a sufficient scattering signal and a good statistical information, a shallow incidence angle of  $\alpha_i < 1^\circ$  is commonly used in the GISAXS measurements. The basic geometry is illustrated in figure 2.14b. In the present thesis, only the elastic scattering phenomena are discussed. Under this condition, the direction of the incident photons is changed whereas their energy is conserved. Therefore, the scattering wave vector  $\vec{q}$  can be written as

$$\vec{q} = \frac{2\pi}{\lambda} \begin{pmatrix} q_x \\ q_y \\ q_z \end{pmatrix} = \frac{2\pi}{\lambda} \begin{pmatrix} \cos(\alpha_f) \cos(\psi) - \cos(\alpha_i) \\ \cos(\alpha_f) \sin(\psi) \\ \sin(\alpha_f) + \sin(\alpha_i) \end{pmatrix}. \quad (2.32)$$



The small angles result in a small wave-vector transfer, and thereby large dimensions in real space. The DWBA is a widely used method to describe the diffuse scattering events during such a reflection geometry experiment. The DWBA is a first order perturbation theory, including first order corrections on an ideal system. The differential cross-section the scattered spherical wave as a function of solid angle is given by

$$\frac{d\sigma}{d\Omega} = \frac{A\pi^2}{\lambda^4} (1 - n^2)^2 |T_i|^2 |T_f|^2 P_{diff}(\vec{q}) \propto P_{diff}(\vec{q}) \quad (2.33)$$

where  $A$  denotes the size of illuminated area,  $T_i$  and  $T_f$  are the Fresnel transmission functions of the incident and scattered beams, respectively, and  $P_{diff}(\vec{q})$  is the diffuse scattering factor which contains information about the film morphology.

The Fresnel transmission coefficients have a maximum at the critical angle of the probed material, which lead to a pronounced scattering intensity (Yoneda peak). Since the critical angle depends on the scattering length density (SLD), the Yoneda peak is a material-sensitive scattering signal. Therefore, by knowing the Yoneda peak position, the critical angle can be determined as well as the density of the material. Based on this correlation, the porosity  $\Phi$  of the probed material can be calculated as

$$\Phi = 1 - \frac{\rho_m}{\rho_{th}} \quad (2.34)$$

where  $\rho_m$  and  $\rho_{th}$  denote the measured and the theoretical SLD of the probed material.

GISAXS measurements only record the intensities of the diffuse scattering waves. In order to extract structural information on the probed material, the intensity signal needs to be modeled. In the case of identical objects in a geometrical arrangement, the diffuse scattering factor  $P_{diff}(\vec{q})$  (recorded intensity) can be determined as

$$P_{diff}(\vec{q}) \propto N |F(\vec{q})|^2 S(\vec{q}) \quad (2.35)$$

where  $N$  is the number of the scattering objects. The form factor  $F(\vec{q})$  describes the scattering objects with a certain shape and size. The electron cloud of the scattering objects react with the incoming x-rays, then the form factor function is the Fourier transform of the electron density distribution of these objects [84].  $S(\vec{q})$  is the structure factor, which is the modulus squared of the spatial Fourier transform of the SLD. Thus, it is related to the spatial arrangement of the scattering objects. As aforementioned, the diffuse scattering is described within the framework of DWBA. In brief, it contains four different modes of reflection and scattering [85]: (1) directly scattered beam, (2) reflected on the substrate and then scattered beam, (3) scattered beam and then reflected on the substrate and (4) reflected-scattered-reflected beam. All these four terms are included. Under the circumstance of rotational-symmetric averages over scattering objects in the plane parallel to

the substrate, the form factor is typically well described by a cylindrical symmetry. The cylinders are assumed to have a short-range order rather than a long-range order, which is modeled by a one-dimensional paracrystalline lattice (1DDL). This spatial distribution is adopted by the structure factor. Therefore, the deviation from the ordered position for the cylinders increases with increasing distance from the target cylinder, i.e. only a local short-range order is present in the structure factor.

In the present thesis, horizontal line cuts at the Yoneda position are modeled to obtain information about lateral structures. Therefore, only lateral correlations in films are taken into account, and then a so-called effective interface approximation can be employed [86]. Within this approximation, the height of the scattering objects is allowed to be decoupled with their radii. Along this route, the so-called local monodisperse approximation (LMA) is introduced. In the LMA assumption, the scattering objects with the same size are assumed to span over a wide range and the collection of these scattering objects is made of monodisperse domains. A Gaussian distribution function is used to describe the polydispersity of the scattering objects. Therefore, monodisperse domains give rise to independent scattering signals, which superimpose incoherently to constitute the total scattering signal [87].

#### 2.4.4 Grazing incidence wide angle x-ray scattering

The grazing incidence wide angle x-ray scattering (GIWAXS) technique can be used for probing atomic and molecular distances in crystal lattices. It is noteworthy that, the setup of GIWAXS measurements is the same as that of GISAXS measurements except for a much shorter sample-to-detector distance. This shifting allows recording the scattered x-ray beams under larger exit angles with the same detector, which is able to provide structural information on the sub-nanometer scale. In this way, single atoms are the scatterers for x-ray rather than mesoscopic objects which are considered as form factors in GISAXS. Moreover, the regular arrays of these atoms determine the intensity of the scattering signal. When  $\{hkl\}$  lattice planes fulfill Bragg's law at a certain angle, constructive interference occurs. Compared to XRD, GIWAXS is able to detect the preferred orientation of the crystals in thin films. For example, in terms of the semiconducting polymer P3HT, the orientation distribution of its crystallites either face-on or edge-on can be quantified using GIWAXS. In order to better understand the correlation between the crystal orientation and scattering signals, four scenarios of GIWAXS pattern are schematically illustrated in figure 2.16.

If the sample is highly crystalline and with a direction of all crystal planes normal to the substrate (lattice spacing of  $d$ ), the resulting GIWAXS pattern shows well-defined Bragg

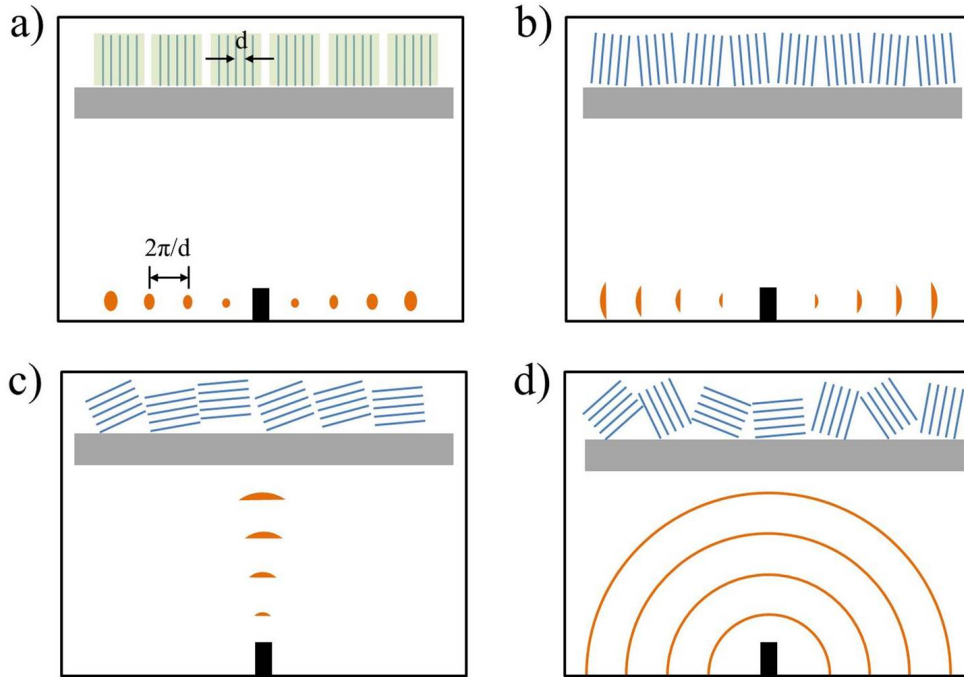


**Figure 2.16:** Sketches of different lamellar stackings in films with their corresponding 2D GIWAXS data underneath in case of a) ideally vertical lamellar stacks, b) slightly disordered vertical lamellar stacks, c) textured lamellar stacks in horizontal direction and d) completely disordered lamellar stacks. The blue line packings and grey blocks indicate lamellar structures and substrates, respectively. The green backgrounds in a) are guide to the eyes for the vertical lamellar stacks. Adapted from reference [88].

peaks with a distance of  $2\pi/d$  only in horizontal direction, as shown in figure 2.16a. If crystal planes are not perfectly perpendicular to the substrate but with a small angular perturbation, broadening Bragg peaks in horizontal direction are present in the GIWAXS data (figure 2.16b). If all crystal planes change their direction from vertical to horizontal, the Bragg peaks shift to vertical direction accordingly, as illustrated in figure 2.16c. In the case of all crystal planes without any preferential orientation, Debye-Scherrer rings are observed in the GIWAXS pattern instead of Bragg peaks (figure 2.16d).

Unlike XRD with a specular reflection, the GIWAXS detector records the signals of diffuse scattering. In this case, the  $\vec{k}_i$  is fixed and all  $\vec{k}_f$  lie on an Ewald sphere. As a consequence, especially in the case of high exit angles,  $q_x$  gives a non-negligible contribution to the  $\vec{k}_f$ . In the GIWAXS measurements, a spherical surface in  $q$ -space is projected to a 2D detector, thus the obtained GIWAXS pattern is distorted. In order to extract structural information, the raw 2D GIWAXS pattern requires to be reconstructed into the natural reciprocal space coordinates [89]. Here,  $q_x$  and  $q_y$  cannot be decoupled, the  $x$  axis in the GIWAXS pattern is  $q_r$  instead of  $q_x$ .  $q_r$  is determined by

$$q_r = \sqrt{q_x^2 + q_y^2} \quad (2.36)$$

The GIXSGUI analysis package is used to retrieve the corrected reciprocal space patterns in the present thesis, which is based on a number of corrections related to the scattering geometry [89]. These corrections include field correction, efficiency correction, solid-angle correction and polarization correction. The field correction is caused by various photon sensitivity between different detector pixels. The efficiency correction is done due to the different lengths of traveling paths for the scattered x-rays under different exit angles. The different distances lead to different medium attenuation and absorption probability for different pixels on the 2D array of the detector. Solid-angle correction takes into account that the recorded intensity depends on the solid angle  $\Omega$  and the pixel area. X-rays generated at synchrotron beamlines are typically horizontally polarized, which leads to an angular dependent intensity of the scattered beams. This impact on intensity is eliminated via the polarization correction. The detailed description of all corrections can be found in reference [90].

An example of the raw 2D GIWAXS data and the data after reconstruction is shown in figure 2.17. A wedge of missing data is observed in the reconstructed 2D GIWAXS data (figure 2.17b), which is caused by the inaccessible  $q$ -range.

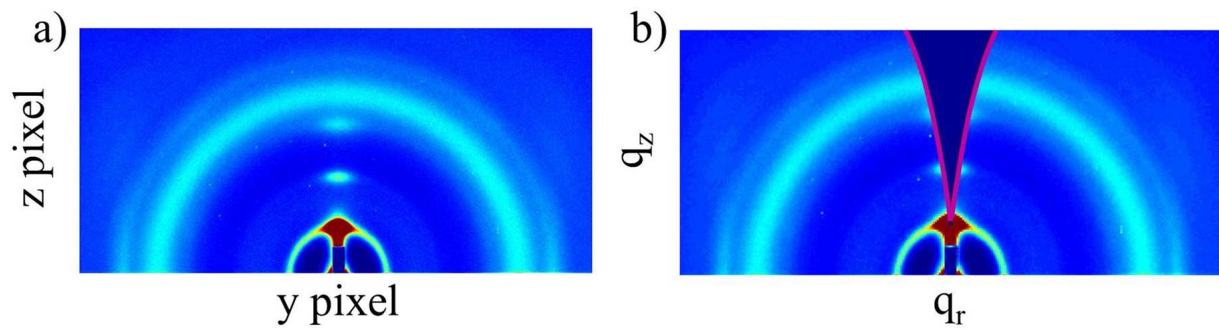


**Figure 2.17:** a) A raw 2D GIWAXS data recorded on the detector. b) The corresponding corrected 2D GIWAXS data retrieved using GIXSGUI. The inaccessible  $q$ -range in a wedge shape is denoted by the pink curves.

## 3 Characterization methods

In the present chapter, various techniques to characterize mesoporous titania films, titania/polymer composite films and solar cells are presented. Different real- and reciprocal-space imaging methods are used to investigate the film form and structure described in section 3.1. Various spectroscopic and electronic characterizations are applied to probe the sample functionality as presented in section 3.2. All the characterization methods are introduced in detail, including instrument specifications, working principles and the principles of data analysis.

### 3.1 Structural characterizations

Two main types of characterization methods are employed in this work. The first type is categorized as real-space techniques, including height profilometry (section 3.1.1), atomic force microscopy (section 3.1.2) and scanning electron microscopy (section 3.1.3). Nitrogen adsorption-desorption isotherms are used for characterization of pore size, specific surface area and pore volume (section 3.1.4). The second type comprises reciprocal-space techniques, like x-ray diffraction (section 3.1.5) and grazing incidence scattering (section 3.1.6).

#### 3.1.1 Height profilometry

Profilometry is a widely used method to measure height differences on samples. In the present thesis, a DektakXT®stylus profiler (Bruker corp.) is applied. The working principle is schematically illustrated in figure 3.1. The sample is mounted on a movable sample stage. Then the diamond-tipped stylus is brought down and in contact with the sample surface by applying a constant force over the sample. By moving the stage forth and back the stylus scans the sample surface. Any changes in surface height are measured by the variation in the vertical displacement, which is converted to a digital signal by a linear variable differential transformer.

The height profilometer is mainly used to determine the sample thickness in the present work. Typically, a scratch is made on the sample to completely remove a piece of film. When the stylus scans over the scratch, the height difference between the film surface and the substrate resembles the film thickness. At least 5 scans on different spots are made for each sample to obtain an average film thickness value. All the measurements are carried out using a contact force of 1 mN, a scan speed of  $100 \mu\text{m s}^{-1}$ , and a scan distance of 3 mm.

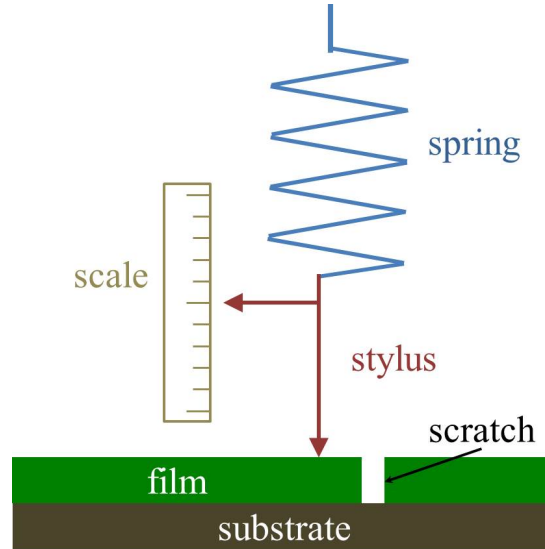


**Figure 3.1:** Sketch of the height profilometer measuring a sample. The sample is loaded on on a movable stage. The stylus contacts to the sample surface with a certain force. The scan on sample surface is achieved by a movable sample stage.

### 3.1.2 Atomic force microscopy

Atomic force microscopy (AFM) is a very high resolution type of scanning probe microscopy. It is a versatile instrument, which can be used for force measurement, imaging, and manipulation. In the present thesis, AFM is employed to map sample topography and phase contrast. From the analysis of topography images, information about structure size and surface roughness can be achieved. The phase images offer information about, for example, the hardness difference between different materials.

A schematic overview of the AFM is illustrated in figure 3.2. The laser source, photodiode, AFM tip, and feedback controller are the main parts of the AFM. There are three commonly used techniques in the AFM operation: contact mode, non-contact mode and tapping mode. In the present thesis, all samples are investigated with an Asylum MFP-3D in tapping mode. Tapping mode plays a very important role in AFM imaging, which

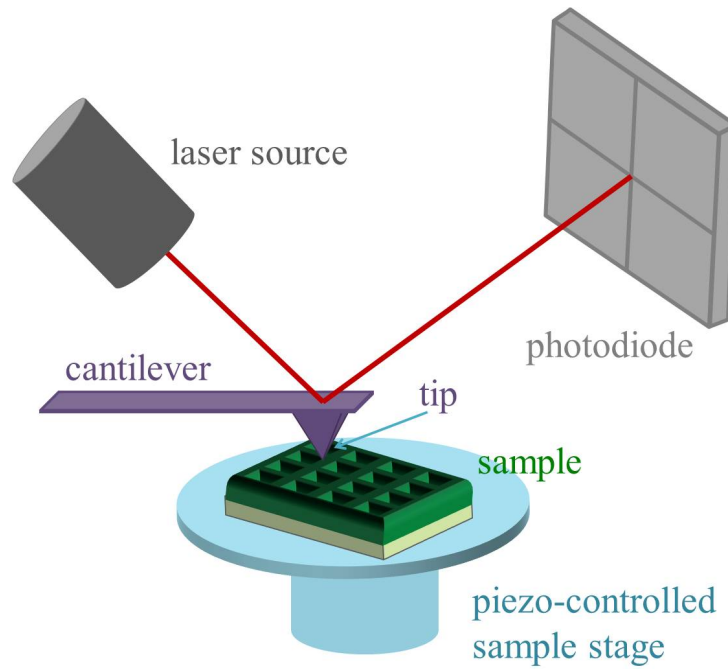


**Figure 3.2:** Sketch of the AFM setup with its main components. The sample is placed on the piezo-controlled sample stage. The tip is faced to the sample surface. The cantilever deflection is measured by a laser system, where the laser beam incidents on the cantilever and the reflected beam strikes a four-segmented photodiode. The signal directs the motion of the sample stage.

is developed as a technique to achieve very high resolution without damaging samples or distorting image data. First, the cantilever oscillates at or near its resonant frequency with a high amplitude by using a piezoelectric crystal when the tip is far away from sample surface. The oscillating cantilever is then brought down towards the sample surface. The cantilever stops moving when it begins to touch the sample surface slightly. Afterwards, the vertically oscillating tip contacts the sample surface and lifts off alternately during scanning. The optimal oscillation frequency and the atomic force on the sample surface is set automatically by the software. The contact force usually is maintained at the lowest possible level. When the tip contacts the sample, it causes an energy loss thereby a reduced oscillation of the cantilever. The reduction of oscillation amplitude is measured by a laser system. The laser beam reflected from the cantilever hits a four-segmented photodiode which is position sensitive. The intensity difference of the laser beam in the four segments indicates the deflection of the cantilever, which transfers the signal to the feedback electronics. The feedback loop then drives the sample stage moving along the z-direction to maintain a constant amplitude and force. Finally, according to the stage motion, the topography and phase images are made.

A pyramid tip with 15-40 nm end radius located at the end of the cantilever is used for the present investigation. The oscillation of the cantilever is set to a frequency of about 100 kHz. The samples are scanned line-wise over an area of  $2 \times 2 \mu\text{m}$  and  $5 \times 5 \mu\text{m}$ . Each image consists of 256 lines and each line comprises 256 data points. All AFM images are analyzed with Gwyddion 2.31 software, mainly for adjusting the image contrast and extracting the height information.

### 3.1.3 Scanning electron microscopy

Scanning electron microscopy (SEM) is used to probe the surface morphology of titania and titania/polymer films on the nanometer scale. Compared to optical microscopy, SEM uses electrons as the illumination source instead of light. As the wavelength of electrons is much shorter than that of visible light, SEM possesses a very high resolution which allows sample being probed in the nanometer range.

All SEM measurements are performed with a FESEM Gemini NVision 40 instrument (Carl Zeiss), which is controlled by the software SmartSEM. The electrons are generated from a field emission gun using a tungsten filament. Subsequently, the electrons are guided to form an electron beam through magnetic and electrostatic lenses, which focus the electron beam. Then the electron beam is accelerated by a voltage on the order of several kV. The resulting beam scans the sample surface in a line-wise manner and the secondary electrons, which are a result of the interaction of incident electrons and sample surface, are emitted from the area very close to the specimen surface and collected by a detector. The intensity of the secondary electrons is mainly correlated to the surface morphology, beam size and the incident angle between beam and sample surface. During scanning, the beam size and incident angle are fixed, thus the obtained grey scaled image with different brightness values is a picture of the sample surface. The lateral resolution typically is below 5 nm. It is important to note, that the intensity of secondary electrons strongly depends on the surface morphology. Therefore, it's wrong to use SEM image to parametrize height information. For example, two nano-objects with different shapes will give different intensity of secondary electrons even if they are at the same height.

A system vacuum of  $2 \times 10^{-6}$  mbar is necessary for the measurements. The acceleration voltage of the electron beam is set in the range of 3 to 5 kV, the working distance (distance between the gun and the sample surface) is adjusted to 2.5 mm - 3.5 mm. The aperture size of the primary electron gun is varied between  $7.5 \mu\text{m}$  and  $10 \mu\text{m}$ . Different measuring parameters are aiming to obtain clear images with high resolution. It is worthwhile to note that a lower acceleration voltage and a smaller working distance are used to measure



the titania/polymer films with poor electrical conductivity. The original SEM images are post-treated with the software ImageJ v1.43u to obtain a better image quality.

In order to do cross sectional measurements, a line-scratch is firstly made on the backside of the sample with a diamond cutter. Then the sample is broken over a metal edge after being immersed into liquid nitrogen for 1 min. Soaking in liquid nitrogen is essential for sample preparation, as it provides a sharp edge after sample breaking. During the measurement, the sample stage is tilted by  $54^\circ$  with respect to the horizon. Thus, a tilt correction of  $36^\circ$  is applied for the correct view of the cross section.

### 3.1.4 Nitrogen adsorption–desorption isotherms

The atoms in the surface of a solid material have fewer neighbors than the atoms inside the material, causing that the electrical force of surface atoms is unbalanced. To compensate this imbalance, surface atoms tend to capture surrounding gas molecules. The process of gas molecules attaching to sample surfaces is called gas absorption. In the present thesis the type of gas adsorption is physisorption, where the adsorbed gas molecules are fairly free to move around the surface. As more and more gas molecules are attracted by the surface atoms, the entire adsorbent surface is covered by a monolayer of adsorbate molecules. Based on the Brunauer-Emmett-Teller (BET) theory, the number of molecules,  $N_m$ , required to cover the sample surface can be estimated. Thus, the adsorbent surface area can be calculated by multiplying  $N_m$  with the cross-section area of the adsorbed gas molecules.

As the number of gas molecules increase, multiple layers form on the top of each other. When this process is progressed to a certain point, the pores of the adsorbent starts to be filled with liquid, which is condensed from the gas. This process is called capillary condensation. The unique feature of the capillary condensation is that the gas can condense into liquid below the saturation vapor pressure. Based on the Kelvin equation, the pore size distribution of the measured solid can be determined with the Barrett-Joyner-Halenda (BJH) method.

Finally the pores are completely filled with the liquid, which condensed from the vapor. Knowing the liquid density, the volume it occupies can be calculated, which is the total pore volume of the sample. At this point, if the gas is withdrawn from the system, the gas desorption will occur. Typically, the adsorption and desorption isotherms are different causing a hysteresis. The resulting hysteresis loop can be related to the pore shapes of the sample.

In this work, the experiment of nitrogen adsorption–desorption isotherms is carried out on a Quantachrome Autosorb-1 instrument. Before the experiment, sample surfaces must be without any contaminants such as water and oils. Therefore, the sample is degassed at 150 °C for 12 h under vacuum. After surface cleaning, the sample is brought to a temperature of the boiling point of liquid nitrogen (approximately 77 K). Then known amounts of nitrogen are released in steps into the evacuated sample chamber. The sample surfaces are quickly adsorbed with nitrogen molecules. The specific surface area is calculated by the BET method, and the pore size distribution is determined by using the nonlocal density functional theory (NLDFT) equilibrium model.

### 3.1.5 X-ray diffraction

X-ray diffraction (XRD) is a tool used for identifying the crystalline phase, crystal size and the degree of crystallinity. In the present thesis, XRD measurements are performed on a Bruker D8 ADVANCE X-ray diffractometer. In the instrument, a copper anode is used as the source to generate the x-ray beam. The copper anode is operated at 40 kV and 40 mA. The resulting Cu  $K_\alpha$  radiation, which has a wavelength of 0.1541 nm, is used for the measurements. The x-ray beam impinges on the sample at an angle  $\theta$ . It is important to note, that the footprint of the x-ray beam on the sample is narrow but very long. In order to ensure the experimental accuracy, the size of the sample should be sufficient big, at least  $2.5 \times 2.5 \text{ cm}^2$ . The specular x-ray beam is detected by a point detector at the same angle. During the entire measuring process, the angle between the incident and the reflected beam is kept at  $2\theta$  as the coupled  $\theta/2\theta$  mode is applied. A typical  $2\theta$  scan ranging from  $20^\circ$  to  $60^\circ$  is used with a step size of  $0.04^\circ$  for scanning all samples. Each step takes 50 s. Thus, about 14 h is required for the measurement of each sample. The probed samples are typically prepared on either glass or silicon substrates. For the sample on silicon substrate, a very strong peak at  $2\theta = 33^\circ$  in the final XRD spectrum originates from the silicon (100) Bragg peak. To get a good quality of the XRD spectra, slits of 0.6 mm are used to collimate the x-rays after the beam source and before the detector. Usually a fast pre-check of the characteristic XRD peak of the sample is done before the 14 h measurement to make sure the diffraction signal can be received by the detector. For example, before measuring titania anatase phase, only the characteristic (101) peak is checked quickly to guarantee the proper setting of the parameters. The instrument is controlled by the software Diffrac.commander, where the measurement protocols are submitted to.

The obtained XRD data is analyzed with the aid of the software PeakFit Version 4.12 (SeaSolve Software Inc.). The XRD peaks are fitted with Gaussian functions. The

extracted full width at half maximum (FWHM) values are used to calculate crystal sizes via the Scherrer equation as described in chapter 2.4.2. The obtained XRD peaks of titania samples are identified by making a comparison with the reference peaks for anatase and rutile phase taken from the International Centre for Diffraction Data (ICDD).

### 3.1.6 Grazing incidence scattering

In order to probe the inner morphology, grazing incidence scattering (GIS) methods are used. Unlike in standard scattering experiments a reflection geometry is employed in GIS measurements instead of transmission geometry, which is schematically shown in figure 3.3.

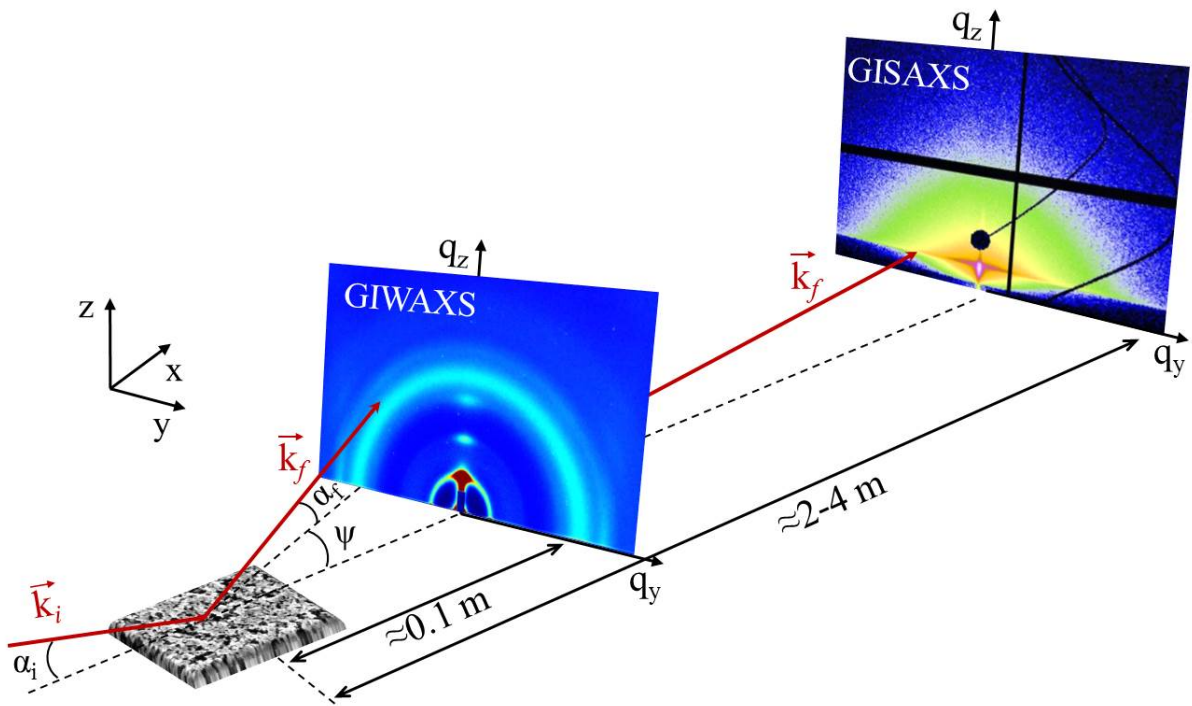


**Figure 3.3:** Schematic presentation of a grazing incidence X-ray scattering setup (GISAXS and GIWAXS). The X-ray beam impinges on the sample with the incident angle  $\alpha_i$  and with a wavevector  $K_i$  (red arrow). It is scattered under an angle  $\alpha_f$ . 2D detectors with short and long sample-detector distances record wide angle and small angle X-ray scattering signals, respectively.

The use of a reflection geometry is particularly suitable for characterizing thin films as grazing incidence conditions give a large footprint of the x-ray beam on the samples. Due to the size of the detector, the sample-detector distance (SDD) determines the accessible scattering angles. Hence, various structural length scales of the sample can be detected

by varying the SDD. For example, very small distance below 1 nm can be probed by setting a short SDD ( $\approx 10$  cm). This measuring technique is named as grazing incidence wide angle x-ray scattering (GIWAXS). A longer SDD ( $\approx 2$ -4 m) usually allows for accessing structural distances ranging from approximately 1 nm up to 1  $\mu$ m. It is called grazing incidence small angle x-ray scattering (GISAXS). For both measurements, it is very important to set a proper incident angle  $\alpha_i$  of the x-ray beam which determines that the measurements are surface or volume sensitive. To probe the volume of the film in the present thesis, all the incident angles are set above the critical angles of the probed materials.

The GIWAXS measurements were performed at the Austrian SAXS beamline of the Elettra synchrotron source (Trieste, Italy). The x-ray wavelength was 1.54 Å, corresponding to an x-ray energy of 8 keV. The GISAXS measurements were conducted at the Elettra synchrotron source and the P03/MiNaXS beamline of the PETRA III storage ring at DESY (Hamburg, Germany). The difference between the two beamlines is that the x-ray energy was higher at P03, which provided an energy of 13 keV, corresponding to a x-ray wavelength of 0.957 Å. Moreover, the intensity of x-ray flux was also higher at the P03 beamline. The smaller wavelength of x-ray results in smaller critical angles of the probed materials, which should be taken into consideration when the value of the incident angle is determined for the measurements.

## GISAXS

The basic setup of GISAXS measurements is schematically displayed in figure 3.3. Due to the long distance between the sample and the detector, a vacuum flight tube is necessary in the x-ray pathway to minimize scattering from air. At the Elettra beamline, a SDD of about 2 m is used, whereas a typical SDD in the range of 3 m to 4 m is chosen at the P03 beamline. Different SDDs meet the demand for different resolvable structural length scales. A Pilatus 1 M (Dectris) detector is used to measure the scattered signal. It consists of ten modules (981 by 1043 pixel array) and each pixel has a size of (172  $\times$  172)  $\mu$ m<sup>2</sup>. The detector has a total area of (169  $\times$  179) mm<sup>2</sup> with blind areas of intermodule gap accounting for 8.4% of the total area. The horizontal black stripe in the 2D GISAXS images shown in figure 3.3 is caused by the intermodule gap. Moreover, the detector has a readout time of 3.6 ms, which allows kinetic measurements with high temporal resolution. To protect the detector from oversaturation, the transmitted and the specularly reflected beams are both blocked with beamstops.

Vertical line cuts of the 2D GISAXS data provide information about the film perpendicular to the substrate (in the vertical direction), whereas horizontal line cuts contain information about lateral structures that are parallel to the substrate. For a quantitative analysis, such line cuts are performed on the 2D GISAXS data with the aid of the software Fit2D (Andy Hammersley, 1987–2005, ESRF, Grenoble) or DPDAK (Gunthard Benecke, DESY Hamburg & MPIKG Potsdam). Afterwards, the line cuts are fitted with a custom-made program, which is modeling the data in the framework of the distorted wave Born approximation (DWBA) using the local monodisperse approximation (LMA). Within this model, the scattering objects, described by their form factor, are assumed to have a certain shape (cylinder or sphere) with a Gaussian size distribution. The distance between two neighboring objects, named as the structure factor, are modeled with an one-dimensional paracrystal approach [91]. From fitting, the lateral structure sizes and their corresponding center-to-center distances can be obtained.

## **GIWAXS**

The setup of the GIWAXS measurements is similar to that of the GISAXS measurements except that the SDD is much shorter. With a SDD in the order of 10 cm, information about the molecular stacking, crystal orientation and crystal size can be achieved with the GIWAXS measurements.

The GIWAXS measurements are conducted at the Elettra beamline in the present thesis. The beam source, detector and experimental environment are the same as for GISAXS measurements except the absence of a flight tube. Due to the very short SDD, the scattering from air is negligible. Before analyzing the 2D GIWAXS data, solid angle correction, q-resaping and conversion, efficiency correction (air path and pixel sensitivity under oblique angles) and polarization correction on the raw 2D GIWAXS data are required in order to retrieve the corrected reciprocal space patterns [90]. 2D GIWAXS data before and after correction are shown in figure 2.17. All corrections are done with the aid of the software Grazingincidence x-ray Scattering Graphical User Interface (GIXS-GUI), which is developed by the Advanced Photon Source, Argonne National Laboratory, USA [89]. Afterwards, the radial integrals are taken in vertical or horizontal directions. The vertical integrals offer crystalline information along the direction perpendicular to the substrate, whereas the horizontal integrals provide crystalline information along the direction parallel to the substrate. The obtained curves can be fitted with Gaussian functions. From fitting, the lattice constants can be revealed from the peak positions, the crystal sizes can be estimated from the full-width-at-half-maximum (FWHM) values, and relative crystallinity between different samples can be compared by a comparison of peak

intensities. Moreover, information about crystal orientations can be extracted with tube integrals.

## 3.2 Spectroscopic and electronic characterizations

The light absorption is probed with UV/Vis spectroscopy (section 3.2.1). The current-voltage ( $I$ - $V$ ) characteristics measurements are conducted under AM 1.5G illumination ( $1000 \text{ W/m}^2$ ) to determine the performance of solar cells (section 3.2.3).  $EQE$  measurements are used to characterize the capacity of photon-charge conversion as described in section 3.2.4.

### 3.2.1 UV/Vis spectroscopy

The absorption and/or reflectance of samples is probed with UV/Vis spectroscopy in the ultraviolet-visible spectral region. The absorption of active layers is measured using two different spectrometers: The first is a Lambda 35 and the second is a Lambda 650 S. Both instruments are equipped with a deuterium lamp and a halogen lamp. In case of the Lambda 35, the deuterium lamp provides the UV light in a wavelength range of 190 nm - 326 nm, and the halogen lamp generates light in the visible and near infrared range (326 nm - 1100 nm). The scanning speed is set to  $120 \text{ nm min}^{-1}$  and the slit width is 1 nm. For the Lambda 650 S, the lamp sources switch at a light wavelength of 320 nm. A scanning speed of  $256 \text{ nm min}^{-1}$  and a slit width of 1 nm are applied.

In the present thesis, glass substrates are used to support the measured films as the measurements are performed in transmission mode. Grating monochromators ensure the generation of a monochromatic beam. The beam is split into two beams before it reaches the sample. One beam goes through the measured sample, whereas the other is used as a reference beam. The intensity of both beams is detected by two separated detectors (photodiodes). The intensity of the reference beam is regarded as 100% transmission for every wavelength, the intensity of the other beam should be smaller than 100% transmission as the measured sample can absorb and/or scatter lights. The obtained UV/Vis data, actually, are the ratios between these two beams at each wavelength. From the data, the wavelength-dependent absorbance ( $A$ ) can be calculated using the Lambert-Beer law:

$$A(\lambda) = -\log_{10}\left(\frac{I_t(\lambda)}{I_0(\lambda)}\right) = a(\lambda)L\log_{10}e \quad (3.1)$$

with the transmitted intensity of the beam going through the sample  $I_t(\lambda)$ , the reference beam intensity  $I_0(\lambda)$  which is 1 in this work, the specific absorption coefficient  $\alpha(\lambda)$ , the light path length through the sample  $L$ , and Euler's number  $e$ .

As glass strongly absorbs the light at wavelengths below 290 nm, the transmission measurements are carried out using 290 nm as a starting point. Moreover, the transmission of bare glass is measured to calibrate the absorbance of the measured sample without glass substrates. Through integrating all wavelength-dependent absorbances, the light absorption capability of different samples can be compared.

### 3.2.2 FT-IR spectroscopy

Fourier transform infrared spectroscopy (FT-IR) is a technique to identify the presence of certain functional groups present in a sample. The  $\text{TiO}_2/\text{PS-b-PEO}$  composite films before and after UV irradiation are investigated with FTIR to qualify the efficiency of polymer-template extraction induced by UV exposure. A VERTEX 70 FT-IR spectrometer is used to measure the samples. It provides a spectral range from  $6000\text{ cm}^{-1}$  to  $130\text{ cm}^{-1}$  in a one step measurement, which covers a complete far and mid IR spectrum. Moreover, it has a spectral resolution of better than  $0.4\text{ cm}^{-1}$ , which is adequate for most measurements.

The spectrum of interest is generated by a light source. Then a interferometer guides the beam to the sample. Before light reaches the sample, a beamsplitter separates the incident light into two parts with equal intensity and sends the two parts in two directions. One part goes to a stationary mirror and then reflected back to the beamsplitter, whereas the other one goes to a moving mirror then back to the beamsplitter as well. The motion of the mirror makes a change of the optical path. When two beams meet at the beamsplitter, the constructive and destructive interference, named as an interferogram, is created due to the difference in light path lengths. Later, the recombined light passes through the sample and then reaches the detector. It is important to note, all light shines on the sample in every scan. The functional groups of the sample absorb the light with different wavelengths, which leads to the subtraction of specific wavelengths from the interferogram. The detector tells the energy difference as a function of time for all wavelengths simultaneously. It is noticeable that the relationship between energy and time is reciprocal. Therefore, a Fourier transform function converts the spectrum of intensity *vs* time spectrum into the spectrum of intensity versus frequency.

In the present thesis, powders instead of films are used for FT-IR measurements. After sample preparation, the films are peeled off from the substrate to obtain powders. The achieved powders subsequently are spread over a sample holder. The sample is then

scanned over a wavenumber range of  $340\text{ cm}^{-1}$  to  $2000\text{ cm}^{-1}$  with a resolution of  $1.9\text{ cm}^{-1}$ .

### 3.2.3 I-V characterization

In order to test the photovoltaic performance of solid-state dye-sensitized and hybrid solar cells, the  $I$ - $V$  curves are probed.  $I$ - $V$  sweeps are recorded with a Keithley 2400 sourcemeter by applying an external bias to the probed cells under simulated solar illumination. The irradiation, which has a similar solar spectrum, is provided using a solar simulator Solar Constant 1200 (K.H. Steuernagel Lichttechnik GmbH) equipped with a rare earth Xenon lamp. Before  $I$ - $V$  measurements, the light intensity is calibrated to  $1000\text{ W/m}^2$ , i.e. AM1.5 solar illumination, by using a silicon-based calibration solar cell (WPVS Reference Solar Cell Typ RS-ID-3 by Fraunhofer ISE).

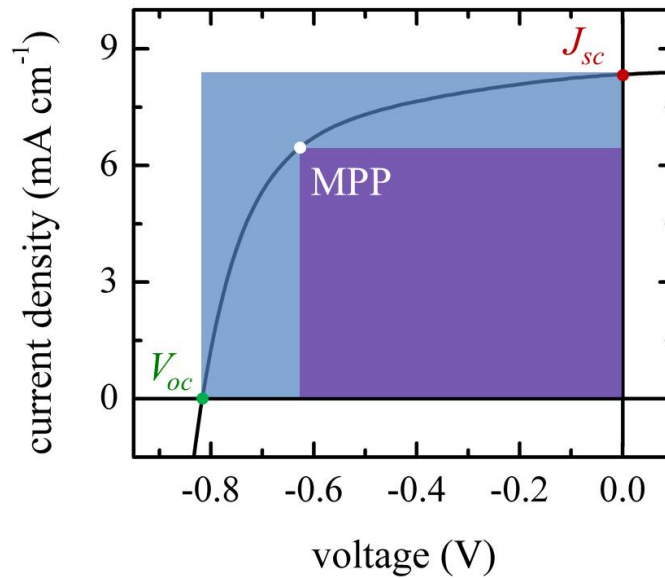


**Figure 3.4:** An exemplary  $I$ - $V$  curve of a solid-state dye-sensitized solar cell which is tested under standard illumination AM1.5 ( $1000\text{ W m}^{-2}$ ). The  $V_{OC}$ ,  $J_{SC}$  and maximal power point (MPP) are indicated by a green dot, a red dot and a white dot, respectively. The violet and blue rectangles indicate the maximal output power and the theoretical maximal output power, respectively. In the example,  $V_{OC} = 0.81\text{ V}$ ,  $J_{sc} = 8.35\text{ mA cm}^{-2}$ ,  $FF = 59\%$ , yielding a  $PCE = 4.1\%$ .

An exemplary  $I$ - $V$  curve of a solid-state dye-sensitized solar cell is shown in figure 3.4. From the curve, the related photovoltaic parameters can be extracted. The open-circuit voltage ( $V_{oc}$ ) and short-circuit current density ( $J_{sc}$ ) are the values of x- and y-intercepts, respectively, as indicated in figure 3.4. In general,  $V_{oc}$  is determined by the n- and p-type



semiconductors in the active layer, whereas  $J_{sc}$  is related to many factors, such as charge carrier generation, transportation, and extraction. Along the curve, a point, where the power density of  $P = J \times V$  is maximum, is defined as maximum power point (MPP) as indicated by a white dot in figure 3.4. The fill factor ( $FF$ ) is the ratio between the power at the MPP (indicated by violet rectangle) and the theoretical maximum possible power of  $P_{max} = V_{oc} \times J_{sc}$  (indicated by blue rectangle):

$$FF = \frac{P_{MPP}}{P_{max}} = \frac{V_{MPP}J_{MPP}}{V_{oc}J_{sc}} \quad (3.2)$$

The  $FF$  is equal to 100% in an ideal device, where the  $I$ - $V$  curve has a rectangle shape. The power conversion efficiency ( $PCE$ ) is defined as the ratio of the device output power ( $P_{out}$ ) and the irradiation input power ( $P_{in}$ ):

$$PCE = \frac{P_{out}}{P_{in}} = \frac{V_{oc}J_{sc}FF}{P_{AM1.5}} \quad (3.3)$$

For the present measurements, a custom-made sample holder provides a shadow mask for the non-measuring area, and ensures that only the probed pixel is under solar illumination. A distance of 320 mm is set between the solar cell and the light source. During measuring, the voltage seeps from -1 V to 0.2 V with 0.01 V increment and 0.01 s delay. Each pixel is measured several times to sort out the best device performance. For an in situ measurement, the pixels are examined continuously in a loop to track the evolution of photovoltaic parameters versus time. After measuring, each metal pixel of the samples is mapped with optical microscopy (OM). Though OM images, the size the pixel is individually calculated with the aid of software ImageJ.

### 3.2.4 External quantum efficiency

Quantum efficiency ( $QE$ ) is defined as the ratio between incident photons and converted electrons. The  $QE$  measurement is commonly carried out over a range of different wavelengths as the energy of a photon is inversely proportional to its wavelength. The ratio between the number of charge carriers collected by the electrodes and the number of incident photons impinging on solar cells is defined as external  $QE$  ( $EQE$ ). Typically, a solar cell with good ability of light absorption and charge carrier collection has a high  $EQE$ .

A “Quantum Efficiency/IPCE Measurement Kit” is used for  $QE$  measurements. A 300-watt xenon arc lamp is employed as light source. An automated filter wheel and a chopper wheel are applied to modulate the light. Later, the light is collimated with a

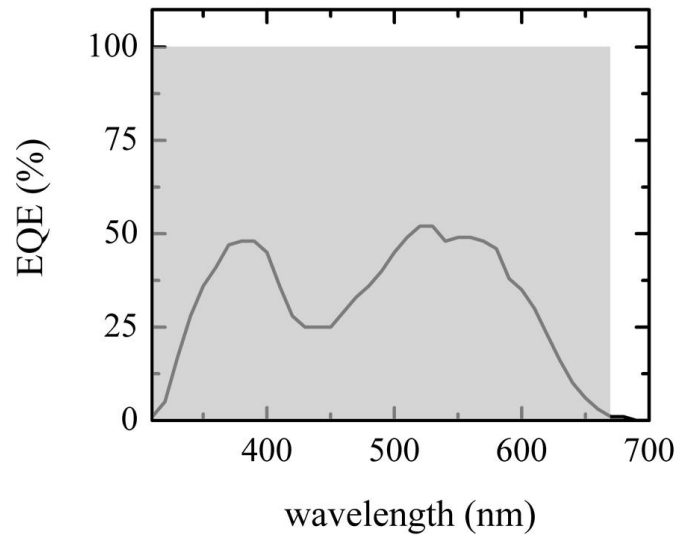


**Figure 3.5:** An exemplary *EQE* curve of a solid-state dye-sensitized solar cell. The grey rectangle indicates the 100% *EQE*.

monochromator before it shines on the sample. A custom-made sample holder is used to control the illumination area of each pixel of the measured solar cell. The generated electrical signal is recorded. Before the measurement, the *EQE* system is calibrated using a silicon reference diode. The measuring parameters are set with the Oriel's TracQ Basic software. For solid-state dye-sensitized solar cells, a wavelength range of 300 nm - 800 nm is chosen for the *EQE* measurement.

An exemplary *EQE* spectra of a solid-state dye-sensitized solar cell is shown in figure 8.19. The ideal case, 100% *EQE* for every wavelength, is indicated by the grey rectangle. However, the experimental *EQE* value is much smaller than the ideal case due to many factors such as substrate reflection, insufficient light absorption, exciton annihilation and charge carrier recombination. By integrating the photo-response over the solar spectrum, the  $J_{SC}$  can be evaluated.

## 4 Sample preparation

The materials and manufacturing processes used for sample preparation for the entire study are presented in this chapter. More detailed parameters and procedures involved in the production and characterization of specific samples are provided in the corresponding chapters 5 to 8.

### 4.1 Materials

The materials used in the present study are sorted into five families: titania precursors, structure-directing templates, dyes, hole-transport materials, and materials used for imprinting. The former four groups are used during the fabrication of solid-state dye-sensitized solar cells (ssDSSCs), and the production of hybrid solar cells includes all materials except dye molecules.

#### **Titania precursors**

Within the frame of this thesis two different titania precursors are employed for the preparation of nanostructured titania films. One is titanium tetra isopropoxide (TTIP) which is used for high-temperature processed ssDSSCs. The other one is ethylene glycol modified titanate (EGMT) which allows fabricating hybrid solar cells at low temperature.

TTIP is purchased from Carl Roth GmbH. It is a transparent or canary yellow liquid with a relative density of  $0.96 \text{ g cm}^{-3}$  and fumes in moist air. Its stoichiometric formula is referred as  $\text{Ti}[\text{OCH}(\text{CH}_3)_2]_4$ , which exists as a monomer with a titanium center having an octahedral coordination environment of isopropoxides, as shown in figure 4.1a. Titania, evolved from TTIP via hydrolysis and condensation reactions, typically requires a high-temperature treatment to be crystallized as anatase or rutile phase. EGMT, also known as titanium glycolate, is synthesized by Thomas Fröschl in the group of Nicola Hüsing and its synthesis method is described in references [92, 93]. It is a white, crystalline powder, which only dissolves under strong acidic conditions. The chemical formula of EGMT is

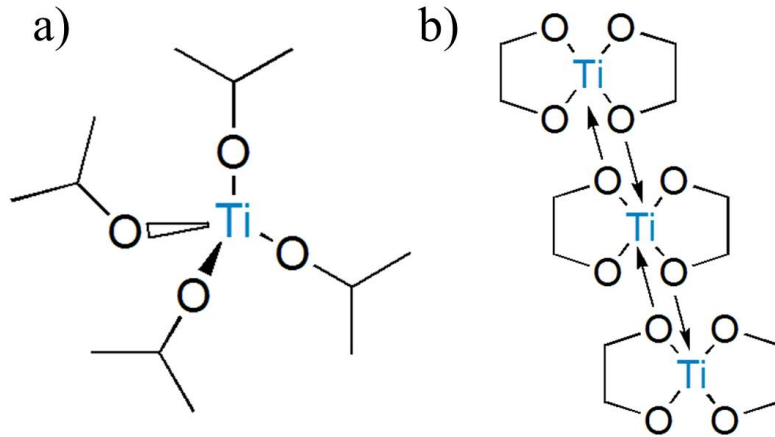


**Figure 4.1:** The chemical structures of *TTIP* and *EGMT*.

quoted as  $\text{C}_4\text{H}_8\text{O}_4\text{Ti}$ , which is presented by the sketch in figure 4.1b. Each titanium atom is connected to six oxygen atoms and each oxygen atom is bound to two titanium atoms. The unit cell of EGMT consists of  $\text{TiO}_6$  octahedrons, which form a one-dimensional chain structure via edge-sharing. The crystalline reflexes of EGMT powder can be found in reference [94]. Crystalline titania can be achieved by using EGMT precursor even at low temperatures via a hydrolytic sol-gel route since the one-dimensional crystalline structure is already present in EGMT. Moreover, the crystal phase of titania can be tuned from anatase to rutile by changing the pH value from above 2 to below 0 during EGMT hydrolysis and condensation reactions [95, 96].

### Structure-directing templates

An amphiphilic diblock copolymer is used as the structure-directing template of titania nanostructures: poly(styrene-block-ethylene oxide), abbreviated as PS-b-PEO. The

polymer	$M_n$ (kg/mol)	PDI	polymer block	$M_n$ (kg/mol)	$T_g$ (°C)
PS-b-PEO	28.5	1.02	PS	20.5	107
			PEO	8	-65
PS-b-PEO	89	1.07	PS	63	93
			PEO	26	-60

**Table 4.1:** Parameters of the diblock polymer templates, including name, number average molar mass  $M_n$ , polydispersity index (PDI), and glass transition temperature ( $T_g$ ).

polystyrene (PS) block is hydrophobic, which forms micelles during the sol-gel synthesis, and the polyethylene oxide block is hydrophilic, which acts as the polymer matrix to incorporate the titania. The diblock copolymer mainly dominates the nanostructured length scale and porosity of the resulting titania films. The chemical formula of the polymer template is shown in figure 4.2.

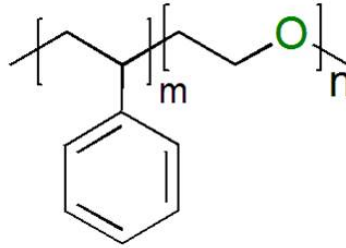


**Figure 4.2:** *The chemical structures of PS-b-PEO.*

Two different molecular weights of PS-b-PEO are used in this thesis and their specific composition parameters are found in table 4.1. All polymers are purchased from Polymer Source Inc., Canada and used directly without any further purification. For the low molecular weight PS-b-PEO, the weight fraction of PEO is  $f_{low} = 0.28$ , while the high molecular weight polymer has the weight fraction of PEO,  $f_{high} = 0.29$ . Similar weight fractions guarantee foam-like nanostructures in the resulting titania films for both templates.

## Dye

The main task of the dye in ssDSSCs is absorbing light and then generating excitons. It acts as a photosensitizer. In this thesis, two types of dyes are used. The first one is 5-[[4-[4-(2,2-diphenylethenyl)phenyl]-1,2,3-3a,4,8b-hexahydrocyclopent[b]indol-7-yl]-methylene]-2-(3-ethyl-4-oxo-2-thioxo-5-thiazolidinylidene)-4-oxo-3-thiazolidineacetic acid (D149). It is a purple indoline dye and its empirical formula can be written as  $C_{42}H_{35}N_3O_4S_3$ . The molecular structure of D149 is shown in figure 4.3a. It has an indoline group in the center acting as an electron donating group. The phenyl rings are added to stabilize the central part. Cyanoacrylic acid serves as an electron accepting group, which is conjugated to the indoline group. The pendant carboxylic acid in this functional group acts as a binder to anchor dye molecules to the surface of titania via the formation of a bidentate complex between the dye and the polar  $TiO_2$  surface. The rhodamine group is beneficial for high electron injection yields. The unique feature of D149 is that it is a pure organic dye (free of any metals), which shows a higher molar extinction coefficient as well as power conversion efficiency (PCE) as compared to the most common ruthenium dye N719 [97, 98].

Moreover, it is cheaper and more environmentally friendly due to the absence of rare earth metals. Therefore, D149 is considered to be one of the most promising indoline dyes since it has already achieved power conversion efficiencies of up to 9 % in DSSCs with liquid iodide ( $I_3^-/I^-$ )-based electrolytes [98].

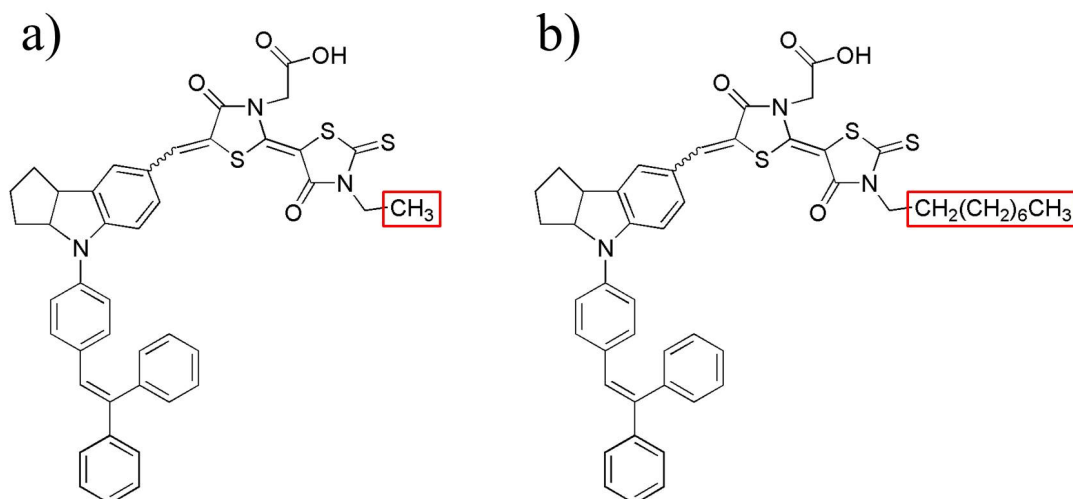


**Figure 4.3:** The chemical structures of a) D149 and b) D205. Their difference is indicated by the red rectangles.

The second dye used in this thesis is 5-[[4-[4-(2,2-Diphenylethenyl)phenyl]-1,2,3,3a,4,8b-hexahydrocyclopent[b]indol-7-yl]methylene]-2-(3-octyl-4-oxo-2-thioxo-5-thiazolidinylidene)-4-oxo-3-thiazolidineacetic acid (D205). D205 has a similar chemical structure compared to D149 as shown in figure 4.3b, except that an n-octyl group instead of the ethyl group bonds to the rhodanine ring. The difference is marked by the red rectangles (figure 4.3). D205 has almost the same molar extinction coefficient as D149, but DSSCs based on D205 have a higher incident monochromatic photon to current conversion efficiency (IPCE) and a lower electron recombination potential than the device using D149 as sensitizers [99].

The dye D149 and D205 are purchased from Sigma Aldrich and used directly without any further treatment. They are dissolved in an acetonitrile/tert-butyl alcohol mixture (volume ratio of 1:1) with a 0.3 mM concentration. Further optimization of the solution is necessary to enhance the performance of the final device. One effective method is to control the aggregation of the dye molecules. The  $\pi$ -stacked aggregation of dyes on the nanostructured titania photoanodes tends to hamper efficient photocurrent generation from dye molecules [100]. Moreover, the aggregation leads to dye residing in the solution instead of binding to the titania surface. Therefore, reducing dye-aggregation is essential during the fabrication of solar cells. Chenodeoxycholic acid (CDCA) has been proved to be an efficient reagent to avoid dye aggregation [101]. Thus, a 0.6 mM concentration of

CDCA is added to the dye solution. CDCA is obtained from Sigma Aldrich with the empirical formula  $C_{24}H_{40}O_4$ . The molecular structure is depicted in figure 4.4. The final solution is sealed to minimize solvent evaporation and shielded against light by wrapping aluminum foil around the solution-containing container.

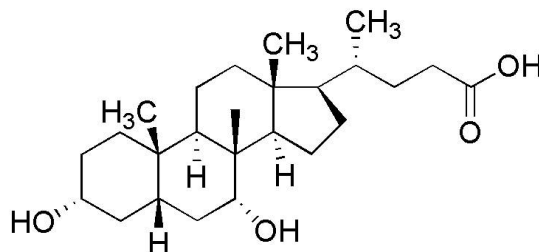


**Figure 4.4:** *The chemical structures of CDCA.*

### Hole-transport materials

Two types of hole transport materials (HTMs) are used in this work. The first one is a molecular HTM 2,2',7,7'-tetrakis(N,N di-p-methoxyphenylamine)9,9'-spiro-bi-fluorene (spiro-OMeTAD). Its chemical structure is shown in figure 4.5a. It has a spiro-center (i.e. a tetrahedral carbon connects to phenyl moieties), which functions to prevent crystallization of this organic materials. Crystallization of the HTM is disadvantageous for solar cell performance as it would lead to a bad contact between the mesoporous titania surface and spiro-OMeTAD. Spiro-OMeTAD was successfully employed as amorphous organic hole-transport materials to build first ssDSSCs since 1998 [102]. After optimization, the device efficiency has reached 7.2 % in 2011 [74]. The unique properties, including the amorphous nature, high solubility, ionization potential and relative easy infiltration into the mesoporous  $TiO_2$  layers, make spiro-OMeTAD one of the best performing hole-conductors for ssDSSCs up to now. However, it has a low charge carrier mobility (in the order of  $10^{-4} \text{ cm}^2 \text{ V}^{-1} \text{ s}^{-1}$ ) in its pristine form. To overcome this problem chemical p-doping is a common technique to improve the electrical property of spiro-OMeTAD and, thereby, enhancing device performance [74, 103]. In this thesis tris(2-(1H-pyrazol-1-yl)-4-tert-butylpyridine)cobalt(III) tri[bis(trifluoromethane)sulfonimide] (FK209) is employed as a proper p-dopant to increase the conductivity of spiro-OMeTAD. The chemical structure of FK 209 is shown in figure 4.5b.

The second HTM is a conducting polymer poly(3-hexyl-thiophene) (P3HT). The chemical structure of the polymer is depicted in figure 4.6. Its backbone consists of thiophene rings with n-hexane side chains. The regular end-to-end arrangement of side groups allows efficient  $\pi$ - $\pi$  stacking of the conjugated backbones. Due to the alkyl chains, the

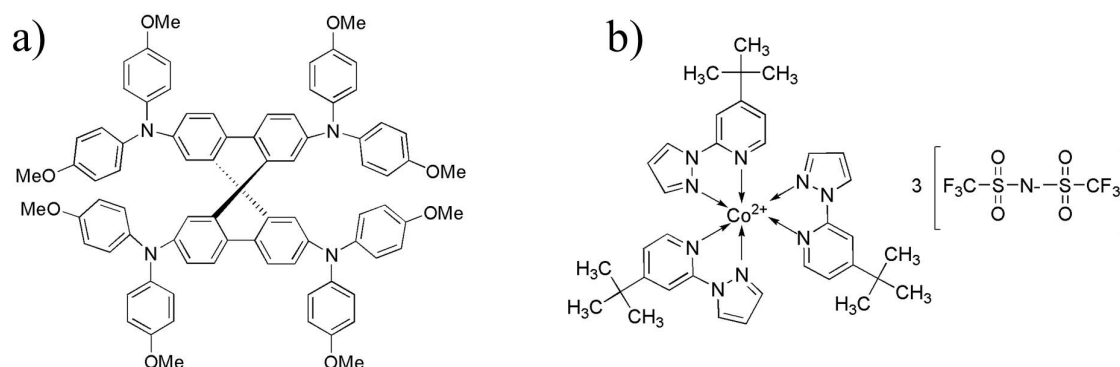


**Figure 4.5:** The chemical structures of a) Spiro-OMeTAD and b) FK 209.

conducting polymer is soluble in organic solvents. P3HT is mostly used in polymer solar cells. In this thesis its application as electron donor material in ssDSSCs or hybrid solar cells have also been studied. Compared to spiro-OMeTAD, P3HT has a high hole mobility of up to  $0.1 \text{ cm}^2 \text{ V}^{-1} \text{ s}^{-1}$  and good solubility in various organic solvents [16]. The P3HT used in this work is purchased from BASF in collaboration with Rieke Metals with a high purity. The molecular weight is given as  $M_w = 53 \text{ kg mol}^{-1}$  and regioregularity as 92 %.

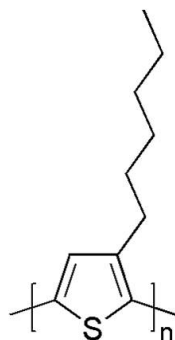


**Figure 4.6:** The chemical structures of P3HT.

## Imprinting Materials

For nano-imprinting of titania/PS-b-PEO composite films, a hard imprint master is required as very high pressure will be applied during nano-imprinting. Soft stamps are not suitable due to the lack of mechanical stability when exposed to high pressures. The pattern of the imprint master is a replica of a patterned silicon substrate. This method reduces the usage of expensive silicon and, thereby, lowers the costs within this production routine. The material used to duplicate the silicon pattern is called OrmoStamp®, which is UV-curable. It is purchased from the company named micro resist technology



GmbH, Germany. This material has many advantageous properties, such as mechanical and thermal stability, excellent pattern replication and compatibility with lithography equipment. To prevent the imprinted titania/PS-b-PEO composite films to stick to the master, an anti-sticking layer is coated onto the master. In the present study, 1H,1H,2H,2H-perfluorooctyltrichlorosilane (PFOTS) is used as an anti-adhesive by lowering the surface energy.

## 4.2 Processing

For titania-based hybrid solar cells, the production procedure comprises several steps, starting from a compact titania layer preparation, mesoporous titania film fabrication, backfilling titania mesopores with HTMs, and metal-electrode evaporation. An overview about all these different steps is given in this section.

### 4.2.1 Compact titania layer

A compact titania layer, acting as hole blocking layer for ssDSSCs, is introduced between the fluorine-doped tin oxide (FTO) and the mesoporous  $\text{TiO}_2$  layer. The compact layer has been proven to be an effective material to prevent recombination of charge carriers [104–106]. It is much denser than the mesoporous  $\text{TiO}_2$  film, reducing the likeliness of short circuits. The manufacturing process of this blocking layer is described in reference [106]. Within this process, 850  $\mu\text{L}$  titanium (IV) n-butoxide is added to 2.625 mL ethanol under vigorous stirring (a Teflon-covered magnetic bar rotates at 800 rpm). After addition of the titania precursor, 210  $\mu\text{L}$  diethanolamine is added. Afterwards, the mixture, denoted as solution 1, is further stirred for 60 min. Separately, 45  $\mu\text{L}$  deionized(DI) water is mixed with 1.25 mL ethanol, denoted as solution 2. After 60 min stirring, solution 2 is added drop-wise into solution 1 under 800 rpm stirring. The resulting solution is stirred further for 24 h at room temperature. Next, the titania solution is spin-coated onto substrates at 2000 rpm for 30 s with an acceleration time of 5 s. After spin coating, the film undergoes a high temperature calcination at 450  $^{\circ}\text{C}$  for 2 h with a heating ramp of 5  $^{\circ}\text{C}/\text{min}$ .

### 4.2.2 Synthesis of mesoporous titania film

The mesoporous titania films are obtained from diblock copolymer template assisted sol-gel synthesis. There are two titania precursors for the sol-gel chemistry. One is TTIP, which is applied to fabricate titania films at high temperature. The other is EGMT, a titania precursor for achieving working photoanodes at low temperatures.

### Sol-gel synthesis with TTIP

The formation of the mesopores in titania films relies on the self-assembly of the template polymer PS-*b*-PEO in a so-called good-poor solvent pair. However, the sol-gel-synthesized titania films from the precursor TTIP normally suffer from a low crystallinity with a low electron conductivity even after long-term calcination at 450 °C [19]. To overcome the shortcomings pre-synthesized crystalline titania nanoparticles are introduced into the framework of mesoporous titania films. The nanoparticles are synthesized by the group of Prof. Dina Fattakhova-Rohlfing from Ludwig-Maximilians-Universität München. The detailed synthesis procedure is described in reference [107, 108]. The enhancement of the conductivity of nanoparticle incorporated titania films is shown in the literature [109]. There are two routes for producing mesoporous titania films in this work.

For the first route, the pre-weighed polymer PS-*b*-PEO is dissolved in 1,4-dioxane ( $C_4H_8O_2$ ), which is achieved by being stirred with a magnetic bar for 30 min (800 rpm). 1,4-dioxane is a good solvent, i.e., non-selective solvent for both PS and PEO blocks. Separately, TTIP is added to ethanol under 800 rpm stirring. 10 min later, a mixture of acetic acid, DI water and ethanol is added in drop-wise with a pipette. 30 min later, the preprepared polymer solution is added. Here, ethanol is a selectively poor solvent for the PS block. As a result of the introduction of ethanol, polymer micelles with PS cores and PEO coronas are formed, and the titania species are bound to PEO chains through coordination bonds [110]. Finally, the solution is stirred at 800 rpm for 20 h. For the nanoparticle suspension, the pre-weighed nanoparticles are added into the polymer solution and then stirred 20 h at 800 rpm until the nanoparticle are dispersed homogeneously in the polymer solution. After 20 h, the prepared sol-gel solution is mixed with the nanoparticle suspension under vigorous stirring. Afterwards, the whole solution is ultrasonicated for 5 min to mix titania-sol and nanoparticles homogeneously in the solution before being deposited onto substrates as described in section 4.2.3. After film deposition, a high temperature sintering (section 4.2.2) is required to obtain the final mesoporous titania films.

For the second route, a binary azeotrope of toluene and 1-butanal is used as good-poor solvent pair, where toluene is the good solvent and 1-butanal is the poor solvent for the polymer template PS-*b*-PEO. The azeotrope with an approximate composition of 72.2 wt% toluene and 27.8 wt% 1-butanal has a constant boiling point of 105.5 °C, which allows simultaneous evaporation of the solvent pair during film deposition, i.e., the fraction of good and poor solvent remains constant. Therefore the driving force of polymer self-assembly is unchanged during solvent evaporation. Particularly, this is crucial for spray deposition, which is a slow process of solvent removal as compared to spin coating. The

self-assembly of the polymer template may change during slow solvent evaporation if the good-poor solvent pair is not an azeotrope. The polymer template PS-b-PEO is dissolved in an azeotrope mixture of toluene and 1-butanol by stirring at 800 rpm for 30 min. Afterwards, TTIP is added precisely via a pipette. After another 30 min stirring, HCl (8 M) is added drop-wise under vigorous stirring. The resulting solution is aged for 20 h at room temperature. The procedure for nanoparticle incorporation is unchanged, except using toluene instead of 1,4-dioxane for the nanoparticle suspension. Mesoporous titania films are synthesized by different deposition methods and subsequent high-temperature process. A schematic overview of both routes is displayed in figure 4.7.

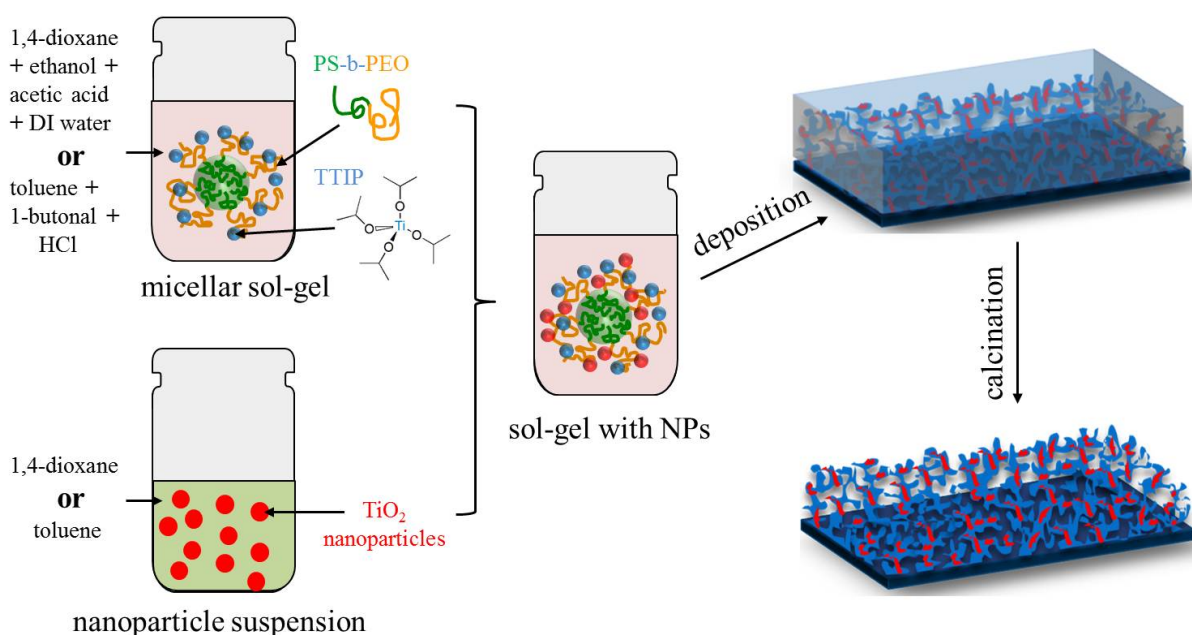


**Figure 4.7:** Schematic illustration of fabricating mesoporous titania films with incorporated nanoparticles. It involves several steps: polymer template assisted sol-gel synthesis using the titania precursor TTIP, film deposition and high-temperature calcination.

### Sol-gel synthesis with EGMT

Mesoporous titania films obtained from sol-gel synthesis of EGMT can be directly used as photoanodes for solar cells without high-temperature processing. The EGMT powder is weighed in a pre-cleaned glass vial before adding the required amount of HCl (12 M), and then the mixture is put into an ultrasonic bath for 10 min until the solution is clear. Separately, the polymer template PS-b-PEO is dissolved in dimethylformamid (DMF) by stirring (800 rpm) for at least 30 min. Afterwards, the polymer solution is carefully transferred to the glass vial with the EGMT solution by a pipette. The final mixture is

stirred at 90 °C for 30 min. A clear solution with the color of pale yellow is obtained, which is then stirred for another 24 h after cooling down to room temperature. The weight ratios in the final solution are 20:1:1:2 of DMF:PS-*b*-PEO:EGMT:HCl. A schematic overview of the hydrolytic sol-gel route at low temperature is shown in figure 4.8a. After 24 h aging the solution is deposited onto substrates and UV irradiation is subsequently used to remove the PS-*b*-PEO template. Furthermore, the obtained sol-gel solution can be mixed with nanoparticle suspension under vigorous stirring, as illustrated in figure 4.8b.

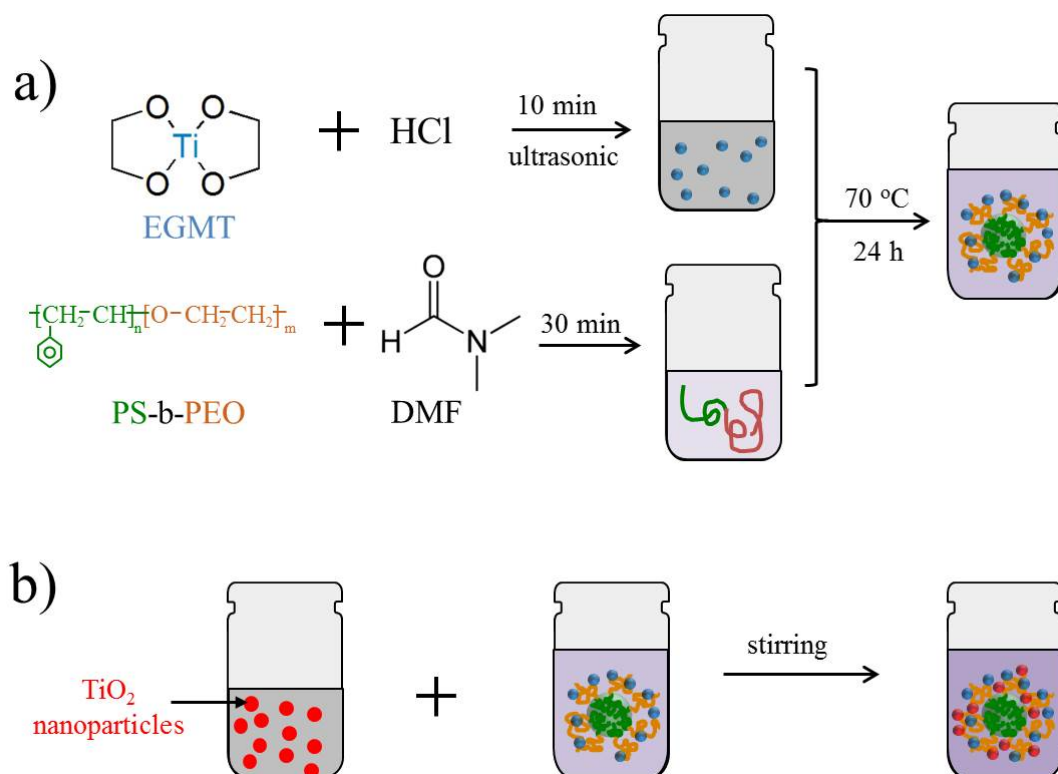


**Figure 4.8:** Schematic overview of the sol-gel chemistry using EGMT as titania precursor.

### Annealing and calcination

After film deposition, annealing of the resulting TiO<sub>2</sub>/PS-*b*-PEO composite films is performed at a temperature above the  $T_g$  of PS. On one hand, the annealing step improves the self-assembly of the polymer template. On the other hand, it completely removes residual solvent. The composite film is more stable under ambient conditions without the existence of solvents, which is beneficial for further film characterization.

The annealed composite films made from TTIP require high-temperature calcination to burn away the diblock copolymer template and to transform titania from its amorphous phase to the crystalline anatase phase. After calcination crystalline mesoporous titania

films are achieved, which are desirable for photovoltaic applications [10, 111–114]. In this work, the calcination is performed in a tube furnace (GERO or Hereaus instruments) under ambient conditions. A calcination protocol of heating ramp, calcination temperature, calcination time can be set according to different requirements. If not specifically mentioned, a standard calcination scheme in the present thesis consists of a heating ramp of 5 °C/min and a calcination temperature of 500 °C for 2 h.

### 4.2.3 Deposition methods

The titania/PS-b-PEO composite films are deposited from the corresponding solutions usually onto solid substrates for film characterization. Common substrates are silicon wafers (Si-Mat, (100)-orientation, 100 mm in diameter) and soda-lime glass sheets (Carl Roth GmbH, 26 × 76 mm<sup>2</sup>). In order to meet various experimental requirements, the silicon or glass substrates are cut into smaller pieces using a diamond cutter. The cut substrates are then cleaned in a sulfuric acid bath as described below. Several deposition techniques are applied to prepare films onto the substrates, such as spin coating, spray coating and solution casting. In the present thesis, the titania/PS-b-PEO composite films are deposited via either spin coating or spray coating. The HTM layer is mainly produced with spin coating, in some special occasions, it is prepared by solution casting.

#### Substrate cleaning

To ensure that the deposited films are not contaminated by surface impurities on the substrate, silicon and glass sheets are cleaned in an acid bath before using them as substrates. Moreover, the cleaning process can keep a defined state of the substrate surface, which is essential to ensure reproducibility. The acid bath is prepared according to the procedure established in reference [115]. DI water (H<sub>2</sub>O), hydrogen peroxide (H<sub>2</sub>O<sub>2</sub>) and sulfuric acid (H<sub>2</sub>SO<sub>4</sub>, 98 %) are mixed in sequence in a glass beaker residing in a water bath at room temperature. The amounts of each component are given in table 4.2. After mixing, the water bath is heated to 80 °C gradually. Separately, the substrates are loaded into a teflon holder and rinsed with DI water to remove dust particles from the substrate surface. Once the temperature reaches 80 °C, the teflon holder is immersed into the acid bath, and kept for 15 min. Thereafter, it is taken out and transferred to a beaker with pure DI water. Each substrate is rinsed with DI water to remove acidic traces before being dried under nitrogen flow. After drying, the substrates are stored in a clean sample box for further use.

component	amount
H <sub>2</sub> O	54 mL
H <sub>2</sub> O <sub>2</sub>	84 mL
H <sub>2</sub> SO <sub>4</sub>	198 mL

**Table 4.2:** Volumetric composition details of the acid bath used for substrate cleaning.

## Spin coating

Spin coating is a procedure to obtain uniform thin films on flat substrates. The process of spin coating can be classified into four steps. (1) The coating material, containing the molecules dissolved in a solvent, is applied onto a substrate. (2) The substrate is rotated at high angular speed and consequently the majority of the coating material is flung off the substrate. The high-speed spinning is necessary for the formation of homogeneous films. The centrifugal force caused by spinning spreads the liquid evenly on top of the substrate. Larger centrifugal force usually lead to better film homogeneity. (3) Airflow caused by the rotation makes the majority of the solvent evaporate rapidly. (4) After solvent evaporation, a homogeneous plasticized film is achieved on the substrate. For spin coating, higher angular speed leads to thinner final films. Furthermore, film thickness also depends on the solvent, the viscosity and concentration of the solution. In case of films derived from pure polymer solutions, the film thickness  $d$  can be estimated using an empirical formula.

$$d = C\omega^{-\frac{1}{2}}c_0M_W^{\frac{1}{4}} \quad (4.1)$$

where  $C$  is an empirical constant,  $\omega$  is the angular speed,  $c_0$  is the solution concentration and  $M_W$  is the molecular weight of the polymer. The solution concentrations need to be in a range, where the thickness is linearly correlated to the solution concentration [116].

For samples deposited by spin coating a Delta 6 RC TT (Süss MicroTec Lithography GmbH) spin coater is applied. The parameters of spin coating including acceleration speed, angular speed of rotation and rotation time are first set. The pre-cleaned substrate is placed on the rotation table of the spin-coater and is then held via an applied vacuum. It is important to note that the center of the substrate has to be aligned to the rotation axis. A certain amount of solution is dripped on the substrate by a pipette. After the rotation stops, the sample is dismounted from the spin-coater and its back side is wiped with a clean tissue to remove residual solution.

## Spray deposition

Spray coating is a process in which the substrate collects dynamic droplets dispersed in a gas. The process of generating these small droplets is known as atomization, which is achieved by pushing out the liquid from a spray nozzle with the aid of a compressed carrier gas [117]. The shape of the spray pattern on the substrates, like solid stream, hollow cone and full cone, strongly depends on the spray nozzles. By selecting the right type of nozzle, a large variety of patterns can be achieved. In this work, a full cone nozzle is chosen for spray deposition, which gives a round shaped area on the substrates with complete spray coverage. Before being sprayed out of the nozzle, a part of the liquid is usually swirled within nozzle and the other part is non-spinning liquid that bypasses an internal vane. When the liquid runs out through the exit point of the nozzle (usually denoted as orifice), the full conical pattern is achieved. By changing the vane design and/or the distance between the vane location and the orifice, the spray angle and liquid distribution of the spray cone can be tuned appropriately. Full spray cone finds itself most widely used in industry.

The process of spray coating with a full cone is schematically illustrated in figure 4.9. The whole liquid breakup is divided into three flow regimes based on the volume fraction during liquid atomization as described below, which has been reported by Jenny et al. [118].

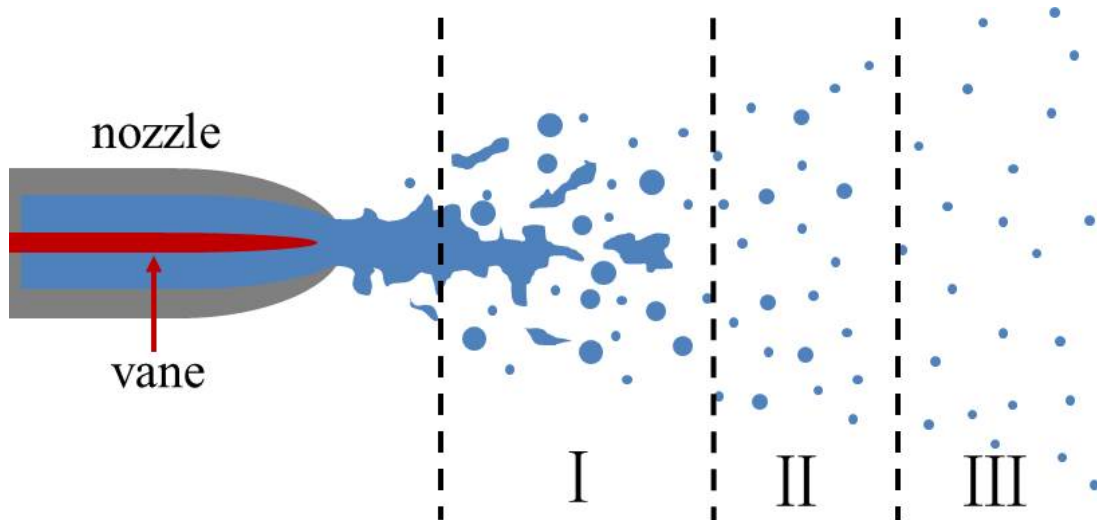


**Figure 4.9:** Schematic illustration of liquid atomization with three flow regimes.

- *regime I:* This regime is named as dense regime. In this region the collision and coalescence of droplets occur frequently, which is the main characteristic of the dispersed

phase dynamics. Due to the abundant existence of droplets, they easily collide with their neighbors and merge together. The dispersed phase volume ration is above  $10^{-3}$ .

- *regime II*: This regime is denoted as dilute regime. In this regime the continuous phase turbulence is dispersed significantly, which dominates the dispersed phase dynamics. The collision and coalescence of droplets can be neglected since the single droplet is far away from its neighbors. The dispersed phase volume ration is in the range of  $10^{-3}$  to  $10^{-6}$ .

- *regime III*: This regime is referred as very dilute regime. Here, the continuous phase turbulence scarcely exists. Small and isolated droplets are presented instead. The dispersed phase volume ration is less than  $10^{-6}$ .

During spray coating the solvent evaporation from the droplets has to be considered as an important factor for the determination of the spray parameters. For example, if solvent evaporates completely during the droplet transport period, the substrate collects a layer of powders rather than a film layer. A very small amount of solvent makes the droplets stick to the substrate and enable them to fuse with pre-arrived droplets. The pressure of the carrier gas and nozzle-to-substrate distance are the key parameters to control the solvent evaporation of the droplets. In the present thesis, the spray device is mounted on a spray set up which allows to regulate the pressure of the carrier gas and nozzle-to-substrate distance. The spray nozzle is orientated perpendicular to the substrate and the nozzle-to-substrate distance is set to 16 cm. The pressure of the carrier gas is kept constant at 2 bar during the whole spray coating process. Under this gas pressure, the flow rate of the coating solution is adjusted to be  $25\text{-}30\text{ }\mu\text{L s}^{-1}$ . The substrate is kept at  $80\text{ }^{\circ}\text{C}$  during the whole process. Two spray protocols are applied in this work: one is using 10 s spray shots and 10 s pause between subsequent shots instead of continuous spray deposition. The other protocol uses that 1 s spray shots and 1 s pauses. A thicker film can be achieved via spraying more solution.

## Solution casting

Usually thick films can be obtained by solution casting. The film thickness can be tuned by the solution concentration and the amount of solution dripped on the substrate. Compared to spin coating and spray coating, solution casting is very cost-effective as no material is lost during the deposition process. However, it lacks homogeneity. Due to Marangoni flow inside a droplet during the solvent evaporation [119], coffee-rings tend to be produced at the solution edge, which destroys the film homogeneity. For the present experiments, solution casting is used to deposit spiro-OMeTAD layers. The substrate is placed onto a flat metal plate before a defined amount of the coating solution is dripped



on the substrates. It is important to note, the substrate needs to be fully covered. It takes much more time for total solvent evaporation as compared to spin coating and spray coating. After solvent evaporation, a spiro-OMeTAD layer is formed, which can be used directly as a HTM layer in ssDSSCs.

#### 4.2.4 Solar cell assembly

Two types of titania-based solar cells are produced within the scope of the present work, ssDSSCs and hybrid solar cells. The difference is that no dye is involved in the architecture of hybrid solar cells whereas ssDSSCs need a dye. The production steps of both solar cells are demonstrated in figure 4.10. The individual steps are discussed in more detail below.

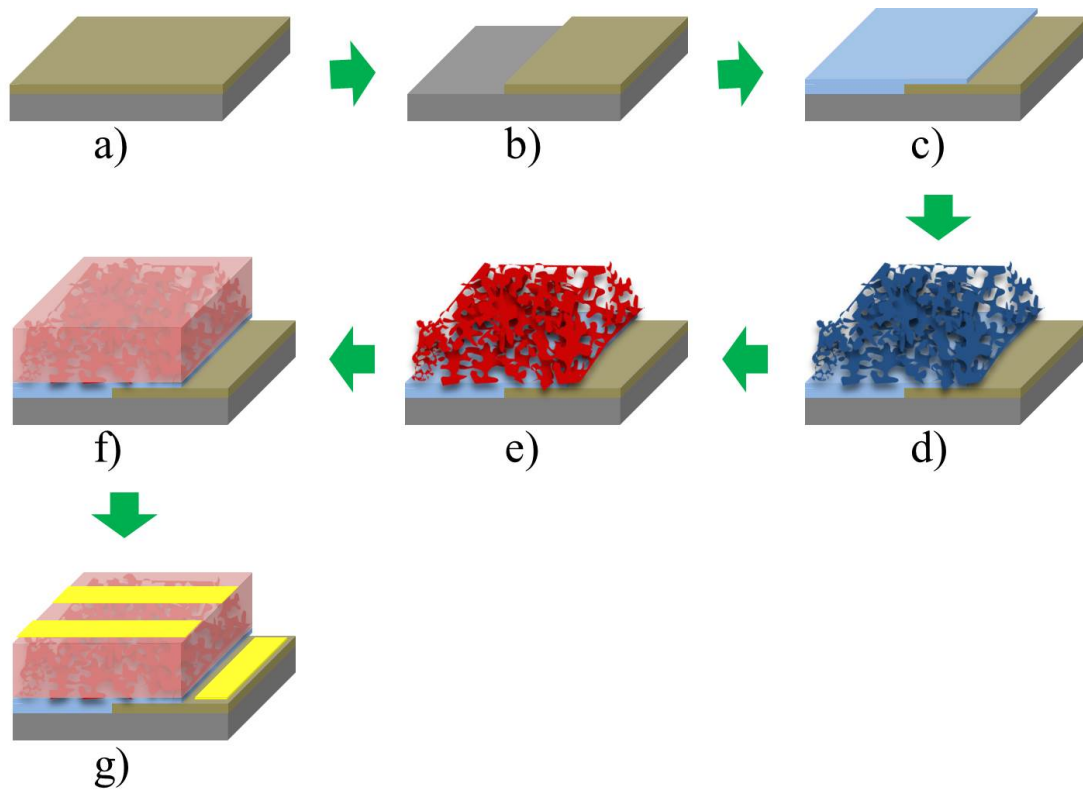


**Figure 4.10:** Schematic illustration of the fabrication of ssDSSCs and hybrid solar cells. Both cells start with a FTO-coated glass substrate. a) FTO sheets are etched to obtain a desirable pattern. b) The patterned FTO sheets are cleaned with organic solvent. c) The compact titania layer is deposited as electron blocking layer. d) The mesoporous titania films are produced. e) Dye molecules anchor to the nanostructured titania. For hybrid solar cells, this step is not present. f) The HTMs are coated on top of the (dyed) titania films. g) The gold back contact is deposited on top to finalize the solar cells.

### Substrate preparation

The production of solar cells starts with the preparation of the bottom electrode. A transparent conductive oxide, namely fluorine-doped tin oxide (FTO), is used as the bottom electrode. The FTO sheets are purchased from Solaronix with a size of  $10 \times 10 \text{ cm}^2$ , a thickness of 1.0 mm and a resistance of about  $15 \Omega \square^{-1}$ . First, the FTO substrate are cut into pieces of  $2.1 \times 2.1 \text{ cm}^2$ . To avoid short circuits in the device, a small stripe of FTO is etched away as shown in figure 4.10b. Therefore, one part is covered with a scotch tape. Then, zinc powder is placed on the the tape-free area. Afterwards, HCl (12 M) is dripped on the zinc powder, the uncovered FTO is etched away. After etching, the substrates are rinsed with DI water to remove leftovers of zinc powder and HCl before tearing off the protective tape. Afterwards, the patterned FTO sheets are cleaned with four organic solvents in sequence in a ultrasonic bath for 10 min. The used solvents are: Alconox® detergent solution ( $16 \text{ mg mL}^{-1}$ ), ethanol (99.8 %), acetone (99.9 %) and 2-propanol (99.8 %). The cleaned substrates are subsequently treated with oxygen plasma for 10 min to remove organic residues.

### Hole blocking layer

A compact titania film is used as hole blocking layer. The detailed sol-gel synthesis is described in section 4.2.1. The deposited method, spin coating, is explained in detail in section 4.2.3. It is important to note that a narrow stripe of FTO is protected by a piece of tape, making sure this area is not coated the compact titania layer. After spin coating, the tape is removed and the compact film is calcined for 1 h at  $450^\circ\text{C}$  with a heating ramp of  $5^\circ\text{C}/\text{min}$ . The final architecture is shown in figure 4.10c.

### TiCl<sub>4</sub> treatment

The compact titania layer is treated with a TiCl<sub>4</sub> bath to improve the adhesion to mesoporous titania layer above [120]. First, the compact titania coated FTO sheets are rinsed with DI water before placed into a beaker with 50 mL DI water inside. Here, make sure all the substrates are immersed in DI water. Afterwards, 1 mL of the TiCl<sub>4</sub> solution (2 M) is added drop-wise. The beaker is then moved into a water bath, which is heated up to  $70^\circ\text{C}$  gradually. After the water bath reaches  $70^\circ\text{C}$ , the samples are kept at this temperature for 30 min. The substrates are subsequently taken out from the TiCl<sub>4</sub> bath and rinsed with DI water and ethanol in sequence before drying with nitrogen. Finally, the samples are calcined at  $500^\circ\text{C}$  for 30 min with a heating ramp of  $600^\circ\text{C}/\text{h}$ .

### Mesoporous titania films

Mesoporous titania films obtained from TTIP and from EMGT are used as photoanodes for ssDSSCs and hybrid solar cells, respectively. The sol-gel synthesis is described in details in section 4.2.2. The titania sol-gel solution is deposited onto the compact titania coated FTO substrates by spin coating or spray coating. Coating methods are explained in section 4.2.3. After film deposition, the titania/PS-*b*-PEO composite films derived from TTIP undergo high temperature calcination to burn away the polymer template, while for EMGT the polymer template is removed by UV irradiation to obtain porous titania films (figure 4.10d). For ssDSSCs, the porous titania structures are again treated with a  $\text{TiCl}_4$  bath.

### Dye loading

Dye loading is only used for ssDSSCs. After the second  $\text{TiCl}_4$  treatment, the mesoporous titania films are taken out from the furnace at 80 °C before again being treated with oxygen plasma for 30 min. Afterwards, the samples are directly soaked into a D149 or D205 dye solution and kept inside for 20 h. The dyed samples are then taken out from the dye solution and rinsed with acetonitrile to remove superfluous dyes which do not anchor to the titania surface. In the end, the samples are dried with nitrogen (figure 4.10e).

### HTM backfilling

For ssDSSCs, the dyed titania films are backfilled with P3HT or spiro-OMeTAD to achieve the active layer (figure 4.10f). The P3HT layer is produced via spin coating, while the spiro-OMeTAD layer is prepared via solution casting.

For hybrid solar cells no dyes are employed for the device fabrication. The achieved mesoporous titania films are pre-soaked in the host solvent of the P3HT solution for 45 min before backfilled with P3HT by spin coating. To obtain more efficient titania photoanodes, artificial superstructures are introduced onto mesoporous titania films. The detailed process of master production is described in section 4.2.5. The features of the superstructured mesoporous titania films and the corresponding hybrid solar cells are shown in chapter 8.

## Gold electrode

A gold electrode is used as the counter electrode for both ssDSSCs and hybrid solar cells. Producing the gold contact is the last step in the solar cell fabrication process, as shown in figure 4.10g. In this work, the gold contact is deposited via thermal evaporation. The samples are placed upside down on into a shadow mask. During evaporation, the gold contact, in form of a pixel, can only be deposited onto the samples through these openings. The evaporation chamber is evacuated to a pressure of less than  $3 \times 10^{-5}$  mbar before about 180 mg of gold is thermally evaporated for 3 min. After the gold electrode is deposited successfully, the performance of solar cells is ready to be tested. The active area of one pixel is defined as the region where the gold contact overlaps with the FTO. During solar cell test, no shadow masks are applied. The accurate area is evaluated from its optical image via the software ImageJ v1.42q.

### 4.2.5 Imprint master fabrication

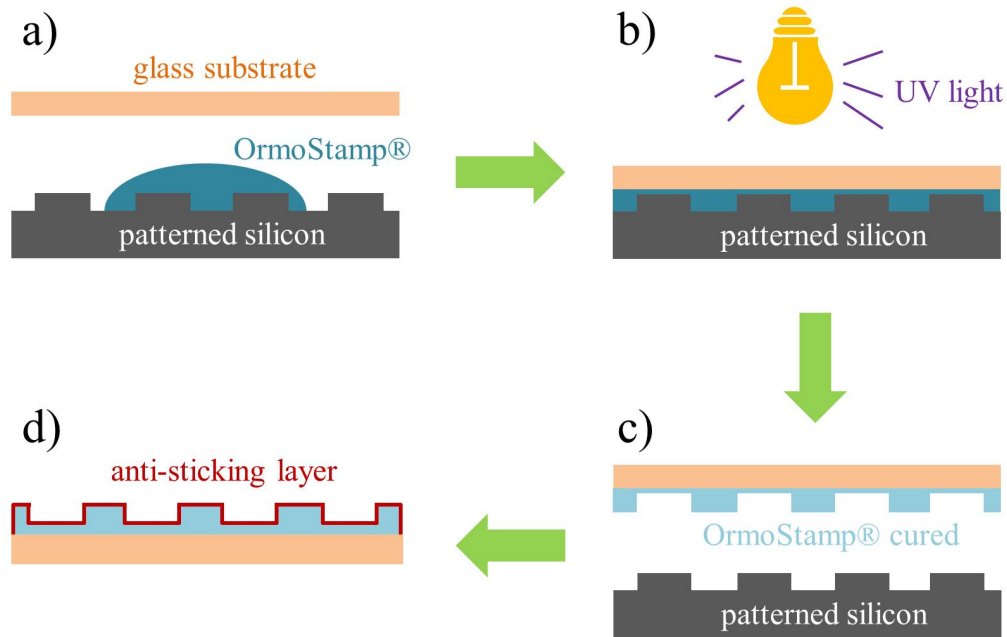


**Figure 4.11:** Schematic illustration of fabricating the master with a negative replica of the silicon relief.

Figure 4.11 schematically illustrates the process steps for the fabrication of the master with a duplicate relief of the silicon template. The UV-curable material (OrmoStamp®) is put on the patterned silicon. Then, a thin glass slide (0.1 mm) is brought to contact with the silicon (figure 4.11a). Thus, the OrmoStamp® material is forged into the relief

structure of the silicon and, finally, sandwiched between the thin glass slide and the silicon substrate as shown in figure 4.11b. After UV exposure, the cured OrmoStamp® can be released from the silicon substrate. A negative replica of the silicon relief is transferred to the imprint master as shown in figure 4.11c. After de-molding, the patterned master is coated with a thin layer of anti-sticking agent to finalize the ready-to-use imprint stamp (figure 4.11d).



## 5 Spray deposition of titania films with incorporated crystalline nanoparticles

Parts of this chapter have been published in the article: Spray deposition of titania films with incorporated crystalline nanoparticles for all-solid-state dye-sensitized solar cells using P3HT [109] (L. Song et al., Adv. Funct. Mater., 26, 1498–1506, 2016, DOI: 10.1002/adfm.201504498).

Over last decades, organic solar cells, especially in the bulk heterojunction (BHJ) configuration, have been the focus of an increasing research interest due to their unique properties, like low costs, light weight, mechanical flexibility, low environmental impact, abundant availability and short time for the energy pay-back [121–127]. Nevertheless, the short lifetimes of organic solar cells, which are caused by negative impact of oxygen, moisture or morphology changes, mainly impede commercial implementation [80,128,129]. Therefore, hybrid solar cells are put forward as a stable alternative. The hybrid devices combine the advantages from organic and inorganic components, such as low fabrication costs, good physical and chemical stability and controllable morphology [130–134]. Currently, the most common hybrid device configuration consists of n-type inorganic nanocrystals and p-type organic materials. Solid-state dye-sensitized solar cell (ssDSSC) is a common hybrid construct, which typically consists of mesoporous titania films as the electron-transport material and p-type conjugated polymers or small organic molecules as the hole-transport material. To date, significant progress has been made on the development of ssDSSCs. The first prototype of ssDSSC was proposed in 1998 by Bach et al., who used mesoporous  $\text{TiO}_2$  as a photoanode and spiro-OMeTAD as a hole conductor. The power conversion efficiency (*PCE*) was only 0.74 %. After nearly two decades of development by technology optimization, the *PCEs* have been pushed beyond the milestone of 7 % by combining the mesoporous titania films, the metal-free dyes and the spiro-MeOTAD layers [74,103]. Recently, by using organometallic halide perovskite sensitizer, efficiencies over 12 % have been attained [135–137]. However, this progress has been made based on the development of more advanced sensitizers or hole-transport materials.

In this work, we are focusing on mesoporous titania films, in order to investigate whether the tailoring of titania nanostructures further influences the final device performance of ssDSSCs.

The morphology of  $\text{TiO}_2$  films can be easily modeled. A large number of  $\text{TiO}_2$  structures in thin films have been reported, such as nanorods [138], flakes [139], nanowires [140], nanogranulas [141], sponges [142] or others. Moreover, there have been many different preparation routes in producing titania thin films [95, 143–145]. A promising approach that, combines sol-gel chemistry and diblock copolymer templates has been extensively used to synthesize titania nanostructures. The copolymer typically consists of a hydrophilic and a hydrophobic block. During the sol-gel process, titania species selectively incorporate into the hydrophilic block of the diblock copolymer due to the formation of covalent bonds. Normally, the solvent system for sol-gel process consists of at least one good solvent and one poor solvent. Both blocks can be dissolved in good solvent, whereas the poor solvent can only dissolve the hydrophilic block. Therefore, the good-poor solvent pair drives the hydrophobic blocks forming micelles in the solution to minimize the system energy. The self-organizing nature of copolymers is the basis of obtaining mesoporous titania films. Moreover, sol-gel chemistry enables reactants to be mixed uniformly at molecular level, which provides the possibility for modifying titania nanostructures at nanometer length scale or even at molecular scale.

Many deposition techniques have been developed to deposit titania films from the prepared sol-gel solution, such as spin coating, spray coating, solution casting, doctor blading or dip coating. Spray coating, compared to others, is facile and potentially cheap method. It does not require complicated experimental apparatus and it can be operated easily. For titania films, spray coating allows the deposition directly from the prepared sol-gel solution, no post treatment of the solution is needed. Moreover, it can be adapted for large-scale industrial applications.

In this work, sol-gel synthesis in combination with the diblock copolymer poly(styrene-block-ethylene oxide) (PS-*b*-PEO), named as copolymer assisted sol-gel synthesis, is employed to produce titania films. To obtain more efficient titania photoanodes, presynthesized crystalline nanoparticles with a titania size of  $\approx 4.5$  nm are incorporated into titania network. The  $\text{TiO}_2$ /PS-*b*-PEO composite films are deposited from the prepared titania sol-gel solution via spray coating. After film deposition, the composite samples undergoes a high-temperature calcination to achieve mesoporous titania films, which serve as electron acceptor in the final ssDSSCs. In this work, the influence of presynthesized crystalline titania nanoparticles on the properties of titania films is the focus of interest. Four films with different concentrations of presynthesized crystalline nanoparticles are prepared. The  $\text{TiO}_2$  derived from sol-gel process and from nanoparticles is at weight ratios of 1:0, 3:1,



1:1 and 1:3. These four films are denoted as 0 wt% NPs, 25 wt% NPs, 50 wt% NPs, and 75 wt% NPs, respectively. After high-temperature processing, the results of these four titania films are described and compared in the first part of this chapter (section 5.1). The surface morphology of the obtained films is studied in section 5.1.1. Section 5.1.2 presents the investigations on film inner morphology. This is followed by the study of film crystallinity and conductivity in section 5.1.3. The device performance of the solar cells with and without electron blocking layer are investigated in section 5.2.1. The obtained results are compared in section 5.2.2.

## 5.1 Titania nanostructures modified with crystalline nanoparticles

The titania nanostructures studied in this chapter are prepared by the first route of sol-gel synthesis with TTIP described in section 4.2.2. The used amounts of reactants are listed in table 5.1.

	sol-gel process					
agent	PS-b-PEO	1,4-dioxane	ethonal	TTIP	acetic acid	DI H <sub>2</sub> O
amount	150 mg	8 mL	3 mL	1 mL	219 $\mu$ L	122 $\mu$ L

**Table 5.1:** *The composition details of sol-gel synthesis.*

For the sol-gel process, the amounts of each chemical are give in table 5.1. After 20 h aging, the sol-gel solution is mixed with nanoparticle solution. The films with different nanoparticle concentration require different amounts of sol-gel and nanoparticle solutions. For example, 515  $\mu$ L, 1.03 mL and 1.545 mL preprepared TiO<sub>2</sub> sol-gel solutions are mixed with nanoparticle solution to obtain a 25 wt% NPs, 50 wt% NPs and 75 wt% NPs solutions, respectively. The used amounts of the nanoparticle solution are listed in table 5.2.

	nanoparticle solution		
sample name	PS-b-PEO	1,4-dioxane	nanoparticles
25 wt% NPs	38.75 mg	3.985 mL	75 mg
50 wt% NPs	32.5 mg	3.47 mL	50 mg
75 wt% NPs	26.25 mg	2.955 mL	25 mg

**Table 5.2:** *The composition details of titania solution with 50 wt.% of titania nanoparticles.*

The 0 wt% NPs, 25 wt% NPs and 75 wt% NPs solutions are prepared under the same procedure as the 50 wt% NPs solution, except for the different amounts of  $\text{TiO}_2$  sol-gel solution and nanoparticle solution that are mixed. It is noteworthy that the nanoparticles consist of titania covered with organic ligands rather than pure titania. The titania core has a size of about 4.5 nm and accounts for 45 wt% of the whole nanoparticle. The titania is mostly in anatase crystalline phase, which is verified by high resolution transmission electron microscopy (HR-TEM) and XRD measurements. The TEM image XRD and pattern are displayed in figure 5.1.

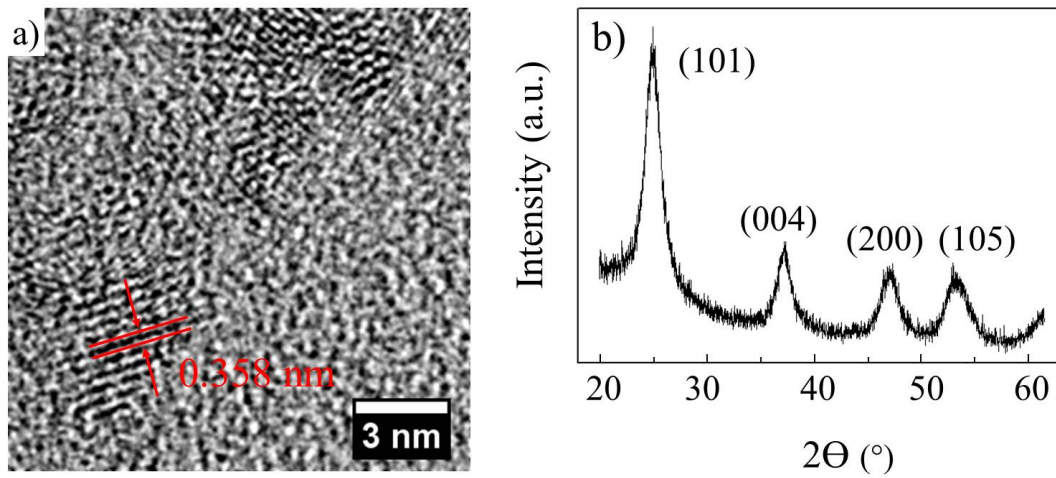


**Figure 5.1:** a) HR-TEM image and b) XRD pattern of the presynthesized nanoparticles. The red lines in a) refer to the interlayer distance of titania crystal.

The sample exhibits a well-resolved interlayer distance of 0.358 nm, which matches well with the lattice spacing of the anatase (101) planes (0.352 nm). The anatase crystalline phase of nanoparticles is further confirmed by the XRD pattern, whose peak positions match the anatase reference data from the International Center for Diffraction Data (ICDD). The resulting titania solutions are then spray-coated onto substrates as described in section 4.2.3. After film deposition, a high temperature calcination step is carried out in order to burn away the polymer template and to transform amorphous titania into anatase crystalline phase as described in section 4.2.2. The thickness of mesoporous titania films has a significant impact on the performance of ssDSSCs. The optimal titania thickness for the solar cells with P3HT as hole-transport layer is in the range of 1.5  $\mu\text{m}$  to 2.0  $\mu\text{m}$  as reported by Lancelle-Beltran et al. [77]. By adjusting the amount of solution for spray coating, the thickness of mesoporous titania layer (after calcination) is well controlled, at about 1.8  $\mu\text{m}$ . The film thickness is measured with DektakXT Stylus Profiler as described in section 3.1.1.

### 5.1.1 Surface morphology

The surface morphology of these four titania films is probed with scanning electron microscopy (SEM), which is a real-space imaging technique for mapping the surface of the investigated samples on a local scale. Plan-view SEM images of the four titania films are displayed in figure 5.2. The mesoporous nature of the sponge-like morphology exists in all samples, suggesting that the interconnected titania nanostructures at the nanoscale can be achieved by spray coating, like by spin coating. The film without nanoparticles has the smallest pores with a average diameter of about 10 nm. Isolated mesopores locate irregularly over the sample surface, and no defects are observed. The 0 wt% NPs film is highly homogeneous.

In figure 5.2b to 5.2d, the top view of the samples with nanoparticles is shown. The surface morphologies of the three samples are different from that of the 0 wt% NPs film. With incorporating nanoparticles, the surface gets roughen and less homogeneous. Unlike isolated pores and planar layout (figure 5.2a), interconnected pore arrays and three dimensional mesostructural arrangements arise with incorporating nanoparticles. Moreover, there are striking differences in topography for the samples with different nanoparticle concentration.

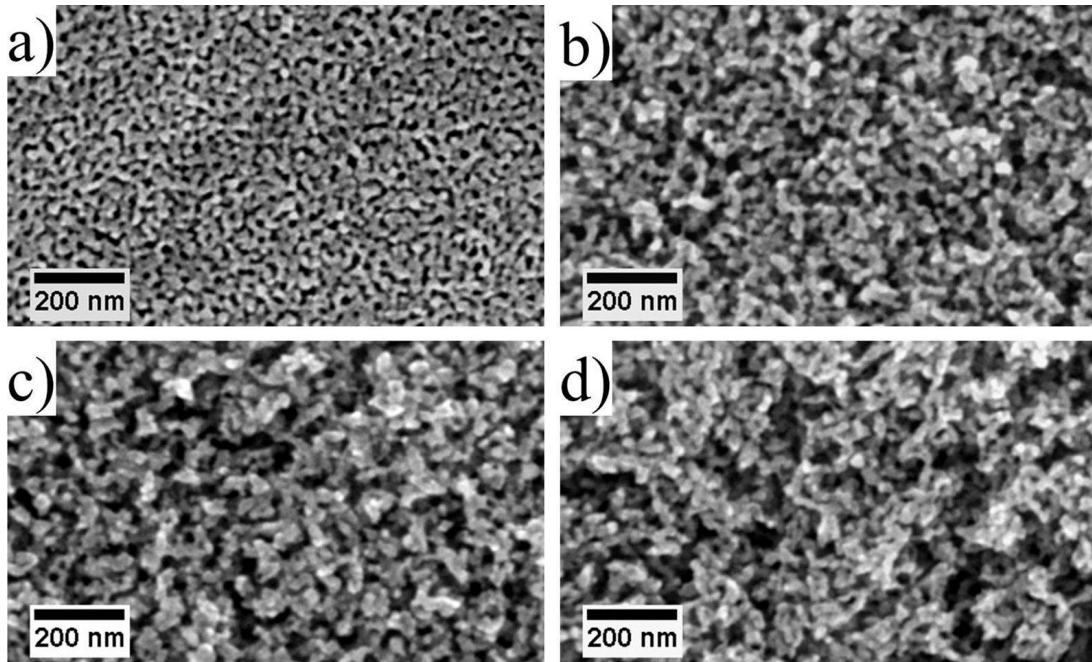


**Figure 5.2:** Plan-view SEM images of spray-deposited titania films after high-temperature calcination. a) 0 wt% NPs, b) 25 wt% NPs, c) 50 wt% NPs and d) 75 wt% NPs.

The 25 wt% NPs and 50 wt% NPs films present larger pores with an average size of around 20 nm as compared to the 0 wt% NPs sample. The large-sized pores and in-

terconnected networks are more beneficial for the infiltration with organic hole-transport materials (HTMs) and for the formation of percolation paths in the backfilled HTMs [146]. Less homogeneous films are achieved with increasing amount of nanoparticles up to weight ratio of 75 %. As seen in figure 5.2d, the pore sizes are not uniform. Some areas have large mesopores whereas some areas present small pores. The whole film differs in density. This film heterogeneity is caused by the large amount of presynthesized crystalline nanoparticles being added to the titania sol-gel solution. For the 25 wt% NPs and 50 wt% NPs films, the presynthesized crystalline nanoparticles are hosted by the titania sol during the sol-gel process. After film deposition and high-temperature calcination, the homogeneous mixture of titania sol and nanoparticles are transformed into interconnected titania nanostructures [107]. While the amount of nanoparticles is much more than that of titania sol in the 75 wt% NPs sample. The dominant presence of presynthesized crystalline nanoparticles results in a fact that titania-sol-induced templated network can not host all the nanoparticles. Thus, a portion of the nanoparticles aggregate in order to lower their surface energy. The presence of nanoparticle clusters dominate the change of film morphology as compared to the 25 wt% NPs and 50 wt% NPs films. The evidence of the formation of large clusters is given by a lower magnification SEM image for the top view of the 75 wt% NPs sample. Figure 5.3 shows the existence of large clusters, which are indicated by red circles. Moreover, the nanoparticle clusters appear in different sizes in the 75 wt% NPs film.

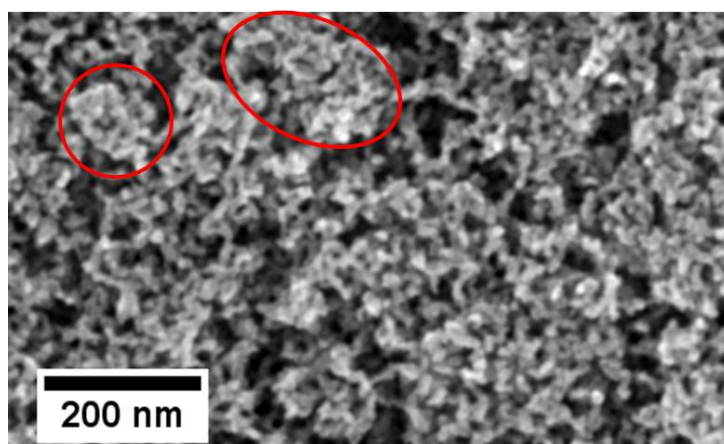


**Figure 5.3:** Plan-view SEM image of the 75 wt% NPs sample taken at a lower magnification. The red circles indicate the existence of large clusters in the film.

### 5.1.2 Inner morphology

With respect to structure characterization, SEM measurements can only access information about surface morphology of a small observable area [147, 148]. In fact, the

film inner morphology is of more interest for studying the photovoltaic performance of the final DSSCs, since the efficiency of charge carrier generation strongly depends on the  $\text{TiO}_2/\text{dye}/\text{HTMs}$  interface, and the efficiency of charge carrier transport is greatly influenced by titania and HTM interconnected network [149–151]. Dye molecules, the birthplace of charge carriers, are adsorbed on the titania surface and then the separated electrons and holes need to travel along the corresponding n- and p-type material phases to the respective electrodes [152–154]. As the surface only has a limited fraction, the film inner structures dominate the device performance. Therefore, information about inner morphology is necessary and highly demanded.

### GISAXS measurements

To obtain information about the morphology inside the films, grazing-incidence small-angle X-ray scattering (GISAXS) measurements are performed at the P03/MiNaXS beamline of the PETRA III storage ring at DESY, as described in section 3.1.6. This advanced scattering technique is very suitable for film characterization [86, 88, 155]. It is able to parametrize the film buried and inner structures without destroying the probed samples. Moreover, the grazing-incidence mode gives a large x-ray footprint on samples, which allows tracking the film inner domains at the nano- and meso-scales with a high statistical relevance [156, 157]. 2D GISAXS data are obtained for these four titania films after calcination and are shown in figure 5.4.

The specular beam is shielded by a circular beamstop for each sample to protect the detector from oversaturation, as shown in figure 5.4. Since the directly reflected x-ray beam does not carry any structural information, shielding it enables to increase the measuring time for higher intensity of diffuse scattering. The intensity maximum observable in the GISAXS data is the Yoneda peak [158], which is located at the critical angle of titania (after calcination only titania remains on substrates). Conspicuous side scattering is observed in the region ranging from low  $q_y$  to high  $q_y$ , which indicates the existence of titania nanostructures in the probed samples. In order to obtain quantitative information regarding the titania domain size and arrangement, horizontal line cuts at the Yoneda peak position are performed along the  $q_y$  direction as shown by the red arrow in the figure 5.4a. For better statistics, the line cut integrates 5 pixels which are centered at the Yoneda peak. The horizontal line cut for each film is plotted in figure 5.5a.

To extract structural information, the data obtained from horizontal line cuts are fitted in the framework of the effective interface approximation of the distorted wave Born approximation (DWBA) using the local monodisperse approximation (LMA) [86, 88, 159–163]. Within this model, form factors with cylindrical geometry distributed over a 1D

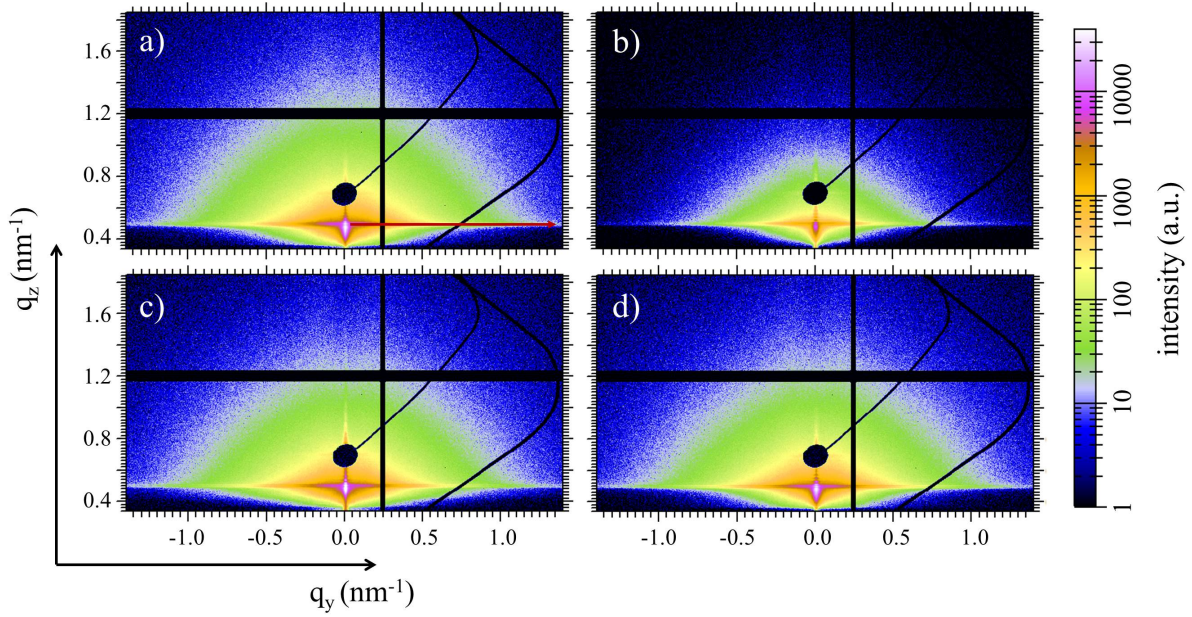


**Figure 5.4:** 2D GISAXS data of spray-coated titania films with different concentration of nanoparticles after high-temperature process. a) 0 wt% NPs, b) 25 wt% NPs, c) 50 wt% NPs, and d) 75 wt% NPs. The scattering intensity scale is shown at the right of the images. The circular black area is the beamstop. The horizontal and vertical black stripes at positions of  $q_z \approx 1.2 \text{ nm}^{-1}$  and  $q_z \approx 0.2 \text{ nm}^{-1}$  are the inter-module gaps of the detector. The red arrow indicates the position of the horizontal line cut.

paracrystalline lattice are used for fitting. The form factors correspond to the scattering objects with a certain size, whereas the center-to-center distance of the scattering objects is obtained from the structure factor. Both form and structure factors are assumed to be Gaussian size distributions. From data modeling, the radii of titania nanostructures (form factors) and the center-to-center distances are extracted and plotted as a function of nanoparticle concentration in figure 5.5b and 5.5c. The data obtained from the 0 wt% NPs, 25 wt% NPs and 50 wt% NPs films are fitted with two characteristic form and structure factors, whereas the fit for the 75 wt% NPs sample requires three characteristic length scales. A fit with only 2 objects was not successful. By comparing small-sized structures, it is found that the size decreases upon the incorporation of nanoparticles, whereas the center-to-center distance increases slightly with the amounts of nanoparticles. As a consequence, the pore size of the titania films is related to the nanoparticle content. The pore size can be calculated using the following equation [164]:

$$\text{pore size} = \text{center-to-center distance} - 2 \times \text{structure radius} \quad (5.1)$$

The titania nanostructures in the 0 wt% NPs films have a radius of  $(3.1 \pm 0.1) \text{ nm}$



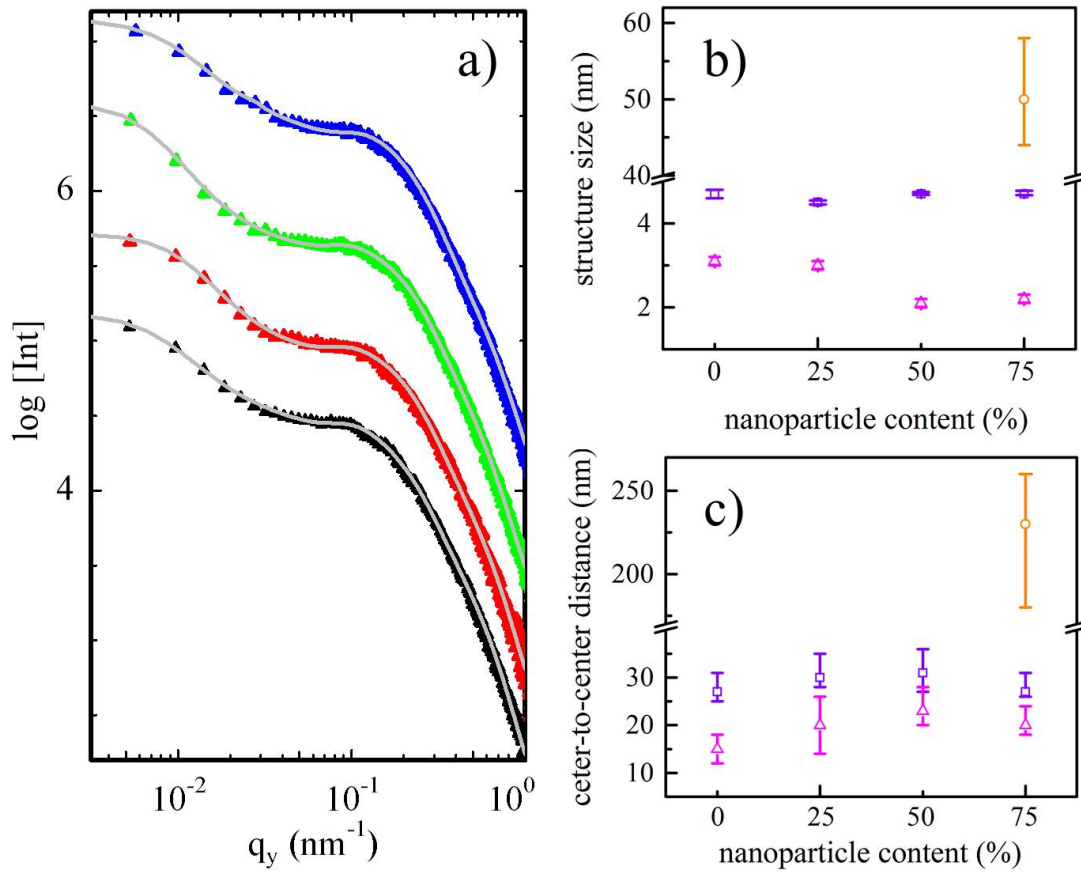


**Figure 5.5:** a) Horizontal line cuts of the 2D GISAXS data obtained from the calcined titania films. Black, red, green and blue curves represent cuts from 0 wt% NPs, 25 wt% NPs, 50 wt% NPs and 75 wt% NPs, respectively. The gray lines represent the fits. All cuts and fits are shifted along the intensity axis for clarity of the presentation. Quantitative information about b) structure radii and c) center-to-center distance are extracted and plotted as a function of nanoparticle concentration. Magenta hollow triangles represent small-sized titania structure and Violet hollow squares represent large-sized structure. Orange hollow circles indicate the nanoparticle aggregation in the 75 wt% NPs.

and a center-to-center distance of  $(15.0 \pm 3.0)$  nm, yielding a pore size of  $(8.8 \pm 3.0)$  nm. For the sample with nanoparticles, the smaller structure radii and larger center-to-center distances give rise to larger pores. The mesopore sizes are of  $(15.0 \pm 6.0)$  nm,  $(18.8 \pm 4.0)$  nm and  $(15.6 \pm 3.0)$  nm in the 25 wt% NPs, 50 wt% NPs and 75 wt% NPs samples, respectively. The large-sized structures in the 0 wt% NPs, 25 wt% NPs and 50 wt% NPs samples and middle-sized structure in the 75 wt% NPs film have the same radii of  $(4.7 \pm 0.1)$  nm, irrespective of nanoparticle addition, whereas the center-to-center distances have similar trend as the distances between small-sized structures. Via equation 5.1, the pore size between large-sized structures can be calculated as well. The average pore

size is  $(16.0 \pm 2.0)$  nm in the 0 wt% NPs film, and it increases to approximately 20 nm upon nanoparticles being added in the preparation, but it decreases to  $(16.0 \pm 3.0)$  nm with further increasing nanoparticle content to the weight ratio of 75 %. The third form factor in the 75 wt% NPs sample originates from nanoparticle aggregates, which are observed in SEM measurements as well. When the nanoparticle concentration in the film exceeds a certain threshold, a part of them tend to agglomerate rather than homogeneously distributing in the sol-gel-synthesized titania network. The large cluster has a structure size of  $(100 \pm 16)$  nm and an average pore size of  $(130 \pm 40)$  nm. Through the comparison of scattering intensities from different form factors, the volume ratio of each form factor can be computed as described in section 2.4.3. Through calculation, the large clusters are rare in the 75 wt% NPs film with a volume fraction of only 4.3 %.

In general, the inner morphologies in all films (from GISAXS measurements) are quite in agreement with the surface morphologies obtained from SEM measurements. During high-temperature calcination, the removal of template polymer leads to a certain collapse of titania nanostructures [165–169], whereas the presynthesized crystalline nanoparticles hinder a titania nanostructure collapse [170]. As a consequence, we find larger pore sizes in the 25 wt% NPs and 50 wt% NPs samples compared to the 0 wt% NPs film. However, the ligands outside of titania nanoparticles are removed by calcination step as well, which will also cause the collapse of the titania nanostructures, and this effect presumably exceeds the stabilization effect of nanoparticles in the 25 wt% NPs sample. This is attributed to be the reason that the pore sizes decrease with further increasing nanoparticle concentration up to 75 wt%.

## **N<sub>2</sub> adsorption–desorption isotherms**

The presence of mesopores in these four samples is confirmed by nitrogen adsorption-desorption isotherms as shown in figure 5.6. The measurements of nitrogen adsorption-desorption isotherms are performed on a Quantachrome Autosorb-1 instrument as described in section 3.1.4.

The N<sub>2</sub> adsorption-desorption isotherms for four samples can be identified as the adsorption and desorption branch of a type *IV* curve, according to IUPAC classification [171]. Type *IV* is a sign of the existence of mesopores in the probed samples [171]. In this type, a monolayer of adsorbed nitrogen is pervading upon surface of titania nanostructures at low relative pressure, while at high relative pressure formation of multilayer starts. When the pressure continues increasing to a point that matches Kelvin-type rules in mesopores, nitrogen condensation takes place, which gives a sharp increase of adsorption volume as shown in figure 5.6. Moreover, hysteresis between the adsorption and



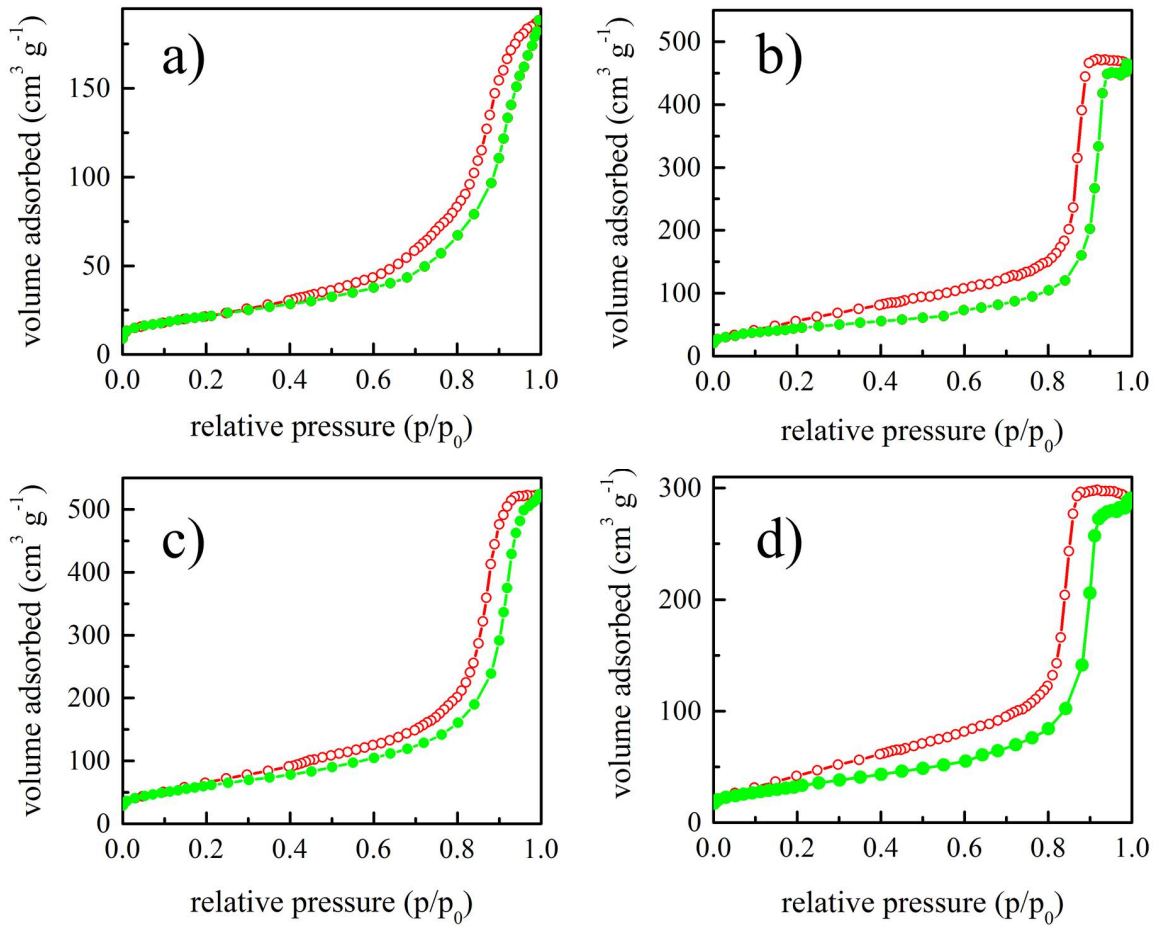


**Figure 5.6:** Nitrogen adsorption-desorption isotherms measured at 77 K of mesoporous titania films after calcination. a) 0 wt% NPs, b) 25 wt% NPs, c) 50 wt% NPs, and d) 75 wt% NPs. Green solid circles indicate nitrogen absorption and red hollow circle represent nitrogen desorption.

desorption curves is observed in all samples, which also reveals the presence of mesopores. After N<sub>2</sub> reaches saturation, desorption, which the opposite of the adsorption, usually takes place. As nitrogen evaporation from mesopores typically occurs at a lower pressure than for capillary condensation, a hysteresis is seen. The hysteresis in figure 5.6 can be categorized as type H<sub>1</sub> loop, indicating the pores have uniform size and shape [171–173]. All samples exhibit pore size distribution with two peaks as shown in figure 5.7. The extracted pore sizes are in good agreement with the value obtained from GISAXS measurements. The trend that pore size increases with addition of nanoparticle and then decreases with further increasing nanoparticle concentration has been confirmed again. The detailed textural parameters derived from nitrogen adsorption–desorption isotherms are summarized in table 5.3.

Amongst all films measured, the 0 wt% NPs film has the lowest Brunauer–Emmett–Teller

sample name	BET surface area ( $\text{m}^2 \text{ g}^{-1}$ )	pore volume ( $\text{cm}^3 \text{ g}^{-1}$ )	pore size (nm)
0 wt% NPs	80.1	0.28	8.8, 16.1
25 wt% NPs	193.1	0.72	17.1, 20.0
50 wt% NPs	225.2	0.80	17.9, 20.0
75 wt% NPss	145.3	0.46	15.0, 16.7

**Table 5.3:** Textural parameters of these four mesoporous samples extracted from nitrogen adsorption–desorption isotherms. Figure 5.7 shows that each film has two dominant pore sizes.

(BET) surface area of  $80.1 \text{ m}^2 \text{ g}^{-1}$  and and pore volume of  $0.28 \text{ cm}^3 \text{ g}^{-1}$ . Both parameters increase significantly with introduction of nanoparticles into titania films. The 50 wt% NPs film possesses highest BET surface area ( $225.2 \text{ m}^2 \text{ g}^{-1}$ ) and pore volume ( $0.80 \text{ cm}^3 \text{ g}^{-1}$ ), almost four times larger than for the 0 wt% NPs sample. Larger surface are predicted to anchor more dye molecules on titania surface, which is very helpful for charge carrier generation. More pore volume enables higher degree of HTM percolation, thereby more interfaces between n- and p-type semiconductors. As discussed before, the interface plays a crucial role in the final device performance. Furthermore, larger pore sizes are easier for efficient infiltration of a hole-transporting conjugated polymer, which can lead to a higher pore filling fraction. Therefore, ssDSSCs based on the 50 wt% NPs photoanodes are expected to have a excellent performance in terms of specific surface area, pore volume and pore size.

### 5.1.3 Crystallinity and conductivity

With respect to the application in photovoltaics, crystalline titania is necessary. In nature, crystalline titania has three polymorphs, namely, anatase, rutile and brookite, as described in section 2.2.1. Generally, anatase is more desirable in energy applications than both rutile and brookite [174–176]. Directly after film deposition, the titania is still in its amorphous phase. The high-temperature calcination not only burns away polymer template to achieve mesoporous titania films, but also transforms amorphous titania to its crystalline phase.

In order to determine the crystalline phase present in the samples, the spray-deposited mesoporous titania films with different nanoparticle concentrations are investigated via XRD measurements. Figure 5.8 exhibits four XRD curves which are obtained from the 0 wt% NPs, 25 wt% NPs, 50 wt% NPs and 75 wt% NPs films on silicon substrates. The

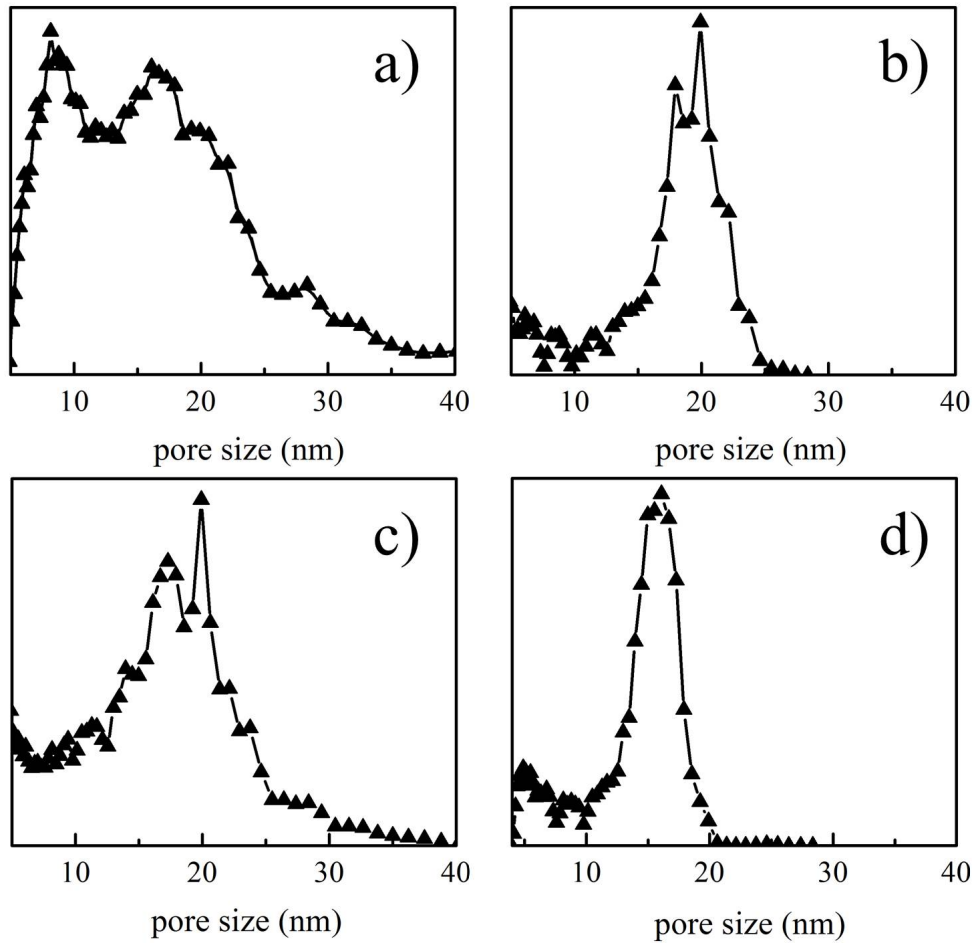


**Figure 5.7:** Mesopore size distributions (model of cylindrical pore geometry, equilibrium model). a) 0 wt% NPs, b) 25 wt% NPs, c) 50 wt% NPs, and d) 75 wt% NPs.

strongest peak intensity in the XRD data is at the position of  $2\theta \approx 33^\circ$ , which derives from the diffraction of (100) crystal plane of the silicon substrate [141]. As its intensity is much stronger than other diffraction peaks, the peak from silicon substrate is cut off to highlight the features from titania samples.

For all samples, the titania is identified as anatase phase, as the position of measured diffraction peaks is in good agreement with the anatase reference peak positions. The vertical orange sticks in figure 5.8 display the anatase reference data of peak positions and their respective relative intensities, which is taken from the International Center for Diffraction Data (ICDD). The reference data shows that the anatase (101) crystal plane has the highest peak intensity, which is confirmed by several previous studies [46, 177]. On the contrary, the most pronounced peaks are given by the (004) crystal plane rather than the (101) crystal plane for all samples in the present work. Moreover, the (004) peak becomes more pronounced with increasing nanoparticle content as seen from the

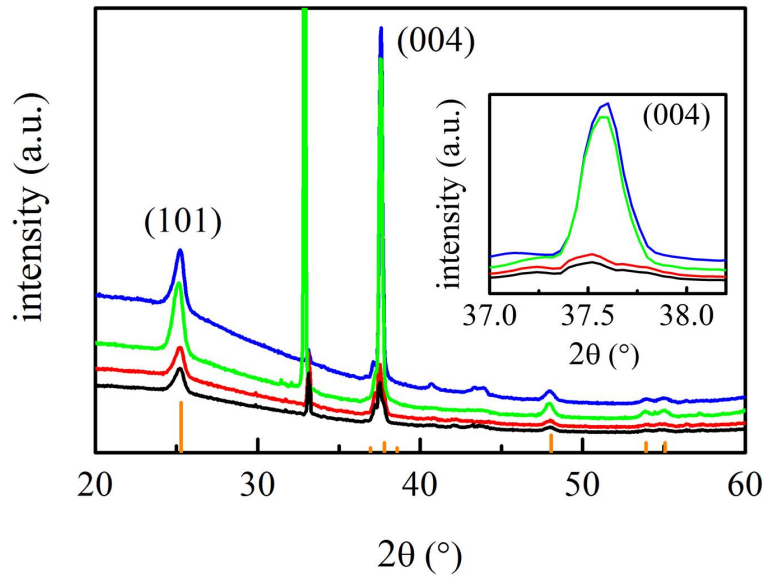


**Figure 5.8:** XRD data of spray-coated titania films with different concentration of nanoparticles after high-temperature process. Black, red, green and blue curves represent cuts from 0 wt% NPs, 25 wt% NPs, 50 wt% NPs and 75 wt% NPs, respectively. All curves are shifted along the intensity axis for the presentation. The vertical orange sticks represent the peak positions and their respective relative intensities of anatase titania. The reference data is taken from ICDD. In the inset, zoom into the area between  $37.0^\circ$  and  $38.3^\circ$  to stress the (004) diffraction peak.

inset in figure 5.8. The fact that strongest intensity shifts from (101) peak to (004) peak indicates a preferred orientation along the (004) direction of the anatase lattice [178,179]. To obtain information about the crystal size, the (101) and (004) peaks of the respective XRD curves are fitted. Using the Scherrer equation 2.30 for the (101) peaks, the crystal size are estimated to be around 11 nm for all samples. While size information obtained from (004) peaks are different in these four samples. The 0 wt% NPs and 25 wt% NPs films have an average crystal size of 11 nm as well, whereas the crystal size in 50 wt% NPs and 75 wt% NPs samples are about 25 nm.

The electron mobility in mesoporous titania films is of central importance for the photovoltaic performance of ssDSSCs [180–182]. Guldin et al. have reported that the performance of ssDSSCs greatly benefits from the increased conductivity of titania photoanodes even in the case of lower specific surface area and dye loading [19]. The low electron mobility in titania nanostructures limits electron transport and collection thereby the device performance [180]. The nanoparticle-concentration dependence of the sheet resistance of mesoporous titania films is shown in figure 5.9.

The resistivity is determined by four points probe method. Increasing the nanopar-

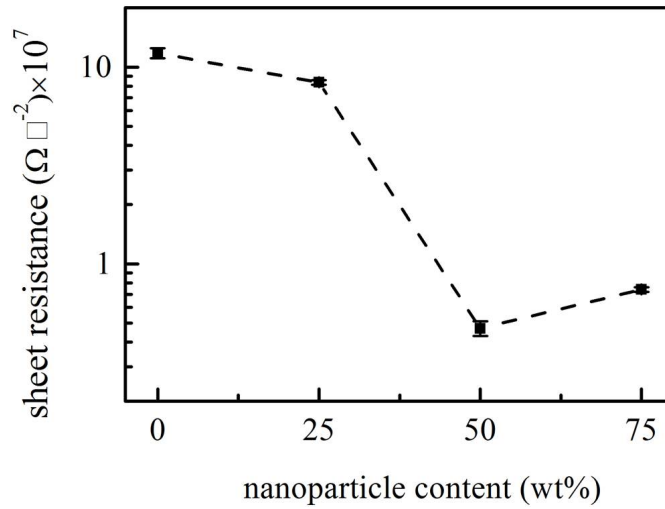


**Figure 5.9:** Sheet resistance of spray-coated titania films with different concentration of nanoparticles after high-temperature process. The dashed line is a guide to the eyes.

tile concentration significantly reduces the film resistivity. The sheet resistance of the 75 wt% NPs sample is lower than that of the 0 wt% NPs sample by over a factor of 2. Higher conductivity typically facilitates electron transport thereby higher short-circuit current density ( $J_{sc}$ ) [181].

## 5.2 Solar cell performance

In order to test the practicability of spray coating and the effect of incorporated nanoparticles, the 0 wt% NPs, 25 wt% NPs, 50 wt% NPs and 75 wt% NPs films are used as photoanodes for ssDSSCs. The implemented solar cell layout is:

$$\text{glass/FTO/c-TiO}_2/\text{n-TiO}_2/\text{D149/P3HT/PEDOT:PSS/Au}$$

With FTO and gold as bottom and top electrodes, respectively; a compact titania layer (c-TiO<sub>2</sub>) and PEDOT:PSS as hole- and electron-blocking layer, respectively; n-type mesoporous titania layer (n-TiO<sub>2</sub>) and P3HT as electron- and hole-transport layer, respectively; D149 as light harvester. The description of used materials are given in section 4.1. The detailed fabrication steps of the DSSCs as well as the device assembly are described in section 4.2.4.

### 5.2.1 Effect of PEDOT:PSS blocking layer

In this work, the n-TiO<sub>2</sub> and PEDOT:PSS layers are deposited by spray coating, which constitutes a novel approach in ssDSSCs fabrication since, no investigations in this di-

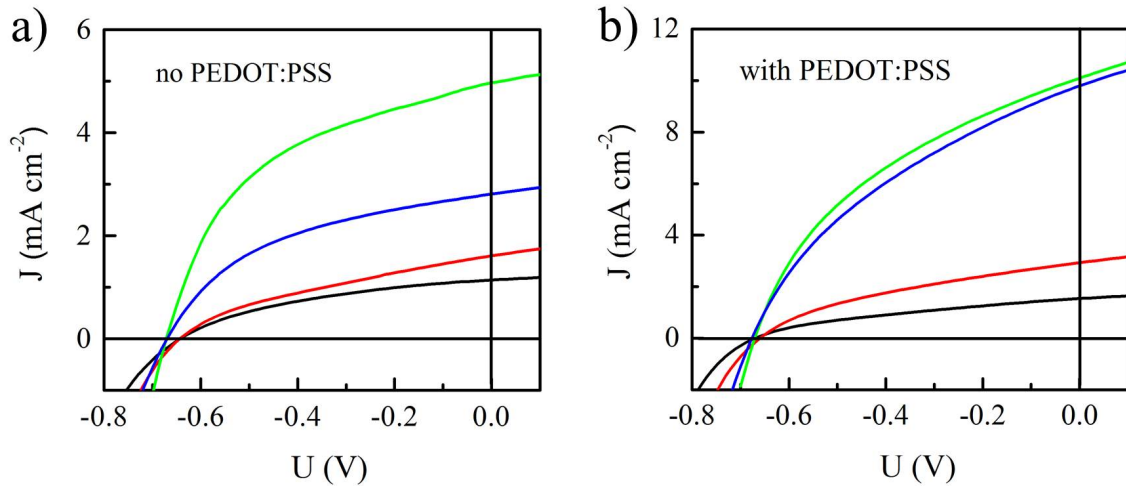


**Figure 5.10:** Current-voltage characteristics for the solar cells based on different titania photoanodes. Black, red, green and blue curves represent *I-V* sweeps from 0 wt% NPs, 25 wt% NPs, 50 wt% NPs and 75 wt% NPs cells, respectively. a) and b) show the solar cells without and with PEDOT:PSS layer, respectively.

rection are published so far. Figure 5.10a and 5.10b depict the current-voltage (*I-V*) characteristics of different ssDSSCs without and with PEDOT:PSS layer, respectively. The extracted photovoltaic parameters of *PCE*,  $J_{sc}$ , open-circuit voltage ( $V_{oc}$ ), and fill factor (*FF*) are displayed in figure 5.11a to 5.11d.

It is noticed that the device performance is tied to the nanoparticle concentration in titania films and the electron-blocking layer (PEDOT:PSS). For the device with PEDOT:PSS layer (solid circles), the solar cell performance is significantly enhanced with respect to the introduction of nanoparticle concentration into titania networks. The *PCE* of the 0 wt% NPs cell is  $(0.43 \pm 0.03) \%$ , it increases with increasing nanoparticle concentration up to the weight ratio of 50 %  $((2.7 \pm 0.1) \%)$  for the 50 wt% NPs cell, and reduces slightly to  $(2.4 \pm 0.2) \%$  for the 75 wt% NPs cell. The enhancement in *PCE* is mainly caused by a dramatic increase of  $J_{sc}$ . Increasing the nanoparticle concentration from 0 wt% to 50 wt% leads to a improvement of  $J_{sc}$  by over a factor of 7, from  $(1.46 \pm 0.07) \text{ mA cm}^{-2}$  for the 0 wt% NPs cell to  $(10.0 \pm 0.4) \text{ mA cm}^{-2}$  for the 50 wt% NPs cell. While the values of  $V_{oc}$  and *FF* remain almost constant irrespective of nanoparticle concentration. For the device without PEDOT:PSS layer (hollow squares), the nanoparticle-concentration-dependent photovoltaic parameters have a similar tendency with that for the device with PEDOT:PSS layer. The *PCE* and  $J_{sc}$  increase with increasing nanoparticle concentration, whereas the change of  $V_{oc}$  and *FF* is not evident. In general, the solar cells with PEDOT:PSS layer behave better than without regarding the photovoltaic performance.

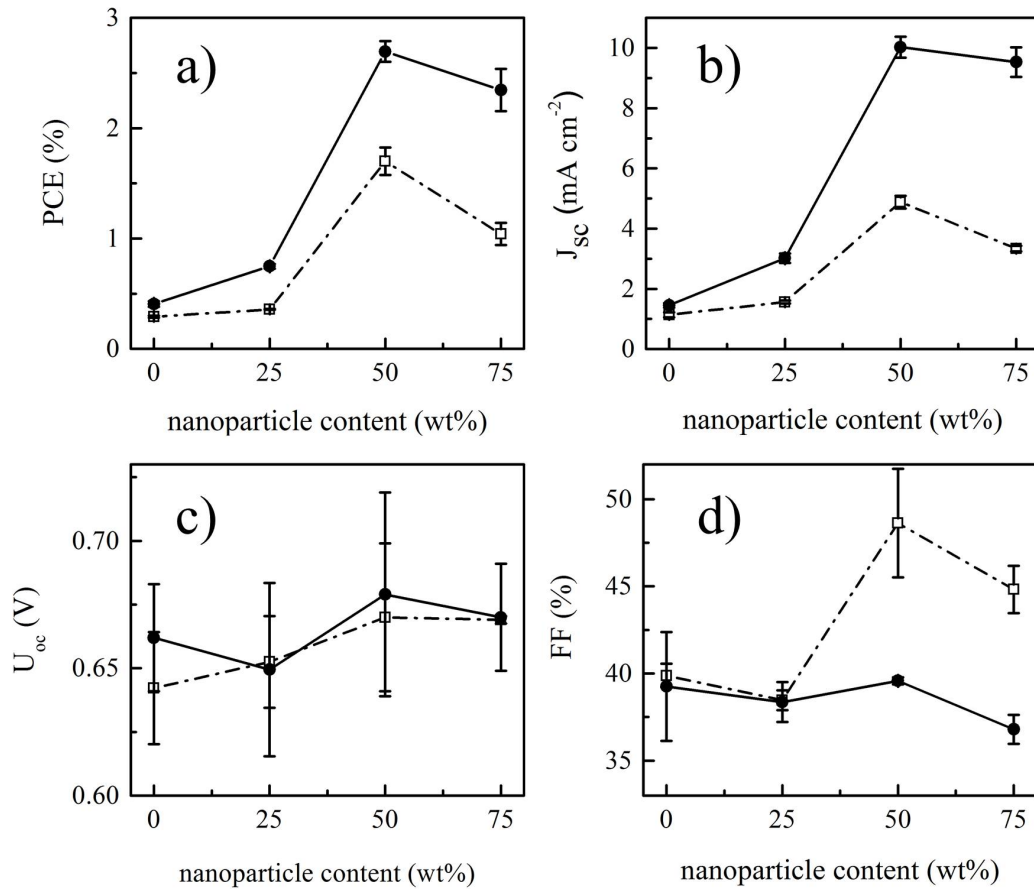


**Figure 5.11:** a)  $PCE$ , b)  $J_{sc}$ , c)  $V_{oc}$ , and d)  $FF$  of the  $ssDSSCs$  extracted from  $I-V$  curves. The solid circles represent the data are obtained from figure 5.10a, guided by dash lines; while the hollow square represent the data are obtained from figure 5.10b, guided by solid line.

### 5.2.2 Discussion

The performance of the device with nanoparticle in the titania photoanodes is much better than for the solar cell without nanoparticle, and the 50 wt% NPs cell gives the best photovoltaic performance. The addition of nanoparticles leads to several improvements which are the reason for the enhanced  $J_{sc}$  thereby  $PCE$ . First of all, larger pores allow for a better P3HT infiltration into the titania networks, which can result in higher efficiency of current generation as reported by Rawolle et al. [183]. Second, a higher specific surface area is beneficial, since dye molecules anchor onto the surface of titania nanostructures in the present work, a higher dye adsorption is allowed. Third, a higher pore volume is advantageous, since electron and hole pairs can only be separated at the interface of n- and p-type semiconductors, more potential sites for exciton dissociation are available.

Fourth, a higher conductivity leads to a higher electron mobility and a remark drop of charge recombination.

On the basis of a comparison of solar cells with and without PEDOT:PSS layer, an additional electron blocking layer is greatly beneficial for current generation. Take the 50 wt% NPs cell for example, the main difference is the higher  $J_{sc}$  and lower  $FF$  in the device with PEDOT:PSS layer. The  $J_{sc}$  grows almost a factor of 3, from  $(3.9 \pm 0.2) \text{ mA cm}^{-2}$  (without PEDOT:PSS layer) to  $(10.0 \pm 0.4) \text{ mA cm}^{-2}$  (with PEDOT:PSS layer). Sista et al. have also observed the  $J_{sc}$  growth when the PEDOT:PSS layer was applied between P3HT and top electrode. They verified that the increase of  $J_{sc}$  is attributed to the high conductivity and electron blocking effect of PEDOT:PSS layer [184]. However, the  $FF$  shows an opposite trend. The  $FF$  of the device with PEDOT:PSS layer is  $(39 \pm 1) \%$ , which is lower than for the device without PEDOT:PSS layer  $((49 \pm 3) \%)$ . P3HT is hydrophobic whereas PEDOT:PSS is hydrophilic, the bad adhesion between them results in inhomogeneous PEDOT:PSS films, which gives rise to lower shunt resistance [185].

## 5.3 Summary

Nanostructures of  $\text{TiO}_2$  are produced using polymer-template-assisted sol-gel synthesis in combination with the introduction of presynthesized crystalline titania nanoparticles. To obtain titania photoanodes for applications in ssDSSCs, spray deposition is used to establish nanostructured titania films with an appropriate thickness. Spray coating is of great interest for film deposition as it has strong potential for large scale manufacturing. To evaluate how the presynthesized crystalline titania nanoparticles influence the resulting titania films, four different weight ratios of nanoparticles are incorporated in the titania networks.

The film morphologies are verified by means of SEM, GISAXS, and nitrogen adsorption – desorption isotherms. A mesoporous nature of sponge-like nanostructures are present in all films, but the nanostructure and pore sizes are different depending on the nanoparticle concentration. The film without nanoparticles has the smallest pore sizes of about 10 nm, a smallest pore volume of  $0.28 \text{ cm}^3 \text{ g}^{-1}$  and a smallest BET surface area of  $80.1 \text{ m}^2 \text{ g}^{-1}$ . With increasing nanoparticle concentration, the average pore size, the pore volume and the BET surface area of titania films increase accordingly. A bicontinuous network structure is formed in the 50 wt% NPs sample with an average pore size of 20 nm, a high pore volume of  $0.80 \text{ cm}^3 \text{ g}^{-1}$  and a very high effective surface area of  $225.2 \text{ m}^2 \text{ g}^{-1}$ . Larger pore size facilitates P3HT infiltration and an increased pore volume provides more interfaces between titania and P3HT. The combined effect of larger pore size and higher pore volume



enables a more efficient photocurrent generation since the interface constitutes the active site for charge carrier separation. Larger BET surface area can load more dyes which are the sensitizers in the present work. This is one of the reasons that the 50 wt% NPs photoanodes give rise to the best performance. Liao et al. have demonstrated a similar pore size in a mesoporous  $\text{TiO}_2$  sample, but the BET specific surface area ( $48.9 \text{ m}^2 \text{ g}^{-1}$ ) is much smaller than for the 50 wt% NPs sample [186]. Although a comparative BET surface area of  $212 \text{ m}^2 \text{ g}^{-1}$  has been reported by Kim et al., a smaller pore size (about 10 nm) was present [187]. The 50 wt% NPs photoanodes combine the large pore sizes and BET surface areas, which is beneficial for the performance of ssDSSCs.

The crystalline phase and conductivity of the titania films are investigated with XRD and four-points probe method, respectively. A preferred orientation along the (004) direction of the anatase lattice is observed in the 50 wt% NPs sample. Wang et al. have also observed the similar strongest diffraction intensity of {004} facets and the {004} facets are highly active [175, 188]. The sheet resistance decreases remarkably with increasing nanoparticle amount in the titania films, indicating the titania films with nanoparticles appear to be more favorable for electron transport.

The titania films are used as photoanodes in ssDSSCs. The device performance enhances greatly with the addition of presynthesized crystalline titania nanoparticles. The 50 wt% NPs cell has the best photovoltaic performance with the *PCE* of  $(2.7 \pm 0.1) \%$ , which is almost seven times higher than for the solar cell without nanoparticles. This efficiency is top-ranking in terms of  $\text{TiO}_2$ -D149-P3HT based ssDSSCs. Liao et al. have reported a *PCE* of 2.63 % in the same system except for using well-defined titania nanorods as photoanodes [189]. Compared to other sensitizers like organometal halide perovskites, the D149 dye is in the middle class of DSSC sensitizers [190]. But it is still of interest due to its high molar extinction coefficient, low cost, non-toxicity and high flexibility of the molecule structure. The enhancement of *PCE* mainly derives from the improvement of  $J_{sc}$ , as only small changes exist in  $V_{oc}$  and *FF*. Linking the findings obtained from SEM, TEM, GISAXS, nitrogen adsorption-desorption isotherms, XRD and conductivity measurements, the high  $J_{sc}$  in the 50 wt% NPs cell is ascribed to relatively larger pores, bi-continuous mesostructural arrangement, higher specific surface area and pore volume, and a higher conductivity of titania photoanodes with incorporating presynthesized crystalline titania nanoparticles. For the solar cell with the same titania photoanodes, the device performs much better by inserting an electron-blocking layer (PEDOT:PSS) between P3HT and gold electrode. Despite lower *FF* caused by spray deposition of the PEDOT:PSS layer, the great enhancement of  $J_{sc}$  gives a higher *PCE*. The electron-blocking layer is of great importance as well in ssDSSCs.



## 6 In situ study of spray-deposited titania films for scalable fabrication of solid-state dye-sensitized solar cells

Parts of this chapter have been prepared as a manuscript: In Situ Study of Spray-Deposited Titania Films for Scalable Fabrication of Solid-State Dye-Sensitized Solar Cells, which is presently submitted for review [191].

In the past decades, nanostructured titania thin films have been widely explored for photovoltaic applications since the groundbreaking study in dye-sensitized solar cells (DSSCs) was developed by O'Regan and Grätzel in 1991 [9, 142, 152, 190, 192]. Many routes have been established to develop titania nanostructures such as sol-gel [193, 194], hydrothermal [195, 196], solvothermal [197, 198], direct oxidation [199, 200] or chemical vapor deposition methods [201] and so on. Among them, sol-gel synthesis is a facile and promising technique for the solar cell fabrication as it can convert a titania solution directly into thin films, which are usually used as photoanodes in DSSCs. Moreover, by incorporating polymer micelles into the sol-gel system, titania nanostructures and mesopore sizes in the resulting thin films can be tailored to meet different needs [202–204]. Amphiphilic block copolymers have been intensively studied as polymer templates to direct the titania nanostructures [110, 205, 206]. However, the titania films produced from polymer-assisted sol-gel synthesis usually have a relatively low conductivity even after high temperature calcination, which limits the photovoltaic performance of final DSSCs [19]. To settle this problem pre-synthesized crystalline titania nanoparticles are introduced into the titania networks [109]. Aside from the nanostructure preparation, deposition techniques matter strongly as well. Many methods, like spin coating, spray coating, dip coating and doctor blading, are developed to deposit titania thin films [207–210]. Compared to laboratory-based routines, spray coating is particularly of interest due to the potential for large-scale industrial applications. Its potential as rapid and large-scale film deposition technique has stimulated extensive research on the spray deposition of titania films. For example, Nomura et al. produced porous titania films with uniform micrometer-sized pores

by electrostatic sol-spray deposition [211]. The preparation of compact titania films by spray pyrolysis has been frequently reported in literature [212–214]. Despite its successful application, the full understanding of this kinetic process is lacking, as spray coating usually features a complex evolution of structures and morphology. In order to clarify the process, in situ morphological investigations are highly demanded, but imply a great challenge as well. The use of conventional real-space mapping techniques is nearly impossible here. First, many liquid droplets are generated during spray coating, hence scanning electron microscopy (SEM) cannot be used as it requires vacuum conditions. Moreover, the solvent splash may contaminate the electron beam generator and detector. Second, atomic force microscopy (AFM) measurements are also not suitable for two reasons. On the one hand, the cantilever may block the way on which the liquid droplets fly to the substrate, which interrupts the process of spray coating. On the other hand, the time needed for obtaining one AFM image is quite long, which cannot provide a sufficient time resolution for detection of the morphological changes. Grazing-incidence small-angle x-ray scattering (GISAXS) works well for in situ morphology characterization as this technique can detect the inner film morphology continuously under ambient environment without interrupting the process of spray coating or destroying the deposited films. Moreover, it allows probing the film's inner structures in the nano- and meso-scale over macroscopic sample areas, which gives very high experimental statistics. Until now, only a few research groups have looked into this aspect in more detail. For example, K. Sarkar et al. made a preliminary exploration on tracking structural kinetics of zinc oxide films in situ during spray deposition by using this advanced scattering technique [215].

In the past decade, many efforts have been made to develop solid-state DSSCs (ss-DSSCs) due to the shortcomings of DSSCs related to electrolyte leakage and electrode corrosion. One of the attractive solid-state hole-transport-materials (ssHTMs) is a small molecule 2,2',7,7'-tetrakis-(N,N-di-p-methoxyphenylamine)-9,9'-bifluorene (spiro-OMeTAD) due to its unique properties, such as the amorphous nature, good solubility, and relatively easy infiltration into mesoporous titania films [74, 216]. Spiro-OMeTAD is typically spin-coated on top of dyed mesoporous titania films to achieve active layers for ssDSSCs [74, 216–219]. However, this laboratory-based technique may not be applied in the device production towards large-scale industrial processing. As an alternative, solution casting as a large-scale process meets the demand. Moreover, solution casting is more cost-efficient than spin coating with respect to material utilization, as a vast majority of spiro-OMeTAD is wasted in the process of spin coating.

In the present work, the titania solution for spray deposition is prepared by sol-gel chemistry in combination with the block copolymer template polystyrene-block-polyethylene oxide (PS-b-PEO). The polymer-template assisted sol-gel synthesis allows for the size

control of nanostructures and mesopores in the resulting  $\text{TiO}_2$  films. In order to improve the conductivity of the titania films, presynthesized crystalline titania nanoparticles with a size of about 6 nm are incorporated into sol-gel-synthesized titania nanostructures. During spray deposition, real-time monitoring on the morphological evolution of the deposited titania/PS-b-PEO composite films with a high temporal resolution is achieved using *in situ* GISAXS measurements, which give a comprehensive view on the spray kinetics. The morphological evolution of two samples, with and without nanoparticles, are compared in the first part of this chapter 6.1. The experimental setup for *in situ* GISAXS measurements of the spray-deposited titania/PS-b-PEO composite films is illustrated in section 6.1.1. The obtained results for the morphological evolution are given in the following section 6.1.2. After film deposition, the titania/PS-b-PEO composite films undergo high-temperature calcination to remove the polymer template thereby obtaining mesoporous titania films. The surface morphologies of the spray-deposited films before and after calcination are compared in section 6.2.1. The inner morphology of calcined titania films is presented in section 6.2.2. After calcination, the mesoporous titania films are modified by dye molecules before solution-casting the spiro-OMeTAD. Development of such active layers by spray coating (titania films) and solution casting (spiro-OMeTAD layers) lowers the production costs and opens up the possibility of a new and large-scale device manufacturing. Finally, ssDSSCs are produced based on this large-scale manufacturing technique to give a proof of the viability as described in section 6.3.

## 6.1 In situ GISAXS measurements during spray coating

GISAXS measurements in combination with *in situ* spray deposition of titania/PS-b-PEO solution are applied to understand the evolution of length scales in the film volume. The GISAXS measurements are carried out at the P03/MiNaXS beamline of the PETRA III storage ring at DESY, as described in section 3.1.6. To serve the purpose of *in situ* experiments, the spray setup is installed at the beamline. The detailed features of spray coating are explained in section 4.2.3.

### 6.1.1 Setup and protocol

Figure 6.1 schematically depicts the experimental setup for *in situ* GISAXS measurements on spray-deposited titania/PS-b-PEO composite films. The whole experiment is performed under ambient conditions using the parameters listed in section 4.2.3.

Before the experiment the substrate is placed on a heating stage which maintains a

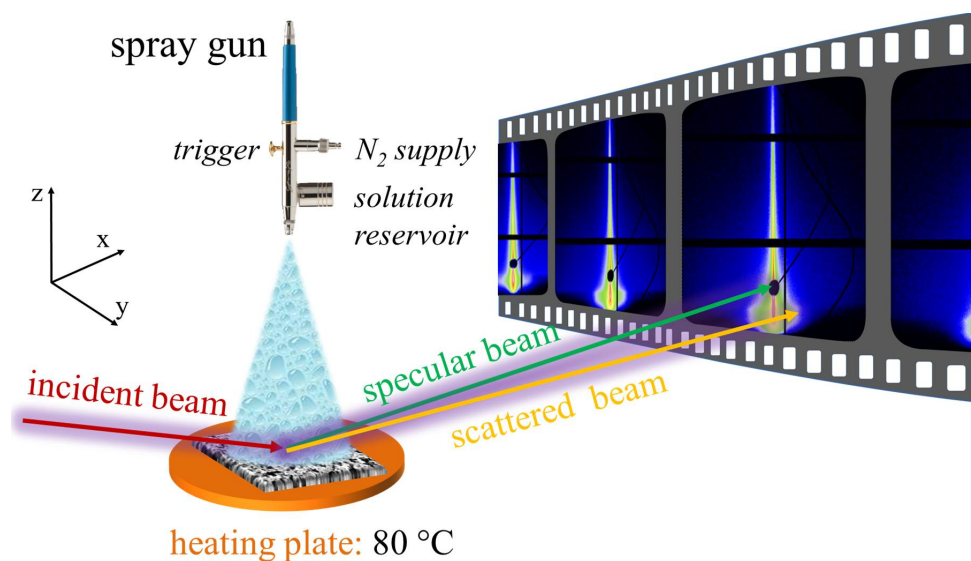


**Figure 6.1:** Schematic illustration of the experimental set up used for *in situ* GISAXS measurements with simultaneous spray deposition.

constant temperature of  $80\text{ }^{\circ}\text{C}$  during the entire *in situ* experiment. The sol-gel solution is loaded into the solution reservoir of the spray gun. Nitrogen as a carrier gas is employed under a constant pressure of 2 bar. The *in situ* experiment starts with GISAXS measurements. The incident x-ray beam with a wavelength of  $0.957\text{ \AA}$  impinges on the substrate at a shallow angle of  $0.23^{\circ}$ . A Pilatus 1M detector is used for recording the scattering signal. The acquisition time for each frame is 0.1 s. This short recording time allows for a high time resolution to track the structural evolution in the film. After several seconds, the spray coating starts. The on and off status is determined by the trigger of the spray gun, which is controlled with the motor of the rotary actuator using the main control program “ONLINE”. The spray protocol can be designed in this program. In the present work a single spray cycle contains a 1 s spray shot with a following 1 s pause. In total 20 cycles (40 s) comprise the spraying protocol. During the measurements, the sample stage sweeps in the y direction in a distance of 2 cm to obtain information over a large surface area and to avoid radiation damage. After spray coating, the obtained titania/PS-b-PEO composite films are continued with GISAXS measurements for another 60 s. The sequence of the GISAXS measurements and spray coating ensures that the evolution of film morphology can be detected from the beginning. After spray coating, the obtained composite films are annealed at  $80\text{ }^{\circ}\text{C}$ . The GISAXS measurements allow for monitoring the homogeneity of the sprayed films in terms of structural length scales during this drying process. For data analysis, the frame of the GISAXS data which corresponds to the starting point of the spray coating must be figured out. Subsequently, other important points of the timeline like the end of the spray coating as well as the

beginning and end of thermal annealing can be precisely determined. In order to increase the statistics of the scattering signal, 10 GISAXS frames are integrated into 1 frame in the present work. After integration, one single frame represents 1 s instead of 0.1 s.

### 6.1.2 Morphological evolution during spray coating

In this work two samples are investigated with in situ GISAXS measurements with respect to their morphological evolution. The applied spray coating parameters are the same, whereas the sol-gel solution is different. The first solution is prepared via the second route of the sol-gel synthesis with TTIP as described in section 4.2.2. The used amount of reactants is listed in table 6.1. The resulting solution is diluted with 20.98 mL toluene

	sol-gel process				
agent	PS-b-PEO	toluene	1-butanal	TTIP	HCl (8M)
amount	307 mg	5.25 mL	1.99 mL	1.14 mL	325 $\mu$ L

**Table 6.1:** *The composition details of sol-gel synthesis.*

and 7.78 mL 1-butanal for spray coating after 20 h of aging. This solution originates from pure TTIP (as no presynthesized nanoparticles are incorporated) is denoted as *pure* solution. The second solution is a mixture of sol-gel solution and nanoparticle solution. The preparation of the sol-gel solution is the same as the *pure* solution except that half of the amount of each chemical is used. The preparation of the nanoparticle solution is described in section 4.2.2 and the amount of each component is listed in table 6.2. After 20 h of stirring, the nanoparticle solution is carefully added to the sol-gel solution before

	nanoparticle solution			
component	PS-b-PEO	toluene	1-butanal	nanoparticles
amount	154 mg	2.63 mL	1 mL	1307 mg

**Table 6.2:** *The composition details of nanoparticle solution.*

being diluted with 23.61 mL toluene and 8.78 mL 1-butanal. Afterwards, the diluted solution mixture is ultrasonicated for 10 min before spray coating. This mixed solution is denoted as *NPs* solution. The nanoparticles used in this work have a titania size of around 6 nm and contain about 50 wt% organic ligands. The detailed information is described in section 5.1. In the following subsections the in situ characterization of the

*pure* and *NPs* composite films are discussed individually. It is noteworthy that only 1 mL of the *pure* solution or *NPs* solution is applied for in situ GISAXS measurements.

### In situ monitoring on spray-deposited pure films

Figure 6.2 shows a selection of 2D GISAXS data for different spray times. Along the  $q_y$  direction at the point of  $q_z = 0.4 \text{ nm}^{-1}$ , it is noticeable that the intensities related to the lateral scattering become stronger with increasing spraying time, because more and more

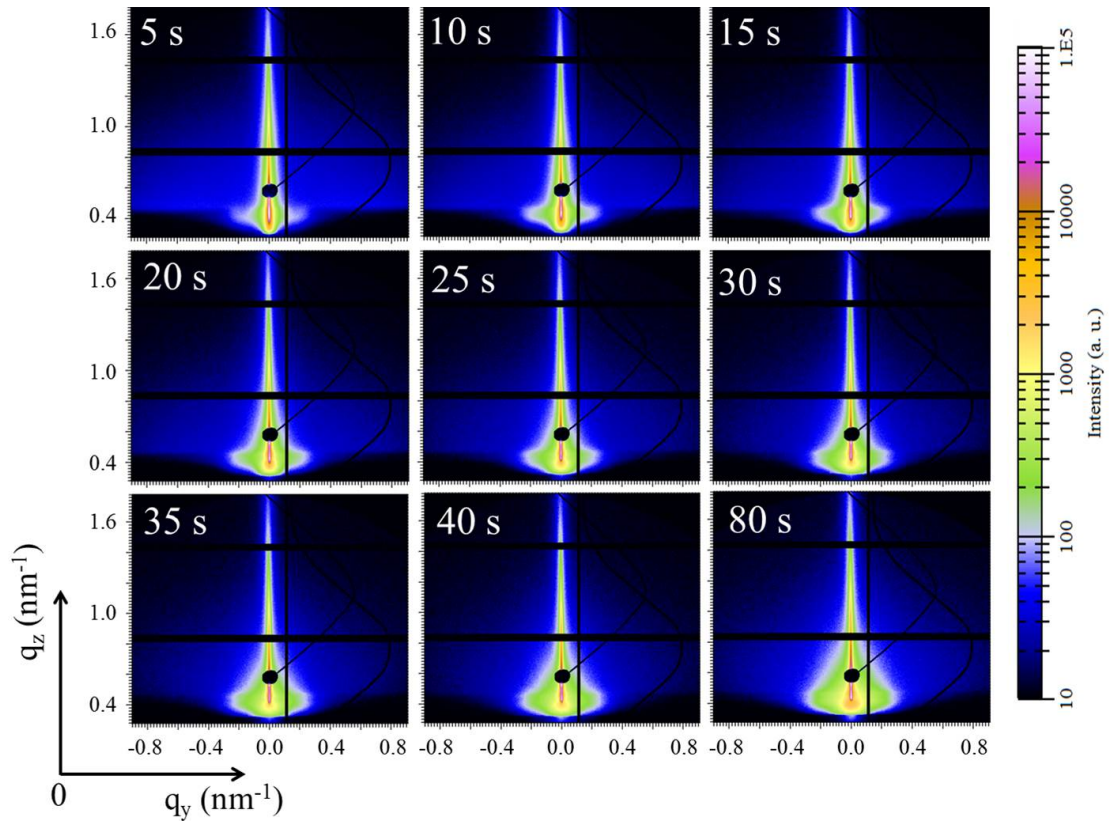


**Figure 6.2:** Selected integrated 2D GISAXS data of the titania/PS-*b*-PEO composite film spray deposited from the pure solution. The patterns are displayed in the order of spray time. The intensity scale for the scattering signal is shown at the right of the images. The circular black area is the beamstop. The horizontal black stripes at  $q_z = 0.84 \text{ nm}^{-1}$  and  $q_z = 1.42 \text{ nm}^{-1}$  as well as the one in the vertical position at  $q_y = 0.12 \text{ nm}^{-1}$  are due to the inter-module detector gaps of the detector.

material is spray-deposited onto the substrate, which gives more x-ray scattering. The specular peak, which appears at the exit angle  $\alpha_f$  equal to the incident angle ( $\alpha_i = 0.23^\circ$  in the present case) at  $q_y = 0 \text{ nm}^{-1}$ , is shielded by a circular beamstop. Therefore, the observed intensity maximum is the Yoneda peak, which is strengthened by the Fresnel



transmission functions at the critical angle of the probed material [158]. The spray-deposited composite film mainly contains three types of materials, PS, PEO and titania. During the sol-gel process, PS chains self-assemble into spherical cores with pendants of hydrophilic PEO coronas, and the titania species are bound to the PEO matrix by forming covalent bonds with the PEO chains [110, 220]. The mixture of titania and PEO has a strong contrast with the PS domains in the corresponding GISAXS measurements and the signal of diffuse scattering from the mixture is much stronger. Thus, horizontal line cuts at the Yoneda peak position of the titania/PEO mixture are performed along the  $q_y$  direction to obtain quantitative information with respect to the mixture's domain size and arrangement. For better statistics, the line cuts integrate 5 pixels centered around the Yoneda peak. The selected horizontal line cuts are displayed in figure 6.3a. In order to obtain quantitative structural information, the line cuts are fitted with the same model as described in section 5.1.2.

For data analysis, two characteristic domain sizes (corresponding to two form factors) and two center-to-center distances (corresponding to two structure factors) are used to model the line cuts in every spray shot and pause. The extracted structural information about the titania/PEO mixture is summarized and plotted as a function of the spraying time in figure 6.3b and 6.3c. During the 1<sup>st</sup> cycle, the small domains of the titania/PEO mixture have a size of  $(7.6 \pm 0.6)$  nm with a center-to-center distance of  $(25.5 \pm 3.7)$  nm, and these values remain almost unchanged during the whole spray-coating process. The domain sizes and center-to-center distances of the large titania/PEO mixture are of  $(45.6 \pm 1.1)$  nm and  $(131 \pm 45)$  nm after 1 s of spray coating, respectively. Then both sizes decrease steadily to approximately the 15th spray cycle, and afterwards stay stable until the end, as shown in figure 6.3b and 6.3c. During spray coating, the nitrogen flow atomizes the solution into droplets with different sizes and then transports the droplets onto the substrate, as described in section 4.2.3. Small droplets contain less solvents than large ones, so that solvents may evaporate completely due to the droplet flying time and the high temperature of the substrate (80 °C). Therefore, solvent-free small domains of titania/PEO mixture stay stable with respect to the morphology when they are arrested on the hot substrate. After spray coating, the structural information is extracted from in situ GISAXS data during 60 s thermal annealing and plotted as a function of annealing time in figure 6.4. It is noted that the domain sizes and center-to-center distances are the same as in the spray coating process. The thermal annealing step confirms the absence of solvent in the small domains of the titania/PEO mixture. Furthermore, the size of the PS domains can be calculated via equation 5.1. Situated between the small domains of the titania/PEO mixture, the PS domains have an average size of about 10.3 nm over the whole spraying and annealing time. In contrast to the

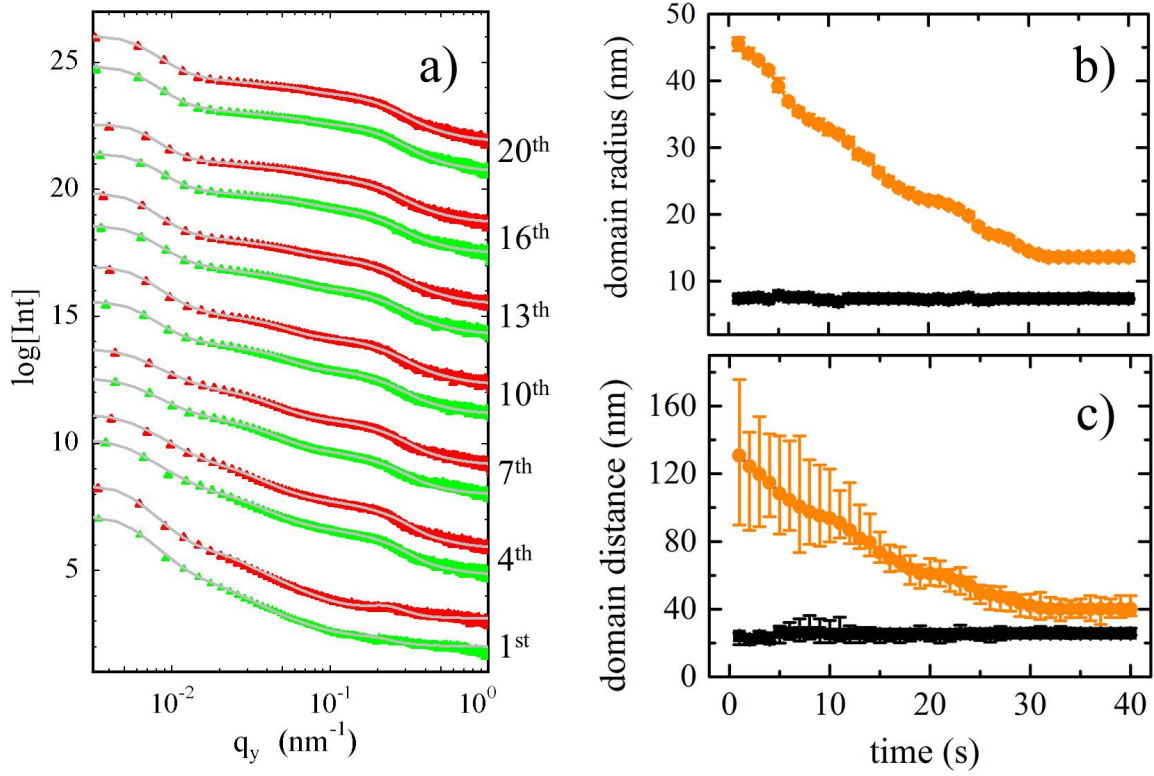


**Figure 6.3:** Analysis of *in situ* GISAXS data for the pure titania/PS-*b*-PEO composite film during spray deposition. a) Selected integrated horizontal line cuts of the 2D GISAXS data plotted from bottom to top for increasing time. Each cut is integrated over 1 s. The green and red curves represent spray shots and pauses, respectively. The corresponding sequences of spray cycles are labeled on the right axis. The gray lines represent the fits to the data. All curves are shifted along the intensity axis for clarity of the presentation. Quantitative information about b) domain radii and c) the corresponding center-to-center distances are extracted and plotted as a function of spraying time. Black rectangles and orange circles indicate small- and large-sized domains, respectively.

already discussed small droplets, large droplets contain more solvent, which cannot evaporate completely during the flying time. The evaporation proceeds after the large domains of titania/PEO are created on the hot substrate. The further solvent evaporation results in a shrinkage of the domain sizes and center-to-center distances. After the solvents are removed completely, the domain sizes and center-to-center distances stay constant at  $(13.6 \pm 0.6)$  nm and  $(40 \pm 4)$  nm, respectively. This can be ensured by the annealing step as well, where domain sizes and center-to-center distances stay the same. The size of PS domains (between the large domains of titania/PEO mixture) can be calculated via equation 5.1 as well; it decreases from around 39.8 nm to about 12.8 nm. After spray coating, it is noticeable that the domain sizes of PS areas is similar, although the small clusters and large clusters of titania/PEO mixture have different domain size.

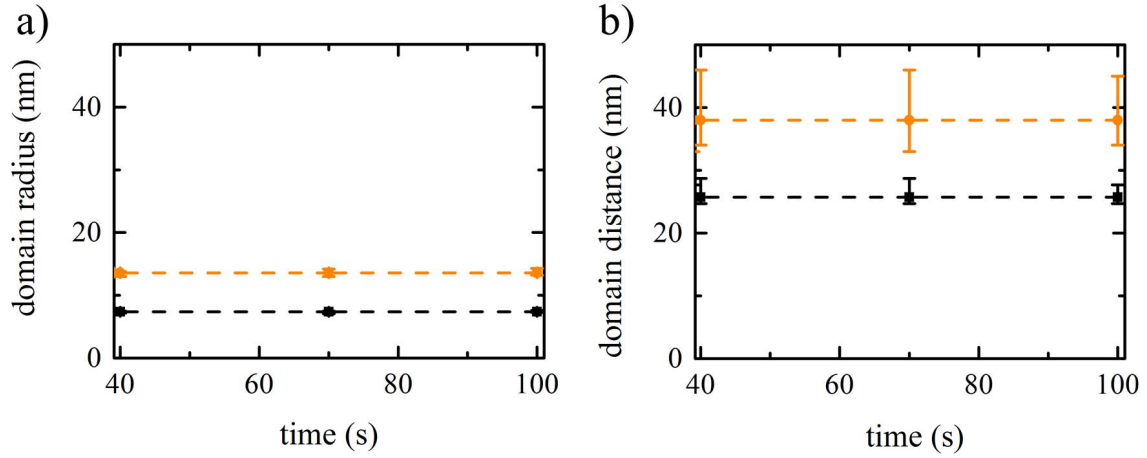


**Figure 6.4:** Analysis of in situ GISAXS data for the pure titania/PS-b-PEO composite film during thermal annealing. a) domain radii and b) the corresponding center-to-center distances are extracted and plotted as a function of annealing time. Black rectangles and orange circles indicate small- and large-sized domains, respectively. The dashed lines are a guide to the eyes.

### In situ monitoring on spray-deposited NPs films

For the investigation of the sample containing pre-synthesized nanoparticles, the experimental parameters and analysis methods used are the same as for the *pure* titania/PEO composite film, with the difference that a portion of pre-synthesized titania nanoparticles are incorporated into the *NPs* solution. Figure 6.5a shows the selected horizontal line cuts and their corresponding fits. The extracted domain sizes and center-to-center distances of the titania/PEO mixture are summarized and plotted as a function of the spraying time in figure 6.5b and 6.5c, respectively. Like the *pure* sample, the sizes of the small domains and their corresponding center-to-center distances stay constant during the whole process of spray coating, but the values are smaller. The domain size and the center-to-center distance are of  $(5.1 \pm 0.2)$  nm and  $(20.5 \pm 3.5)$  nm, respectively. The large domains of titania/PEO mixture have a similar trend as for the *pure* sample with respect to the evolution of the size and the center-to-center distance. They start decreasing from  $(39.2 \pm 1.0)$  nm and  $(104 \pm 38)$  nm, and stabilize at  $(27.5 \pm 0.5)$  nm and  $(66.0 \pm 10.0)$  nm, respectively. The size of the PS domains between the large domains of titania/PEO mixture can be calculated as well. It decreases from about 25.6 nm to about 11.0 nm. During thermal annealing, the morphology does not change as compared to the last stage of spray coating, as shown in figure 6.6.

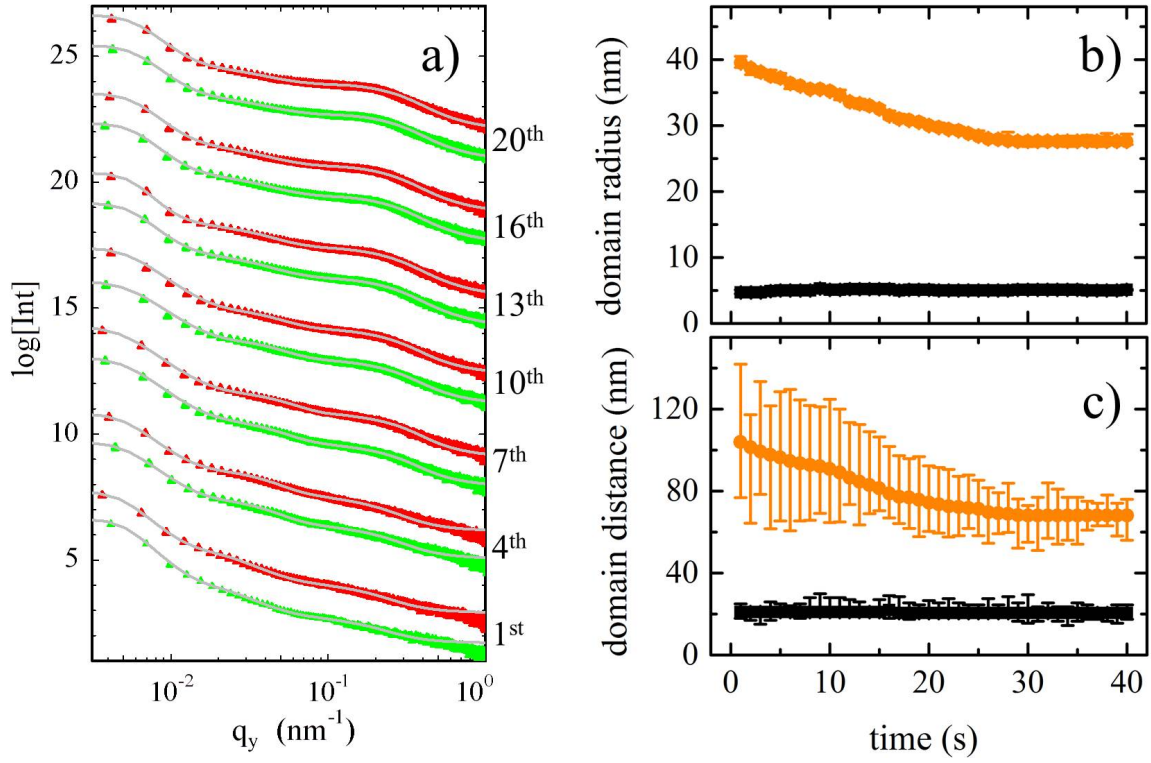


**Figure 6.5:** Analysis of *in situ* GISAXS data for the NPs titania/PS-*b*-PEO composite film during spray coating. a) Selected integrated horizontal line cuts of the 2D GISAXS data plotted from bottom to top for increasing time. Each cut is integrated over 1 s. The green and red curves represent spray shots and pauses, respectively. The sequence of spray cycles are labeled beside the right axis. The gray lines represent the fits to the data. All curves are shifted along the intensity axis for clarity of the presentation. Quantitative information about b) domain radii and c) the corresponding center-to-center distances are extracted and plotted as a function of spraying time. Black rectangles and orange circles indicate small- and large-sized domains, respectively.

## Discussion

Based on the *in situ* study on the spray-deposited *pure* and *NPs* composite films, it is found that the domain size in the titania/PEO mixture strongly depend on the introduction of nanoparticles, whereas the size of PS domain is not affected. For the small clusters of the titania/PEO mixture, the size is about 5.1 nm in the *NPs* composite film, smaller than that in the *pure* composite film (about 7.6 nm). As the incorporated nanoparticles are bigger than the small cluster, it is inferred that the pre-synthesized nanoparticles only exist in the large clusters of titania/PEO mixture, not in the small clusters. In addition, the amount of the sol-gel-synthesized titania in the *NPs* solution is only half of that in the *pure* solution. Therefore, the size of the small clusters in the *NPs* film is smaller

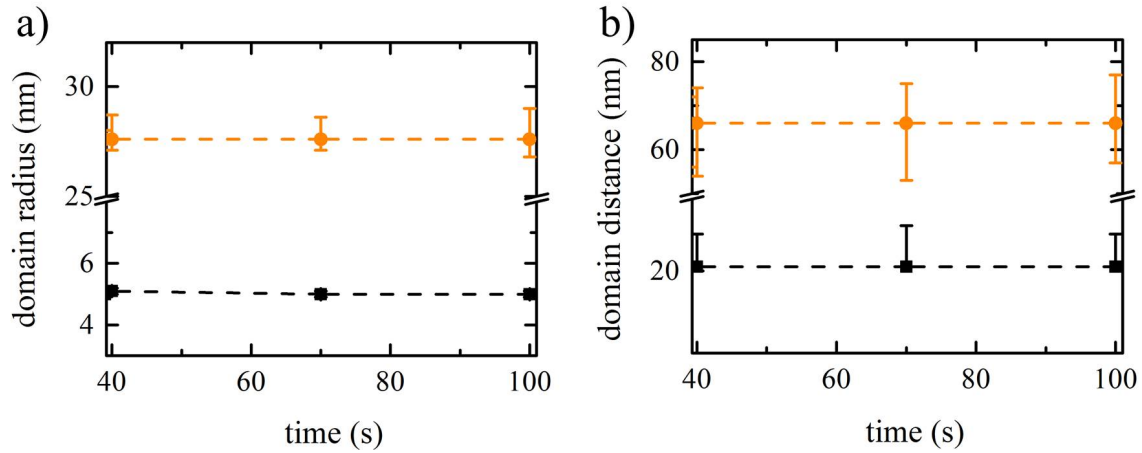


**Figure 6.6:** Analysis of *in situ* GISAXS data for the NPs titania/PS-b-PEO composite film during thermal annealing. a) domain radii and b) the corresponding center-to-center distances are extracted and plotted as a function of annealing time. Black rectangles and orange circles indicate small- and large-sized domains, respectively. The dashed lines are a guide to the eyes.

than in the *pure* film. The large clusters of the titania/PEO mixture show an opposite trend, being much larger in the *NPs* film than in the *pure* film. All nanoparticles are incorporated into the large clusters in the *NPs* sample, which gives rise to a larger size. The PS domains, situated either between the small clusters or between the large clusters of titania/PEO mixture, have a quite similar size of about 11 nm for both *pure* and *NPs* samples. The size similarity implies that the PS domain does not incorporate either sol-gel-synthesized titania or titania nanoparticles.

## 6.2 Morphologies before and after calcination

After spray coating, both titania/PS-b-PEO composite films are investigated with respect to their surface morphology. The morphological difference induced by the introduction of presynthesized nanoparticles is discussed. Afterwards, the composite films are calcined at 500 °C to combust the PS-b-PEO templates and to crystallize the titania. The surface and inner morphologies for both *pure* and *NPs* films are compared before and after the polymer-template sacrifice.

### 6.2.1 Surface morphology

Figure 6.7 shows the surface morphology of the *pure* and *NPs* composite films after spray deposition. The films are mapped with scanning electron microscopy (SEM). The sol-gel synthesized titania and presynthesized nanoparticles are evenly distributed over the sample surface, suggesting that the nanostructured titania is uniformly directed into the polymer matrix. The darker areas in figure 6.7a and 6.7b are recognized as PS domains, as PS has a lower conductivity than the mixture of PEO and titania. During SEM measurements, the incident electrons tend to accumulate on the PS domains, leading to a darker scale. The average size of PS domains can be extracted to be about 10 nm in both films, which is in good agreement with the values obtained from the in situ GISAXS data (last stage). The size consistency indicates that spray coating reproduces the surface morphology within the bulk of both samples. However, in the *pure* composite film PS domains are almost isolated, whereas some of them are connected in the *NPs* composite film, as indicated by red rectangles in figure 6.7b.

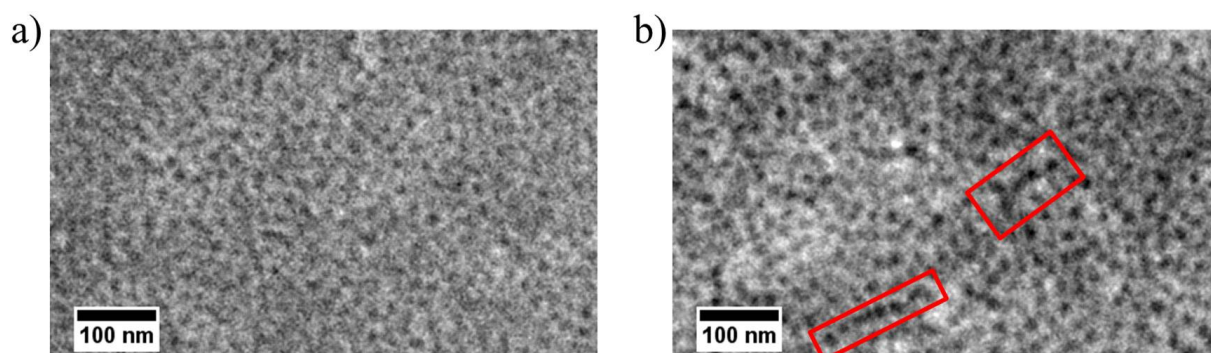


**Figure 6.7:** Plan view SEM images of the spray deposited titania/PS-b-PEO composite films of a) *pure* and b) *NPs*. The red rectangles in b) indicate the connected PS cores.

After high-temperature calcination the PS cores are burned away and leave mesopores behind, while the titania nanostructures fuse together after the removal of the PEO matrix (figure 6.8). As compared to figure 6.7, the SEM images of the calcined samples have stronger contrast. The mesopores and titania nanostructures in both films are clearly observable. The mesopores have an average size of about 15 nm, which are larger than the PS domains before calcination in both samples. Moreover, the titania walls between the mesopores are much smaller than in the mixture of titania/PS-b-PEO. This is because that the titania nanostructures collapse during the sacrifice of the polymer scaffold [165,167–170]. The difference of the PS core array leads to a different mesopore array after calcination. The mesopores are isolated by titania nanowalls in the calcined *pure* titania film, while the calcined *NPs* titania film features some worm-like pores which are indicated by red



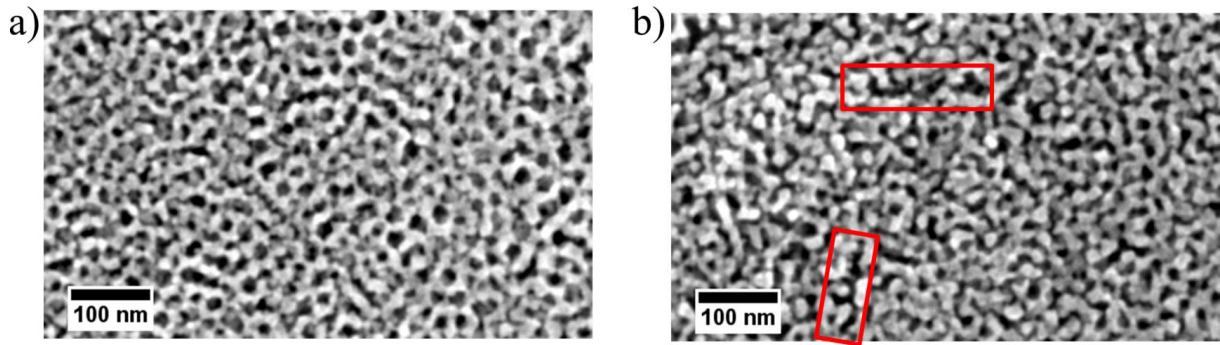


**Figure 6.8:** Plan view SEM images of the calcined titania films after spray deposition. a) pure and b) NPs. The red rectangles in b) indicate the connected mesopores.

rectangles in figure 6.8b. These worm-like pores originate from the connected PS cores as mentioned before. The film layouts for both samples are quite consistent before and after high-temperature process, although the size features are changed.

### 6.2.2 Inner morphology

Since SEM measurements only provide surface information, GISAXS measurements are used to obtain more insights about the inner morphology of both calcined titania films. The measurements were conducted at the P03/MiNaXS beamline of the PETRA III storage ring at DESY, as described in section 3.1.6. A grazing incident angle of  $0.25^\circ$  and a sample-detector distance of 3989 mm were selected to obtain a desired  $q$  range.

Figure 6.9 shows the 2D GISAXS data of the calcined *pure* and *NPs* titania films. For both samples, conspicuous scattering is observed near the Yoneda peak in the lateral direction, indicating the existence of titania nanostructures. However, the two GISAXS data differ in the detailed features. It is noted that Bragg rods reside symmetrically at  $q_y = \pm 0.19 \text{ nm}^{-1}$  in the mesoporous *pure* film, while this feature is not found in figure 6.9b. The existence of Bragg rods implies the pore arrangement is more ordered in the bulk of the mesoporous *pure* film. In order to obtain quantitative information about the titania nanostructures in the film volume, horizontal line cuts are performed at the titania Yoneda peak, as only titania remains on the sample after high-temperature processing. The cuts for both samples are displayed in figure 6.10a. The obtained data are fitted with the same models as for the analysis of the in situ GISAXS data. The obtained results are plotted in figure 6.10b and 6.10c.

For the calcined *pure* titania film, two characteristic domain sizes (form factors) and center-to-center distances (structure factors) are used to model the horizontal line cuts. In detail, the small-sized titania structures have a domain size of  $(2.9 \pm 0.1) \text{ nm}$  and a

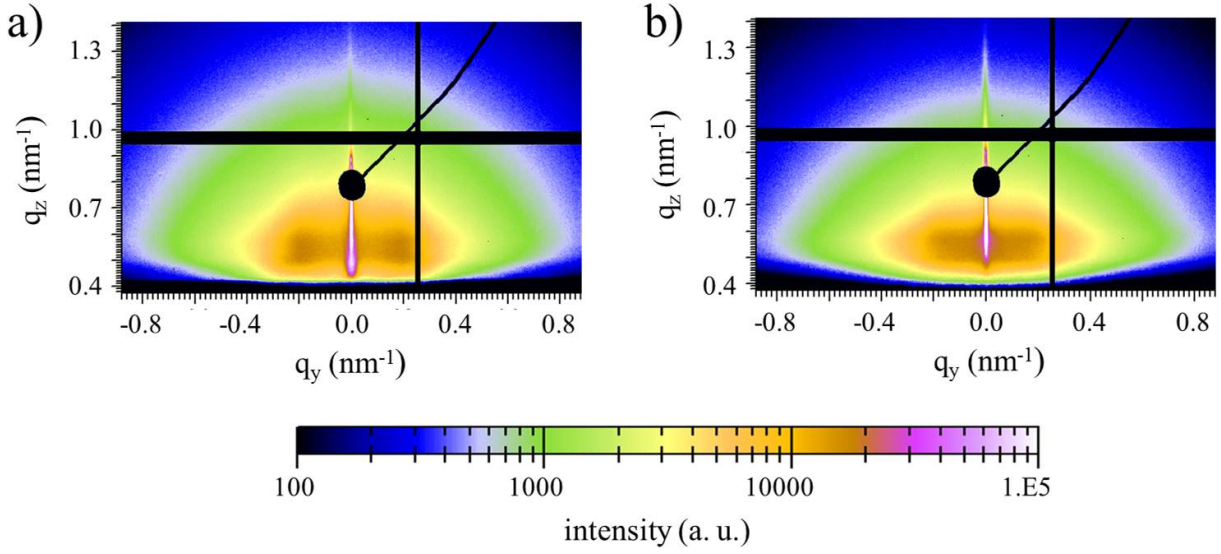


**Figure 6.9:** 2D GISAXS data of the calcined titania films after spray deposition. a) pure and b) NPs. The intensity scale for the scattering signal is shown at the bottom of the images. The circular black area is the beamstop. The horizontal black stripe at  $q_z = 0.96 \text{ nm}^{-1}$  and the vertical one at  $q_y = 0.26 \text{ nm}^{-1}$  correspond to the inter-module gaps of the used detector.

domain center-to-center distance of  $(20.0 \pm 5.0) \text{ nm}$ . According to the equation 5.1, the pore size between small-sized structures is calculated to be  $(14.2 \pm 5.0) \text{ nm}$ . A domain size of  $(4.6 \pm 0.1) \text{ nm}$  and the corresponding center-to-center distance of  $(23.0 \pm 0.5) \text{ nm}$  are obtained for the large-sized titania nanostructures, yielding a pore size of  $(13.8 \pm 0.3) \text{ nm}$ . For the calcined *NPs* titania film, three form and structure factors are needed for data modeling. The sizes of small and middle titania domains are similar to the small- and large-sized titania nanostructures in the *pure* film. Titania nanostructure radii of  $(2.1 \pm 0.1) \text{ nm}$  and  $(5.2 \pm 0.1) \text{ nm}$  with their corresponding center-to-center distances of  $(19.0 \pm 4.0) \text{ nm}$  and  $(22.8 \pm 0.5) \text{ nm}$  are obtained, yielding the mesopore sizes of  $(14.6 \pm 4.0) \text{ nm}$  and  $(12.4 \pm 0.3) \text{ nm}$ . The third nanostructure is much bigger than the others, with a domain size of  $(20.0 \pm 5.0) \text{ nm}$  and the center-to-center distance of  $(80.0 \pm 30.0) \text{ nm}$ . The corresponding pore size can be calculated to be  $(40.0 \pm 20.0) \text{ nm}$ . This feature quite fits the structure with worm-like pores observed in the SEM measurements. However, the third titania domains can be calculated to have a volume fraction of only 5.2%. The detailed information can be found in section 5.1.2.

### 6.2.3 Discussion

Before and after high-temperature calcination, both *pure* and *NPs* samples have a significant change in their morphology according to the SEM and GISAXS measurements.



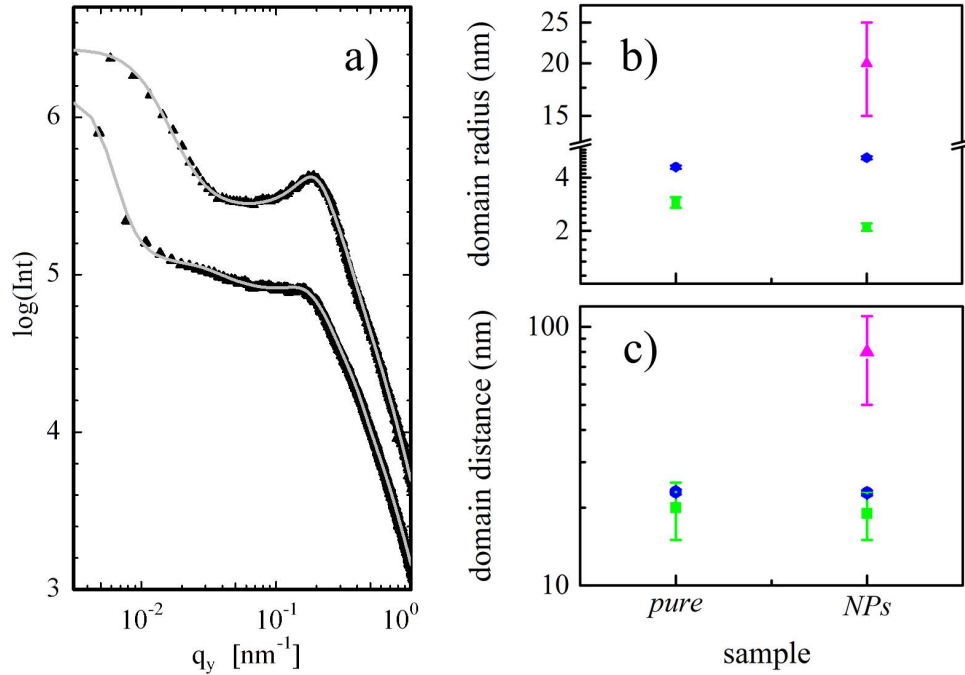


**Figure 6.10:** a) Horizontal line cuts of the 2D GISAXS data obtained from the calcined titania films. The top and bottom curves represent cuts from the pure and NPs films, respectively. The gray lines represent the fits. All cuts and fits are shifted along the intensity axis for clarity of the presentation. Quantitative information about b) domain radii and c) center-to-center distances are extracted. Green squares represent small-sized titania structure and blue circles represent large-sized structure. Magenta triangles indicate the third titania domain in the NPs film.

First, a distinct size shrinkage occurs when the titania/PEO mixture turns into pure titania. For the *pure* sample, the domain sizes of the titania/PEO mixtures are found to be  $(7.6 \pm 0.2)$  nm and  $(13.6 \pm 0.4)$  nm after spray deposition. After calcination, the small- and large-sized titania nanostructures have domain sizes of  $(2.9 \pm 0.1)$  nm and  $(4.6 \pm 0.1)$  nm, respectively. Through calculation it is found that the small structures in the calcined film are only 38% of small clusters of titania/PEO mixture in the titania/PEO composite film with respect to domain size, and 34% for the large-sized nanostructures. Guldin et al. have reported a similar observation that the film thickness contracted to 33% - 42% of their initial thickness in the spin-coated titania/PI-b-PEO composite films and this shrinkage is ascribed to the removal of the polymer template and the condensation of  $\text{Ti}(\text{OH})_4$  to  $\text{TiO}_2$ . For the *NPs* sample, 41% size shrinkage occurs in the small-sized nanostructures, which is quite in line with the observation by Guldin et al. as well. However, the large-sized structures contract to only about 19% of initial clusters of the titania/PEO mixture. The extra size shrinkage is caused by the combustion of the organic ligands of nanoparticles during 500 °C calcination. Secondly,

the mesopore sizes are larger than the PS domain sizes for both samples. This is caused by the collapse of titania nanostructures and subsequent fusing into large domains during the high-temperature processing.

## 6.3 Solar cell performance

The spray-deposited mesoporous *pure* and *NPs* titania films are individually served as photoanodes for ssDSSCs. The thickness of the titania films is controlled to be about 2.5  $\mu\text{m}$ . 5-[[4-[4-(2,2-Diphenylethenyl)phenyl]-1,2,3,3a,4,8b-hexahydrocyclopent[b]indol-7-yl]methylene]-2-(3-octyl-4-oxo-2-thioxo-5-thiazolidinylidene)-4-oxo-3-thiazolidineacetic acid (D205) and spiro-OMeTAD are used as light harvester and HTM, respectively. The layer consisting of mesoporous titania layer, dye D205 and spiro-OMeTAD acts as the active layer for ssDSSCs. Fluorine-doped tin oxide (FTO) and gold are applied as bottom and top electrodes, respectively. The implemented layout of ssDSSCs in this work is:

$$\text{glass/FTO/compact-TiO}_2/\text{mesoporous TiO}_2/\text{D205/spiro-OMeTAD/Au}$$

In the present work the spiro-OMeTAD layer is produced by two different deposition methods, spin coating and solution casting. Together with two different titania photoanodes, three types of ssDSSCs are fabricated. The first type is referred as *pure/sol-spiro* cell. The mesoporous *pure* titania film is used as photoanode and the spiro-OMeTAD layer is deposited with solution casting. The active layer of the second type consists of the mesoporous *NPs* titania film, D205 and solution-cast spiro-OMeTAD. This type is denoted as *NPs/sol-spiro* cell. The third type is denoted as *NPs/spin-spiro* cell, which is the same as the second one except that the spiro-OMeTAD layer is deposited by spin coating. Detailed information about the used materials is given in section 4.1. The solar cell assembly described in detail in section 4.2.4.

After preparation, the ssDSSCs are tested immediately under simulated AM 1.5G illumination with 100  $\text{mW cm}^{-2}$  intensity. Detailed information about the solar cell characterization is given in section 3.2.3. Figure 6.11 compares the current-voltage ( $I$ - $V$ ) characteristics of these three types of ssDSSCs. From  $I$ - $V$  curves, related photovoltaic parameters such as power conversion efficiency ( $PCE$ ), short-circuit current density ( $J_{sc}$ ), open-circuit voltage ( $V_{oc}$ ) and fill factor ( $FF$ ) can be extracted. The obtained results are listed in table 6.3. It is noted that the solar cell performance matters strongly with the addition of pre-synthesized nanoparticles and the deposition method of the spiro-OMeTAD layer. Firstly, the performance comparison is made between the *pure/sol-spiro* cell and the *NPs/sol-spiro* cell. Both cells have the same preparation methods for solar cell assembly, but the components of their titania photoanodes are different. An extra portion

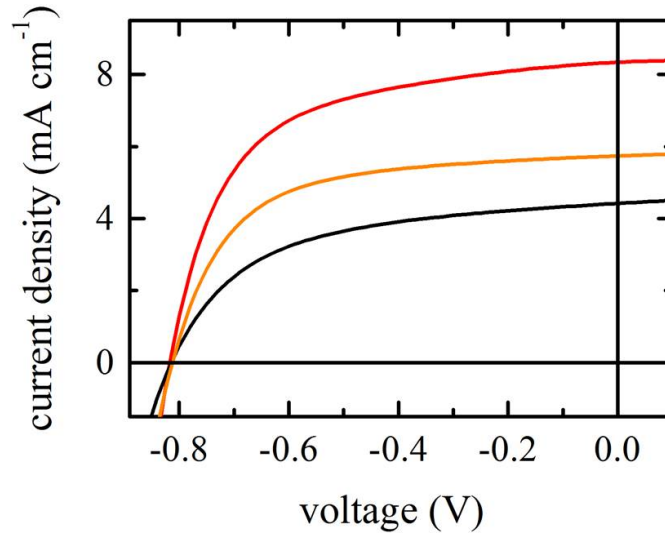


**Figure 6.11:** Current-voltage characteristics for these three types of ssDSSCs: the pure/sol-spiro cell (black), the NPs/sol-spiro cell (red) and the NPs/spin-spiro cell (orange).

of pre-synthesized crystalline titania nanoparticles are introduced into the mesoporous titania photoanodes for the *NPs/sol-spiro* cell. The addition of nanoparticles results in a doubling of the *PCE* for the *NPs/sol-spiro* cell as compared to the *pure/sol-spiro* cell. The enhancement mainly originates from the improved  $J_{sc}$  and  $FF$ , as the  $V_{oc}$  of both devices is similar. The  $J_{sc}$  of the *NPs/sol-spiro* cell is  $(8.37 \pm 0.03) \text{ mA cm}^{-2}$ , which is almost twice as large as that for the *pure/sol-spiro* cell. The  $FF$  increases about 12% with incorporating nanoparticles into titania network,  $(60.2 \pm 0.7) \%$  for the *pure/sol-spiro* cell and  $(53.4 \pm 0.4) \%$  for the *NPs/sol-spiro* cell. The improvement of  $J_{sc}$  and  $FF$  is due to the higher specific surface area, higher pore volume and higher conductivity of the titania photoanodes in the *NPs/sol-spiro* cell, as described in section 5.2.2.

The *NPs/sol-spiro* cell and the *NPs/spin-spiro* cell possess the same composition, while the spiro-OMeTAD layer is deposited by solution casting in the *NPs/sol-spiro* cell and by spin coating in the *NPs/spin-spiro* cell. The different deposition methods for the spiro-OMeTAD layer lead to a difference in only the  $J_{sc}$  for both cells ( $V_{oc}$  and  $FF$  are very similar). The spin coating gives rise to a  $J_{sc}$  of  $(5.80 \pm 0.07) \text{ mA cm}^{-2}$  in the *NPs/spin-spiro* cell, which is about 34% less than that for the *NPs/spin-spiro* cell. According to our previous studies on poly(3-hexylthiophene) (P3HT) deposition with different preparation methods, it is found that the filling ratio of P3HT into mesoporous titania films by solution casting is higher than by spin coating [183]. This way, the infiltration of spiro-OMeTAD into the mesoporous *NPs* titania films is investigated. Figure 6.12 shows the cross-sectional SEM images of both active layers. For cross-section SEM measurements, the samples are broken along the direction normal to the substrate after being immersed

solar cell	$J_{sc}$ (mA cm <sup>-2</sup> )	$V_{oc}$ (V)	$FF$ (%)	$PCE$ (%)
<i>pure/sol-spiro</i>	4.40 ± 0.03	0.80 ± 0.03	53.4 ± 0.4	1.9 ± 0.1
<i>NPs/sol-spiro</i>	8.37 ± 0.03	0.80 ± 0.02	60.2 ± 0.7	4.0 ± 0.1
<i>NPs/spin-spiro</i>	5.80 ± 0.07	0.81 ± 0.01	60.6 ± 0.6	2.8 ± 0.1

**Table 6.3:** The composition details of nanoparticle solution.

into liquid nitrogen for 1 min. It is noticeable that the *NPs/spin-spiro* active layer has a better infiltration of the spiro-OMeTAD than the *NPs/sol-spiro* active layer. The infiltration of the spiro-OMeTAD into mesoporous titania films plays a critical role in the device performance, as the TiO<sub>2</sub>/dye/spiro-OMeTAD interfacial areas are the sites for exciton dissociation. Less efficient backfilling results in a lower interfacial area, which gives a lower  $J_{sc}$  and thereby a lower  $PCE$  in the *NPs/spin-spiro* cell.

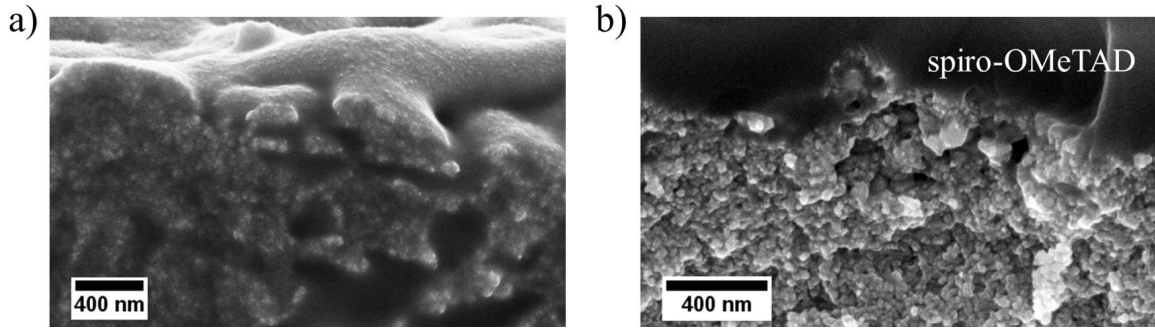


**Figure 6.12:** Cross-sectional SEM images of the active layers for ssDSSCs. a) the *pure/sol-spiro* cell and b) the *NPs/spin-spiro* cell.

## 6.4 Summary

Titania is used as photoanode in ssDSSCs in the present work. As the charge separation only takes place at the TiO<sub>2</sub>/dye/spiro-OMeTAD interface, nanostructured titania films with a high surface-to-volume ratio are preferable. In order to obtain controllable nanostructures and pore sizes, polymer-template assisted sol-gel synthesis is selected to prepare mesoporous titania films.

Spray coating is chosen to deposit the film directly from titania sol-gel solution, as it has a strong potential to be adapted for large-scale industrial applications. In order to understand the complex spray dynamics, in situ GISAXS measurements are used to track the structural evolution of deposited films. For both the *pure* and *NPs* composite

films during the spray-coating process, the small clusters of the titania/PEO mixture stay unchanged in size whereas the large clusters of the titania/PEO mixture decreases with spraying time to a certain point and then stays stable until the end. Sarkar et al. have observed the structural evolution of ZnO films with the aid of in situ GISAXS measurements during the spray deposition [215]. The ZnO clusters showed a rapid increase in size at the beginning stage and then remained at a constant size till the end of spray-coating process. This observation is distinct from the findings in the present work, which may be caused by two main factors. On the one hand, a different sol-gel system is used for the solution preparation. A titania precursor and A solvent of a binary azeotrope is used in this work. On the other hand, the polymer template is combined with sol-gel system in the present work instead of spray coating a pure precursor solution.

After spray deposition, the surface structural information (revealed by SEM measurements) of both samples is in accordance with the results obtained from in situ GISAXS measurements, suggesting that the surface morphology is reproduced within bulk of the sample. After calcination, the polymer template is extracted and thereby the mesoporous titania film forms. A distinct size shrinkage from the titania/PEO mixture to pure titania and a slight size expansion from the PS cores to mesopores can be found in both the *pure* and *NPs* samples, which is caused by the combined effect of polymer-template sacrifice and titania-nanostructure collapse. The worm-like pores are only found in the *NPs* sample, which is attributed to the addition of pre-synthesized nanoparticles. Guldin et al. have reported the change of surface morphology for a titania/PI-b-PEO composite film before and after high-temperature processing [19]. The observation of surface-morphology change is similar to the findings of the *pure* sample in this work. Until now, however, no investigations about the morphology change before and after calcination are performed on the sample with incorporation of nanoparticles into nanostructured titania network.

By using different titania photoanodes and different preparation methods of the spiro-OMeTAD layer, three types of ssDSSCs are fabricated. The *NPs/sol-spiro* cell gives the best photovoltaic performance of the final ssDSSCs. Since its titania film and spiro-OMeTAD layer are produced using spray coating and solution casting techniques, respectively, the success of the *NPs/sol-spiro* cell gives an evidence that ssDSSCs can be produced with large-scale manufacturing processes.



## 7 In situ study of degradation in P3HT-titania based solid-state dye-sensitized solar cells

Parts of this chapter have been published in the article: In Situ Study of Degradation in P3HT-Titania Based Solid-State Dye-Sensitized Solar Cells [221] (L. Song et al., ACS Energy Lett., 2, 991-997, 2017, DOI: 10.1021/acsenerylett.7b00117).

Mesoscopic dye-sensitized solar cells (DSSCs) have received great attention for being a promising alternative to conventional silicon photovoltaic devices [151, 190, 192, 222, 223]. They are cheap, easily processable and capable of achieving a high efficiency of over 12% [8, 224, 225]. Although DSSCs have achieved commercial breakthrough, concerns over liquid-electrolyte leakage and electrode corrosion hinder their market expansion [102, 226, 227]. In recent years, many solid-state hole-transporting materials (HTMs) have been proposed to replace liquid electrolytes in DSSCs [228–233]. So far, the organic small-molecule 2,2,7,7-tetrakis-(N,N-di-p-methoxyphenylamine)-9,9-bifluorene (spiro-OMeTAD) is one of the most favorable hole conductors for solid-state DSSCs (ssDSSCs) due to its light weight, proper ionization potential and flexibility [130, 234–237]. However, the low hole mobility ( $\sim 10^{-4} \text{ cm}^2 \text{ V}^{-1} \text{ s}^{-1}$ ) and the high manufacturing cost of spiro-OMeTAD motivate researchers to develop other organic substitutes [238, 239], like conjugated polymers. Poly(3-hexylthiophene) (P3HT) as a low-cost polymer semiconductor has been widely used as HTM in solid-state DSSCs, as it has a good solubility in various solvents, a high hole mobility (up to  $0.1 \text{ cm}^2 \text{ V}^{-1} \text{ s}^{-1}$ ) and a prominent light-absorbing ability in the visible-light region [109, 240–242]. To date, many efforts have been devoted to enhancing efficiencies of solar cells based on mesoporous  $\text{TiO}_2$  films and P3HT. For example, a variety of sensitizers were developed to modify  $\text{TiO}_2$  films for optimization of photovoltaic performance. Devices with ruthenium complex, metal-free organic dye and quantum-dot sensitizer have been reported to reach a power-conversion efficiency of 3.5%, 3.2% and

5.2%, respectively [133, 189, 243]. Insufficient infiltration of mesoporous  $\text{TiO}_2$  films with P3HT was widely assumed to cause relatively low efficiencies. The pore filling fraction was only 8% when P3HT was directly deposited onto a dye-modified mesoporous  $\text{TiO}_2$  film. While coating with bis(trifluoromethane)sulfonimide lithium salt (LiTFSI) and tert-butylpyridine (tBP) prior to P3HT infiltration pore filling fraction rose to 23.8% [241]. Alternatively, pre-soaking of mesoporous  $\text{TiO}_2$  films in the host solvent of P3HT solution gave rise to a pore filling degree of 84% [183]. These facts have encouraged many research groups to improve device performance by inventing more efficient sensitizers or by improving P3HT backfilling ratios.

Given the difficulty to synthesize new sensitizers and to permeate P3HT into mesopores, another way around this issue is to increase the P3HT crystalline order, which greatly influences the mobility of positive charge carriers [16, 18]. Nevertheless, only a few research groups dedicated studies to the behavior of P3HT in ssDSSCs. Coakley et al. demonstrated that infiltration of regioregular P3HT in straight nanopores gave rise to more ordered polymer structures and consequently to an enhanced hole mobility [244]. Lin et al. utilized a rod-coil diblock polymer, P3HT-b-P2VP, as the additive to boost the efficiency of  $\text{TiO}_2$ :P3HT hybrid solar cells [245]. P3HT crystallinity and crystal size has been widely studied in [6,6]-phenyl-C61-butyric acid methyl ester:P3HT (PCBM:P3HT) system as they play a crucial role in photovoltaic performance. However, a direct evidence for P3HT crystallization in solid-state DSSCs especially inside  $\text{TiO}_2$  mesopores is still missing. Based on this point, an in-depth study is initiated for the very first time in the present work. Moreover, the P3HT crystalline evolution is tracked in situ under continuous solar illumination since its crystallinity has a great impact on the photovoltaic device performance. In order to understand the relationship between P3HT crystalline evolution and solar cell performance, the development of the device photovoltaic characteristics is probed in parallel.

In the present thesis, a versatile route is presented for fabricating  $\text{TiO}_2$  films with ordered mesopore arrays, which relies on templating by the diblock copolymer poly(styrene-block-ethylene oxide) (PS-b-PEO) in combination with sol-gel chemistry. In this approach, a micro-phase separation of PS-b-PEO is prompted by so-called good-bad solvent pairs, which allows for the extended control of structure and pore sizes in the resulting  $\text{TiO}_2$  films [19, 141, 142, 246, 247]. The active layer of solar cells is completed by using a mesoporous  $\text{TiO}_2$  film as an n-type semiconductor, a metal-free organic dye (D149) as a light harvester, and P3HT as an HTM. In order to understand whether different titania pore sizes affect the key P3HT crystalline properties like lattice distances or crystal sizes, two types of titania films with different mesopore sizes are fabricated for P3HT infiltration in this study. Furthermore, the photovoltaic performance and stability of the ssDSSCs



with different pore-size-featured titania photoanodes are compared. Two titania films with different mesopore sizes are described in the first part of this chapter (section 7.1). The surface and inner morphologies of the mesoporous  $\text{TiO}_2$  films are examined with scanning electron microscopy (SEM) and grazing incidence small-angle x-ray scattering (GISAXS), respectively. The corresponding results are presented in section 7.1.1 and section 7.1.2. This is followed by the comparison of the crystallization of these two titania films in section 7.1.3. These two titania films are dyed and subsequently backfilled with P3HT to form the active layer of ssDSSCs (section 7.2). P3HT crystallization inside different sized mesopore is compared in section 7.2.1. In order to probe the evolution of P3HT crystallinity with continuous solar illumination, in situ grazing incidence wide angle x-ray scattering (GIWAXS) is used (section 7.2.2), which allows for studying P3HT crystallization and for tracking the development of crystallinity. Finally, links between P3HT crystallization evolution and current density-voltage ( $I$ - $V$ ) characteristics of the final solar cells are discussed in section 7.3.

## 7.1 Mesoporous titania film with different pore sizes

The mesoporous titania films investigated in this chapter are prepared via the second route of sol-gel synthesis with TTIP as described in section 4.2.2. The different mesopore sizes are achieved using polymer templates with different molecular weights. In the present work two types of PS-*b*-PEO block copolymers are used: one with a small molecular weight of  $M_n(\text{PS}) = 20.5 \text{ kg mol}^{-1}$ ,  $M_n(\text{PEO}) = 8 \text{ kg mol}^{-1}$ , polydispersity index (PDI) = 1.02, and the other one with a large molecular weight of  $M_n(\text{PS}) = 63 \text{ kg mol}^{-1}$ ,  $M_n(\text{PEO}) = 26 \text{ kg mol}^{-1}$ , PDI = 1.07. For the sol-gel process, all experimental parameters and procedures are the same, only the molecular weights of the polymer template are varied. To obtain better device performance, pre-synthesized crystalline titania nanoparticles are incorporated into sol-gel-synthesized titania networks, as such titania photoanodes have been proven to be more efficient in earlier studies [109]. The nanoparticles used in this work, which are synthesized by the Dina Fattakhova-Rohlfing group, have an average size of around 4 nm and contained about 40 wt% organic ligands. The detailed information is described in section 5.1. The used amounts of reactants is listed in table 7.1.

The sol-gel and nanoparticle solutions are mixed under vigorous stirring for 20 h after solution preparation. Afterwards, the resulting solution is ultrasonicated for 10 min before being spin-cast onto the substrates. The spin-coating parameters used in this work are kept constant at 1000 rpm for 10 s with an acceleration of 400 rounds  $\text{s}^{-1}$ . After spin-coating, the titania/PS-*b*-PEO composite films are annealed at 100 °C for 5 min, followed by another 5 min at 200 °C. After this step, the samples are transferred back to 100 °C

	sol-gel process					nanoparticle solution	
agent	PS-b-PEO	toluene	1-butanal	TTIP	HCl	NPs	toluene
amount	200 mg	2.35 mL	1.34 mL	369 $\mu$ L	76.1 $\mu$ L	166 mg	1 mL

**Table 7.1:** *The composition details about the acid bath for substrate cleaning.*

again for 5 min, and finally they are cooled down to room temperature. The procedure of spin-coating and thermal annealing is repeated four times to achieve a proper film thickness. In the present work the sol-gel-synthesized  $\text{TiO}_2$  and  $\text{TiO}_2$  from pre-synthesized nanoparticles have a weight ratio of 1:1, and the weight ratio of total  $\text{TiO}_2$  and PS-b-PEO is also fixed at 1:1. Finally, all films are calcined in the ambient condition at 500  $^\circ\text{C}$ , as described in section 4.2.2 to obtain mesoporous and crystalline titania films. Normally, the final film thickness is around 1.8  $\mu\text{m}$  after high-temperature calcination.

### 7.1.1 Surface Morphology

The surface morphology of the mesoporous titania films is studied by scanning electron microscopy (SEM). Figure 7.1a and 7.1b demonstrate plan-view SEM images of the mesoporous titania films after 500  $^\circ\text{C}$  calcination.

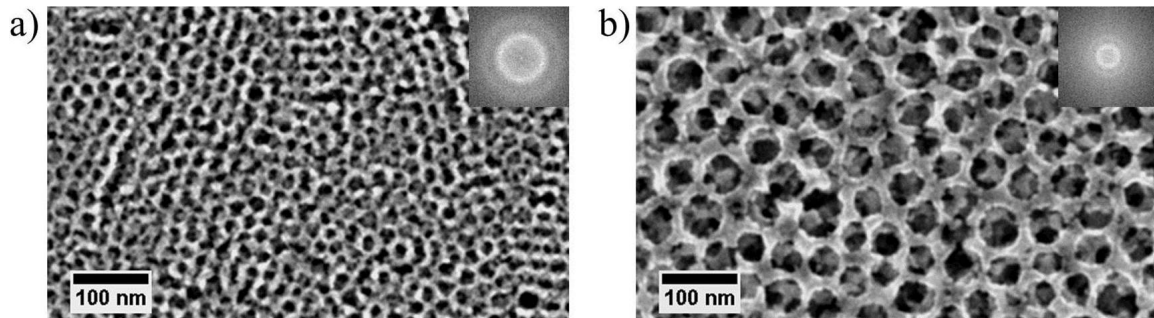


**Figure 7.1:** *Plan-view SEM images of a) small-pore and b) large-pore mesoporous titania films. The insets in a) and b) are the corresponding FFT patterns.*

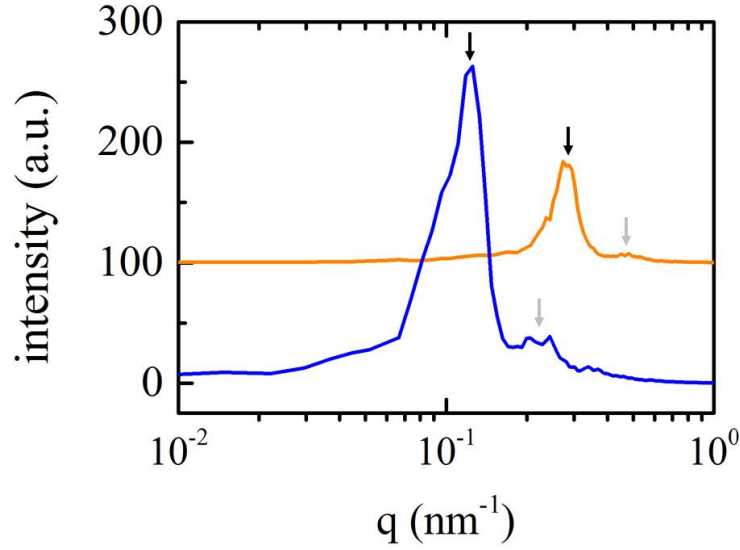
Both samples present interconnected titania networks and ordered mesopore arrays. Compared to our previous work where the sponge-like titania nanostructures with irregular mesopore arrangements are shown [109, 141], it is inferred that the binary azeotrope of toluene and 1-butanal used as good-poor solvent pair is the key point for the formation of ordered pore arrays. As seen, the pore sizes in both films vary significantly. During the whole fabrication procedure of both samples, all parameters are kept the same except the molecular ratio of polymer template. Obviously, the pore-size difference originates

from the different PS-b-PEO chain lengths, which can be used to tune the pore size of the titania films during polymer assisted sol-gel synthesis [12]. The films using the low molecular weight template feature an average pore size of around 12 nm (figure 7.1a), whereas the high molecular weight PS-b-PEO results in large pores with 40 nm average size (figure 7.1b). The difference demonstrates once again that it is possible to tailor mesoporous titania films by varying the molecular weight of polymer template. Moreover, the longer polymer chain gives rise to larger pore size in the resulting titania films. The samples with small and large mesopore arrays in this chapter are denoted as *small-pore* and *large-pore*, respectively. Beside pore-size difference both samples show different thickness of titania walls between the mesopores. The *small-pore* samples exhibit titania walls of about 8 nm thickness (figure 7.1a), whereas thicker titania frameworks of around 13 nm are present in the *large-pore* films (figure 7.1b). The difference is due to the fact that longer PEO chains can hold more titania during the sol-gel process as titania species are bound with the PEO matrices through covalent bounds [110,248]. The insets in figure 7.1a and 7.1b are the Fast Fourier transform (FFT) patterns of the corresponding SEM images. Each FFT pattern has two discernible rings. The brighter full rings in both samples indicate a isotropical pore distribution over the surface and a narrow distribution of pore center-to-center distance. The outer rings suggest the presence of some long-range lateral ordering of the mesopores over the surface. However, both FFT rings in figure 7.1a are larger than those in figure 7.1b, indicating smaller features in the *small-pore* sample. To obtain quantitative information, power spectral density (PSD) functions are calculated by azimuthal integration of the FFT patterns. The results are shown in figure 7.2. For both samples, the stronger peak originates from the brighter inner ring of the FFT pattern, whereas the weaker peak comes from the outer ring. The  $q$  positions of the stronger peak for orange and blue curves are at  $0.273 \text{ nm}^{-1}$  and  $0.126 \text{ nm}^{-1}$ , respectively. Accordingly, the center-to-center distances are computed via equation 7.1 to be about 23.0 nm for the *small-pore* sample and 50.0 nm for the *large-pore* sample.

$$d = \frac{2\pi}{q} \quad (7.1)$$

### 7.1.2 Inner Morphology

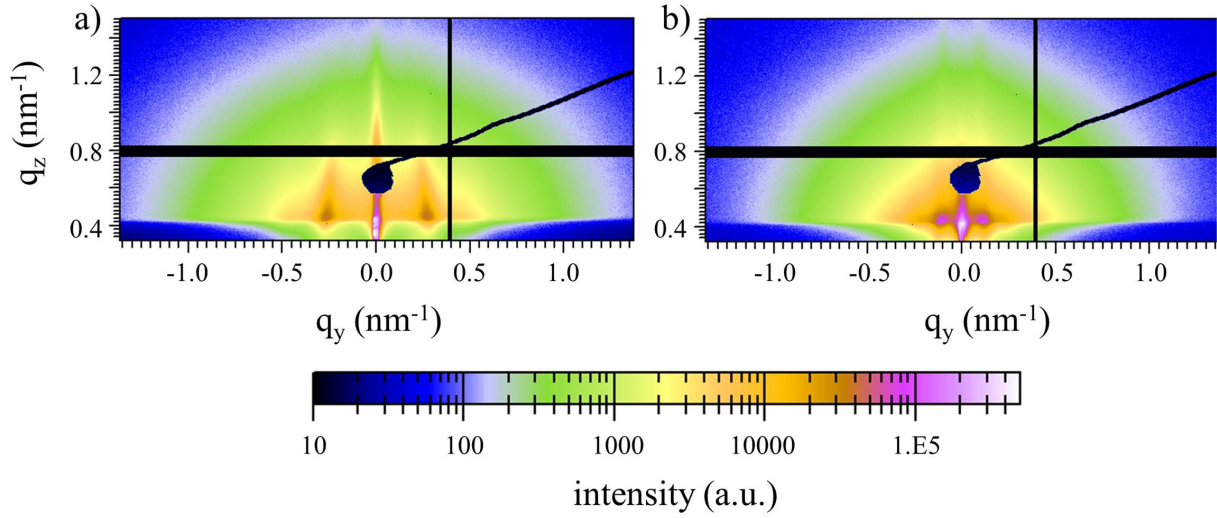
The inner film morphology is investigated with GISAXS since x-rays can penetrate the whole sample. This advanced scattering technique offers the possibility to probe the full film volume over a macroscopic sample area and therefore the structural information of the probed sample is obtained in the nano- and meso-scale with a high statistical relevance. The GISAXS experiments are performed at the Elettra SAXS beamline as described in



**Figure 7.2:** Power spectral density (PSD) functions obtained from the SEM data. Orange and blue curves are extracted from the small-pore and large-pore mesoporous titania films, respectively. The orange curve is shifted along the intensity axis for clarity of the presentation. The peaks highlighted by black arrows indicate the brighter rings of the FFT patterns, whereas the weaker peaks are marked by gray arrows showing the position of the outer rings.

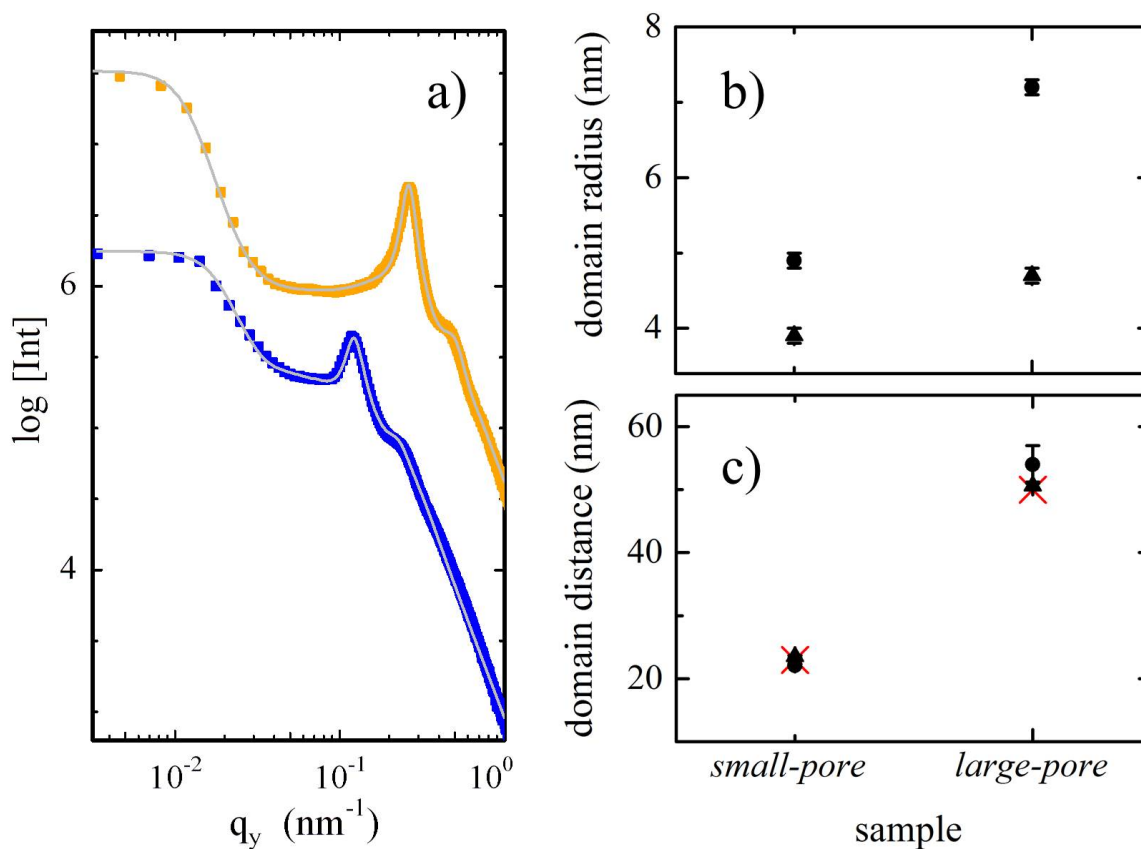
section 3.1.6. For these measurements the mesoporous titania films are produced on silicon substrates. A incident angle of  $0.43^\circ$  and a sample-detector distance of 1.96 m are selected to obtain the desired  $q$  range.

Figure 7.3 shows the 2D GISAXS data of the *small-pore* sample and the *large-pore* sample. The horizontal black stripe at  $q_z=0.8 \text{ nm}^{-1}$  and the vertical one at  $q_y = 0.4 \text{ nm}^{-1}$  are the inter-module gaps of the detector. To protect the detector from oversaturation, the specular x-ray beam is shielded by a circular beamstop. The diffuse scattering maximum observable is called Yoneda peak, which is located at the critical angle of titania. Directly from the 2D GISAXS data it can be seen that two distinct Bragg rods are positioned symmetrical around the center of  $q_y=0 \text{ nm}^{-1}$  in lateral direction for both samples, indicating ordered arrangements in the film volume. However, the position of Bragg rods for both film differs. In the *small-pore* sample the Bragg rods reside symmetrical at  $q_y = \pm 0.27 \text{ nm}^{-1}$ , while two Bragg rods are closer to the Yoneda peak in the *large-pore* sample, located at  $q_y = \pm 0.13 \text{ nm}^{-1}$ . The smaller  $q$  values in the *large-pore* sample suggest a larger predominant structural length scale in real space as compared to the *small-pore* sample. For quantitative analysis, horizontal line cuts at the Yoneda peak position are performed along the  $q_y$  direction. For better statistics, the line cuts integrate five pixels which are centered at the Yoneda peak. The horizontal line cuts allow for extracting structural information of the probed titania samples such



**Figure 7.3:** 2D GISAXS data of the a) small-pore mesoporous titania film and of the b) large-pore mesoporous titania film. The intensity scale for the scattering signal is shown at the bottom of the images. The circular black area is the beamstop shielding the specular peak. The horizontal black stripe at  $q_z = 0.8 \text{ nm}^{-1}$  and the vertical one at  $q_y = 0.4 \text{ nm}^{-1}$  correspond to the inter-module gaps of the used detector.

as domain size and domain center-to-center distance. The horizontal line cuts of both films are illustrated in figure 7.4a. The sharp and narrow peaks in both curves derive from the Bragg rods in the 2D GISAXS data for both samples. However, both curves demonstrate weak higher-order peaks, which are not observed in the 2D GISAXS data due to the relative low scattering intensity. The existence of higher-order peaks implies long-range lateral ordering of the mesopores inside both films. To obtain quantitative information about titania nanostructures, the line cuts are fitted with the same model as described in section 5.1.2. From the data modeling, two titania domain radii (form factors) and the corresponding center-to-center distances (structure factors) are extracted for both samples and displayed in figure 7.4b and 7.4c. For the *small-pore* sample, the small-sized titania structures have a domain size of  $(3.9 \pm 0.1) \text{ nm}$  and a domain center-to-center distance of  $(23.5 \pm 0.2) \text{ nm}$ . According to equation 5.1, the pore size between small-sized structures is calculated to be  $(15.7 \pm 0.2) \text{ nm}$ . A characteristic domain size of  $(4.7 \pm 0.1) \text{ nm}$  and the corresponding center-to-center distance of  $(22.1 \pm 0.3) \text{ nm}$  are observed for the large-sized titania nanostructures, yielding a pore size of  $(12.7 \pm 0.3) \text{ nm}$ . For the *large-pore* sample, titania domain radii of  $(4.9 \pm 0.1) \text{ nm}$  and  $(7.2 \pm 0.1) \text{ nm}$  with center-to-center distances of  $(50.0 \pm 0.5) \text{ nm}$  and  $(54.0 \pm 3.1) \text{ nm}$  are extracted for the small- and larger-sized titania structures, respectively, which gives rise to the mesopore sizes of  $(40.2 \pm 0.5) \text{ nm}$  and  $(39.6 \pm 3.1) \text{ nm}$ . Compared to the results obtained from the PSD analysis of the SEM data, the center-to-center distances of both films obtained from



**Figure 7.4:** a) Horizontal line cuts obtained from the 2D GISAXS data for titania films with different pore sizes. The orange and blue curves represent the mesoporous small-pore and large-pore samples, respectively. The grey lines show the fits to the data. The curves are shifted along the intensity axis for clarity of the presentation. Extracted characteristic length scales: b) titania domain radii and c) corresponding center-to-center distance. Triangles indicate small-sized structure and circles indicate large-sized structure. The red crosses in c) are the center-to-center distances calculated from SEM images.

SEM and GISAXS evaluation are quite similar, suggesting that the surface morphology is reproduced within the bulk of the sample.

In general, it is found that both *small-pore* and *large-pore* titania films demonstrate ordered mesostructural arrays in the sample surface and inside the films. As intended, the average pore sizes on these two samples are different. The low molecular weight PS-b-PEO leads to smaller titania nanostructures and mesopores, while the bigger titania nanostructures and mesopores are present in the film using the high molecular weight polymer template.

### 7.1.3 Crystallinity of the titania template

Crystalline titania is crucial for photovoltaic applications as described in section 5.1.3. Crystalline information about the calcined *small-pore* and *large-pore* samples is obtained by XRD measurements, which are performed on a Bruker D8 ADVANCE X-ray diffractometer as described in section 3.1.5. Figure 7.5 shows the three XRD curves which are obtained from the calcined *small-pore* and *large-pore* samples, both being deposited on soda-lime glass substrates. Since glass is not crystalline, it does not give any diffraction peaks during the XRD measurements. All measured peaks are significantly discernible and can be identified as the anatase phase according to the reference data from the International Center for Diffraction Data (ICDD). Titania with an anatase structure is more favorable in photovoltaic application due to its high photoactivity [10]. Interestingly, both XRD curves are very similar in terms of having the same peak positions, the same peak widths and the same peak intensities, indicating that the crystalline phase, crystal size and the degree of crystallinity in both sample are very similar. This similarity signifies that titania crystallization is not influenced by the chain length of the template polymer. To obtain more quantitative information about the titania crystals, the (101) peaks of the respective XRD curves of both samples are fitted with Gaussian functions and analyzed using the Scherrer equation 2.30. This way, a crystal size of  $(7.7 \pm 0.1)$  nm for the *small-pore* sample and  $(7.9 \pm 0.3)$  nm for the *large-pore* sample are obtained. It is noteworthy that this is an average value of all crystals along the  $\langle 101 \rangle$  crystal direction present in the samples.

## 7.2 Dyed titania films backfilled with P3HT

Both mesoporous titania films are modified with the metal-free dye D149 as described in section 4.2.4. Detailed information about the dye molecules is given in section 4.1. Afterwards, the dyed mesoporous titania films are backfilled with P3HT to form the active layer of ssDSSCs. The backfilling procedure is described in section 4.2.4. The degree of P3HT infiltration determines the interface areas between titania and P3HT. The importance of the interface is explained in section 5.3. Cross sectional SEM measurements are applied to characterize the quality of P3HT backfilling. Figure 7.6 shows both the *small-pore* and *large-pore* films before and after P3HT infiltration. Before P3HT backfilling, a mesoporous nature of spong-like networks are present in the volume of both films (figure 7.6a and 7.6c). But the mesopore sizes are different, which is in line with the GISAXS results. After P3HT backfilling, a rather good infiltration for both films is observed (figure 7.6b and 7.6d). P3HT is an essential part of the active layer as it is the

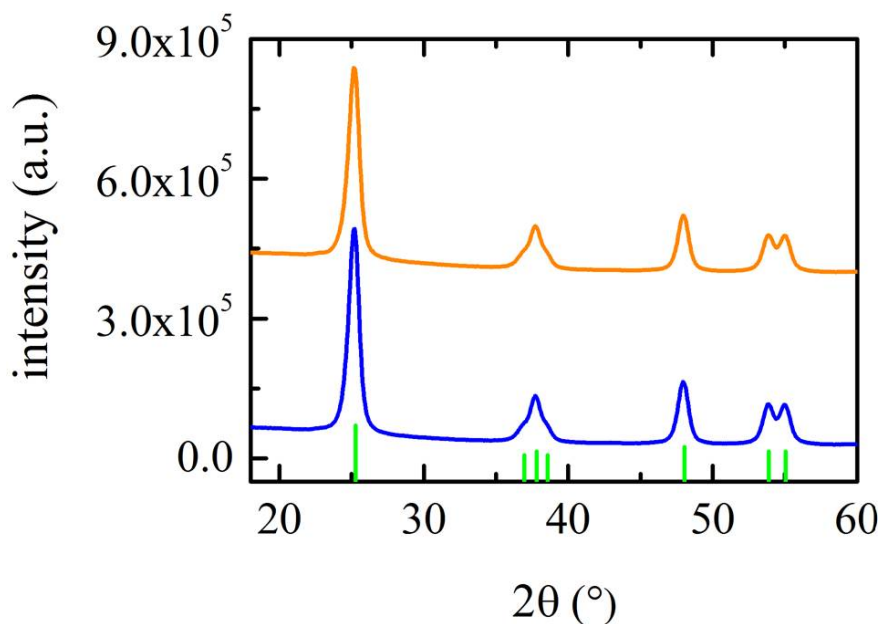


**Figure 7.5:** XRD patterns of the mesoporous titania films. Orange and blue curves represent the mesoporous small-pore and large-pore samples, respectively. Both curves are shifted along the y axis for clarity of the presentation. Green vertical bars represent reference peaks for anatase  $\text{TiO}_2$  taken from The International Centre for Diffraction Data (ICDD).

medium for the positive charge carrier transport, which plays a crucial role in the device performance. The capacity of the positive charge carrier transport is closely related to P3HT crystallinity. Therefore the P3HT crystalline order is of great interest. Grazing incidence wide-angle x-ray scattering (GIWAXS) measurements are performed on these active layers to investigate P3HT crystalline properties like lattice distances or crystal sizes. Moreover, to link it to the stability of the photovoltaic performance of ssDSSCs, the evolution of P3HT crystalline order under continuous light illumination are studied via in situ GIWAXS. GIWAXS is a powerful technique to characterize polymer crystallization. The measurements are carried out at the Elettra SAXS beamline as described in section 3.1.6. An incident angle of  $0.56^\circ$  and a sample-detector distance of 252 mm are chosen for the GIWAXS measurements.

### 7.2.1 P3HT crystallization inside the titania mesopores

In order to retrieve the corrected reciprocal space patterns, a number of appropriate corrections, including solid-angle correction, q-reshaping and conversion, efficiency correction and polarization correction, are applied to the raw 2D GIWAXS data with the aid of the software GIXSGUI. These corrections are discussed in detail in elsewhere [90]. The corrected 2D GIWAXS data of the *small-pore* and *large-pore* active layers are displayed



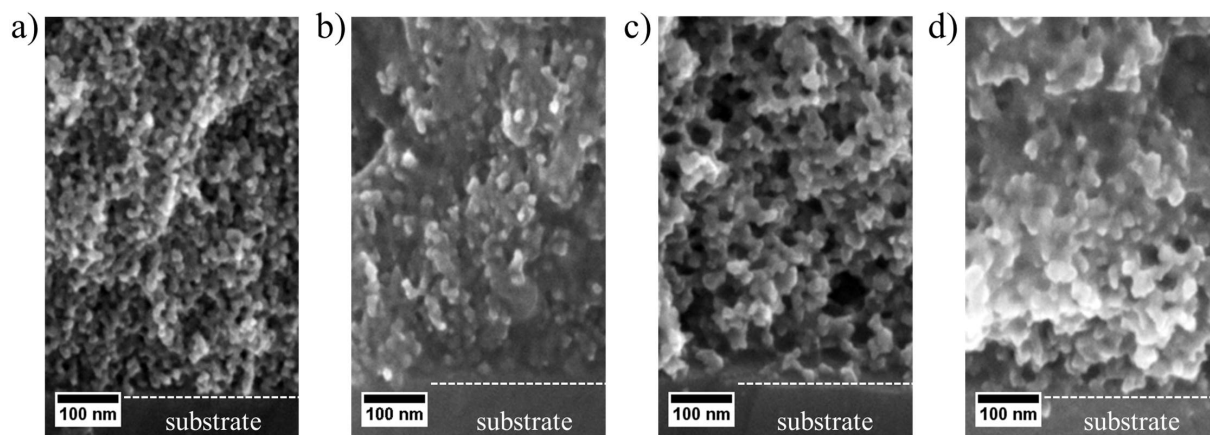


**Figure 7.6:** 2D GIWAXS data. a) A small-pore mesoporous titania film, b) a dyed small-pore film backfilled with P3HT, c) a large-pore mesoporous titania film, and d) a dyed large-pore film backfilled with P3HT.

in figure 7.7. For both samples there is a peak at  $q \approx 4 \text{ nm}^{-1}$  mainly in the vertical direction, which is assigned to (100) lattice plane of the P3HT crystals. The P3HT (010) peak is located at  $q_z \approx 18 \text{ nm}^{-1}$ , which is overlapped with the (101) crystalline order of the titania anatase phase ( $q = 17.85 \text{ nm}^{-1}$ ). The 2D GIWAXS data show the existence of P3HT and anatase titania crystals in both samples. Moreover, (100) peaks are clearly observed in the vertical direction, indicating an edge-on dominated orientation of P3HT. The  $\text{TiO}_2$  (101) peaks smear out into Debye-Scherrer rings, elucidating that anatase crystals are presented in the films in an orientational disorder. This result is in agreement with the XRD measurements where no preferential orientation is observed for the  $\text{TiO}_2$ .

To obtain quantitative information about the P3HT crystalline order, radially-integrated cuts are performed on the corrected 2D GIWAXS data using an angular range from  $5^\circ$  to  $15^\circ$ . The cuts for both active layers are shown in figure 7.8. It has to be mentioned at first that the intensities of the same peaks obtained from both active layers cannot be compared as the intrinsic difference might exist between the samples like film thickness and amount of material. In both active layers the (100) peaks in the vertical direction are the dominant scattering signal, which indicates a predominantly edge-on orientation of the P3HT crystal. The (100) peak acts as a good indicator of the polymer crystallinity and is chosen to parametrize the P3HT crystallites. It is noteworthy that the P3HT capping layer is negligible in this work as it is very thin with a thickness of a few nanometers, as shown in figure 7.9. Therefore, the signal of diffuse scattering mainly originates from the P3HT inside titania mesopores, which might give insight that whether the key P3HT crystalline properties are influenced by different titania pore sizes. From figure 7.7, it is noticeable that the (010) peak in the vertical direction is not accessible, which is another

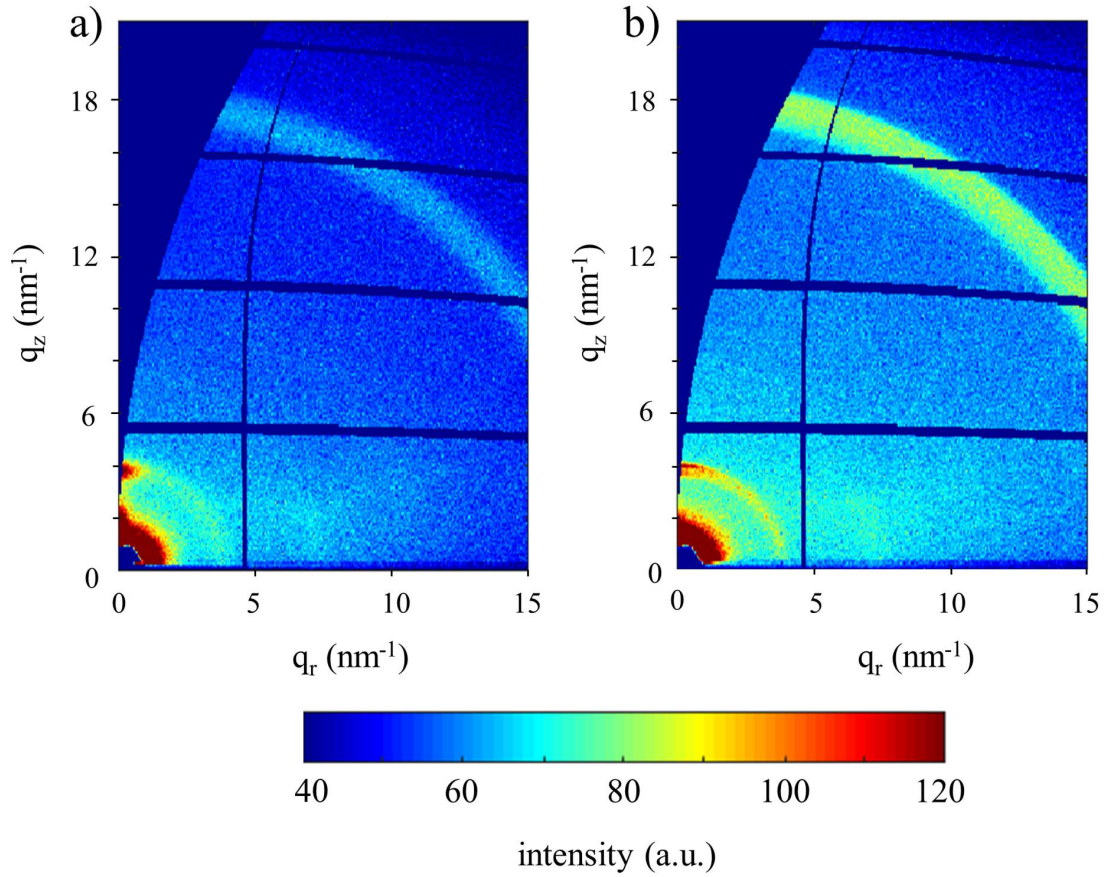


**Figure 7.7:** 2D GIWAXS data of the a) small-pore mesoporous titania film and of the b) large-pore mesoporous titania film. The intensity scale for the scattering signal is shown at the bottom of the images. The circular black area at the lowerleft corner is the beamstop for the transmitted beam. The horizontal black stripe at  $q_z \approx 5.5 \text{ nm}^{-1}$ ,  $q_z \approx 11.2 \text{ nm}^{-1}$ ,  $q_z \approx 15.8 \text{ nm}^{-1}$  and  $q_z \approx 20.5 \text{ nm}^{-1}$ , and the vertical one at  $q_r \approx 4.7 \text{ nm}^{-1}$  correspond to the inter-module gaps of the used detector.

reason why only the (100) peaks in the vertical direction are chosen for the analysis of P3HT crystallinity.

For analysis both cuts are modeled with Gaussian functions as shown in figure 7.8 (grey curves). From data modeling, the amplitude,  $q$  position and mean crystal size of the P3HT crystals in  $\langle 100 \rangle$  direction are extracted. Here, the crystal size is obtained via the full-width-at-half-maximum (FWHM) and the Scherrer equation under the assumption of constant paracrystallinity. For the *small-pore* active layer, the P3HT (100) peak located at  $q \approx 3.84 \text{ nm}^{-1}$  gives the strongest intensity. According to equation 7.1 the polymer backbone spacing is calculated to be 1.64 nm and the average crystal size is calculated to be around 9.4 nm. The values are in line with the previous observations of P3HT crystals in P3HT:[6,6]-phenyl-C61-butyric acid methyl ester (P3HT:PCBM) blend systems [249,250],

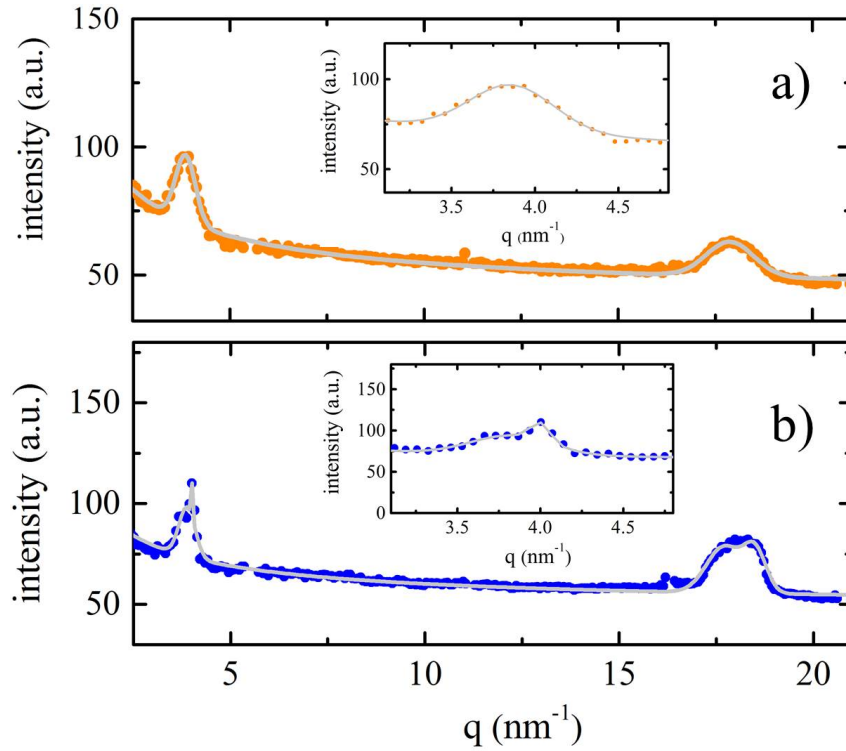


**Figure 7.8:** Vertical sector integrals obtained from the corrected 2D GIWAXS data for both active layers. The orange and blue curves in a) and b) represent the small-pore and large-pore samples, respectively. The grey lines are the fits to the data. The curves are shifted along the intensity axis for clarity of the presentation. In the insets of a) and b), a zoom-in of the region between  $q = 3.1 \text{ nm}^{-1}$  and  $q = 4.8 \text{ nm}^{-1}$  to stress the presence of two (100) peaks in the large-pore samples.

meaning that P3HT crystallization inside small mesopores behaves similarly to that in P3HT:PCBM films. For the *large-pore* active layer, two (100) peaks are observed as shown in figure 7.8b. The one located at  $q \approx 3.84 \text{ nm}^{-1}$  is denoted as the first (100) peak, and the other on at  $q \approx 4.05 \text{ nm}^{-1}$  is referred as the second (100) peak. These two (100) peaks indicate the existence of two types of P3HT crystals inside the large mesopores, which is distinctly different from the *small-pore* active layer. A similar observation of P3HT polymorphism is found in the P3HT:PCBM system with cyclohexanone as solvent additive after thermal annealing [251]. The polymer backbone spacing of 1.64 nm and crystal size of about 10.0 nm are obtained for the first (100) peak, which is similar to the counterpart in the *small-pore* active layer. While for the second (100) peak denser polymer backbone spacings of about 1.55 nm and much larger crystals of about 38.3 nm are found. The crystal size is almost the same size as the pore size of the *large-pore* titania film, indicating a single P3HT crystal nearly fills one mesopore completely. However, from fitting it is noted that the second (100) peak possesses only 20% the intensity of the first

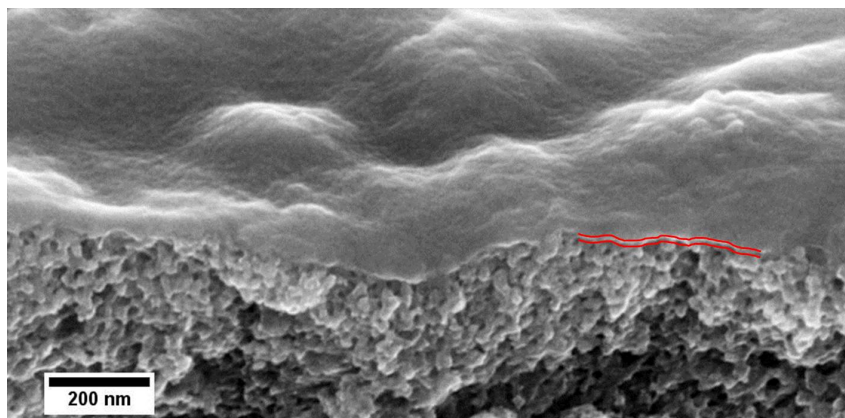


**Figure 7.9:** Cross-section SEM image of the small-pore active layer. The P3HT capping layer is highlighted by the area between red curves.

(100) peak, indicating that the volume fraction of the crystal causing the second (100) peak is much lower than for the first (100) peak.

In general, the backfilled P3HT crystalline order is greatly influenced by the titania pore size. Both active layers possess one type of crystals with polymer backbone spacing of 1.64 nm and crystal size of about 10.0 nm, whereas a second type of crystals only exists in the *large-pore* active layer with denser backbone spacing and larger crystal size.

### 7.2.2 Temporal evolution of the P3HT crystalline order

As known, the use of a solid and stable titania network allows to stabilize P3HT in terms of domain size. The change of P3HT domain size has been verified to result in the drop of short-circuit current density ( $J_{sc}$ ) in P3HT:PCBM organic solar cells [80], which can be canceled out in this work as the P3HT domains contributing to the current generation are confined by the titania scaffold. Therefore, the change of P3HT crystallization over time is the only reason for the change of final device performance from a morphological perspective. In order to track the evolution of the P3HT crystallization under continuous AM1.5 solar illumination, in situ GIWAXS measurements are performed on the *small-pore* and *large-pore* active layers which are built on glass substrates. The whole in situ measurements last for 30 min, and each GIWAXS frame is acquired with a measuring time of 3 s. Thus in total 600 frames are recorded. The vertical integral and analysis for each frame are obtained by the same method as described in section 7.2.1. The amplitude,  $q$  position and mean crystal size as a function of illumination time are extracted from data modeling for both active layers and plotted in figure 7.10. For the *small-pore* active layer, the (100) peak position and peak FWHM remain constant over time, whereas the

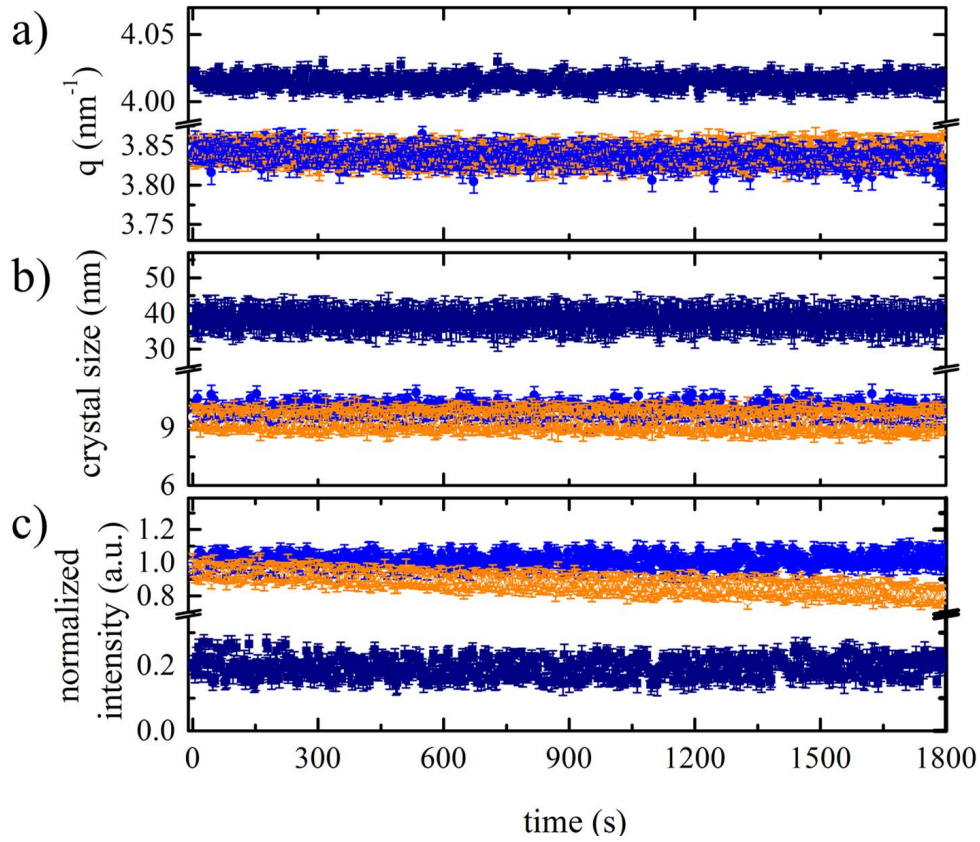


**Figure 7.10:** Temporal evolution of a)  $q$ -position, b) crystal size and c) Bragg peak amplitude obtained from fits of (100) P3HT peaks under continuous solar illumination for 30 min. Orange hollow circles represent the small-pore active layer, blue solid circles and dark blue solid rectangles represent the first and second (100) peaks of the large-pore active layer, respectively. In c), for the small-pore sample, the intensities are normalized to its initial peak intensity, while all intensities are normalized to the initial intensity of the first (100) peak for the large-pore sample.

peak intensity decreases gradually under 30 min solar illumination. A constant (100) peak position indicates the polymer backbone spacing is unchanged, remaining at 1.64 nm with illumination. The average crystal size is unchanged as well at 9.4 nm as the size change merely on the order of 0.5 nm even smaller than the error bar given in Figure 7.10b. The decrease of the (100) peak intensity over time indicates a decrease of the volume fraction of crystalline regions in the sample. For the *large-pore* active layer, all the parameters extracted from either the first or the second (100) peak are stable over time. Similar to the *small-pore* active layer, the distance between adjacent P3HT backbones and crystal size for both types of P3HT crystals are unchanged. In detail, for the first (100) peak the polymer backbone spacing remains constant at 1.64 nm and crystal size is unchanged at 10.0 nm. For the second (100) peak these two parameters are stable at 1.55 nm and 38.8



nm, respectively. The stable intensities of both first and second (100) peaks mean that the volume fraction of P3HT crystalline regions does not reduce over time and also rules out potential radiation damage in our study. Moreover, the intensity ratio of the first and second (100) peak does not change either, indicating the volume fraction of both types of P3HT crystals always constant.

In general, the stability of the backfilled P3HT crystalline order is closely related to mesopore size. The P3HT inside the large titania pores is more stable than inside the small pores in terms of the volume fraction of P3HT crystalline regions.

### 7.3 Temporal evolution of photovoltaic performance

The *small-pore* and *large-pore* active layers are sandwiched between fluorine-doped tin oxide (FTO) and gold electrodes to complete the full ssDSSCs. In order to avoid direct contact between the active layer and two electrodes, a thin compact titania layer (about 100 nm) is inserted between FTO and active layer as a hole-blocking layer, and a capping P3HT layer was introduced by spin-coating of a P3HT solution on top of the active layer acting as an electron blocking layer. The implemented solar cell layout is:

$$\text{glass/FTO/compact-TiO}_2/\text{active layer/P3HT/Au}$$

The used materials in fabricating ssDSSCs are described in detail in section 4.1. The detailed steps of solar cell assembly is given in section 4.2.4.

In order to test the stability of ssDSSCs, two types of ssDSSCs are measured under simulated AM1.5 G illumination for 30 min. Current-voltage ( $I$ - $V$ ) curves of the *small-pore* and *large-pore* solar cells with best performance are compared in figure 7.11. From  $I$ - $V$  curves, related photovoltaic parameters such as power conversion efficiency ( $PCE$ ), short-circuit current density ( $J_{sc}$ ), open-circuit voltage ( $V_{oc}$ ), and fill factor ( $FF$ ) can be extracted as described in section 3.2.3. A  $J_{sc}$  of  $6.72 \text{ mA cm}^{-2}$ , a  $V_{oc}$  of  $0.74 \text{ V}$  and a  $FF$  of  $47 \%$  give rise to a  $PCE$  of  $2.32 \%$  for the *small-pore* cell, while the *large-pore* solar cell performs slightly better with a  $J_{sc}$  of  $7.31 \text{ mA cm}^{-2}$ , a  $V_{oc}$  of  $0.71 \text{ V}$ , a  $FF$  of  $58 \%$  and a  $PCE$  of  $2.95 \%$ . This  $PCE$  value is among the best reported values for ssDSSCs. The higher  $PCE$  in the *large-pore* device mainly originates from the enhancement of  $J_{sc}$  and  $FF$  as compared to the *small-pore* cell. The enhancement may be due to the existence of large P3HT crystals in the *large-pore* active layer as larger crystals give rise to a higher mobility of positive charge carriers which reduces geminate-pair recombination [18]. The  $V_{oc}$  of both cells is similar, indicating  $V_{oc}$  is not influenced by the pore size of titania photoanodes.

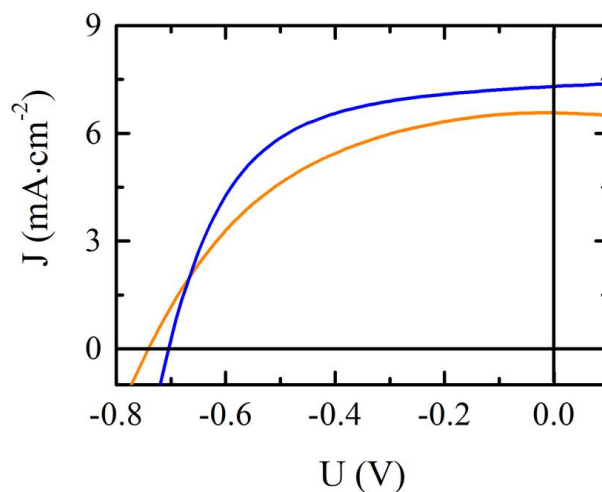


**Figure 7.11:** *I-V curves of the small-pore (orange) and large-pore (blue) ssDSSCs with the best performance.*

Figure 7.12 shows the temporal evolution of photovoltaic parameters for both devices under ambient working conditions. All the parameters are normalized to their initial values. For both cells, the  $V_{oc}$  drops gradually over time. Many accounts in literature have reported that  $V_{oc}$  in ssDSSCs is strongly influenced by dye molecules in terms of light-harvesting ability or  $\text{TiO}_2$  surface modification [252,253]. Additionally, dye molecules degrade via oxidation and reductive processes under light illumination [254–256]. Therefore, it is believed that the  $V_{oc}$  decay in ssDSSCs is directly related to the dye degradation. The degradation of the dye D149 used in the present work is investigated. Figure 7.13 shows the UV/Vis absorption spectra of the dye-adsorbed *small-pore* and *large-pore* samples with different illuminating times. The UV/Vis absorption peaks at around 385 nm and 525 nm smear out with continuous solar illumination for both dye-adsorbed *small-pore* and *large-pore* titania films, indicating the decreased ability of dye molecules for light harvesting. To quantify the dye degradation, the UV/Vis absorbances of each sample are integrated in the range from 300 nm to 700 nm. For both samples, the obtained integrated absorbances are normalized to their own initial values which are measured without solar illumination and plotted in figure 7.12a and 7.12b, respectively. It is noted that the downtrend of dye absorbance matches the  $V_{oc}$  decay quite well for both *small-pore* and *large-pore* samples, indicating that the  $V_{oc}$  decrease is mainly caused by the dye degradation in light harvesting in the first 30 min. Instead of continuous decrease, the  $J_{sc}$  of both cells increases in the initial tens of seconds and then decrease over measuring time. The growth of  $J_{sc}$  in the initial stage is due to the light soaking effect which improves the electron lifetime significantly [257]. After slight increase, the  $J_{sc}$  in the *small-pore* cells, then, drops faster than in the *large-pore* cells. As can be seen for figure 7.12b, the

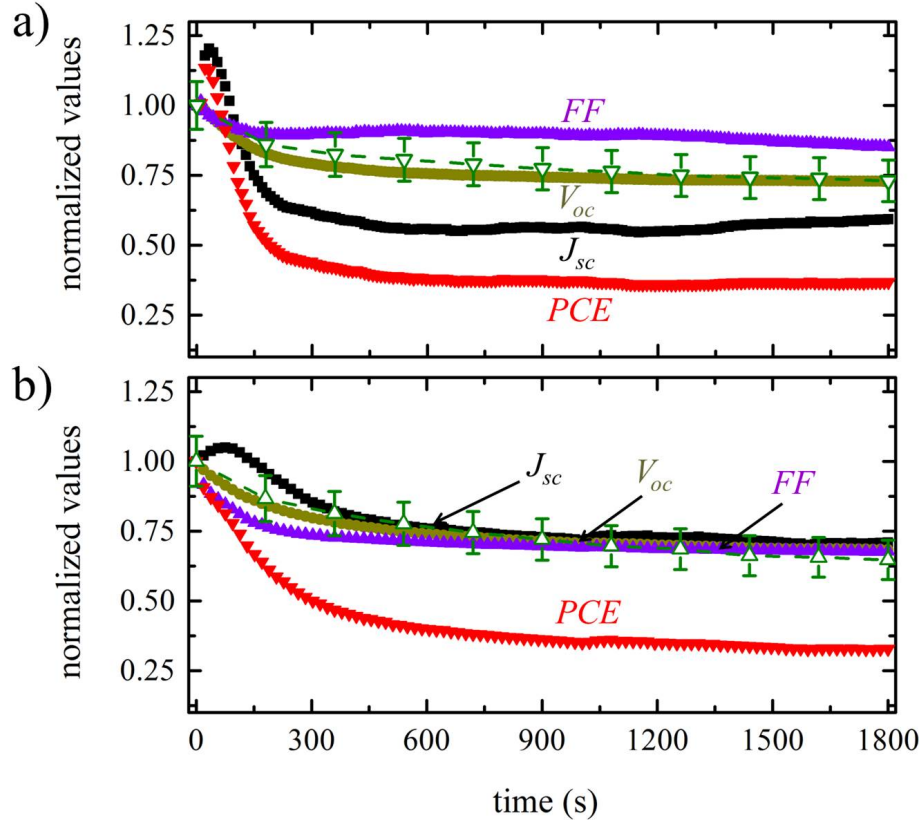


**Figure 7.12:** Temporal evolution of  $J_{sc}$  (black),  $V_{oc}$  (dark yellow),  $FF$  (violet) and  $PCE$  (red) for a) the small-pore and b) large-pore ssDSSCs, respectively. The hollow green triangles in a) and b) represent the temporal evolution of integrated absorbance for the dye-adsorbed small-pore and large-pore titania films, respectively. All the parameters are normalized to their initial values.

similar decrease tendency of  $J_{sc}$  and dye are presented after 300 s, it is believed that the dye degradation is also the main reason for  $J_{sc}$  decay in the *large-pore* cells. For the *small-pore* cells, the drop for  $J_{sc}$  is more than for dye absorbance after 300 s, meaning that some other factors contribute to  $J_{sc}$  decay, besides the contribution from dye degradation. From GIWAXS and in-situ GIWAXS measurements, the absence of large P3HT crystals and the decrease of the volume fraction of P3HT crystalline regions may result in a stronger  $J_{sc}$  decay. In contrast,  $FF$  decreases slower in the device with small pores than in the *large-pore* solar cells. The decrease of  $J_{sc}$ ,  $V_{oc}$  and  $FF$  together results in the  $PCE$  reduction for both photovoltaic devices.



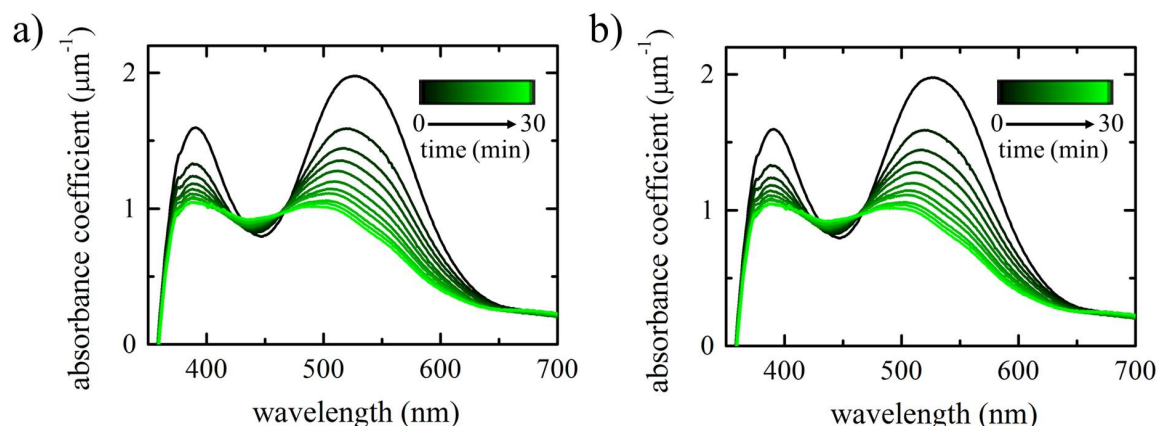


**Figure 7.13:** UV/Vis absorption spectra of a) dye-adsorbed small-pore and b) dye-adsorbed large-pore titania films. The data are recorded every 3 min during solar illumination as indicated with the used color code.

## 7.4 Summary

Titania films are fabricated via polymer-template-assisted sol-gel synthesis. By using PS-*b*-PEO with different molecular weights as structure directing agents, two different pore sizes are achieved. In short, the use of the binary azeotrope of toluene and 1-butanal as a good-poor solvent pair results in ordered mesopore arrays in the titania film. The simultaneous evaporation of the binary azeotrope gives a constant driving force of polymer self-assembly during the whole drying process, which is able to reserve polymer micellar structures very well. The details are given in section 2.2.3 and section 4.2.2. A binary azeotrope used as good-poor solvent pair has been also reported by Guldin et al., who demonstrated an ordered mesopore array over the surface of titania films by employing poly(isoprene-block-ethylene oxide) (PI-*b*-PEO) as templates [247]. Moreover, this paper also showed that the pore size and porosity can be tuned efficiently by varying the weight ratio of titania and polymer template. The low molecular weight of polymer template leads to small mesopores and titania structures, whereas the PS-*b*-PEO with longer chains gives rise to large mesopores and titania structures. The size differences confirm that the pore size and titania-nanostructure size can be tuned by changing the chain length of polymer template. A similar observation has been found in literature [12], where the different molecular weight of PI-*b*-PEO lead to different titania pore sizes.

The XRD measurements verify the presence of anatase phase in both mesoporous titania films after 500 °C calcination. Moreover, it is found that the titania crystallization is not influenced by the molecular weight of the polymer template as XRD curves of both sample are very similar.

After P3HT backfilling, the crystalline order of the conducting polymer is studied using GIWAXS measurements. It is found that titania pore sizes have a strong impact on P3HT crystalline behavior. Two types of P3HT crystals are observed in the *large-pore* active layers, while only one type exists in the *small-pore* active layers. Polymorphism has been frequently observed in crystalline polymers under the confinement inside mesopores [258, 259]. With respect to the size, P3HT crystals are larger in the *large-pore* active layers than in the *small-pore* active layers. Moreover, in situ GIWAXS measurements shows that under 30 min solar illumination P3HT inside large titania mesopores is more stable than inside small pores in terms of lattice constants, crystal sizes and volume fraction of crystalline regions.

The ssDSSCs are assembled based on the *small-pore* and *large-pore* active layers and tested continuously under AM1.5G solar illumination. The result shows that the  $V_{oc}$  loss of both cells is mainly caused by the dye degradation. In the *large-pore* solar cell, the reduction in light harvesting of dye molecules is the main reason for the  $J_{sc}$  decay as well. For the *small-pore* device, the combined effect of the dye degradation, the decreased P3HT crystallinity and the absence of large P3HT crystals contributes a faster  $J_{sc}$  decrease. It is the first time to observe the correlation between P3HT crystalline structure and device performance of P3HT-based ssDSSCs. The pore size of titania photoanodes greatly impacts the performance and stability of P3HT-titania based ssDSSCs.

## 8 Low temperature synthesis of hierarchically structured titania films

Parts of this chapter have been published in the article: A low temperature route toward hierarchically structured titania films for thin hybrid solar cells [51] (L. Song et al., *Adv. Funct. Mater.*, 26, 7084–7093, 2016, DOI: 10.1002/adfm.201603867).

Since the prototype of dye-sensitized solar cells (DSSCs) was firstly put forward by O'Regan and Grätzel in 1991 [153], titania-based solar cells have been extensively studied due to their potential for low cost, ease of manufacturing processes and high solar power conversion efficiency (PCE) [102, 107, 192, 216, 217, 226, 260–262]. Nevertheless, the leakage and corrosion problems of conventional liquid electrolytes are widespread in DSSCs, which motivates research groups to develop new hole-transport materials (HTMs) to replace the liquid electrolyte [263–265]. Many titania-based solar cells with solid-state HTMs, ranging from all-solid-state DSSCs (ssDSSCs) to hybrid solar cells, have received considerable attention [266–270]. Particularly, hybrid solar cells have been the focus of an increasing interest due to high demand for devices with low cost, light weight, flexible design and facile production [271–274]. Hybrid solar cells are dye-free in the device configuration and only consist of n-type semiconductors like  $\text{TiO}_2$  and conjugated polymers like poly(3-hexylthiophene) (P3HT). In hybrid solar cells, incoming light is absorbed by the conjugated polymers instead of sensitizing dyes. Upon light excitation, conjugated polymers inject electrons into the conduction band of the n-type semiconductor. Thus, the conjugated polymer in hybrid solar cells is the charge carrier generator and the positive charge carrier transport material. As charge generation only occurs at the interface of n- and p-type semiconductors, the mesoporous titania nanostructures are very suitable for the photoanodes of hybrid solar cells due to the n-type semiconductor nature with a very high surface-to-volume ratio [109]. Great progress has been made for the development of hybrid solar cells using mesoporous titania nanostructures as the photoanode and P3HT as the light harvester and the photocathode [133, 189, 275]. For titania photoanodes, a high-temperature calcination step (typically above 400 °C) usually is required to

crystallize  $\text{TiO}_2$  as a crystalline phase of titania is more favorable for photovoltaic applications [10, 41, 276, 277]. However, it's impossible to involve a high-temperature process in the fabrication of lightweight and flexible solar cells. For this kind of photovoltaic devices, the substrate for supporting the active layer usually is a transparent polymer thin foil such as a poly(ethylene terephthalate) (PET) or polyethylene naphthalate (PEN) foil, which are not heat-resistant. In addition, a reduction of the synthesis temperature is beneficial in reducing production costs and energy consumption, shortening pay-back times and lowering environmental impact of solar cells.

Up to now, different approaches to synthesize crystalline titania at low temperatures have been explored, such as non-hydrolytic sol-gel synthesis [278], fast and slow hydrolysis routes [279], use of inorganic precursors [280], and solvothermal method [281]. However, these methods result in the precipitation of titania nanorods or nanoparticles in the solution. To meet the demand of mesoporous titania films, the premade nanorods or nanoparticles require mixing with particular binders and pore forming materials to form titania pastes, which can be deposited on the substrate via doctor-blading [120]. Binders are used to connect individual nanorods or nanoparticles and to make them stick to the substrate. Pore forming materials are used to create mesopores in the resulting titania films. To obtain pure mesoporous titania films, removing the binders and pore forming materials is necessary but implies a great challenge at low temperatures. As an alternative, a novel sol-gel approach is established to fabricate mesoporous titania films at low temperatures in this work. In this route, a special titania precursor, ethylene glycol-modified titanate (EGMT), is used, which can crystallize during the sol-gel process. Polystyrene-block-polyethylene oxide (PS-*b*-PEO) is used as polymer template, which is sacrificed after film deposition to create mesopores.

Although considerable efforts have been made concerning titania based hybrid solar cells, to date, the performance of most devices cannot compete with ssDSSCs. The reported power conversion efficiencies (*PCEs*) of hybrid solar cells are still lower than 1 % even with high-temperature processed  $\text{TiO}_2$  photoanodes [189, 261, 275, 282, 283]. To obtain more efficient titania photoanodes thereby better photovoltaic performance, artificial superstructures in sub-micrometer length scales are introduced to mesoporous titania films as it has been shown in several studies that the structured  $\text{TiO}_2$  could enhance light harvesting [284–288]. Many research groups have reported on the production of hierarchical structures. For example, Yang et al. introduced well-defined microchannel networks to porous oxides for use as materials in the fields of advanced catalysts, sensors, optoelectronics, and integrated photonic crystal devices [289]. Chou et al. demonstrated 83 % improvement in the overall *PCE* for the case of hierarchically structured ZnO films with primary nanoparticles and secondary colloidal spheres [290]. Kaune et al. showed the

reduction of light reflection in hierarchically structured titania films with various pore sizes from nanometer to micrometer length scales [146]. The hierarchical structures offer multifunctionality to the produced films. Currently, patterning mesoporous titania films with well-defined structural order on larger length scales has received great attention in many different applications [291–294]. Amongst the different concepts, imprinting mesoporous films with nano-imprint lithography (NIL) is of great interest in fabrication of titania films with hierarchical structures [295–300]. NIL, also referred to as soft-embossing [301–303], allows fabricating well-defined structural order over multiple length scales with low cost, high throughput and high resolution. Moreover, the NIL can be done below 150 °C, offering a great potential for targeting low-temperature fabrication.

A novel approach of fabricating hierarchically structured titania thin films at low temperatures is developed in this work. The approach relies on polymer-template assisted sol-gel synthesis in combination with NIL processing. EGMT is used as titania precursor, which allows tuning the crystal phase of titania via changing the pH-value and has been applied successfully to the fabrication of nanostructured titania thin films [92, 93, 95, 96]. The hierarchically structured titania films produced at low temperatures are described and compared to results of films without artificial superstructures (denoted as original titania films) in the first part of this chapter (section 8.1). The sol-gel-synthesized titania/PS-b-PEO composite films are imprinted using NIL technique and subsequently the polymer template is removed by UV irradiation and a chlorobenzene bath. The entire process is schematically illustrated in section 8.1.1. The surface morphology of the imprinting master and imprinted titania films is studied in section 8.1.2 with atomic force microscopy (AFM) and scanning electron microscopy (SEM). This is followed by an inner morphology study using grazing-incidence small-angle x-ray scattering (GISAXS) measurements in section 8.1.3. The hierarchical titania films are backfilled with P3HT to form the active layer of hybrid solar cells (section 8.2), the active layer morphology is investigated in section 8.2.1. Section 8.2.2 depicts the investigations on optical properties of the active layer. In the end, hybrid solar cells with hierarchical titania photoanodes are made to give a proof of practicability (section 8.3).

## 8.1 Film before and after polymer-template extraction

The titania nanostructures studied in this chapter are prepared by the low-temperature sol-gel synthesis with EGMT as described in section 4.2.2. The used amount of reactants is listed in table 8.1. After 20 h aging, the sol-gel solution is spin coated onto different substrates as described in section 4.2.3. Silicon substrates are used for SEM and GISAXS

measurements, glass substrates for UV-vis measurements, and FTO/compact-TiO<sub>2</sub> substrates for solar cell fabrication. The substrate cleaning and preparation is explained in section 4.2.3 and section 4.2.4.

component	EGMT	HCl	N,N-dimethylformamide	PS-b-PEO
amount	100 mg	171 $\mu$ L	2.12 mL	100 mg

**Table 8.1:** *The composition details of the sol-gel synthesis.*

For imprinting, a master with a pillar pattern of 200 nm width, 200 nm length and 90 nm height and of a periodicity of 400 nm is used in this work. The manufacturing technique is described in detail in section 4.2.5.

### 8.1.1 Fabrication routine of hierarchical titania nanostructures

A workflow description is schematically illustrated in figure 8.1 for producing the active layer with hierarchical structured titania photoanodes. After aging, the sol-gel solution is deposited on a silicon or glass or FTO/compact-TiO<sub>2</sub> substrate by spin coating (figure 8.1a). In this step, the nano titania species are embedded in the PEO matrices, and the titania/PS-b-PEO composite film is gained (figure 8.1b). Due to the presence of the diblock copolymer scaffold, the composite film has a certain pliability compared to a purely inorganic titania film. This pliability allows embossing precise superstructures into the composite film during the imprinting step. The artificial superstructures are introduced onto the composite film by the NIL process, which is performed at an Obducat NIL-2.5 instrument for 10 min at an elevated temperature of 120 °C and a pressure of 30 bar, as shown in figure 8.1c. The applied temperature is slightly higher than the glass transition temperature of the polymer, thus the composite film is softened. Under the high pressure, the softened composite films is forced into the cavities of the relief structure of the used master stamp. After 10 min, the whole system is cooled down to 60 °C to lift off the master. This temperature is lower than the glass transition temperature of PS blocks and the crystal melting temperature of PEO blocks, thus the patterned composite films hardens in the cooling-down process. After master demolding, the inverse replica of the master mold structures is transferred to the composite film and the artificial superstructures are constituted (figure 8.1d). Afterwards, the composite film undergoes continuous UV irradiation for 24 h to remove the PS-b-PEO template as shown in figure 8.1e. After UV exposure, the obtained mesoporous titania films with artificial superstructures are soaked in chlorobenzene for 60 min (figure 8.1f). The soaking process serves two functions. The first is to remove residual template polymer after the UV treatment since chlorobenzene

is a good solvent for PS-*b*-PEO as well. The other is to enhance infiltration ability of the hole-transport polymer as chlorobenzene is the host solvent of P3HT [183]. Therefore, the steps of figure 8.1e and 8.1f are denoted as polymer extraction as both have the effect of polymer removal. After the soaking process, the pure mesoporous titania film with NIL pattern is achieved (figure 8.1h). Finally, P3HT is spin coated on top of the superstructured mesoporous titania film to form the active layer of hybrid solar cells (figure 8.1g). The filling degree of P3HT into the hierarchical structured titania film is of crucial importance for photovoltaic device performance as charge carrier can only be generated at the interface of titania and P3HT [183].

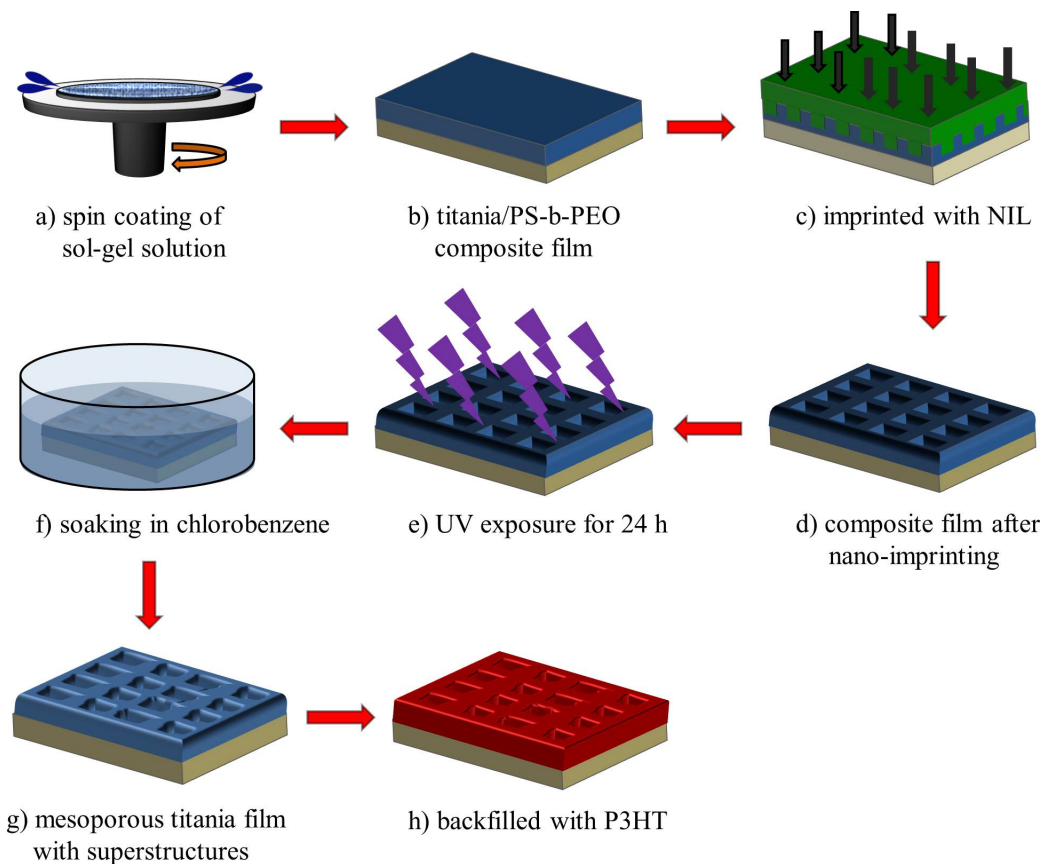


**Figure 8.1:** Schematic illustration of nano-imprinted active layers. a) The prepared sol-gel solution is deposited via spin coating. b) The spin coated titania/PS-*b*-PEO composite film (dark blue) on a silicon or glass or FTO/compact-TiO<sub>2</sub> substrate (tan). c) The composite film is patterned with NIL at an elevated temperature of 120 °C (indicated by light tan substrate) and a pressure of 30 bar (indicated by black arrows). d) Inverse master structures are transferred to the composite film. e) UV irradiation is used to remove the polymer template. f) Soaking of the film in chlorobenzene for 60 min. f) Mesoporous titania films with artificial superstructures after polymer extraction. g) Hierarchical structured titania films backfilled with P3HT to form active layer.

### 8.1.2 Surface morphology

Figure 8.2a shows an AFM image of the surface of the master used in the NIL process. It shows a regular arrangement of uniform nano-pillars, which have a size of  $200\text{ nm} \times 200\text{ nm}$  and a lattice period of  $400\text{ nm}$ . Figure 8.2b is an AFM topographic height profile of the nano-pillars that is extracted from Figure 8.2a. The data shows that the nano-pillars have an average height of about  $90\text{ nm}$ .

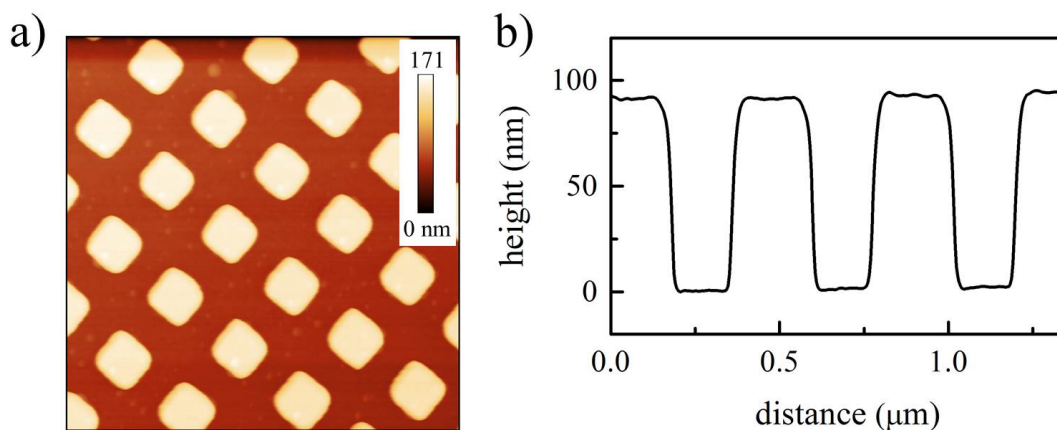


**Figure 8.2:** Master for nano-imprinting: a) AFM topography of the imprint master. The size is  $2 \times 2\text{ }\mu\text{m}^2$  and b) corresponding height profile.

This type of master is used as pattern source for nano-imprinting on the titania/PS-b-PEO composite films. After NIL process, the surface morphology of the resulting nano-imprinted composite films is characterized with SEM and AFM measurements. Figure 8.3a illustrates plan-view SEM images at a low magnification. It shows that a highly ordered square pitch-like lattice superstructure are present in the nano-imprinted composite, suggesting a successful nano-imprinting process. Figure 8.3b is a close-up of Figure 8.3a, which is taken at a high magnification. From this image, the size of  $200\text{ nm} \times 200\text{ nm}$  and the periodicity of  $400\text{ nm}$  for the pitch-like structures is observed, which corresponds to the negative replica of the master mold structure. The success of NIL process is confirmed by AFM measurements as well. Figure 8.3c shows the similar superstructure array with the figure 8.3a. To obtain depth information of the pitch-like structures, the height profile is extracted from the AFM images and the result is displayed in figure 8.3d. The pitch depth is around  $90\text{ nm}$ , which is the same value as for the height of mater nano-pillars, suggesting a complete transfer of the stamp relief structures into the composite films. In order to obtain mesoporous nanostructures of pure titania, the PS-b-PEO template must be removed from the nano-imprinted composite films. For tar-



getting low-temperature fabrication, the removal of polymer template is achieved by UV irradiation and chlorobenzene treatment rather than high-temperature calcination.

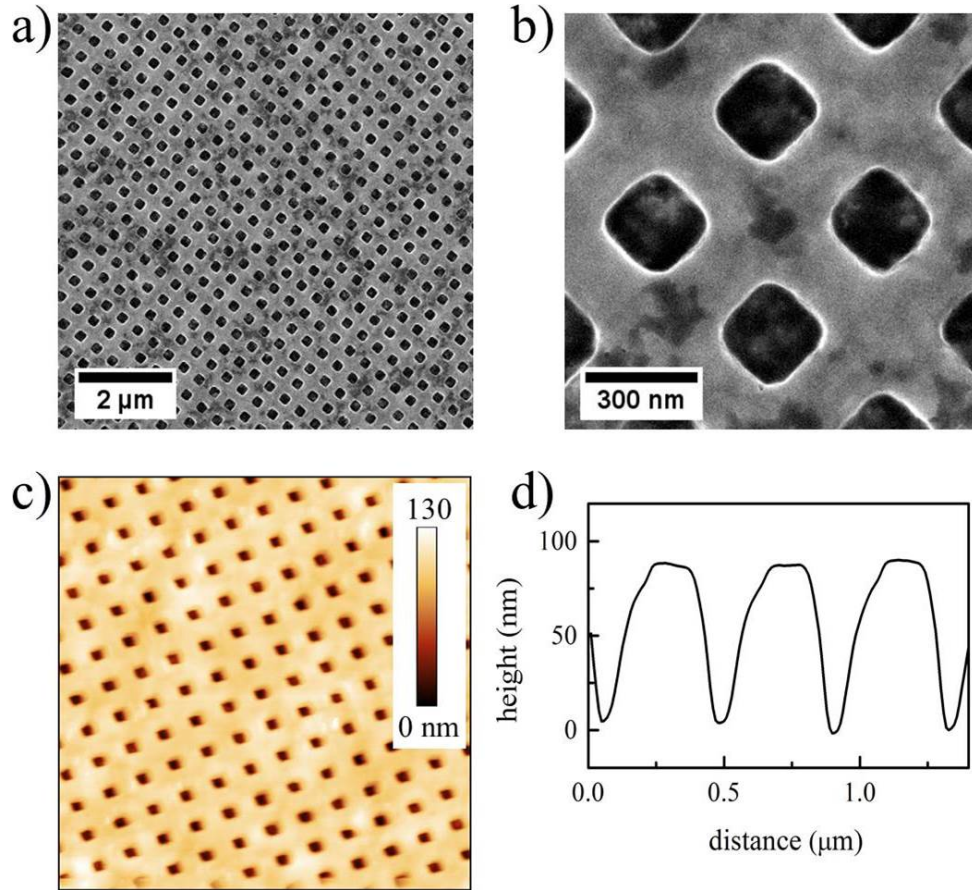


**Figure 8.3:** a) Low magnification and b) high magnification of the nano-imprinted titania/PS-b-PEO composite films. c) AFM topography of the composite films. The size is  $2 \times 2 \mu\text{m}^2$  and d) corresponding height profile.

To evaluate the efficiency of the low-temperature route for polymer-template extraction, Fourier transform infrared spectroscopy (FTIR) is used to determine traces of residual polymer template. Figure 8.4 depicts the FTIR data of the composite films before and after polymer extraction. A broad band is observed in the region of  $400 - 700 \text{ cm}^{-1}$  for both samples. This band corresponds to the bending vibration of Ti–O bonds [304–306]. However, distinct differences exist in the range of  $700 - 1800 \text{ cm}^{-1}$ . The sample before polymer extraction process shows many absorption peaks, whereas the sample after polymer extraction demonstrates no absorption peaks. In the present system, all absorption bands in this region are identified as features of organic bonds. For example, the strongest absorption bands at  $1030 \text{ cm}^{-1}$  and  $1480 \text{ cm}^{-1}$  in the titania/PS-b-PEO composite film are ascribed to the presence of aromatic rings (PS) and C–O bonds (PEO), respectively [307,308]. However, absorption bands are absent in the sample after polymer

extraction during this region, suggesting that the PS-*b*-PEO is removed thoroughly by the combination of UV exposure and chlorobenzene soaking.

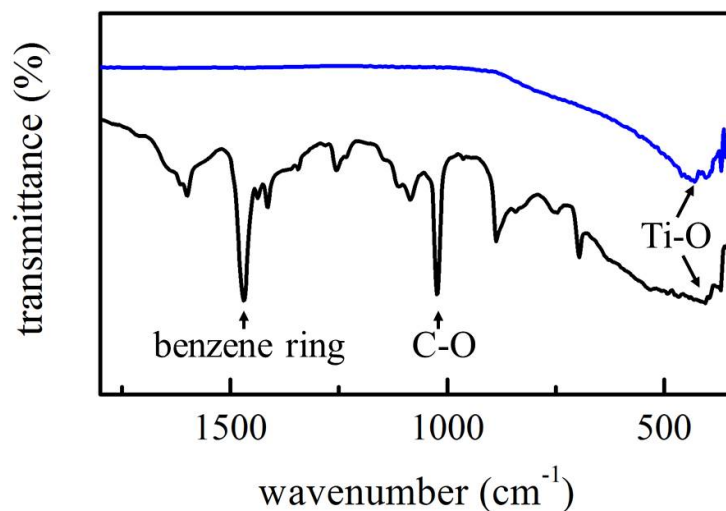


**Figure 8.4:** FTIR spectra of the titania/PS-*b*-PEO composite film (black curve) and the film after polymer extraction process (blue curve).

After polymer extraction, the pitch-like superstructures are preserved but deformed from their original square-shape in the nano-imprinted titania/PS-*b*-PEO composite film as shown in figure 8.5a. The deformation is caused by a certain collapse of the titania nanostructures after removal of the polymer scaffold. To further probe the titania nanostructures inside the pitches and on the walls between pitches, a cross-section of the nano-imprinted titania film is examined after breaking the sample vertically. Figure 8.5b shows the mesoporous nature of a sponge-like morphology on the walls between pitches and in the region underneath pitches. Moreover, a compact and extremely thin titania crust is found on top of the mesoporous titania nanostructures, which makes the interconnected titania network invisible in the plan view picture. For a comparison, an original titania film after polymer extraction is measured via SEM as displayed in figure 8.5c, the mesoporous titania sponge-like structures are observed as well, but without compact titania layer on the surface. Therefore, it is concluded that the formation of the compact titania crust is caused by the NIL process. Irrespective of imprinting, the mesopore sizes are in the range of 10-20 nm in both, the original and the nano-imprinted titania films. To obtain more quantitative information about the impact of polymer extraction, the surface morphology of the nano-imprinted titania film is probed via AFM measurements. Figure 8.5d confirms the existence of deformed pitch-like superstructures and the preservation of superstructure arrangements. After polymer extraction, the AFM height profile reveals that the depth of pitch-like structures remain around 90 nm, indicating that the

polymer-extraction process induces a similar collapse degree in the wall between pitches and the region underneath pitches.

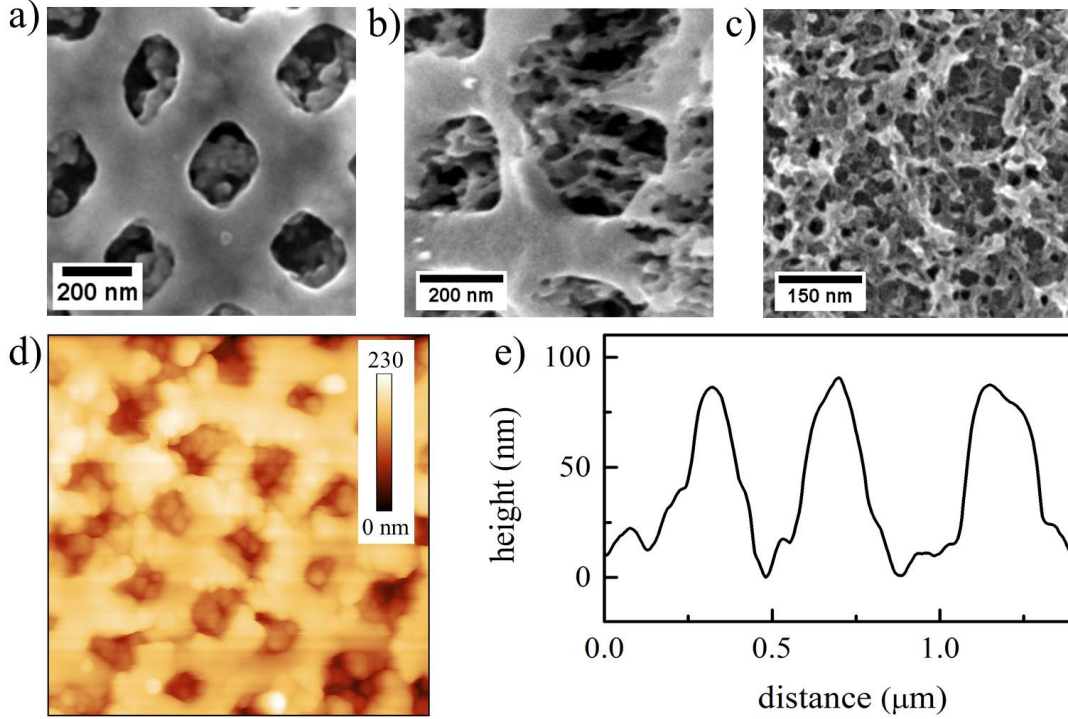


**Figure 8.5:** a) Plan view and b) cross-section SEM images of the nano-imprinted sample after polymer extraction. c) SEM topography of the original titania film after polymer extraction. d) Surface morphology of the nano-imprinted titania film probed by AFM. The scan range is  $2 \times 2 \mu\text{m}^2$  and e) corresponding height profile.

### 8.1.3 Inner morphology

In order to gain more insights on the volume of the films after the NIL process, GISAXS experiments are performed at the the Austrian SAXS beamline of the Elettra synchrotron source, as described in section 3.1.6. The original composite films before and after polymer extraction are used as reference. The 2D GISAXS data obtained from the measurements are shown in figure 8.6.

Figure 8.6a and 8.6b show the original titania/PS-b-PEO composite samples before and after polymer removal, respectively. Unlike to GISAXS measurements shown in previous chapters, no beamstop is introduced into the system to block the specular peak. Therefore, the intensity maximum locates at the specular peak for the measurements. The positions of the specular and Yoneda peaks are labeled in figure 8.6a. For the side scattering, the signal in figure 8.6b is much stronger than that in figure 8.6a. The difference is mainly

ascribed to the contrast. The scattering strength is related to the contrast between titania and PS-b-PEO in the composite sample, and to the contrast between titania and air in the sample after polymer extraction. The sample with greater contrast between titania and air gives stronger side scattering (figure 8.6b) as compared with titania and PS-b-PEO (figure 8.6a). The contrast difference is the reason for the intensity difference in figure 8.6c and 8.6d as well. Moreover, the scattering patterns of both titania/PS-b-PEO composite films without and with superstructures are distinctly different, as shown in figure 8.6a and 8.6c. A long interference streak in the center along the  $q_z$  direction is observed in the superstructured composite sample, which is enclosed by a red rectangle. This prominent feature is the result of the NIL process as it is absent in figure 8.6a. The long interference streak is identified as Bragg rod, which originates from the periodic order of the NIL-induced superstructures [87, 309, 310].

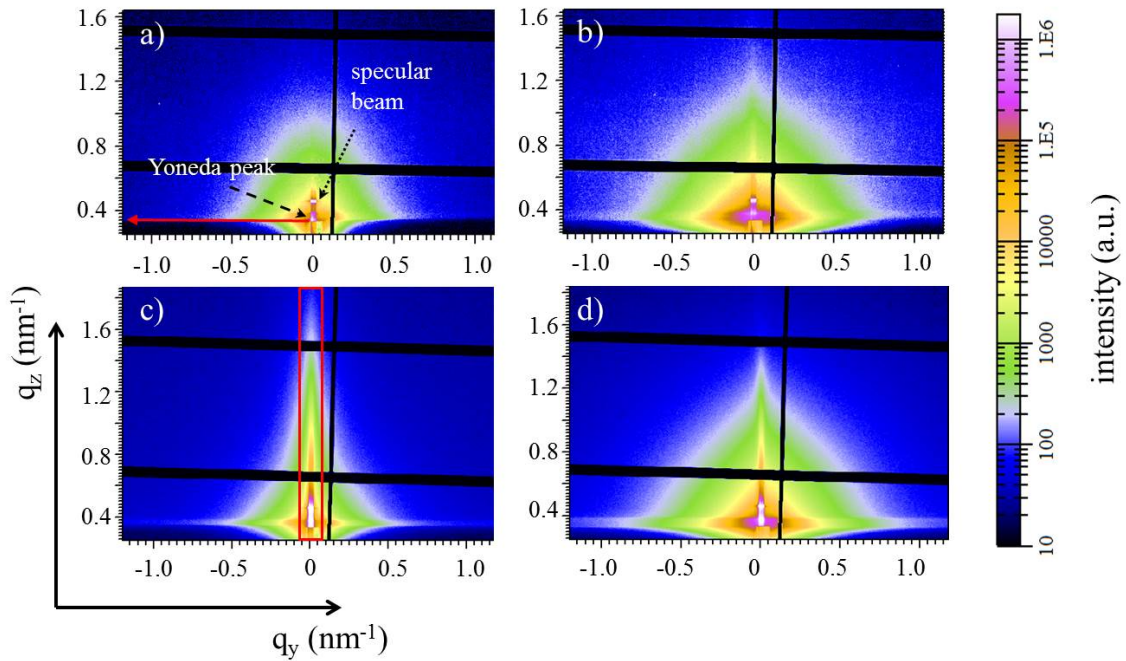


**Figure 8.6:** 2D GISAXS data. The original titania/PS-b-PEO composite films a) before and b) after polymer extraction; the nano-imprinted composite films c) before and d) after polymer extraction. The positions of specular and Yoneda peaks are labeled in image a), and the red arrow indicates the horizontal line cut. The red rectangle in image c) indicates the region of the Bragg rods. The horizontal black stripe at  $q_z = 0.66 \text{ nm}^{-1}$  and  $q_z = 1.52 \text{ nm}^{-1}$  as well as the one in the vertical position at  $q_y = 0.12 \text{ nm}^{-1}$  are due to the inter-module detector gaps of the detector.

In order to obtain quantitative information about lateral nanostructures inside the probed samples, horizontal line cuts are performed at the Yoneda peak position of titania,



as indicated by the red arrow in figure 8.6a. These cuts along with their fits are shown in figure 8.7a.

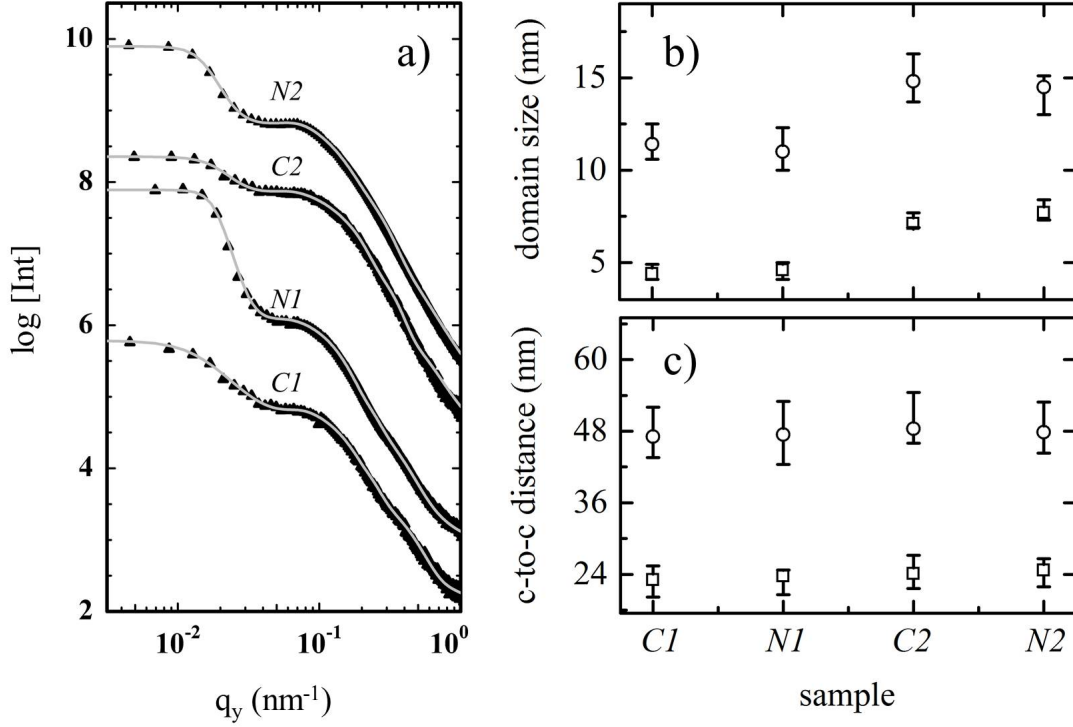


**Figure 8.7:** a) Black curves represent horizontal line cuts of 2D GISAXS data for (C1) original titania/PS-*b*-PEO composite film, (N1) nano-imprinted titania/PS-*b*-PEO composite film, (C2) titania film after polymer extraction, and (N2) nano-imprinted titania film after polymer extraction. The grey lines represent the fits to the corresponding line cuts. All curves are shifted along the  $y$ -axis for clarity of the presentation. The extracted characteristics: b) titania domain size and c) the corresponding center-to-center distance. Hollow circles and hollow squares indicate the large- and small-sized titania structures, respectively.

From modeling, two structural characteristics are extracted for all samples. The titania domain sizes and the corresponding center-to-center distances are summarized in figure 8.7b and 8.7c. Both titania/PS-*b*-PEO composite films (original and nano-imprinted) have similar domain sizes and center-to-center distances. In detail, the size of small titania domain is  $(4.6 \pm 0.2)$  nm with the corresponding center-to-center distance of  $(23.1 \pm 2.1)$  nm, whereas the large-sized titania domains possess a characteristic radius of  $(11.1 \pm 1.3)$  nm and center-to-center distance of  $(47.1 \pm 4.2)$  nm. The structural similarity suggests that NIL only creates large pitch-like patterns onto the composite film but does not have an impact on titania nanostructures that are introduced from the sol-gel synthesis. After polymer extraction, both domain size and center-to-center distance are still the same in original and nano-imprinted films, implying that NIL does also

not influence the mesopore formation even after the treatment of UV and chlorobenzene. Compared to the sample before polymer extraction, the titania domain size increases slightly whereas the center-to-center distance remains almost unchanged. The increase of domain size could be due to the fact that the removal of the polymer template results in a certain collapse of the titania nanostructures as this phenomenon is frequently reported in literature [165–169]. Through equation 5.1, the mesopore size can be calculated in both original and nano-imprinted titania films after polymer extraction. The small-sized titania domains have an average radius of  $(7.5 \pm 0.5)$  nm with a center-to-center distance of  $(24.7 \pm 2.3)$  nm, yielding a pore size of  $(10.3 \pm 1.8)$  nm. The large domains have a mean radius of  $(14.5 \pm 1.0)$  nm and the center-to-center distance is of  $(47.8 \pm 4.3)$  nm, giving rise to a pore size of  $(19.0 \pm 3.3)$  nm.

#### 8.1.4 Incorporation of pre-synthesized nanoparticles into titania network at low temperatures

As discussed in chapter 5, pre-synthesized titania nanoparticles have been incorporated successfully into the templated titania network structure. To make a comparison, the nanoparticles are also incorporated into a metal oxide phase which is derived from EGMT at low temperatures. The sol-gel process at low temperatures is described in section 4.2.2. The detailed information of the incorporation of the nanoparticles is given in section 4.2.2. After solution preparation, the titania/PS-b-PEO composite films are deposited with spray coating. The parameters for spray deposition are listed in section 4.2.3. The mesoporous titania films are obtained by the removal of polymer template via UV irradiation and solvent extraction. In the present work the sol-gel-synthesized  $\text{TiO}_2$  and  $\text{TiO}_2$  from pre-synthesized nanoparticles have a weight ratio of 1:1. This mesoporous titania sample is denoted as 50 % EGMT.

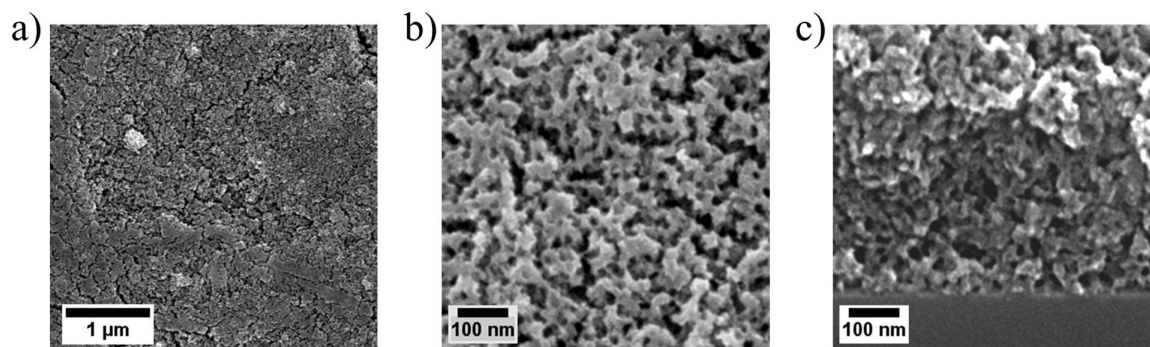


**Figure 8.8:** Plan-view of the 50 % EGMT film at a) low and b) high magnifications and c) corresponding cross-section SEM image.

The surface morphology of the 50 % EGMT film is investigated by SEM and the results are shown in figure 8.8. A rough surface is obtained as a result of the spray deposition. Moreover, some tiny cracks are present in the surface (figure 8.8a). When zoomed in, a mesoporous nature of the sponge-like morphology is observed in figure 8.8b. The mesopore sizes are in the range of 10 nm to 20 nm. However, some pores are connected to form macropores. The cross-section SEM image gives a proof that the polymer template is extracted completely.

The inner film morphology is investigated with the time-of-flight grazing incidence small-angle neutron scattering (TOF-GISANS). The measurement was performed at the beamline REFSANS of the Helmholtz Zentrum Geesthacht at FRM II, Garching. An incident angle of  $0.45^\circ$  and a sample-detector distance of 10.534 m were set for the experiment. The wavelengths of the neutrons ranges from  $2.00 \text{ \AA}$  to  $14.93 \text{ \AA}$ . Due to gravity for neutrons, the real incident angle needs to be corrected. Selected 2D GISANS data with various wavelengths are illustrated in figure 8.9. As noted, the position of the

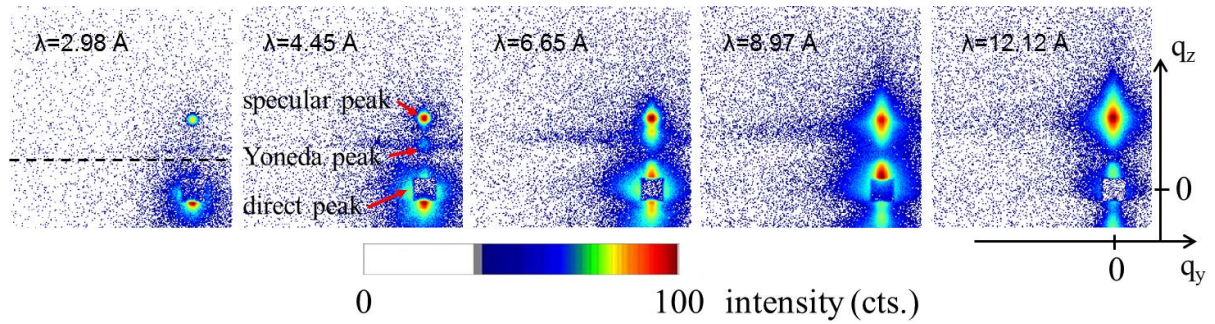


**Figure 8.9:** Selected 2D GISANS data. The wavelengths are labeled in each image. The dashed line in the first image indicates the sample horizon. The specular peak, the Yoneda peak and the direct beam are labeled in the second image.

Yoneda peak moves upwards with increasing wavelength of the neutron beam. This is caused by the proportional relationship between the critical angle of the probed materials and the neutron wavelength. The vertical line cuts obtained from the 2D TOF-GISANS data are performed at  $q_y = 0$  and the results are shown in figure 8.10a for the probed wavelengths of  $4.45 \text{ \AA}$ ,  $4.92 \text{ \AA}$ ,  $5.44 \text{ \AA}$ ,  $6.01 \text{ \AA}$ ,  $6.98 \text{ \AA}$ ,  $7.71 \text{ \AA}$ ,  $8.12 \text{ \AA}$ ,  $8.97 \text{ \AA}$ ,  $9.92 \text{ \AA}$  and  $10.96 \text{ \AA}$ . The position of the specular peaks remain unchanged at  $\alpha_i + \alpha_f \approx 0.9$ , whereas the Yoneda peaks of the titania and silicon shift towards higher  $\alpha_i + \alpha_f$  values with increasing neutron wavelengths. Determined by the Yoneda peak positions, the critical angles of the silicon substrate and the probed 50 % EGMT film are plotted in figure 8.10b as a function of neutron wavelengths. By a linear fitting function, both scattering length densities (SLDs) can be extracted via equation 2.28. The SLD of the silicon substrate is

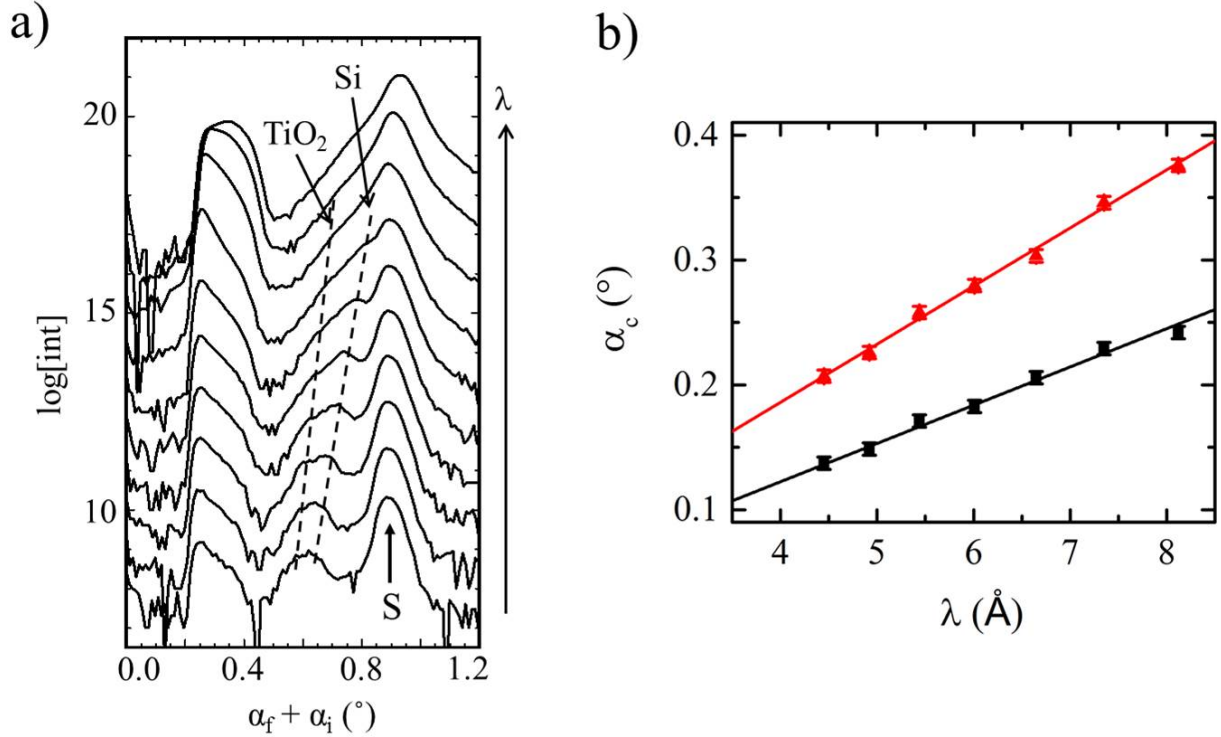


**Figure 8.10:** a) Selected vertical line cuts obtained from 2D TOF-GISANS data. The curves are shifted along the intensity axis with increasing wavelength from bottom to top. The corresponding wavelengths are 4.45 Å, 4.92 Å, 5.44 Å, 6.01 Å, 6.98 Å, 7.71 Å, 8.12 Å, 8.97 Å, 9.92 Å, 10.96 Å. The position-shifting trend of the Yoneda peaks of titania and silicon are labeled by dashed lines. The arrow indicates the specular peak. b) The wavelength-dependent critical angles of the silicon substrate (red triangles) and the 50 % EGMT film (black rectangles) obtained from the vertical cuts in a). Red and black lines are their corresponding linear fits.

determined to be  $(2.06 \times 10^{-6} \pm 2.68 \times 10^{-7}) \text{ Å}^{-2}$ , which fits quite well to the theoretical value  $(2.07 \times 10^{-6} \text{ Å}^{-2})$ . The SLD of the 50 % EGMT sample ( $\rho$ ) is calculated to be  $(8.97 \times 10^{-7} \pm 1.76 \times 10^{-7}) \text{ Å}^{-2}$ . According to previous studies, the SLD of a compact titania layer ( $\rho_c$ ) is  $2.41 \times 10^{-6} \text{ Å}^{-2}$  [183]. Since the porosity ( $\Phi$ ) can be calculated via equation 2.34, a porosity of  $(62.8 \pm 7.3) \%$  is obtained for the 50 % EGMT sample.

Information about lateral structures can be obtained from horizontal line cuts which are performed at the position of the titania Yoneda peak. The selected horizontal line cuts are displayed in figure 8.11 with the same wavelengths as for the vertical line cuts. It is noteworthy that, the whole film volume is probed when the neutron wavelengths are smaller than 9 Å in the present work. If they are larger than 9 Å the penetration depth of neutrons reduces exponentially and surface structures are probed instead. In order to parametrize the lateral structures in the 50 % EGMT film, the horizontal line



cuts are fitted with the same model for used for GISAXS measurements as described in section 5.1.2. From modeling, two characteristic structure sizes are extracted. In detail, lateral structure radii of  $(8.8 \pm 1.6)$  nm and  $(40.0 \pm 8.9)$  nm with center-to-center distances of  $(30.0 \pm 6.6)$  nm and  $(175.0 \pm 40.6)$  nm are obtained. Therefore, the pore sizes of  $(12.4 \pm 6.8)$  nm and  $(95.0 \pm 41.6)$  nm can be calculated via equation 5.1. Furthermore, it is noted that the horizontal line cuts for all wavelengths give the same information about the lateral structures, which means that surface structures are similar to structures in the volume of the film.

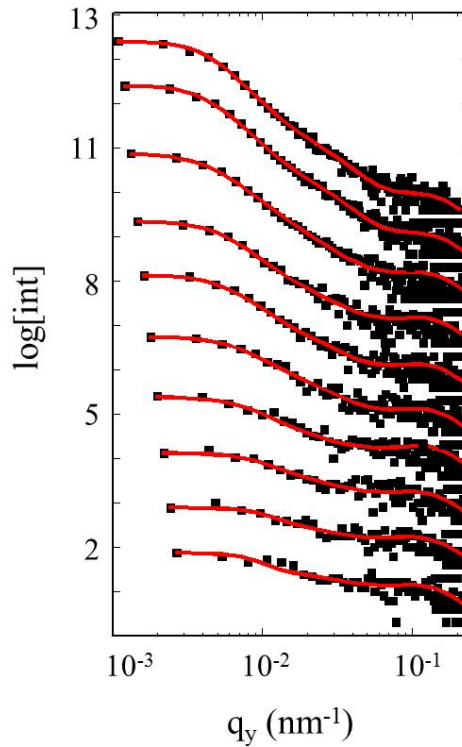


**Figure 8.11:** Selected horizontal line cuts obtained from 2D TOF-GISANS data. The curves are shifted along the intensity axis with increasing wavelength from bottom to top. The corresponding wavelengths are 4.45 Å, 4.92 Å, 5.44 Å, 6.01 Å, 6.98 Å, 7.71 Å, 8.12 Å, 8.97 Å, 9.92 Å, 10.96 Å. The red lines represent the fits to the data.

## 8.2 P3HT-backfilled titania films

As an exciton is excited by the absorption of a photon in P3HT and subsequently the exciton is only split at the titania/P3HT interface over a built-in gradient in the electrochemical potential, a successful backfilling of P3HT into mesoporous titania films is of great importance for the performance of the final device. The experimental details

regarding backfilling are described in section 4.2.4. The P3HT-backfilled titania film, named as active layer, is the core part of hybrid solar cells which is responsible for the charge carrier generation and transport.

### 8.2.1 Active layer morphology

To obtain a more crystalline P3HT film, the backfilled sample is post-annealed at 120 °C for 10 min under nitrogen atmosphere.

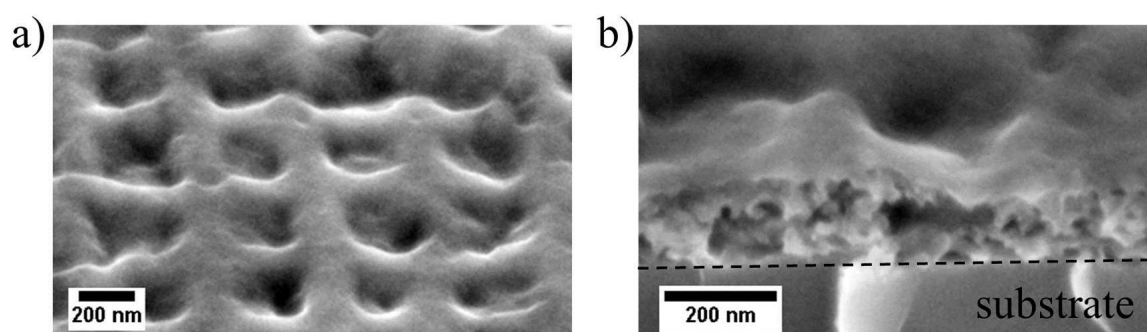


**Figure 8.12:** a) SEM image of the P3HT back-filled hierarchical titania films measured at a tilt angle of 54 ° and b) corresponding cross-section SEM image.

Figure 8.12a shows the surface morphology of the hierarchical titania films (with mesopores and artificial superstructures) backfilled with P3HT. To yield a better view, the sample stage is tilted with respect to the electron beam. After backfilling with P3HT, the mesoporous titania film is covered with P3HT and the artificial superstructures are preserved instead of being filled completely. A similar observation is reported by Ding et al., who forged nanodome-superstructures onto mesoporous titania films and backfilled then with spiro-OMeTAD as a hole transport material [293]. It was shown that the preserved nanodomains after backfilling give a significant enhanced light-harvesting capability in the active layer. Therefore, the preservation of NIL-induced patterns is of importance. If the P3HT capping layer is too thin, the top electrode might contact with titania photoanodes directly, leading to shunting paths. If the capping layer is too thick, the pitch-like superstructures might be filled with P3HT completely, which results in less light harvesting in the active layer. Later on, gold electrodes need to be deposited on top of the active layer to finalize solar cells. To investigate the superstructure conditions after gold deposition, SEM is used to probe the sample. The sample stage is tilted as well. Figure 8.13 shows that the NIL-induced pattern on the active layer are still preserved after gold deposition.

The thickness of the active layer is revealed by cross-section SEM images (figure 8.12b). A very thin layer of about 170 nm is observed. Moreover, the cross-section image shows a

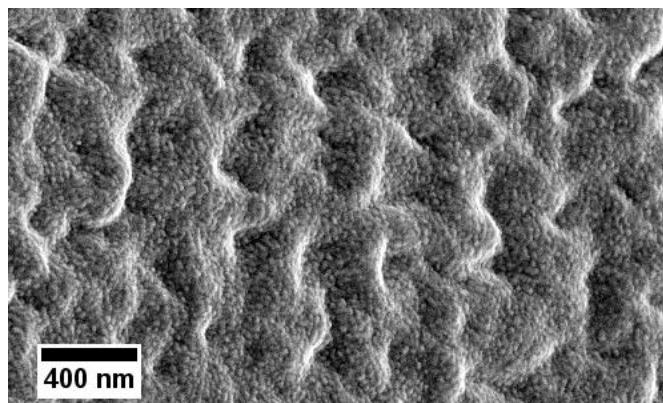


**Figure 8.13:** SEM image of the superstructured active layer with gold contact on top. The sample is measured at a tilt angle of  $54^\circ$ .

good infiltration of P3HT into the mesoporous titania films. As SEM measurements only provide the surface information, the inner morphology of the active layer is investigated with GISAXS measurements. The 2D GISAXS data of the superstructured active layer is displayed in figure 8.14a. As seen from the images, an arc locates at the high  $q_z$  region, which is identified as the (100) Bragg reflection of P3HT crystals. To characterize P3HT infiltration, a horizontal line cut is performed at the position of the P3HT Yoneda peak instead of the titania Yoneda peak. The cut along with the corresponding fit are presented in figure 8.14b. From data modeling, characteristic radii of  $(4.6 \pm 0.2)$  nm and  $(9.5 \pm 0.4)$  nm with center-to-center distances of  $(24.6 \pm 2.9)$  nm and  $(47.1 \pm 8.3)$  nm are determined for P3HT domains. From the GISAXS measurements on the nano-imprinted titania film after polymer extraction, the pore size is computed to be  $(19.0 \pm 3.3)$  nm, which agrees well with the large-sized P3HT domains, suggesting a fairly good infiltration of P3HT into large-sized mesopores. In contrast, the small P3HT domains are slightly smaller than the small-sized pores, elucidating that P3HT infiltrates the small-sized mesopores not perfectly. Moreover, the distances between P3HT domains can be calculated via equation 5.1 as well, to be  $(15.4 \pm 2.7)$  nm and  $(28.1 \pm 7.9)$  nm. Both values are commensurate with the small- and large-sized titania domains after polymer extraction, implying that the P3HT backfilling process does not influence the pre-existing titania nanostructures.

### 8.2.2 Optical properties of the active layer

To evaluate the enhancement of light harvesting in the superstructured active layer, the light absorption is investigated at various angles of light incidence. To make a comparison, the angular-dependent light absorption in the original active layer is measured as well.

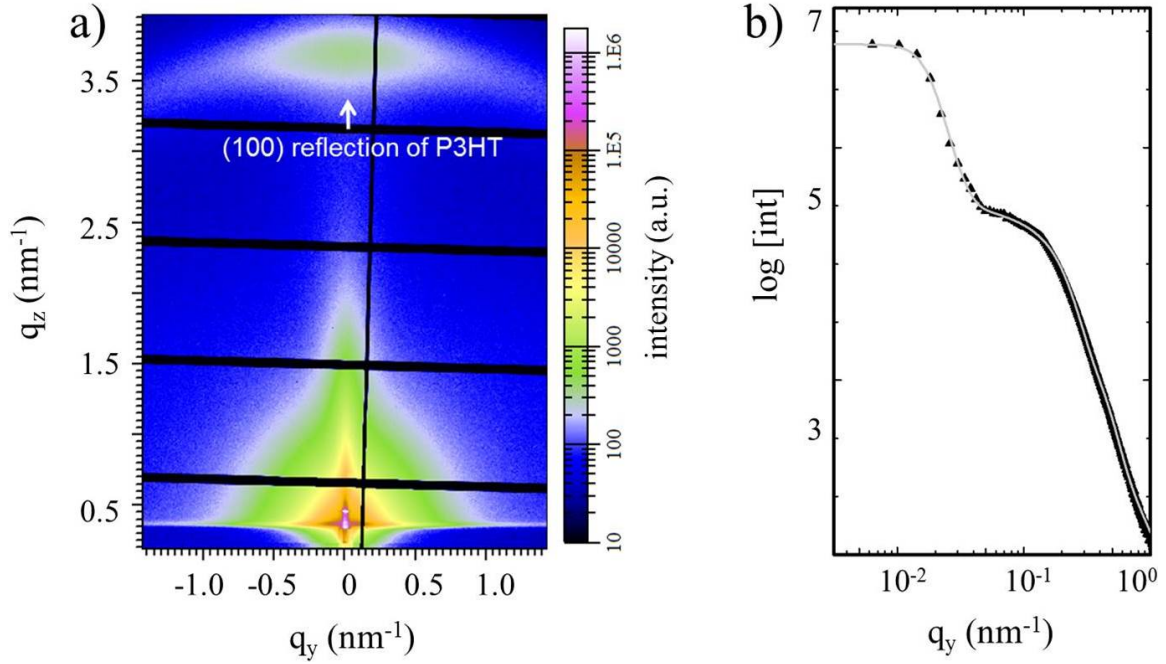


**Figure 8.14:** a) 2D GISAXS data of the active layer with artificial superstructures. b) The black curve represents the horizontal line cut obtained from the 2D GISAXS data. The grey line indicates the fit to the data.

For UV/Vis measurements, the active layers are fabricated on glass substrates and the light is shone through the glass substrate to mimic the real situation of illumination for solar cells. In order to eliminate the influence of the glass surface reflection, the UV-Vis absorption spectra of the pure glass is deducted from the spectra of glass-substrate/active-layer sample at each angle of incidence. The corrected UV/Vis absorption spectra of the active layers at various angles of incidence are shown in figure 8.15. For both active layers (without and with superstructures), the main absorption is in the wavelength region of 400 - 600 nm, which is assigned to the absorption characteristics of P3HT [123]. Moreover, all spectra have a similar shape and the peak positions stay nearly unchanged, indicating that the NIL pattern does not lead to remarkable changes in the optical properties.

Under standard conditions (at 0° light incident angle), the maximum absorbance of both active layers at 525 nm is approximately 0.54. The absorption resemblance implies that the light absorption at 0° incidence is not affected by the artificial superstructures, which is due to the fact that the incident light is perpendicular to the pitch-like superstructures in the hierarchical titania film and thereby no obvious scattering occurs. In addition, both active layers show a similar thickness, (154 ± 9) nm for the original sample and (157 ± 19) nm for the non-imprinted active layer. The thickness is measured with height profilometry, as described in section 3.1.1. With increasing incidence angles, the

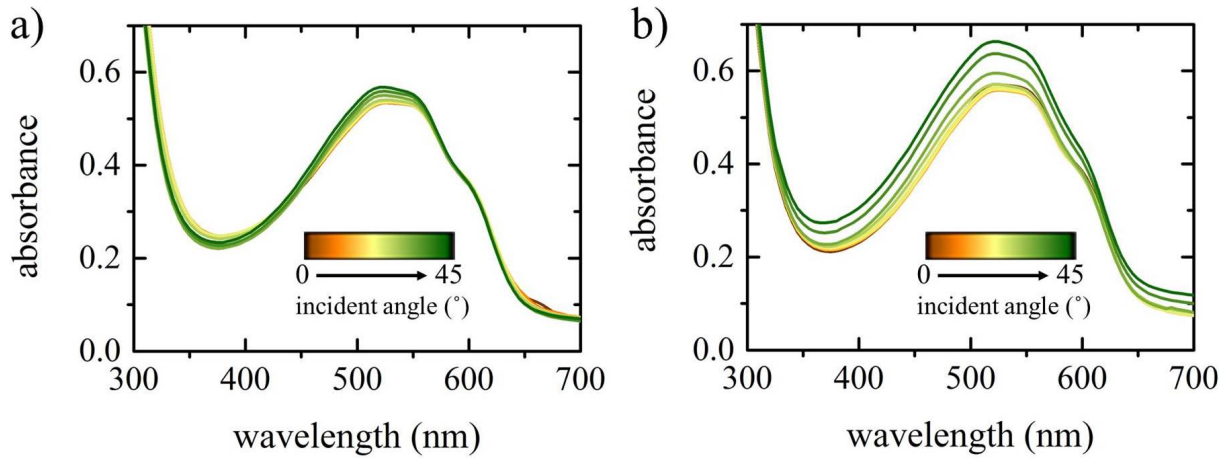


**Figure 8.15:** Angular dependent UV/Vis absorption spectra. The data are recorded every  $5^\circ$ : a) Original active layer and b) superstructured active layer.

active layers behave quite differently with respect to the degree of light absorption. Only a slight increase of light absorption is formed in the original active layer whereas a significant enhancement of light absorption is present in the nano-imprinted active layer. For the original active layer, the increase arises from a geometrically elongated pathway at nonzero angles. The light path with a certain incident angle is schematically illustrated in figure 8.16. In the present study, the refractive index of titania and P3HT is 2.2 and 2.37,

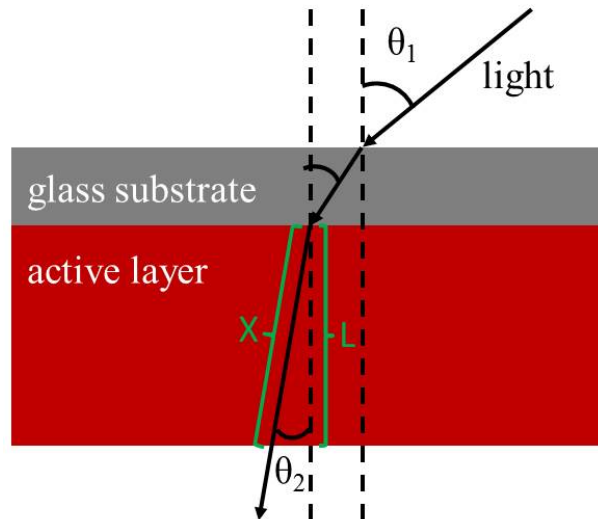


**Figure 8.16:** Schematic illustration of the light path in the active layer. Black arrows indicate the light path,  $X$  and  $L$  indicate the light traveling distances at nanozero and zero incidence angle, respectively.  $\theta_1$  and  $\theta_2$  represent incidence angle and refraction angle, respectively.

respectively. The porosity of mesoporous titania films is about 0.62, which is determined by white light interferometry. The refractive index of the active layer can be calculated

to be 2.30 via a so-called Bruggeman effective medium approximation which is described in literature [311]. The relation between  $\theta_1$  and  $\theta_2$  can be interpreted by Snell's law:

$$n_1 \sin \theta_1 = n_2 \sin \theta_2 \quad (8.1)$$

For example, the light incident angle is assumed to be  $45^\circ$ , by knowing  $n_1 = 1$  for the air and  $n_2 = 2.30$  for the active layer, the  $\theta_2$  can be computed to be about  $18^\circ$ . Thus,  $X = 1.051 L$  is obtained. From theoretical calculation, the light pathway at  $45^\circ$  incident angle is 5.1 % longer than that at zero incident angle. The UV/Vis measurements show that the absorbance at  $45^\circ$  incident angle is 5.8% higher as compared to  $0^\circ$  incident angle. The increased absorbance agrees well with the calculated elongated light pathway, confirming that the changes of absorption in the original active layer are caused by the distance changes of the light pathway.

For the nano-imprinted active layer, the absorbance at  $45^\circ$  incident angle is about 0.66 at 525 nm, i.e. almost 20 % enhancement as compared to  $0^\circ$  absorbance. Besides the longer light travel path (about 6 %), the rest of 14 % enhancement of the light absorption originates from scattering in the active layer superstructures. Moreover, it is noticed that the first prominent increase in light absorbance occurs at  $35^\circ$  incident angle (figure 8.15b), indicating this angle is a threshold for large amount of light scattering in this specific film with special superimposed structural order.

### 8.3 Current-voltage characteristic

Hybrid solar cells (dye-free) are fabricated and discussed in the present section prepared from the aforementioned nano-imprinted active layers. The full device is prepared according to the procedure explained in section 4.2.4. It is important to note that, the electron blocking layer is not incorporated into the hybrid photovoltaic device as the main focus of this study is on investigating the influence of artificial superstructures on solar cell performance at various angles of light incidence, as optimization lies out of scope of this work. Moreover, the addition of an electron blocking layer or spacer layer between P3HT and the gold electrode might destroy the situation that the gold contact replicates the superstructure patterns from the P3HT layer. In order to confirm the feasibility and practicality of the superimposed structural order on hybrid solar cells, the original solar cells (without superstructures) are manufactured for a comparative analysis. The photographs of both hybrid solar cells (as prepared) are shown in figure 8.17. As seen from the images, there is no big difference between the two types of solar cells with respect to their

macroscopic appearance. Both devices have four gold electrode pixels with similar sizes. The only difference is that there is a mark made by the NIL master in the nano-imprinted solar cells (figure 8.17a).

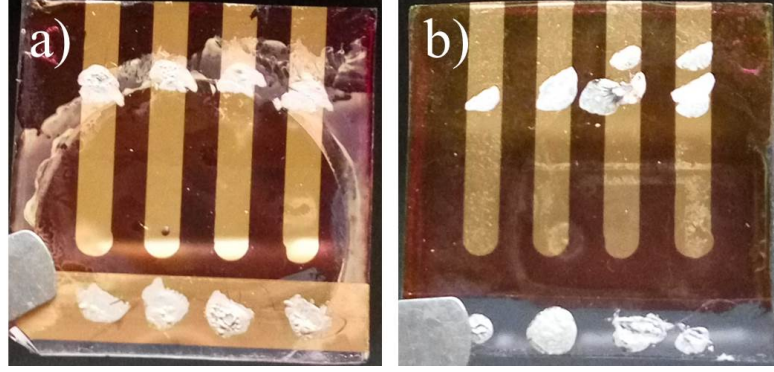


**Figure 8.17:** Real images for a) nano-imprinted and b) original hybrid solar cells. The semicircle in a) is caused by imprinting master under high pressure. The silver spot in both a) and b) are the silver paste, which is used to improve the contact between the measuring device and gold electrode.

After preparation, hybrid solar cells are tested immediately under simulated AM 1.5G illumination with  $100 \text{ mW cm}^{-2}$  intensity. During illumination, current-voltage ( $I$ - $V$ ) sweeps are recorded at various angles of light incidence. Figure 8.18 compares the  $I$ - $V$  characteristics of the original and nano-imprinted solar cells at  $0^\circ$  incident angle. From  $I$ - $V$  curves, related photovoltaic parameters such as  $PCE$ , short-circuit current density ( $J_{sc}$ ), open-circuit voltage ( $V_{oc}$ ), and fill factor ( $FF$ ) can be extracted. For the original hybrid solar cells,  $V_{oc}$  of  $(0.63 \pm 0.02) \text{ V}$ ,  $J_{sc}$  of  $(0.46 \pm 0.03) \text{ mA cm}^{-2}$  and  $FF$  of  $(30.4 \pm 1.0) \%$  are obtained, resulting in a  $PCE$  of  $(0.09 \pm 0.004) \%$ . The photovoltaic performance of the nano-imprinted hybrid cell is slightly better with  $V_{oc}$  of  $(0.65 \pm 0.03) \text{ V}$ ,  $J_{sc}$  of  $(0.51 \pm 0.03) \text{ mA cm}^{-2}$  and  $FF$  of  $(30.1 \pm 1.1) \%$  and  $PCE$  of  $(0.10 \pm 0.003) \%$ . In general, the obtained device efficiencies are only very moderate as compared to current DSSCs technology. Nevertheless, a  $PCE$  over 0.1% is achieved for the first time in a dye-free  $\text{TiO}_2/\text{P3HT}$  hybrid solar cell in particular when low-temperature routes are applied, as to the best of our knowledge. From the analysis of UV/Vis measurements the light absorption of both active layers is similar at  $0^\circ$  incident angle, but the  $J_{sc}$  and  $PCE$  for the nano-imprinted devices are slightly higher than those for the original solar cells. The slight improvement can be attributed to two factors. On the one hand, more efficient light back reflection is given by the superstructured metal contact, which is reported by Ding et al. in case of ssDSSCs [293]. On the other hand, the travel distances of charge carriers are reduced in the structured solar cells, which benefits from the structured top electrode



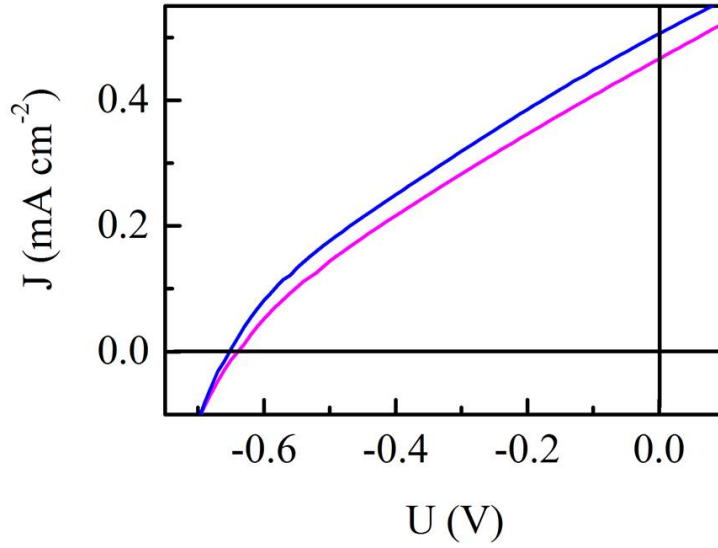


**Figure 8.18:** Photovoltaic performance of dye-free hybrid solar cells. *I-V* curves of original (magenta) and nano-imprinted (blue) hybrid solar cells measured at  $0^\circ$  of light incidence.

as already verified in P3HT:[6,6]-phenyl-C61-butyric acid methyl ester (P3HT:PCBM) system with superstructured metal electrodes [312].

The external quantum efficiency (*EQE*) spectra of these two cells are probed and displayed in figure 8.19. Both *EQE* curves constitute a similar shape and the peak positions since the same ingredients are presented in both devices. However, a lower *EQE* is observed in the original solar cells, which agrees well with the results from *J-V* measurements. By integrating the photoresponse over the solar spectrum, the  $J_{sc}$  in original and nano-imprinted hybrid solar cells are evaluated to be  $0.45 \text{ mA cm}^{-2}$  and  $0.52 \text{ mA cm}^{-2}$ , respectively, which are in good agreement with the  $J_{sc}$  values obtained from *I-V* curves.

To show the dependency between angular incidence of light and device performance, all photovoltaic parameters are normalized to the values of the original solar cells at  $0^\circ$  of light incidence. The normalized results are shown in figure 8.20. In general, *PCE* for nano-imprinted hybrid solar cells is higher than for the original hybrid solar cells at various angles of light incidence (from  $0^\circ$  to  $45^\circ$ ). The performance improvement mainly originates from the enhanced  $J_{sc}$  as  $V_{oc}$  and *FF* are similar for each angular incidence. For the original hybrid solar cells, the *PCE* and  $J_{sc}$  remain almost unchanged in the angular range of  $0^\circ$  to  $10^\circ$  and then experience a continuous decrease from  $15^\circ$  to  $45^\circ$ . For the nano-imprinted hybrid solar cells, the *PCE* and  $J_{sc}$  increase slightly before they decrease from  $15^\circ$  on with a similar tendency as the original solar cells. The  $V_{oc}$  values are almost unchanged up to  $30^\circ$  and then decrease slightly at higher incident angles, whereas the *FF* values stay stable irrespective of different angles of light incidence.



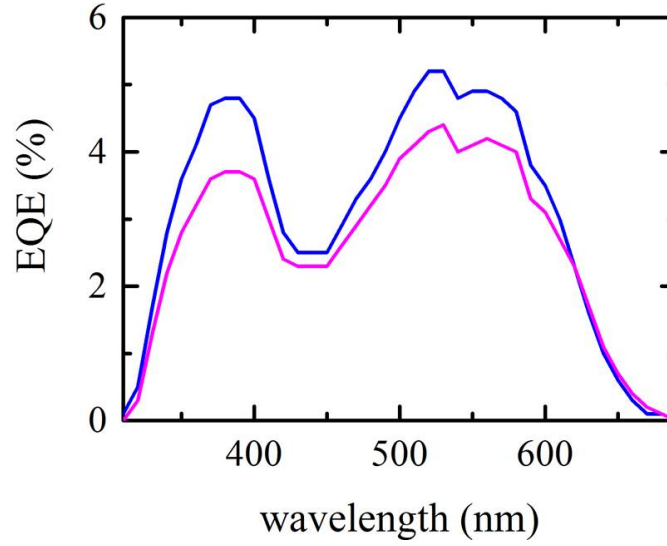


**Figure 8.19:** External quantum efficiency (EQE) spectra of original (magenta) and nano-imprinted (blue) hybrid solar cells measured at  $0^\circ$  of light incidence.

Putting all information together, we conclude that the device performance is closely related to the light angular incidence. The decrease of  $J_{sc}$  from  $15^\circ$  to  $45^\circ$  in both solar cells is due to the fact that the light reflection of the glass substrate increases with increasing the angle of oblique incident light thereby less light reaches active layers. However, the nano-imprinted hybrid solar cells have a higher  $J_{sc}$  in this range of angular incidence. As revealed by UV/Vis measurements, more light absorption in the nano-imprinted active layers contributes to the higher  $J_{sc}$  as compared to the original hybrid solar cells. From  $0^\circ$  to  $10^\circ$ , the  $J_{sc}$  only have subtle variations in the original hybrid solar cells since the back reflection of glass substrate is similar in this angular region. In contrast, for the nano-imprinted hybrid solar cells the  $J_{sc}$  increases for the region between  $5^\circ$  and  $10^\circ$  as compared to  $0^\circ$  of light incidence. The increase up to 20% is ascribed to the presence of artificial superstructures, which enhance light harvesting in the active layer and promote back-reflection from gold electrodes. The slight decrease in  $V_{oc}$  from  $35^\circ$  on might be caused by the negative impact of increasing temperature along with sustained illumination [80]. The unchanged  $FF$ s in both cells have a value of about 30%, which are lower than previously reported values of P3HT based hybrid solar cells [189,269,283]. The low  $FF$  is probably caused by insufficient P3HT infiltration into titania small-sized pores (revealed by GISAXS measurements), where the tiny gap between P3HT and titania could be a charge recombination center therewith reducing the opportunity for charge carriers reaching the electrodes. Moreover, the intrinsic defects in titania crystal structures could also result in a reduced  $FF$ .

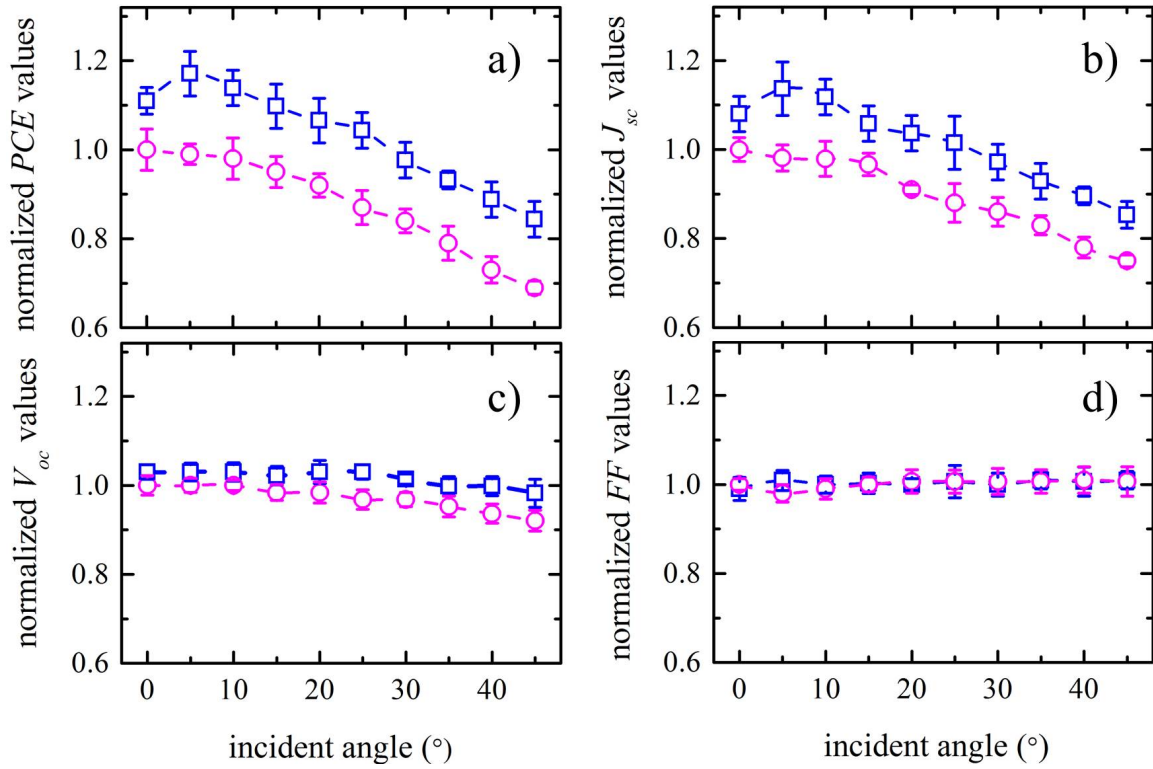


**Figure 8.20:** Angular dependence of photovoltaic parameters. For clarity of the presentation, all parameters are normalized to the values of the original solar cell measured  $0^\circ$  of light incidence. a) PCE, b)  $J_{sc}$ , c)  $V_{oc}$ , and d) FF. The blue hollow squares and the magenta hollow circles represent nano-imprinted and original hybrid solar cells, respectively. The dashed lines are guides to the eyes.

## 8.4 Summary

Hierarchically structured titania films are successfully achieved by the polymer-template-assisted sol-gel synthesis in combination with the NIL process at low temperatures. A complete transfer of the relief structures to the composite films has been confirmed using SEM and AFM measurements. The inner film morphology is revealed by GISAXS measurements, which show that the NIL process only transfers the artificial superstructures (on the submicrometer scale) into the film but does not influence mesopores and titania nanostructures. This phenomenon is observed for the first time with quantitative evidence. Ordered hierarchical titania structures have been demonstrated by Yang et al. with very large produced structure sizes in the length scales of sub-micrometer and micrometer [289]. The larger structures typically have a smaller surface-to-volume ratio. Kaune et al. have reported small multiple length scales, but the superstructures were distributed over the entire film in an arbitrary manner [146]. The present hierarchically structured titania films combine periodicity with small length scales in a decent way,

which is beneficial for photovoltaic applications. Moreover, a low-temperature route has been successfully established to fabricate superstructured titania photoanodes, which has a great significance with respect to energy saving and lowering production costs. With respect to the introduction of pre-synthesized nanoparticles into nanostructured titania network, mesoporous nature and a high porosity of  $(62.8 \pm 7.3) \%$  are observed in the 50 % EGMT film. Since the existence of pre-synthesized nanoparticles can efficiently improve the photoactivity of titania photoanodes [109], the 50 % EGMT film is considered to have a great potential to enhance the performance of hybrid solar cells that are fabricated at low temperatures.

The nano-imprinted mesoporous titania film couples with P3HT to form the active layer of hybrid solar cells. A significant enhancement of light absorption in the nano-imprinted active layer at various angles of light incidence is verified with UV/Vis measurements. To give a proof of practicability, hybrid solar cells are made out of the nano-imprinted active layers at low temperatures. The nano-imprinted hybrid solar cells perform better than the original solar cells at each angle of light incidence, suggesting that the additional superstructures in titania photoanode can enhance the device performance. The similarity of  $V_{oc}$  and  $FF$  in reference and nano-imprinted hybrid solar cells indicates that the  $V_{oc}$  and  $FF$  are not influenced by the incorporated superstructures. The improved  $PCE$  is mainly from the enhanced  $J_{sc}$  in the present work. This finding is in good agreement with the observation from Ding et al, who demonstrated a 16 % enhancement of  $J_{sc}$  in nanodome-patterned ssDSSCs [293]. Moreover, it is the first time to achieve a  $PCE$  over 0.1% in a dye-free  $TiO_2$ /P3HT hybrid solar cell based on low temperature process. Although some relatively higher efficiencies have reported (still lower than 1 %), most of these hybrid devices were produced under the condition of high-temperature processing.

In summary, a low-temperature route is established successfully to fabricate hierarchically structured titania films for dye-free hybrid solar cells. This is of high significance to optimize the current DSSC technology with respect to energy efficiency and lower production costs.



## 9 Conclusion and outlook

In the present thesis, the main focus is on custom-tailoring of titania photoanodes for the performance optimization of solar cells. For solid-state dye-sensitized solar cells (ss-DSSCs), a high-temperature processing is employed in the fabrication of mesoporous titania films. The device performance is affected by the modification of the titania nanostructures with pre-synthesized crystalline titania nanoparticles and by the mesopore size. For hybrid solar cells, the hierarchically structured titania films are produced based on a low-temperature route. The impact of artificial superstructures on the device performance is studied on basis of angular dependent efficiencies of light harvesting.

In order to improve crystallinity of titania photoanodes and thereby device performance, the pre-synthesized crystalline titania nanoparticles are incorporated into the sol-gel-synthesized titania network structures. The modified mesoporous titania films are prepared using a novel structuring route of block copolymer assisted sol-gel synthesis in combination with a large-scale film deposition technique namely spray coating. Such a manufacturing process allows for an up-scale in production of mesoporous titania films with a high degree of control over nanostructures and meopores, which is demonstrated for the first time for application in ssDSSCs. Regarding the nanoparticle incorporation, the pore size, specific surface area, pore volume and conductivity of the titania films increase significantly with increasing the concentration of nanoparticles under the condition of 500 °C calcination. The improvement of the film properties is very beneficial for the solar cell performance. Therefore, the ssDSSCs based on the modified titania photoanodes give a better performance than the solar cells with the pure sol-gel-synthesized titania photoanodes. Particularly, the 50 wt% NPs cells give a *PCE* of  $(2.7 \pm 0.1) \%$ , which is capable of competing with the ssDSSCs in which the titania photoanodes are typically fabricated using hydrothermal synthesis in combination with screen-printing.

Although the length scales of the nanostructures and the thickness of the titania films can be tuned effectively via spray coating, this deposition technique contains kinetic processes with great complexity. In the present work, the structural evolution of the titania/PS-b-PEO composite films is successfully monitored by in situ grazing incidence small angle x-ray scattering (GISAXS) measurements during spray deposition. This is the

first time to document the spray-coating kinetics upon a block copolymer assisted sol-gel system. The GISAXS results show that irrespective of nanoparticle incorporation the size of the small titania/PEO clusters stays constant, whereas the size of the large titania/PEO clusters decreases over time. Also, the influence of different deposition methods for spiro-OMeTAD layers on the photovoltaic performance of ssDSSCs is studied. The results demonstrate that solution casting gives a higher degree of spiro-OMeTAD infiltration than spin coating, and thereby a better photovoltaic performance. Depending on the modification of titania photoanodes with nanoparticles and solution casting of the spiro-OMeTAD layer, the performance of ssDSSCs is optimized. The investigation shows that ssDSSCs can be manufactured with large-scale manufacturing methods, namely spray coating and solution casting which are examined in the present thesis.

Aside from titania nanostructures, the influence of mesopores of titania photoanodes on solar cell performance and stability is studied as well. The different pore sizes of titania films are realized by applying the template polymers with different chain lengths in the block copolymer assisted sol-gel synthesis. Not only a precise control over the pore size is achieved, but also the ordered pore arrays are established in this work. After P3HT backfilling, the evolution of the polymer crystalline order under continuous solar illumination is investigated by in situ grazing incidence wide angle x-ray scattering (GIWAXS) measurements. The stability of the P3HT crystalline order is compared for the first time under different confinement effects (inside two differently sized mesopore scaffolds). The results show that the P3HT crystallization inside the small titania mesopores is similar to that in P3HT:PCBM films and the volume fraction of P3HT crystalline regions decreases along with solar illumination, while the large pores induce P3HT polymorphism, i.e. two types of crystals are present, and the volume fraction of P3HT crystalline regions stay unchanged over illumination time. As a consequence, ssDSSCs featured with large pores have a higher  $J_{sc}$  stability than the small-sized ssDSSCs. In addition, the solar cells with the large pores give a *PCE* of 2.95 %, which is top-ranking in terms of TiO<sub>2</sub>-D149-P3HT based ssDSSCs.

With aim for lowering production costs and environmental impact, a low-temperature route is established to fabricate hybrid solar cells. Due to lack of dye molecules, the thickness of the active layer is around 150 nm for hybrid solar cells, which is much thinner than for ssDSSCs. Therefore, artificial superstructures are introduced to mesoporous titania films to obtain more efficient titania photoanodes for hybrid solar cells. A comparison of nano-imprinted and original titania films is made, and the results show that titania nanostructures and mesopores are not affected by the nano-imprinting process. While a better ability of light harvesting is observed in the nano-imprinted active layer than in the original active layer. As a result, the nano-imprinted hybrid solar cells present higher

*PCE* than the original hybrid solar cells at various angles of light incidence. Moreover, the nano-imprinted hybrid solar cells have a *PCE* of 0.12 % at 5° incident angle of light, which is the first time to reach a *PCE* value over 0.1 % in dye-free titania/P3HT hybrid solar cells based on purely low-temperature processes.

On the basis of the present studies, several feasible aspects can be explored in future investigations. Firstly, since pre-synthesized crystalline titania nanoparticles have been successfully incorporated into template titania nanostructures in the present thesis, further modification of titania photoanodes is possible using nanoparticles with relatively larger size and different crystal phase such as rutile. The anatase crystals with a size in the range of 10 nm to 20 nm usually are more favorable for photovoltaic applications. The mixture of anatase and rutile titania, like P25, has demonstrated an excellent performance in photocatalysis applications. Secondly, a successful route of spray coating has been already established in fabrication of titania-based solar cells. Other large-scale deposition processes like inkjet printing or slot-die coating are surely promising methods for future investigations. Finally, hybrid solar cells have been successfully produced without high-temperature processing. Manufacturing hybrid solar cells on flexible polymer substrates would be an intriguing project. As most polymer substrates are not UV-resistant, other techniques are required to explore to extract polymer template from nanostructured titania films at low temperatures. The crystallinity of low-temperature-synthesized titania films is still too low, and therefore a route to improve the crystallinity, such as incorporating pre-synthesized crystalline titania nanoparticles into titania films at low temperatures, would be attractive as well.





# Bibliography

- [1] *Bp statistical review of world energy june 2016*. tech. rep., BP, London, 2016.
- [2] T. M. L. Wigley and S. C. B. Raper, “Interpretation of high projections for global-mean warming,” *Science*, vol. 293, pp. 451–454, 2001.
- [3] D. M. Chapin, C. S. Fuller, and G. L. Pearson, “A new silicon p-n junction photocell for converting solar radiation into electrical power,” *J. Appl. Phys.*, vol. 25, no. 5, pp. 676–677, 1954.
- [4] N. Naghavi, S. Spiering, M. Powalla, B. Cavana, and D. Lincot, “High-efficiency copper indium gallium diselenide (cigs) solar cells with indium sulfide buffer layers deposited by atomic layer chemical vapor deposition (alcvd),” *Prog. Photovolt: Res. Appl.*, vol. 11, no. 7, pp. 437–443, 2003.
- [5] G. Fulop, M. Doty, P. Meyers, J. Betz, and C. H. Liu, “High-efficiency electrodeposited cadmium telluride solar cells,” *Appl. Phys. Lett.*, vol. 40, no. 4, pp. 327–328, 1982.
- [6] J. Britt and C. Ferekides, “Thin-film cds/cdte solar cell with 15.8efficiency,” *Appl. Phys. Lett.*, vol. 62, no. 22, pp. 2851–2852, 1993.
- [7] C. K. Chiang, C. R. Fincher, Y. W. Park, A. J. Heeger, H. Shirakawa, E. J. Louis, S. C. Gau, and A. G. MacDiarmid, “Electrical conductivity in doped polyacetylene,” *Phys. Rev. Lett.*, vol. 39, no. 17, pp. 1098–1101, 1977.
- [8] A. Yella, H.-W. Lee, H. N. Tsao, C. Yi, A. K. Chandiran, M. K. Nazeeruddin, E. W.-G. Diau, C.-Y. Yeh, S. M. Zakeeruddin, and M. Grätzel, “Porphyrin-sensitized solar cells with cobalt (ii/iii)-based redox electrolyte exceed 12 percent efficiency,” *Science*, vol. 334, no. 6056, pp. 629–634, 2011.
- [9] W. S. Yang, J. H. Noh, N. J. Jeon, Y. C. Kim, S. Ryu, J. Seo, and S. I. Seok, “High-performance photovoltaic perovskite layers fabricated through intramolecular exchange,” *Science*, vol. 348, no. 6240, pp. 1234–1237, 2015.
- [10] A. L. Linsebigler, G. Lu, and J. T. Yates, “Photocatalysis on tio<sub>2</sub> surfaces: Principles, mechanisms, and selected results,” *Chem. Rev.*, vol. 95, no. 3, pp. 735–758, 1995.

- [11] M. A. Henderson, "Photooxidation of acetone on  $\text{tio}_2$  (110): Conversion to acetate via methyl radical ejection," *J. Phys. Chem. B*, vol. 109, no. 24, pp. 12062–12070, 2005.
- [12] S. Guldin, P. Kohn, M. Stefik, J. Song, G. Divitini, F. Ecarla, C. Ducati, U. Wiesner, and U. Steiner, "Self-cleaning antireflective optical coatings," *Nano Lett.*, vol. 13, no. 11, pp. 5329–5335, 2013.
- [13] P. Hartmann, D.-K. Lee, B. M. Smarsly, and J. Janek, "Mesoporous  $\text{tio}_2$ : Comparison of classical sol-gel and nanoparticle based photoelectrodes for the water splitting reaction," *ACS Nano*, vol. 4, no. 6, pp. 3147–3154, 2010.
- [14] Y. Liu and Y. Yang, "Recent progress of  $\text{tio}_2$ -Based anodes for li ion batteries," *J. Nanomater.*, vol. 2016, pp. 1–15, 2016.
- [15] L. Schmidt-Mende and M. Grätzel, " $\text{Tio}_2$  pore-filling and its effect on the efficiency of solid-state dye-sensitized solar cells," *Thin Solid Films*, vol. 500, no. 1-2, pp. 296–301, 2006.
- [16] H. Sirringhaus, P. J. Brown, R. H. Friend, M. M. Nielsen, K. Bechgaard, B. M. W. Langeveld-Voss, A. J. H. Spiering, R. A. J. Janssen, E. W. Meijer, P. Herwig, and D. M. de Leeuw, "Two-dimensional charge transport in self-organized, high-mobility conjugated polymers," *Nature*, vol. 401, no. 6754, pp. 685–688, 1999.
- [17] M. Kobashi and H. Takeuchi, "Inhomogeneity of spin-coated and cast non-regioregular poly(3-hexylthiophene) films. structures and electrical and photophysical properties," *Macromolecules*, vol. 31, no. 21, pp. 7273–7278, 1998.
- [18] T. Agostinelli, S. Lilliu, J. G. Labram, M. Campoy-Quiles, M. Hampton, E. Pires, J. Rawle, O. Bikondoa, D. D. C. Bradley, T. D. Anthopoulos, J. Nelson, and J. E. Macdonald, "Real-time investigation of crystallization and phase-segregation dynamics in p3Ht:pcbm solar cells during thermal annealing," *Adv. Funct. Mater.*, vol. 21, no. 9, pp. 1701–1708, 2011.
- [19] S. Guldin, S. Hüttner, P. Tiwana, M. C. Orilall, B. Ülgüt, M. Stefik, P. Docampo, M. Kolle, G. Divitini, C. Ducati, S. A. T. Redfern, H. J. Snaith, U. Wiesner, and U. Steiner, "Improved conductivity in dye-sensitized solar cells through block-copolymer confined  $\text{tio}_2$  crystallisation," *Energy Environ. Sci.*, vol. 4, no. 1, pp. 225–233, 2011.
- [20] C. Fournier, M. Dosièrre, M. H. J. Koch, and J. Roovers, "Morphological study and melting behavior of narrow molecular weight fractions of poly(aryl ether ether ketone) (peek) annealed from the glassy state," *Macromolecules*, vol. 31, no. 18, pp. 6266–6274, 1998.

- [21] A. Fromhold, "Stress in dielectric contact layers on metals," *Surf. Sci.*, vol. 29, no. 2, pp. 396–410, 1972.
- [22] L. Zhu, S. Z. D. Cheng, B. H. Calhoun, Q. Ge, R. P. Quirk, E. L. Thomas, B. S. Hsiao, F. Yeh, and B. Lotz, "Crystallization temperature-dependent crystal orientations within nanoscale confined lamellae of a self-assembled crystalline-amorphous diblock copolymer," *J. Am. Chem. Soc.*, vol. 122, no. 25, pp. 5957–5967, 2000.
- [23] M. A. Niedermeier, *Novel structuring routines of titania films for application in photovoltaics*. PhD thesis, TECHNISCHE UNIVERSITÄT MÜNCHEN, 2013.
- [24] P. J. Flory, "Thermodynamics of high polymer solutions," *J. Chem. Phys.*, vol. 10, no. 1, pp. 51–61, 1942.
- [25] M. L. Huggins, "Thermodynamic properties of solutions of long-chain compounds," *Ann. N.Y. Acad. Sci.*, vol. 43, no. 1, pp. 1–32, 1942.
- [26] M. D. Ward and M. J. Horner, "Structure and order in soft matter: symmetry transcending length scale," *CrystEngComm*, vol. 6, no. 67, p. 401, 2004.
- [27] Y. Mai and A. Eisenberg, "Self-assembly of block copolymers," *Chem. Soc. Rev.*, vol. 41, no. 18, pp. 5969–5985, 2012.
- [28] L. Corvazier, L. Messé, C. L. Salou, R. N. Young, J. P. A. Fairclough, and A. J. Ryan, "Lamellar phases and microemulsions in model ternary blends containing amphiphilic block copolymers," *J. Mater. Chem.*, vol. 11, no. 11, pp. 2864–2874, 2001.
- [29] G. Strobl, *The Physics of Polymers: Concepts for Understanding their Structures and Behavior*. Springer Berlin Heidelberg, 3 ed., 2007.
- [30] C. Deibel and V. Dyakonov, "Polymer-fullerene bulk heterojunction solar cells," *Rep. Prog. Phys.*, vol. 73, no. 9, p. 096401, 2010.
- [31] A. Yamakata, T.-a. Ishibashi, and H. Onishi, "Time-resolved infrared absorption study of nine  $\text{tio}_2$  photocatalysts," *Chem. Phys.*, vol. 339, no. 1-3, pp. 133–137, 2007.
- [32] M. Xu, Y. Gao, E. M. Moreno, M. Kunst, M. Muhler, Y. Wang, H. Idriss, and C. Wöll, "Photocatalytic activity of bulk  $\text{tio}_2$  Anatase and rutile single crystals using infrared absorption spectroscopy," *Phys. Rev. Lett.*, vol. 106, no. 13, pp. 138302–1–138302–4, 2011.
- [33] H. Tang, K. Prasad, R. Sanjinès, P. E. Schmid, and F. Lévy, "Electrical and optical properties of  $\text{tio}_2$  anatase thin films," *J. Appl. Phys.*, vol. 75, no. 4, pp. 2042–2047, 1994.

- [34] Q. Tay, X. Liu, Y. Tang, Z. Jiang, T. C. Sum, and Z. Chen, “Enhanced photocatalytic hydrogen production with synergistic two-phase anatase/brookite  $\text{TiO}_2$  Nanostructures,” *J. Phys. Chem. C*, vol. 117, no. 29, pp. 14973–14982, 2013.
- [35] A. Di Paola, M. Bellardita, and L. Palmisano, “Brookite, the least known  $\text{TiO}_2$  photocatalyst,” *Catalysts*, vol. 3, no. 1, pp. 36–73, 2013.
- [36] A. Beltrán, L. Gracia, and J. Andrés, “Density functional theory study of the brookite surfaces and phase transitions between natural titania polymorphs,” *J. Phys. Chem. B*, vol. 110, no. 46, pp. 23417–23423, 2006.
- [37] U. Diebold, “The surface science of titanium dioxide,” *Surf. Sci. Rep.*, vol. 48, no. 5-8, pp. 53–229, 2003.
- [38] L. Kavan, M. Grätzel, S. E. Gilbert, C. Klemen, and H. J. Scheel, “Electrochemical and photoelectrochemical investigation of single-crystal anatase,” *J. Am. Chem. Soc.*, vol. 118, no. 28, pp. 6716–6723, 1996.
- [39] D. Reyes-Coronado, G. Rodríguez-Gattorno, M. E. Espinosa-Pesqueira, C. Cab, R. de Coss, and G. Oskam, “Phase-pure  $\text{TiO}_2$  nanoparticles: anatase, brookite and rutile,” *Nanotechnology*, vol. 19, no. 14, p. 145605, 2008.
- [40] H. Tang, H. Berger, P. Schmid, F. Lévy, and G. Burri, “Photoluminescence in  $\text{TiO}_2$  anatase single crystals,” *Solid State Commun.*, vol. 87, no. 9, pp. 847–850, 1993.
- [41] D. O. Scanlon, C. W. Dunnill, J. Buckeridge, S. A. Shevlin, A. J. Logsdail, S. M. Woodley, C. R. A. Catlow, M. J. Powell, R. G. Palgrave, I. P. Parkin, and et al., “Band alignment of rutile and anatase  $\text{TiO}_2$ ,” *Nat. Mater.*, vol. 12, no. 9, pp. 798–801, 2013.
- [42] J. Zhang, P. Zhou, J. Liu, and J. Yu, “New understanding of the difference of photocatalytic activity among anatase, rutile and brookite  $\text{TiO}_2$ ,” *Phys. Chem. Chem. Phys.*, vol. 16, no. 38, pp. 20382–20386, 2014.
- [43] N. Satoh, T. Nakashima, K. Kamikura, and K. Yamamoto, “Quantum size effect in  $\text{TiO}_2$  nanoparticles prepared by finely controlled metal assembly on dendrimer templates,” *Nat. Nanotechnol.*, vol. 3, no. 2, pp. 106–111, 2008.
- [44] N. Serpone, D. Lawless, and R. Khairutdinov, “Size effects on the photophysical properties of colloidal anatase  $\text{TiO}_2$  Particles: Size quantization versus direct transitions in this indirect semiconductor?,” *J. Phys. Chem.*, vol. 99, no. 45, pp. 16646–16654, 1995.
- [45] I. Gur, N. A. Fromer, M. L. Geie, and A. P. Alivisatos, “Air-stable all-inorganic nanocrystal solar cells processed from solution,” *Science*, vol. 310, no. 5747, pp. 462–465, 2005.

- [46] C.-C. Wang and J. Y. Ying, "Sol-gel synthesis and hydrothermal processing of anatase and rutile titania nanocrystals," *Chem. Mater.*, vol. 11, no. 11, pp. 3113–3120, 1999.
- [47] P. Lim Soo and A. Eisenberg, "Preparation of block copolymer vesicles in solution," *J. Polym. Sci., Part B: Polym. Phys.*, vol. 42, no. 6, pp. 923–938, 2004.
- [48] D. Zhao, Q. Huo, J. Feng, B. F. Chmelka, and G. D. Stucky, "Nonionic triblock and star diblock copolymer and oligomeric surfactant syntheses of highly ordered, hydrothermally stable, mesoporous silica structures," *J. Am. Chem. Soc.*, vol. 120, no. 24, pp. 6024–6036, 1998.
- [49] C. J. Brinker, Y. Lu, A. Sellinger, and H. Fan, "Evaporation-induced self-assembly: Nanostructures made easy," *Adv. Mater.*, vol. 11, no. 7, pp. 579–585, 1999.
- [50] M. Rawolle, E. V. Braden, M. A. Niedermeier, D. Magerl, K. Sarkar, T. Fröschl, N. Hüsing, J. Perlich, and P. Müller-Buschbaum, "Low-temperature route to crystalline titania network structures in thin films," *ChemPhysChem*, vol. 13, no. 9, pp. 2412–2417, 2012.
- [51] L. Song, A. Abdelsamie, C. J. Schaffer, V. Körstgens, W. Wang, T. Wang, E. D. Indari, T. Fröschl, N. Hüsing, T. Haeberle, P. Lugli, S. Bernstorff, and P. Müller-Buschbaum, "A low temperature route toward hierarchically structured titania films for thin hybrid solar cells," *Adv. Funct. Mater.*, vol. 26, no. 39, pp. 7084–7093, 2016.
- [52] J. Franck and E. G. Dymond, "Elementary processes of photochemical reactions," *Trans. Faraday Soc.*, vol. 21, pp. 536–542, 1926.
- [53] E. Condon, "A theory of intensity distribution in band systems," *Phys. Rev.*, vol. 28, no. 6, pp. 1182–1201, 1926.
- [54] H. Gerischer and F. Willig, "Reaction of excited dye molecules at electrodes," *Physical and Chemical Applications of Dyestuffs, Topics in Current Chemistry*, vol. 61, pp. 31–84, 1976.
- [55] N. Robertson, "Optimizing dyes for dye-sensitized solar cells," *Angew. Chem. Int. Ed.*, vol. 45, no. 15, pp. 2338–2345, 2006.
- [56] T. A. Heimer, C. A. Bignozzi, and G. J. Meyer, "Molecular level photovoltaics: the electrooptical properties of metal cyanide complexes anchored to titanium dioxide," *J. Phys. Chem.*, vol. 97, no. 46, pp. 11987–11994, 1993.
- [57] A. Islam, H. Sugihara, K. Hara, L. P. Singh, R. Katoh, M. Yanagida, Y. Takahashi, S. Murata, H. Arakawa, and G. Fujihashi, "Dye sensitization of nanocrystalline titanium dioxide with square planar platinum(ii) diimine dithiolate complexes," *Inorg. Chem.*, vol. 40, no. 21, pp. 5371–5380, 2001.

- [58] G. M. Hasselmann and G. J. Meyer, "Diffusion-limited interfacial electron transfer with large apparent driving forces," *J. Phys. Chem. B*, vol. 103, no. 36, pp. 7671–7675, 1999.
- [59] T. Bessho, E. C. Constable, M. Graetzel, A. Hernandez Redondo, C. E. Housecroft, W. Kylberg, M. K. Nazeeruddin, M. Neuburger, and S. Schaffner, "An element of surprise—efficient copper-functionalized dye-sensitized solar cells," *Chem. Commun.*, no. 32, pp. 3717–3719, 2008.
- [60] S. Ferrere and B. A. Gregg, "Photosensitization of  $\text{TiO}_2$  by  $[\text{Fe}^{\text{I}}(2,2'\text{-bipyridine-4,4'-dicarboxylic acid})_2(\text{CN})_2]$ : Band selective electron injection from ultra-short-lived excited states," *J. Am. Chem. Soc.*, vol. 120, no. 4, pp. 843–844, 1998.
- [61] J. N. Clifford, E. Martínez-Ferrero, A. Viterisi, and E. Palomares, "Sensitizer molecular structure-device efficiency relationship in dye sensitized solar cells," *Chem. Soc. Rev.*, vol. 40, no. 3, pp. 1635–1646, 2011.
- [62] L. Giribabu, R. K. Kanaparthi, and V. Velkannan, "Molecular engineering of sensitizers for dye-sensitized solar cell applications," *Chem. Rec.*, vol. 12, no. 3, pp. 306–328, 2012.
- [63] T. Higashino and H. Imahori, "Porphyrins as excellent dyes for dye-sensitized solar cells: recent developments and insights," *Dalton Trans.*, vol. 44, no. 2, pp. 448–463, 2015.
- [64] M.-E. Ragoussi, M. Ince, and T. Torres, "Recent advances in phthalocyanine-based sensitizers for dye-sensitized solar cells," *Eur. J. Org. Chem.*, vol. 2013, no. 29, pp. 6475–6489, 2013.
- [65] J. M. Rehm, G. L. McLendon, Y. Nagasawa, K. Yoshihara, J. Moser, and M. Grätzel, "Femtosecond electron-transfer dynamics at a sensitizing dye-semiconductor ( $\text{TiO}_2$ ) interface," *J. Phys. Chem.*, vol. 100, no. 23, pp. 9577–9578, 1996.
- [66] W. Zhao, Y. Jun Hou, X. Song Wang, B. Wen Zhang, Y. Cao, R. Yang, W. Bo Wang, and X. Rui Xiao, "Study on squarylium cyanine dyes for photoelectric conversion," *Sol. Energy Mater. Sol. Cells*, vol. 58, no. 2, pp. 173–183, 1999.
- [67] S. Ferrere and B. A. Gregg, "Large increases in photocurrents and solar conversion efficiencies by UV illumination of dye sensitized solar cells," *J. Phys. Chem. B*, vol. 105, pp. 7602–7605, Aug 2001.
- [68] T. Horiuchi, H. Miura, and S. Uchida, "Highly-efficient metal-free organic dyes for dye-sensitized solar cells," *Chem. Commun.*, no. 24, pp. 3036–3037, 2003.

- [69] N. Kopidakis, N. R. Neale, K. Zhu, J. van de Lagemaat, and A. J. Frank, "Spatial location of transport-limiting traps in tio<sub>2</sub> nanoparticle films in dye-sensitized solar cells," *Appl. Phys. Lett.*, vol. 87, no. 20, pp. 202106–(1–3), 2005.
- [70] Y. Yang, K. Ri, A. Mei, L. Liu, M. Hu, T. Liu, X. Li, and H. Han, "The size effect of tio<sub>2</sub> nanoparticles on a printable mesoscopic perovskite solar cell," *J. Mater. Chem. A*, vol. 3, no. 17, pp. 9103–9107, 2015.
- [71] D. Poplavskyy and J. Nelson, "Nondispersive hole transport in amorphous films of methoxy-spirofluorene-arylamine organic compound," *J. Appl. Phys.*, vol. 93, no. 1, pp. 341–346, 2003.
- [72] H. J. Snaith and M. Grätzel, "Electron and hole transport through mesoporous tio<sub>2</sub> infiltrated with spiro-meotad," *Adv. Mater.*, vol. 19, no. 21, pp. 3643–3647, 2007.
- [73] A. Abate, T. Leijtens, S. Pathak, J. Teuscher, R. Avolio, M. E. Errico, J. Kirkpatrick, J. M. Ball, P. Docampo, I. McPherson, and H. J. Snaith, "Lithium salts as "redox active" p-type dopants for organic semiconductors and their impact in solid-state dye-sensitized solar cells," *Phys. Chem. Chem. Phys.*, vol. 15, no. 7, pp. 2572–2579, 2013.
- [74] J. Burschka, A. Dualeh, F. Kessler, E. Baranoff, N.-L. Cevey-Ha, C. Yi, M. K. Nazeeruddin, and M. Grätzel, "Tris(2-(1H-pyrazol-1-yl)pyridine)cobalt(iii) as p-type dopant for organic semiconductors and its application in highly efficient solid-state dye-sensitized solar cells," *J. Am. Chem. Soc.*, vol. 133, no. 45, pp. 18042–18045, 2011.
- [75] Z. Bao, A. Dodabalapur, and A. J. Lovinger, "Soluble and processable regioregular poly(3-hexylthiophene) for thin film field-effect transistor applications with high mobility," *Appl. Phys. Lett.*, vol. 69, no. 26, pp. 4108–4110, 1996.
- [76] H. Sirringhaus, "Integrated optoelectronic devices based on conjugated polymers," *Science*, vol. 280, no. 5370, pp. 1741–1744, 1998.
- [77] E. Lancelle-Beltran, P. Prené, C. Boscher, P. Belleville, P. Buvat, and C. Sanchez, "All-solid-state dye-sensitized nanoporous tio<sub>2</sub> Hybrid solar cells with high energy-conversion efficiency," *Adv. Mater.*, vol. 18, no. 19, pp. 2579–2582, 2006.
- [78] H. J. Snaith, R. Humphry-Baker, P. Chen, I. Cesar, S. M. Zakeeruddin, and M. Grätzel, "Charge collection and pore filling in solid-state dye-sensitized solar cells," *Nanotechnology*, vol. 19, no. 42, pp. 424003–1–12, 2008.

- [79] D. Moseguí González, V. Körstgens, Y. Yao, L. Song, G. Santoro, S. V. Roth, and P. Müller-Buschbaum, “Improved power conversion efficiency of p3Ht:pcbm organic solar cells by strong spin-orbit coupling-induced delayed fluorescence,” *Adv. Energy Mater.*, vol. 5, no. 8, p. 1401770, 2015.
- [80] C. J. Schaffer, C. M. Palumbiny, M. A. Niedermeier, C. Jendrzejewski, G. Santoro, S. V. Roth, and P. Müller-Buschbaum, “A direct evidence of morphological degradation on a nanometer scale in polymer solar cells,” *Adv. Mater.*, vol. 25, no. 46, pp. 6760–6764, 2013.
- [81] M. Tolan, *X-Ray Scattering from Soft-Matter Thin Films*. Springer Berlin Heidelberg, 1999.
- [82] H. Dosch, B. W. Batterman, and D. C. Wack, “Depth-controlled grazing-incidence diffraction of synchrotron x radiation,” *Phys. Rev. Lett.*, vol. 56, no. 11, pp. 1144–1147, 1986.
- [83] S. Miyake, S. Takagi, and F. Fujimoto, “The extinction rule for reflexions in symmetrical spot patterns of electron diffraction by crystals,” *Acta Cryst.*, vol. 13, no. 4, pp. 360–361, 1960.
- [84] A. Naudon, D. Babonneau, D. Thiaudière, and S. Lequien, “Grazing-incidence small-angle x-ray scattering applied to the characterization of aggregates in surface regions,” *Physica B: Condensed Matter*, vol. 283, no. 1-3, pp. 69–74, 2000.
- [85] P. Müller-Buschbaum, *Polymer Surfaces and Interfaces: Characterization, Modification and Applications*. Springer-Verlag Berlin Heidelberg, 2008.
- [86] P. Müller-Buschbaum, “Grazing incidence small-angle x-ray scattering: an advanced scattering technique for the investigation of nanostructured polymer films,” *Anal. Bioanal. Chem.*, vol. 376, no. 1, pp. 3–10, 2003.
- [87] G. Renaud, R. Lazzari, and F. Leroy, “Probing surface and interface morphology with grazing incidence small angle x-ray scattering,” *Surf. Sci. Rep.*, vol. 64, no. 8, pp. 255–380, 2009.
- [88] P. Müller-Buschbaum, “The active layer morphology of organic solar cells probed with grazing incidence scattering techniques,” *Adv. Mater.*, vol. 26, no. 46, pp. 7692–7709, 2014.
- [89] Z. Jiang, “Gixsgui: a matlab toolbox for grazing-incidence x-ray scattering data visualization and reduction, and indexing of buried three-dimensional periodic nanostructured films,” *J. Appl. Crystallogr.*, vol. 48, no. 3, pp. 917–926, 2015.



- 
- [90] C. M. Palumbiny, *Polymeric PEDOT:PSS electrodes for organic electronics: Understanding the conductivity-structure relation*. PhD thesis, TECHNISCHE UNIVERSITÄT MÜNCHEN, 2015.
- [91] R. Hosemann, W. Vogel, D. Weick, and F. J. Baltá Calleja, “Novel aspects of the real paracrystal,” *Acta Crystallogr., Sect. A: Found. Crystallogr.*, vol. 37, no. 1, pp. 85–91, 1981.
- [92] X. Jiang, T. Herricks, and Y. Xia, “Monodispersed spherical colloids of titania: Synthesis, characterization, and crystallization,” *Adv. Mater.*, vol. 15, no. 14, pp. 1205–1209, 2003.
- [93] X. Jiang, Y. Wang, T. Herricks, and Y. Xia, “Ethylene glycol-mediated synthesis of metal oxide nanowires,” *J. Mater. Chem.*, vol. 14, no. 4, pp. 695–703, 2004.
- [94] J. Geserick, *Synthese mesoskopisch organisierter Nanopartikel*. PhD thesis, Universität Ulm, Ulm, Germany, 2009.
- [95] R. Rossmanith, C. K. Weiss, J. Geserick, N. Hüsing, U. Hörmann, U. Kaiser, and K. Landfester, “Porous anatase nanoparticles with high specific surface area prepared by miniemulsion technique,” *Chem. Mater.*, vol. 20, no. 18, pp. 5768–5780, 2008.
- [96] Y. Denkwitz, M. Makosch, J. Geserick, U. Hörmann, S. Selve, U. Kaiser, N. Hüsing, and R. Behm, “Influence of the crystalline phase and surface area of the  $\text{TiO}_2$  support on the co oxidation activity of mesoporous  $\text{Au/TiO}_2$  catalysts,” *Appl. Catal. B: Environ.*, vol. 91, no. 1-2, pp. 470–480, 2009.
- [97] T. Horiuchi, H. Miura, K. Sumioka, and S. Uchida, “High efficiency of dye-sensitized solar cells based on metal-free indoline dyes,” *J. Am. Chem. Soc.*, vol. 126, no. 39, pp. 12218–12219, 2004.
- [98] S. Ito, S. Zakeeruddin, R. Humphry-Baker, P. Liska, R. Charvet, P. Comte, M. Nazeeruddin, P. Péchy, M. Takata, H. Miura, and et al., “High-efficiency organic-dye-sensitized solar cells controlled by nanocrystalline- $\text{TiO}_2$  electrode thickness,” *Adv. Mater.*, vol. 18, no. 9, pp. 1202–1205, 2006.
- [99] H.-M. Cheng and W.-F. Hsieh, “High-efficiency metal-free organic-dye-sensitized solar cells with hierarchical  $\text{ZnO}$  photoelectrode,” *Energy Environ. Sci.*, vol. 3, no. 4, pp. 442–447, 2010.
- [100] S. Ito, H. Miura, S. Uchida, M. Takata, K. Sumioka, P. Liska, P. Comte, P. Péchy, and M. Grätzel, “High-conversion-efficiency organic dye-sensitized solar cells with a novel indoline dye,” *Chem. Commun.*, no. 41, pp. 5194–5196, 2008.

- [101] A. Kay and M. Grätzel, “Artificial photosynthesis. 1. photosensitization of titania solar cells with chlorophyll derivatives and related natural porphyrins,” *J. Phys. Chem.*, vol. 97, no. 23, pp. 6272–6277, 1993.
- [102] U. Bach, D. Lupo, P. Comte, J. E. Moser, F. Weissörtel, J. Salbeck, H. Spreitzer, and M. Grätzel, “Solid-state dye-sensitized mesoporous  $\text{TiO}_2$  solar cells with high photon-to-electron conversion efficiencies,” *Nature*, vol. 395, no. 6702, pp. 583–585, 1998.
- [103] X. Zhang, Y. Xu, F. Giordano, M. Schreier, N. Pellet, Y. Hu, C. Yi, N. Robertson, J. Hua, S. M. Zakeeruddin, H. Tian, and M. Grätzel, “Molecular engineering of potent sensitizers for very efficient light harvesting in thin-film solid-state dye-sensitized solar cells,” *J. Am. Chem. Soc.*, vol. 138, no. 34, pp. 10742–10745, 2016.
- [104] T. Hoshikawa, T. Ikebe, R. Kikuchi, and K. Eguchi, “Effects of electrolyte in dye-sensitized solar cells and evaluation by impedance spectroscopy,” *Electrochim. Acta*, vol. 51, no. 25, pp. 5286–5294, 2006.
- [105] S. A. Haque, E. Palomares, B. M. Cho, A. N. M. Green, N. Hirata, D. R. Klug, and J. R. Durrant, “Charge separation versus recombination in dye-sensitized nanocrystalline solar cells : the minimization of kinetic redundancy,” *J. Am. Chem. Soc.*, vol. 127, no. 10, pp. 3456–3462, 2005.
- [106] H. Yu, S. Zhang, H. Zhao, G. Will, and P. Liu, “An efficient and low-cost  $\text{TiO}_2$  compact layer for performance improvement of dye-sensitized solar cells,” *Electrochim. Acta*, vol. 54, no. 4, pp. 1319–1324, 2009.
- [107] J. M. Szeifert, D. Fattakhova-Rohlfing, D. Georgiadou, V. Kalousek, J. Rathouský, D. Kuang, S. Wenger, S. M. Zakeeruddin, M. Grätzel, and T. Bein, ““brick and mortar” strategy for the formation of highly crystalline mesoporous titania films from nanocrystalline building blocks,” *Chem. Mater.*, vol. 21, no. 7, pp. 1260–1265, 2009.
- [108] B. Mandlmeier, N. K. Minar, J. M. Feckl, D. Fattakhova-Rohlfing, and T. Bein, “Tuning the crystallinity parameters in macroporous titania films,” *J. Mater. Chem. A*, vol. 2, no. 18, pp. 6504–6511, 2014.
- [109] L. Song, W. Wang, V. Körstgens, D. Moseguí González, Y. Yao, N. K. Minar, J. M. Feckl, K. Peters, T. Bein, D. Fattakhova-Rohlfing, G. Santoro, S. V. Roth, and P. Müller-Buschbaum, “Spray deposition of titania films with incorporated crystalline nanoparticles for all-solid-state dye-sensitized solar cells using p3ht,” *Adv. Funct. Mater.*, vol. 26, no. 10, pp. 1498–1506, 2016.

- [110] Y.-J. Cheng and J. S. Gutmann, "Morphology phase diagram of ultrathin anatase  $\text{TiO}_2$  films templated by a single ps-*b*-peo block copolymer," *J. Am. Chem. Soc.*, vol. 128, no. 14, pp. 4658–4674, 2006.
- [111] Z. Zainal and C. Y. Lee, "Properties and photoelectrocatalytic behaviour of sol-gel derived  $\text{TiO}_2$  thin films," *J. Sol-Gel Sci. Technol.*, vol. 37, no. 1, p. 19–25, 2006.
- [112] K. Liu, W. Zhou, K. Shi, L. Li, L. Zhang, M. Zhang, and H. Fu, "Influence of calcination temperatures on the photocatalytic activity and photo-induced hydrophilicity of wormhole-like mesoporous  $\text{TiO}_2$ ," *Nanotechnology*, vol. 17, no. 5, p. 1363–1369, 2006.
- [113] S. Costacurta, G. D. Maso, R. Gallo, M. Guglielmi, G. Brusatin, and P. Falcaro, "Influence of temperature on the photocatalytic activity of sol-gel  $\text{TiO}_2$  films," *ACS Appl. Mater. Interfaces*, vol. 2, no. 5, pp. 1294–1298, 2010.
- [114] L. Cao, D. Chen, W. Li, and R. A. Caruso, "Hierarchically porous titania networks with tunable anatase:rutile ratios and their enhanced photocatalytic activities," *ACS Appl. Mater. Interfaces*, vol. 6, no. 15, pp. 13129–13137, 2014.
- [115] P. Müller-Buschbaum, "Influence of surface cleaning on dewetting of thin polystyrene films," *Eur. Phys. J. E Soft Matter*, vol. 12, no. 3, pp. 443–448, 2003.
- [116] D. W. Schubert and T. Dunkel, "Spin coating from a molecular point of view: its concentration regimes, influence of molar mass and distribution," *Mater. Res. Innovations*, vol. 7, no. 5, pp. 314–321, 2003.
- [117] E. J. Lavernia and Y. Wu, "Spray atomization and deposition," *Wiley*, vol. 0, no. 5, pp. 314–321, 1996.
- [118] P. Jenny, D. Roekaerts, and N. Beishuizen, "Modeling of turbulent dilute spray combustion," *Prog. Energy Combust. Sci.*, vol. 38, no. 6, pp. 846–887, 2012.
- [119] H. Hu and R. G. Larson, "Marangoni effect reverses coffee-ring depositions," *J. Phys. Chem. B*, vol. 110, no. 14, pp. 7090–7094, 2006.
- [120] S. Ito, T. N. Murakami, P. Comte, P. Liska, C. Grätzel, M. K. Nazeeruddin, and M. Grätzel, "Fabrication of thin film dye sensitized solar cells with solar to electric power conversion efficiency over 10 %," *Thin Solid Films*, vol. 516, no. 14, pp. 4613–4619, 2008.
- [121] S. Guo, J. Ning, V. Körstgens, Y. Yao, E. M. Herzig, S. V. Roth, and P. Müller-Buschbaum, "The effect of fluorination in manipulating the nanomorphology in  $\text{p}^+\text{b}^7\text{:pc}^7\text{1bm}$  bulk heterojunction systems," *Adv. Energy Mater.*, vol. 5, no. 4, p. 1401315, 2014.

- [122] W. Wang, S. Pröller, M. A. Niedermeier, V. Körstgens, M. Philipp, B. Su, D. Moseguí González, S. Yu, S. V. Roth, and P. Müller-Buschbaum, "Development of the morphology during functional stack build-up of p3Ht:pcbm bulk heterojunction solar cells with inverted geometry," *ACS Appl. Mater. Interfaces*, vol. 7, no. 1, p. 602–610, 2015.
- [123] M. A. Ruderer, S. Guo, R. Meier, H.-Y. Chiang, V. Körstgens, J. Wiedersich, J. Perlich, S. V. Roth, and P. Müller-Buschbaum, "Solvent-induced morphology in polymer-based systems for organic photovoltaics," *Adv. Funct. Mater.*, vol. 21, no. 17, pp. 3382–3391, 2011.
- [124] Y. Yuan, T. J. Reece, P. Sharma, S. Poddar, S. Ducharme, A. Gruverman, Y. Yang, and J. Huang, "Efficiency enhancement in organic solar cells with ferroelectric polymers," *Nat. Mater.*, vol. 10, no. 4, pp. 296–302, 2011.
- [125] P. Peumans, S. Uchida, and S. R. Forrest, "Efficient bulk heterojunction photovoltaic cells using small-molecular-weight organic thin films," *Nature*, vol. 425, no. 6954, pp. 158–162, 2003.
- [126] Z. Liu, J. Li, and F. Yan, "Package-free flexible organic solar cells with graphene top electrodes," *Adv. Mater.*, vol. 25, no. 31, pp. 4296–4301, 2013.
- [127] G. Dennler, M. C. Scharber, and C. J. Brabec, "Polymer-fullerene bulk-heterojunction solar cells," *Adv. Mater.*, vol. 21, no. 13, pp. 1323–1338, 2009.
- [128] K. Norrman and F. C. Krebs, "Lifetimes of organic photovoltaics: Using tof-sims and  $^{18}\text{O}$  isotopic labelling to characterise chemical degradation mechanisms," *Sol. Energy Mater. Sol. Cells*, vol. 90, no. 2, pp. 213–227, 2006.
- [129] K. Norrman, S. A. Gevorgyan, and F. C. Krebs, "Water-induced degradation of polymer solar cells studied by  $h_2$   $^{18}\text{O}$  labeling," *ACS Appl. Mater. Interfaces*, vol. 1, no. 1, pp. 102–112, 2009.
- [130] H. J. Snaith, A. J. Moule, C. Klein, K. Meerholz, R. H. Friend, and M. Grätzel, "Efficiency enhancements in solid-state hybrid solar cells via reduced charge recombination and increased light capture," *Nano Lett.*, vol. 7, no. 11, pp. 3372–3376, 2007.
- [131] A. H. Ip, S. M. Thon, S. Hoogland, O. Voznyy, D. Zhitomirsky, R. Debnath, L. Levina, L. R. Rollny, G. H. Carey, A. Fischer, K. W. Kemp, I. J. Kramer, A. J. Ning, Zhijun and Labelle, K. W. Chou, A. Amassian, and E. H. Sargent, "Hybrid passivated colloidal quantum dot solids," *Nat. Nanotechnol.*, vol. 7, no. 9, pp. 577–582, 2012.

- [132] X. Liu, W. Zhang, S. Uchida, L. Cai, B. Liu, and S. Ramakrishna, "An efficient organic-dye-sensitized solar cell with in situ polymerized poly(3,4-ethylenedioxythiophene) as a hole-transporting material," *Adv. Mater.*, vol. 22, no. 20, pp. E150–E155, 2010.
- [133] K.-J. Jiang, K. Manseki, Y.-H. Yu, N. Masaki, K. Suzuki, Y.-I. Song, and S. Yanagida, "Photovoltaics based on hybridization of effective dye-sensitized titanium oxide and hole-conductive polymer p3ht," *Adv. Funct. Mater.*, vol. 19, no. 15, pp. 2481–2485, 2009.
- [134] K. Sarkar, C. J. Schaffer, D. Moseguí González, A. Naumann, J. Perlich, and P. Müller-Buschbaum, "Tuning the pore size of zno nano-grids via time-dependent solvent annealing," *J. Mater. Chem. A*, vol. 2, no. 19, pp. 6945–6951, 2014.
- [135] J. H. Heo, S. H. Im, J. H. Noh, T. N. Mandal, C.-S. Lim, J. A. Chang, Y. H. Lee, H.-j. Kim, A. Sarkar, M. K. Nazeeruddin, M. Grätzel, and S. I. Seok, "Efficient inorganic–organic hybrid heterojunction solar cells containing perovskite compound and polymeric hole conductors," *Nat. Photonics*, vol. 7, no. 6, pp. 486–491, 2013.
- [136] J. Burschka, N. Pellet, S.-J. Moon, R. Humphry-Baker, P. Gao, M. K. Nazeeruddin, and M. Grätzel, "Sequential deposition as a route to high-performance perovskite-sensitized solar cells," *Nature*, vol. 499, no. 7458, pp. 316–319, 2013.
- [137] M. Liu, M. B. Johnston, and H. J. Snaith, "Efficient planar heterojunction perovskite solar cells by vapour deposition," *Nature*, vol. 501, no. 7467, pp. 395–398, 2013.
- [138] Y. Li, M. Guo, M. Zhang, and X. Wang, "Hydrothermal synthesis and characterization of tio2 nanorod arrays on glass substrates," *Mater. Res. Bull.*, vol. 44, no. 6, pp. 1232–1237, 2009.
- [139] M.-C. Yang, Y.-Y. Lee, B. Xu, K. Powers, and Y. S. Meng, "Tio2 flakes as anode materials for li-ion-batteries," *J. Power Sources*, vol. 207, pp. 166–172, 2012.
- [140] J. Jitputti, Y. Suzuki, and S. Yoshikawa, "Synthesis of tio2 nanowires and their photocatalytic activity for hydrogen evolution," *Catal. Commun.*, vol. 9, no. 6, pp. 1265–1271, 2008.
- [141] M. A. Niedermeier, D. Magerl, Q. Zhong, A. Nathan, V. Körstgens, J. Perlich, S. V. Roth, and P. Müller-Buschbaum, "Combining mixed titania morphologies into a complex assembly thin film by iterative block-copolymer-based sol-gel templating," *Nanotechnology*, vol. 23, no. 14, p. 145602, 2012.

- [142] M. Rawolle, M. A. Niedermeier, G. Kaune, J. Perlich, P. Lellig, M. Memesa, Y.-J. Cheng, J. S. Gutmann, and P. Müller-Buschbaum, "Fabrication and characterization of nanostructured titania films with integrated function from inorganic-organic hybrid materials," *Chem. Soc. Rev.*, vol. 41, no. 15, p. 5131, 2012.
- [143] A. Revaux, G. Dantelle, D. Decanini, F. Guillemot, A.-M. Haghiri-Gosnet, C. Weisbuch, J.-P. Boilot, T. Gacoin, and H. Benisty, "Photonic crystal patterning of luminescent sol-gel films for light extraction," *Nanotechnology*, vol. 22, no. 36, p. 365701, 2011.
- [144] P. Kubiak, T. Fröschl, N. Hüsing, U. Hörmann, U. Kaiser, R. Schiller, C. K. Weiss, K. Landfester, and M. Wohlfahrt-Mehrens, "TiO<sub>2</sub> Anatase nanoparticle networks: Synthesis, structure, and electrochemical performance," *Small*, vol. 7, no. 12, pp. 1690–1696, 2011.
- [145] S. Colodrero, A. Mihi, L. Häggman, M. Ocaña, G. Boschloo, A. Hagfeldt, and H. Míguez, "Porous one-dimensional photonic crystals improve the power-conversion efficiency of dye-sensitized solar cells," *Adv. Mater.*, vol. 21, no. 7, pp. 764–770, 2009.
- [146] G. Kaune, M. Memesa, R. Meier, M. A. Ruderer, A. Diethert, S. V. Roth, M. D'Acunzi, J. S. Gutmann, and P. Müller-Buschbaum, "Hierarchically structured titania films prepared by polymer/colloidal templating," *ACS Appl. Mater. Interfaces*, vol. 1, no. 12, pp. 2862–2869, 2009.
- [147] P. Müller-Buschbaum, E. Bauer, O. Wunnicke, and M. Stamm, "The control of thin film morphology by the interplay of dewetting, phase separation and microphase separation," *J. Phys.: Condens. Matter*, vol. 17, no. 9, pp. S363–S386, 2005.
- [148] B. Lee, I. Park, J. Yoon, S. Park, J. Kim, K.-W. Kim, T. Chang, and M. Ree, "Structural analysis of block copolymer thin films with grazing incidence small-angle x-ray scattering," *Macromolecules*, vol. 38, no. 10, pp. 4311–4323, 2005.
- [149] A. J. Haring, S. R. Ahrenholtz, and A. J. Morris, "Rethinking band bending at the p3Ht-tio<sub>2</sub> interface," *ACS Appl. Mater. Interfaces*, vol. 6, no. 6, pp. 4394–4401, 2014.
- [150] C. Anselmi, E. Mosconi, M. Pastore, E. Ronca, and F. De Angelis, "Adsorption of organic dyes on tio<sub>2</sub> surfaces in dye-sensitized solar cells: interplay of theory and experiment," *Phys. Chem. Chem. Phys.*, vol. 14, no. 46, pp. 15963–15974, 2012.
- [151] B. O'Regan, L. Xiaoe, and T. Ghaddar, "Dye adsorption, desorption, and distribution in mesoporous tio<sub>2</sub> films, and its effects on recombination losses in dye sensitized solar cells," *Energy Environ. Sci.*, vol. 5, no. 5, p. 7203, 2012.

- [152] B. O'Regan and M. Grätzel, "A low-cost, high-efficiency solar cell based on dye-sensitized colloidal  $\text{TiO}_2$  films," *Nature*, vol. 353, no. 6346, pp. 737–740, 1991.
- [153] M. Grätzel, "Dye-sensitized solar cells," *J. Photochem. Photobiol. C: Photochem. Rev.*, vol. 4, no. 2, pp. 145–153, 2003.
- [154] T. W. Hamann, R. A. Jensen, A. B. F. Martinson, H. Van Ryswyk, and J. T. Hupp, "Advancing beyond current generation dye-sensitized solar cells," *Energy Environ. Sci.*, vol. 1, no. 1, pp. 66–78, 2008.
- [155] W. A. Hamilton, "Conformation, directed self-assembly and engineered modification: some recent near surface structure determinations by grazing incidence small angle x-ray and neutron scattering," *Curr. Opin. Colloid Interface Sci.*, vol. 9, no. 6, pp. 390–395, 2005.
- [156] J. Perlich, G. Kaune, M. Memesa, J. S. Gutmann, and P. Müller-Buschbaum, "Sponge-like structures for application in photovoltaics," *Philos. Trans. R. Soc. London, Ser. A*, vol. 367, no. 1894, pp. 1783–1798, 2009.
- [157] A. Buffet, A. Rothkirch, R. Döhrmann, V. Körstgens, M. M. Abul Kashem, J. Perlich, G. Herzog, M. Schwartzkopf, R. Gehrke, P. Müller-Buschbaum, and S. V. Roth, "P03, the microfocus and nanofocus x-ray scattering (minaxs) beamline of the PETra iii storage ring: the microfocus endstation," *J. Synchrotron Rad.*, vol. 19, no. 4, pp. 647–653, 2012.
- [158] Y. Yoneda, "Anomalous surface reflection of x rays," *Phys. Rev.*, vol. 131, no. 5, pp. 2010–2013, 1963.
- [159] M. Rauscher, R. Paniago, H. Metzger, Z. Kovats, J. Domke, J. Peisl, H.-D. Pfannes, J. Schulze, and I. Eisele, "Grazing incidence small angle x-ray scattering from free-standing nanostructures," *J. Appl. Phys.*, vol. 86, no. 12, p. 6763, 1999.
- [160] J. S. Pedersen, "Determination of size distribution from small-angle scattering data for systems with effective hard-sphere interactions," *J. Appl. Crystallogr.*, vol. 27, no. 4, pp. 595–608, 1994.
- [161] S. K. Sinha, E. B. Sirota, S. Garoff, and H. B. Stanley, "X-ray and neutron scattering from rough surfaces," *Phys. Rev. B*, vol. 38, no. 4, pp. 2297–2311, 1988.
- [162] T. Salditt, T. H. Metzger, J. Peisl, B. Reinker, M. Moske, and K. Samwer, "Determination of the height-height correlation function of rough surfaces from diffuse x-ray scattering," *Europhys. Lett.*, vol. 32, no. 4, pp. 331–336, 1995.
- [163] R. Lazzari, "Isgisax: a program for grazing-incidence small-angle x-ray scattering analysis of supported islands," *J. Appl. Crystallogr.*, vol. 35, no. 4, pp. 406–421, 2002.

- [164] K. Sarkar, C. J. Schaffer, D. M. González, A. Naumann, J. Perlich, and P. Müller-Buschbaum, "Tuning the pore size of zno nano-grids via time-dependent solvent annealing," *J. Mater. Chem. A*, vol. 2, no. 19, pp. 6945–6951, 2014.
- [165] S. Y. Choi, M. Mamak, S. Speakman, N. Chopra, and G. A. Ozin, "Evolution of nanocrystallinity in periodic mesoporous anatase thin films," *Small*, vol. 1, no. 2, pp. 226–232, 2005.
- [166] S. Das, Q. Wu, R. K. Garlapalli, S. Nagpure, J. Strzalka, Z. Jiang, and S. E. Rankin, "In-situ GISaxs investigation of pore orientation effects on the thermal transformation mechanism in mesoporous titania thin films," *J. Phys. Chem. C*, vol. 118, no. 2, pp. 968–976, 2014.
- [167] M. Stefik, J. Song, H. Sai, S. Guldin, P. Boldrighini, M. C. Orilall, U. Steiner, S. M. Gruner, and U. Wiesner, "Ordered mesoporous titania from highly amphiphilic block copolymers: tuned solution conditions enable highly ordered morphologies and ultra-large mesopores," *J. Mater. Chem. A*, vol. 3, no. 21, pp. 11478–11492, 2015.
- [168] C. Karakaya, Y. Türker, and O. Dag, "Molten-salt-assisted self-assembly (masa)-synthesis of mesoporous metal titanate-titania, metal sulfide-titania, and metal selenide-titania thin films," *Adv. Funct. Mater.*, vol. 23, no. 32, pp. 4002–4010, 2013.
- [169] D. Fattakhova-Rohlfing, A. Zaleska, and T. Bein, "Three-dimensional titanium dioxide nanomaterials," *Chem. Rev.*, vol. 114, no. 19, pp. 9487–9558, 2014.
- [170] D. Grosso, G. J. d. A. A. Soler-Illia, E. L. Crepaldi, F. Cagnol, C. Sinturel, A. Bourgeois, A. Brunet-Bruneau, H. Amenitsch, P. A. Albouy, and C. Sanchez, "Highly porous tio<sub>2</sub> Anatase optical thin films with cubic mesostructure stabilized at 700 °c," *Chem. Mater.*, vol. 15, no. 24, pp. 4562–4570, 2003.
- [171] G. Leofanti, M. Padovan, G. Tozzola, and B. Venturelli, "Surface area and pore texture of catalysts," *Catal. Today*, vol. 41, no. 1-3, pp. 207–219, 1998.
- [172] A. Baeza, E. Guisasola, E. Ruiz-Hernández, and M. Vallet-Regí, "Magnetically triggered multidrug release by hybrid mesoporous silica nanoparticles," *Chem. Mater.*, vol. 24, no. 3, pp. 517–524, 2012.
- [173] A. El-Toni, M. Ibrahim, J. Labis, A. Khan, and M. Alhoshan, "Optimization of synthesis parameters for mesoporous shell formation on magnetic nanocores and their application as nanocarriers for docetaxel cancer drug," *Int. J. Mol. Sci.*, vol. 14, no. 6, pp. 11496–11509, 2013.



- [174] J. Zhang, P. Zhou, J. Liu, and J. Yu, "New understanding of the difference of photocatalytic activity among anatase, rutile and brookite tio 2," *Phys. Chem. Chem. Phys.*, vol. 16, no. 38, pp. 20382–20386, 2014.
- [175] H. G. Yang, C. H. Sun, S. Z. Qiao, J. Zou, G. Liu, S. C. Smith, H. M. Cheng, and G. Q. Lu, "Anatase tio2 single crystals with a large percentage of reactive facets," *Nature*, vol. 453, no. 7195, pp. 638–641, 2008.
- [176] A. Sclafani and J. M. Herrmann, "Comparison of the photoelectronic and photocatalytic activities of various anatase and rutile forms of titania in pure liquid organic phases and in aqueous solutions," *J. Phys. Chem.*, vol. 100, no. 32, pp. 13655–13661, 1996.
- [177] D. Fattakhova-Rohlfing, M. Wark, T. Brezesinski, B. M. Smarsly, and J. Rathouský, "Highly organized mesoporous tio2 Films with controlled crystallinity: A li-insertion study," *Adv. Funct. Mater.*, vol. 17, no. 1, pp. 123–132, 2007.
- [178] Z. Zhang, X. Zhong, S. Liu, D. Li, and M. Han, "Aminolysis route to monodisperse titania nanorods with tunable aspect ratio," *Angew. Chem. Int. Ed.*, vol. 44, no. 22, pp. 3466–3470, 2005.
- [179] X. Wang, G. Liu, L. Wang, J. Pan, G. Q. M. Lu, and H.-M. Cheng, "Tio 2 films with oriented anatase 001 facets and their photoelectrochemical behavior as cds nanoparticle sensitized photoanodes," *J. Mater. Chem.*, vol. 21, no. 3, pp. 869–873, 2011.
- [180] H. J. Snaith and M. Grätzel, "Electron and hole transport through mesoporous tio2 infiltrated with spiro-meotad," *Adv. Mater.*, vol. 19, no. 21, pp. 3643–3647, 2007.
- [181] Y.-C. Tu, J.-F. Lin, W.-C. Lin, C.-P. Liu, J.-J. Shyue, and W.-F. Su, "Improving the electron mobility of tio2 nanorods for enhanced efficiency of a polymer-nanoparticle solar cell," *CrystEngComm*, vol. 14, no. 14, p. 4772, 2012.
- [182] P. Tiwana, P. Docampo, M. B. Johnston, H. J. Snaith, and L. M. Herz, "Electron mobility and injection dynamics in mesoporous zno, sno 2 , and tio 2 Films used in dye-sensitized solar cells," *ACS Nano*, vol. 5, no. 6, pp. 5158–5166, 2011.
- [183] M. Rawolle, K. Sarkar, M. A. Niedermeier, M. Schindler, P. Lellig, J. S. Gutmann, J.-F. o. Moulin, M. Haese-Seiller, A. S. Wochnik, C. Scheu, and P. Müller-Buschbaum, "Infiltration of polymer hole-conductor into mesoporous titania structures for solid-state dye-sensitized solar cells," *ACS Appl. Mater. Interfaces*, vol. 5, no. 3, pp. 719–729, 2013.

- [184] S. Sista, M.-H. Park, Z. Hong, Y. Wu, J. Hou, W. L. Kwan, G. Li, and Y. Yang, "Highly efficient tandem polymer photovoltaic cells," *Adv. Mater.*, vol. 22, no. 3, pp. 380–383, 2010.
- [185] Z. Hu, J. Zhang, Z. Hao, and Y. Zhao, "Influence of doped pedot:pss on the performance of polymer solar cells," *Sol. Energy Mater. Sol. Cells*, vol. 95, no. 10, pp. 2763–2767, 2011.
- [186] Y. Liao, W. Que, Q. Jia, Y. He, J. Zhang, and P. Zhong, "Controllable synthesis of brookite/anatase/rutile tio<sub>2</sub> nanocomposites and single-crystalline rutile nanorods array," *J. Mater. Chem.*, vol. 22, no. 16, pp. 7937–7944, 2012.
- [187] E.-Y. Kim, D. S. Kim, and B.-T. Ahn, "Synthesis of mesoporous tio<sub>2</sub> and its application to photocatalytic activation of methylene blue and e. coli," *Bull. Korean Chem. Soc.*, vol. 30, no. 1, pp. 193–196, 2009.
- [188] X. Wang, G. Liu, L. Wang, J. Pan, G. Q. M. Lu, and H.-M. Cheng, "Tio<sub>2</sub> films with oriented anatase 001 facets and their photoelectrochemical behavior as cds nanoparticle sensitized photoanodes," *J. Mater. Chem.*, vol. 21, no. 3, pp. 869–873, 2011.
- [189] W.-P. Liao, S.-C. Hsu, W.-H. Lin, and J.-J. Wu, "Hierarchical tio<sub>2</sub> Nanostructured array/p3Ht hybrid solar cells with interfacial modification," *J. Phys. Chem. C*, vol. 116, no. 30, pp. 15938–15945, 2012.
- [190] M. Ye, X. Wen, M. Wang, J. Iocozzia, N. Zhang, C. Lin, and Z. Lin, "Recent advances in dye-sensitized solar cells: from photoanodes, sensitizers and electrolytes to counter electrodes," *Mater. Today*, vol. 18, no. 3, pp. 155–162, 2015.
- [191] L. Song, W. Wang, V. Körstgens, D. Moseguí González, F. C. Löhner, C. J. Schaffer, J. Schlipf, K. Peters, T. Bein, D. Fattakhova-Rohlfing, S. V. Roth, and P. Müller-Buschbaum, "In situ study of spray deposited titania photoanodes for scalable fabrication of solid-state dye-sensitized solar cells," *submitted for review*, 2017.
- [192] B. E. Hardin, H. J. Snaith, and M. D. McGehee, "The renaissance of dye-sensitized solar cells," *Nat. Photonics*, vol. 6, no. 3, pp. 162–169, 2012.
- [193] E. A. Barringer and H. K. Bowen, "High-purity, monodisperse tio<sub>2</sub> powders by hydrolysis of titanium tetraethoxide. 1. synthesis and physical properties," *Langmuir*, vol. 1, no. 4, pp. 414–420, 1985.
- [194] C. Kormann, D. W. Bahnemann, and M. R. Hoffmann, "Preparation and characterization of quantum-size titanium dioxide," *J. Phys. Chem.*, vol. 92, no. 18, pp. 5196–5201, 1988.

- [195] M. Andersson, L. Österlund, S. Ljungström, and A. Palmqvist, "Preparation of nanosize anatase and rutile  $\text{TiO}_2$  by hydrothermal treatment of microemulsions and their activity for photocatalytic wet oxidation of phenol," *J. Phys. Chem. B*, vol. 106, no. 41, pp. 10674–10679, 2002.
- [196] J. Yang, S. Mei, and J. M. F. Ferreira, "Hydrothermal synthesis of nanosized titania powders: Influence of peptization and peptizing agents on the crystalline phases and phase transitions," *J. Am. Chem. Soc.*, vol. 83, no. 6, pp. 1361–1368, 2000.
- [197] X. Wang, J. Zhuang, Q. Peng, and Y. Li, "A general strategy for nanocrystal synthesis," *Nature*, vol. 437, no. 7055, pp. 121–124, 2005.
- [198] B. Wen, C. Liu, and Y. Liu, "Depositional characteristics of metal coating on single-crystal  $\text{TiO}_2$  Nanowires," *J. Phys. Chem. B*, vol. 109, no. 25, pp. 12372–12375, 2005.
- [199] J.-M. Wu, "Low-temperature preparation of titania nanorods through direct oxidation of titanium with hydrogen peroxide," *J. Cryst. Growth*, vol. 269, no. 2-4, pp. 347–355, 2004.
- [200] X. Peng and A. Chen, "Aligned  $\text{TiO}_2$  nanorod arrays synthesized by oxidizing titanium with acetone," *J. Mater. Chem.*, vol. 14, no. 16, p. 2542, 2004.
- [201] J. Zhao, X. Wang, R. Chen, and L. Li, "Fabrication of titanium oxide nanotube arrays by anodic oxidation," *Solid State Commun.*, vol. 134, no. 10, pp. 705–710, 2005.
- [202] Y.-J. Cheng, S. Zhou, and J. S. Gutmann, "Morphology transition in ultrathin titania films: From pores to lamellae," *Macromol. Rapid Commun.*, vol. 28, no. 13, pp. 1392–1396, 2007.
- [203] N. Steunou, S. Förster, P. Florian, C. Sanchez, and M. Antonietti, "Synthesis of nanostructured polymer-titanium oxide composites through the assembly of titanium-oxo clusters and amphiphilic block copolymers micelles," *J. Mater. Chem.*, vol. 12, no. 12, pp. 3426–3430, 2002.
- [204] M. Yin, Y. Cheng, M. Liu, J. Gutmann, and K. Müllen, "Nanostructured  $\text{TiO}_2$  Films templated by amphiphilic dendritic core-double-shell macromolecules: From isolated nanorings to continuous 2D mesoporous networks," *Angew. Chem. Int. Ed.*, vol. 47, no. 44, pp. 8400–8403, 2008.
- [205] A. Choucair and A. Eisenberg, "Control of amphiphilic block copolymer morphologies using solution conditions," *Eur. Phys. J. E Soft Matter*, vol. 10, no. 1, pp. 37–44, 2003.

- [206] S. Guldin, S. Hüttner, M. Kolle, M. E. Welland, P. Müller-Buschbaum, R. H. Friend, U. Steiner, and N. Tétreault, “Dye-sensitized solar cell based on a three-dimensional photonic crystal,” *Nano Lett.*, vol. 10, no. 7, pp. 2303–2309, 2010.
- [207] X. Wang, F. Shi, X. Gao, C. Fan, W. Huang, and X. Feng, “A sol-gel dip/spin coating method to prepare titanium oxide films,” *Thin Solid Films*, vol. 548, pp. 34–39, 2013.
- [208] M. Gardon and J. M. Guilemany, “Milestones in functional titanium dioxide thermal spray coatings: A review,” *J. Therm. Spray Technol.*, vol. 23, no. 4, pp. 577–595, 2014.
- [209] B.-H. Moon, Y.-M. Sung, and C.-H. Han, “Titanium oxide films prepared by sputtering, sol gel and dip coating methods for photovoltaic application,” *Energy Procedia.*, vol. 34, pp. 589–596, 2013.
- [210] S. Ito, P. Chen, P. Comte, M. K. Nazeeruddin, P. Liska, P. t. Pé chy, and M. Grä tzel, “Fabrication of screen-printing pastes from tio<sub>2</sub> powders for dye-sensitised solar cells,” *Prog. Photovolt: Res. Appl.*, vol. 15, no. 7, pp. 603–612, 2007.
- [211] M. Nomura, B. Meester, J. Schoonman, F. Kapteijn, and J. A. Moulijn, “Improvement of thermal stability of porous titania films prepared by electrostatic sol-spray deposition (essd),” *Chem. Mater.*, vol. 15, no. 6, pp. 1283–1288, 2003.
- [212] H. Wang, G. Liu, X. Li, P. Xiang, Z. Ku, Y. Rong, M. Xu, L. Liu, M. Hu, Y. Yang, and H. Han, “Highly efficient poly(3-hexylthiophene) based monolithic dye-sensitized solar cells with carbon counter electrode,” *Energy Environ. Sci.*, vol. 4, no. 6, p. 2025, 2011.
- [213] N. Tétreault, E. Horváth, T. Moehl, J. Brillet, R. Smajda, S. Bungener, N. Cai, P. Wang, S. M. Zakeeruddin, L. Forró, and M. Grätzel, “High-efficiency solid-state dye-sensitized solar cells: Fast charge extraction through self-assembled 3D fibrous network of crystalline tio<sub>2</sub> Nanowires,” *ACS Nano*, vol. 4, no. 12, pp. 7644–7650, 2010.
- [214] I.-K. Ding, N. Tétreault, J. Brillet, B. E. Hardin, E. H. Smith, S. J. Rosenthal, F. Sauvage, M. Grätzel, and M. D. McGehee, “Pore-filling of spiro-ometad in solid-state dye sensitized solar cells: Quantification, mechanism, and consequences for device performance,” *Adv. Funct. Mater.*, vol. 19, no. 15, pp. 2431–2436, 2009.
- [215] K. Sarkar, E. V. Braden, S. Pogorzalek, S. Yu, S. V. Roth, and P. Müller Buschbaum, “Monitoring structural dynamics of in situ spray-deposited zinc oxide films for application in dye-sensitized solar cells,” *ChemSusChem*, vol. 7, no. 8, pp. 2140–2145, 2014.

- [216] J. Zhang, Y. Deng, D. Gu, S. Wang, L. She, R. Che, Z.-S. Wang, B. Tu, S. Xie, and D. Zhao, "Ligand-assisted assembly approach to synthesize large-pore ordered mesoporous titania with thermally stable and crystalline framework," *Adv. Energy Mater.*, vol. 1, no. 2, pp. 241–248, 2011.
- [217] N. Cai, S.-J. Moon, L. Cevey-Ha, T. Moehl, R. Humphry-Baker, P. Wang, S. M. Zakeeruddin, and M. Grätzel, "An organic d- $\pi$ -a dye for record efficiency solid-state sensitized heterojunction solar cells," *Nano Lett.*, vol. 11, no. 4, pp. 1452–1456, 2011.
- [218] X. Zhang, Y. Xu, F. Giordano, M. Schreier, N. Pellet, Y. Hu, C. Yi, N. Robertson, J. Hua, S. M. Zakeeruddin, H. Tian, and M. Grätzel, "Molecular engineering of potent sensitizers for very efficient light harvesting in thin-film solid-state dye-sensitized solar cells," *J. Am. Chem. Soc.*, vol. 138, no. 34, pp. 10742–10745, 2016.
- [219] S. K. Pathak, A. Abate, P. Ruckdeschel, B. Roose, K. C. Gädél, Y. Vaynzof, A. Santhala, S.-I. Watanabe, D. J. Hollman, N. Noel, A. Sepe, R. Wiesner, Ullrich and-Friend, H. J. Snaith, and U. Steiner, "Performance and stability enhancement of dye-sensitized and perovskite solar cells by al doping of  $\text{tio}_2$ ," *Adv. Funct. Mater.*, vol. 24, no. 38, pp. 6046–6055, 2014.
- [220] Y.-J. Cheng, L. Zhi, W. Steffen, and J. S. Gutmann, "Surface-supported, highly ordered macroporous crystalline  $\text{tio}_2$  Thin films robust up to 1000 °c," *Chem. Mater.*, vol. 20, no. 21, pp. 6580–6582, 2008.
- [221] L. Song, W. Wang, S. Pröller, D. Moseguí González, J. Schlipf, C. J. Schaffer, K. Peters, E. M. Herzig, S. Bernstorff, T. Bein, D. Fattakhova-Rohlfing, and P. Müller-Buschbaum, "In situ study of degradation in p3Ht-titania-based solid-state dye-sensitized solar cells," *ACS Energy Lett.*, vol. 2, pp. 991–997, 2017.
- [222] M. Guo, K. Xie, J. Lin, Z. Yong, C. T. Yip, L. Zhou, Y. Wang, and H. Huang, "Design and coupling of multifunctional  $\text{tio}_2$  nanotube photonic crystal to nanocrystalline titania layer as semi-transparent photoanode for dye-sensitized solar cell," *Energy Environ. Sci.*, vol. 5, no. 12, pp. 9881–9888, 2012.
- [223] N. Tétreault and M. Grätzel, "Novel nanostructures for next generation dye-sensitized solar cells," *Energy Environ. Sci.*, vol. 5, no. 9, p. 8506, 2012.
- [224] A. Mishra, M. K. R. Fischer, and P. Bäuerle, "Metal-free organic dyes for dye-sensitized solar cells: From structure: Property relationships to design rules," *Angew. Chem. Int. Ed.*, vol. 48, no. 14, pp. 2474–2499, 2009.

- [225] S. Zhang, X. Yang, Y. Numata, and L. Han, "Highly efficient dye-sensitized solar cells: progress and future challenges," *Energy Environ. Sci.*, vol. 6, no. 5, p. 1443, 2013.
- [226] I. Chung, B. Lee, J. He, R. P. H. Chang, and M. G. Kanatzidis, "All-solid-state dye-sensitized solar cells with high efficiency," *Nature*, vol. 485, no. 7399, pp. 486–489, 2012.
- [227] H.-S. Kim, J.-W. Lee, N. Yantara, P. P. Boix, S. A. Kulkarni, S. Mhaisalkar, M. Grätzel, and N.-G. Park, "High efficiency solid-state sensitized solar cell-based on submicrometer rutile  $\text{TiO}_2$  Nanorod and  $\text{CH}_3\text{NH}_3\text{PbI}_3$  perovskite sensitizer," *Nano Lett.*, vol. 13, no. 6, pp. 2412–2417, 2013.
- [228] J. Wu, S. Hao, Z. Lan, J. Lin, M. Huang, Y. Huang, P. Li, S. Yin, and T. Sato, "An all-solid-state dye-sensitized solar cell-based poly(*n*-alkyl-4-vinyl-pyridine iodide) electrolyte with efficiency of 5.64%," *J. Am. Chem. Soc.*, vol. 130, no. 35, pp. 11568–11569, 2008.
- [229] A. Midya, Z. Xie, J.-X. Yang, Z.-K. Chen, D. J. Blackwood, J. Wang, S. Adams, and K. P. Loh, "A new class of solid state ionic conductors for application in all solid state dye sensitized solar cells," *Chem. Commun.*, vol. 46, no. 12, pp. 2091–2093, 2010.
- [230] K. Tennakone, G. K. R. Senadeera, D. B. R. A. De Silva, and I. R. M. Kottegoda, "Highly stable dye-sensitized solid-state solar cell with the semiconductor  $\text{4CuBr}_3\text{S}(\text{C}_4\text{H}_9)_2$  as the hole collector," *Appl. Phys. Lett.*, vol. 77, no. 15, p. 2367, 2000.
- [231] G. Kumara, A. Konno, G. Senadeera, P. Jayaweera, D. De Silva, and K. Tennakone, "Dye-sensitized solar cell with the hole collector p-cuScn deposited from a solution in *n*-propyl sulphide," *Sol. Energy Mater. Sol. Cells*, vol. 69, no. 2, pp. 195–199, 2001.
- [232] K. Murakoshi, R. Kogure, Y. Wada, and S. Yanagida, "Solid state dye-sensitized  $\text{TiO}_2$  Solar cell with polypyrrole as hole transport layer," *Chem. Lett.*, vol. 26, no. 5, pp. 471–472, 1997.
- [233] D. Gebeyehu, C. Brabec, and N. Sariciftci, "Solid-state organic/inorganic hybrid solar cells based on conjugated polymers and dye-sensitized  $\text{TiO}_2$  electrodes," *Thin Solid Films*, vol. 403–404, pp. 271–274, 2002.
- [234] J. Krüger, R. Plass, L. Cevey, M. Piccirelli, M. Grätzel, and U. Bach, "High efficiency solid-state photovoltaic device due to inhibition of interface charge recombination," *Appl. Phys. Lett.*, vol. 79, no. 13, pp. 2085–2087, 2001.

- [235] J. Krüger, R. Plass, M. Grätzel, and H.-J. Matthieu, "Improvement of the photovoltaic performance of solid-state dye-sensitized device by silver complexation of the sensitizer cis-bis(4,4'-dicarboxy-2,2'-bipyridine)-bis(isothiocyanato) ruthenium(II)," *Appl. Phys. Lett.*, vol. 81, no. 2, pp. 367–369, 2002.
- [236] L. Schmidt-Mende, S. M. Zakeeruddin, and M. Grätzel, "Efficiency improvement in solid-state-dye-sensitized photovoltaics with an amphiphilic ruthenium-dye," *Appl. Phys. Lett.*, vol. 86, no. 1, p. 013504, 2005.
- [237] L. Schmidt-Mende, U. Bach, R. Humphry-Baker, T. Horiuchi, H. Miura, S. Ito, S. Uchida, and M. Grätzel, "Organic dye for highly efficient solid-state dye-sensitized solar cells," *Adv. Mater.*, vol. 17, no. 7, pp. 813–815, 2005.
- [238] H. J. Snaith and M. Grätzel, "Enhanced charge mobility in a molecular hole transporter via addition of redox inactive ionic dopant: Implication to dye-sensitized solar cells," *Appl. Phys. Lett.*, vol. 89, no. 26, p. 262114, 2006.
- [239] H. J. Snaith and L. Schmidt-Mende, "Advances in liquid-electrolyte and solid-state dye-sensitized solar cells," *Adv. Mater.*, vol. 19, no. 20, pp. 3187–3200, 2007.
- [240] S. Ren, L.-Y. Chang, S.-K. Lim, J. Zhao, M. Smith, N. Zhao, V. Bulović, M. Bawendi, and S. Gradečak, "Inorganic-organic hybrid solar cell: Bridging quantum dots to conjugated polymer nanowires," *Nano Lett.*, vol. 11, no. 9, pp. 3998–4002, 2011.
- [241] A. Abrusci, I.-K. Ding, M. Al-Hashimi, T. Segal-Peretz, M. D. McGehee, M. Heeney, G. L. Frey, and H. J. Snaith, "Facile infiltration of semiconducting polymer into mesoporous electrodes for hybrid solar cells," *Energy Environ. Sci.*, vol. 4, no. 8, pp. 3051–3058, 2011.
- [242] R. Zhu, C.-Y. Jiang, B. Liu, and S. Ramakrishna, "Highly efficient nanoporous tio<sub>2</sub>-polythiophene hybrid solar cells based on interfacial modification using a metal-free organic dye," *Adv. Mater.*, vol. 21, no. 9, pp. 994–1000, 2009.
- [243] J. A. Chang, J. H. Rhee, S. H. Im, Y. H. Lee, H.-j. Kim, S. I. Seok, M. K. Nazeeruddin, and M. Grätzel, "High-performance nanostructured inorganic-organic heterojunction solar cells," *Nano Lett.*, vol. 10, no. 7, pp. 2609–2612, 2010.
- [244] K. M. Coakley, B. S. Srinivasan, J. M. Ziebarth, C. Goh, Y. Liu, and M. D. McGehee, "Enhanced hole mobility in regioregular polythiophene infiltrated in straight nanopores," *Adv. Funct. Mater.*, vol. 15, no. 12, pp. 1927–1932, 2005.
- [245] J.-F. Lin, W.-C. Yen, C.-Y. Chang, Y.-F. Chen, and W.-F. Su, "Enhancing organic-inorganic hybrid solar cell efficiency using rod-coil diblock polymer additive," *J. Mater. Chem. A*, vol. 1, no. 3, pp. 665–670, 2013.

- [246] J. Lee, M. Christopher Orilall, S. C. Warren, M. Kamperman, F. J. DiSalvo, and U. Wiesner, "Direct access to thermally stable and highly crystalline mesoporous transition-metal oxides with uniform pores," *Nat. Mater.*, vol. 7, no. 3, pp. 222–228, 2008.
- [247] S. Guldin, M. Kolle, M. Stefik, R. Langford, D. Eder, U. Wiesner, and U. Steiner, "Tunable mesoporous Bragg reflectors based on block-copolymer self-assembly," *Adv. Mater.*, vol. 23, no. 32, pp. 3664–3668, 2011.
- [248] M.-A. Cha, C. Shin, D. Kannaiyan, Y. H. Jang, S. T. Kochuveedu, D. Y. Ryu, and D. H. Kim, "A versatile approach to the fabrication of  $\text{tio}_2$  nanostructures with reverse morphology and mesoporous  $\text{ag}/\text{tio}_2$  thin films via cooperative ps-b-peo self-assembly and a sol-gel process," *J. Mater. Chem.*, vol. 19, no. 39, pp. 7245–7250, 2009.
- [249] S. Pröller, F. Liu, C. Zhu, C. Wang, T. P. Russell, A. Hexemer, P. Müller-Buschbaum, and E. M. Herzig, "Organic solar cells: Following the morphology formation in situ in printed active layers for organic solar cells," *Adv. Energy Mater.*, vol. 6, no. 1, p. 1401770, 2016.
- [250] M. Sanyal, B. Schmidt-Hansberg, M. F. G. Klein, A. Colsmann, C. Munuera, A. Vorobiev, U. Lemmer, W. Schabel, H. Dosch, and E. Barrena, "In situ x-ray study of drying-temperature influence on the structural evolution of bulk-heterojunction polymer-fullerene solar cells processed by doctor-blading," *Adv. Energy Mater.*, vol. 1, no. 3, pp. 363–367, 2011.
- [251] J. F. M. Grisales, "Effects of a selective solvent additive on p3ht:pcbm based solar cells," mater thesis, TECHNISCHE UNIVERSITÄT MÜNCHEN, München, Germany, 2015.
- [252] P. Chen, J. H. Yum, F. D. Angelis, E. Mosconi, S. Fantacci, S.-J. Moon, R. H. Baker, J. Ko, M. K. Nazeeruddin, and M. Grätzel, "High open-circuit voltage solid-state dye-sensitized solar cells with organic dye," *Nano Lett.*, vol. 9, no. 6, pp. 2487–2492, 2009.
- [253] S.-R. Jang, K. Zhu, M. J. Ko, K. Kim, C. Kim, N.-G. Park, and A. J. Frank, "Voltage-enhancement mechanisms of an organic dye in high open-circuit voltage solid-state dye-sensitized solar cells," *ACS Nano*, vol. 5, no. 10, pp. 8267–8274, 2011.
- [254] C. Chen, X. Yang, M. Cheng, F. Zhang, and L. Sun, "Degradation of cyanoacrylic acid-based organic sensitizers in dye-sensitized solar cells," *ChemSusChem*, vol. 6, no. 7, pp. 1270–1275, 2013.



- [255] S. M. K. Rendon, D. Mavrynsky, A. Meierjohann, A. Tiihonen, K. Miettunen, I. Asghar, J. Halme, L. Kronberg, and R. Leino, "Analysis of dye degradation products and assessment of the dye purity in dye-sensitized solar cells," *Rapid Commun. Mass Spectrom.*, vol. 29, no. 23, pp. 2245–2251, 2015.
- [256] F. Nour-Mohhamadi, S. D. Nguyen, G. Boschloo, A. Hagfeldt, and T. Lund, "Determination of the light-induced degradation rate of the solar cell sensitizer n719 on  $\text{TiO}_2$  Nanocrystalline particles," *J. Phys. Chem. B*, vol. 109, no. 47, pp. 22413–22419, 2005.
- [257] L. Yang, B. Xu, D. Bi, H. Tian, G. Boschloo, L. Sun, A. Hagfeldt, and E. M. J. Johansson, "Initial light soaking treatment enables hole transport material to outperform spiro-ometad in solid-state dye-sensitized solar cells," *J. Am. Chem. Soc.*, vol. 135, no. 19, pp. 7378–7385, 2013.
- [258] J. L. Lutkenhaus, K. McEnnis, A. Serghei, and T. P. Russell, "Confinement effects on crystallization and curie transitions of poly(vinylidene fluoride-co-trifluoroethylene)," *Macromolecules*, vol. 43, no. 8, pp. 3844–3850, 2010.
- [259] H. Wu, W. Wang, Y. Huang, C. Wang, and Z. Su, "Polymorphic behavior of syndiotactic polystyrene crystallized in cylindrical nanopores," *Macromolecules*, vol. 41, no. 20, pp. 7755–7758, 2008.
- [260] S.-Q. Fan, C. Kim, B. Fang, K.-X. Liao, G.-J. Yang, C.-J. Li, J.-J. Kim, and J. Ko, "Improved efficiency of over 10% ruthenium complex and an organic dye heterogeneously positioning on a single  $\text{TiO}_2$  electrode," *J. Phys. Chem. C*, vol. 115, no. 15, pp. 7747–7754, 2011.
- [261] J. Weickert, R. B. Dunbar, H. C. Hesse, W. Wiedemann, and L. Schmidt-Mende, "Nanostructured organic and hybrid solar cells," *Adv. Mater.*, vol. 23, no. 16, pp. 1810–1828, 2011.
- [262] P. Atienzar, T. Ishwara, M. Horie, J. R. Durrant, and J. Nelson, "Hybrid polymer-metal oxide solar cells by in situ chemical polymerization," *J. Mater. Chem.*, vol. 19, no. 30, pp. 5377–5380, 2009.
- [263] M. Grätzel, "Photoelectrochemical cells," *Nature*, vol. 414, no. 6861, pp. 338–344, 2001.
- [264] W. Zhang, R. Zhu, F. Li, Q. Wang, and B. Liu, "High-performance solid-state organic dye sensitized solar cells with p3Ht as hole transporter," *J. Phys. Chem. C*, vol. 115, no. 14, pp. 7038–7043, 2011.

- [265] J. A. Chang, S. H. Im, Y. H. Lee, H.-j. Kim, C.-S. Lim, J. H. Heo, and S. I. Seok, "Panchromatic photon-harvesting by hole-conducting materials in inorganic-organic heterojunction sensitized-solar cell through the formation of nanostructured electron channels," *Nano Lett.*, vol. 12, no. 4, pp. 1863–1867, 2012.
- [266] T. Leijtens, I.-K. Ding, T. Giovenzana, J. T. Bloking, M. D. McGehee, and A. Sellinger, "Hole transport materials with low glass transition temperatures and high solubility for application in solid-state dye-sensitized solar cells," *ACS Nano*, vol. 6, no. 2, pp. 1455–1462, 2012.
- [267] W. H. Nguyen, C. D. Bailie, E. L. Unger, and M. D. McGehee, "Enhancing the hole-conductivity of spiro-ometad without oxygen or lithium salts by using spiro(tfsi) 2 in perovskite and dye-sensitized solar cells," *J. Am. Chem. Soc.*, vol. 136, no. 31, pp. 10996–11001, 2014.
- [268] U. B. Cappel, T. Daeneke, and U. Bach, "Oxygen-induced doping of spiro-meotad in solid-state dye-sensitized solar cells and its impact on device performance," *Nano Lett.*, vol. 12, no. 9, pp. 4925–4931, 2012.
- [269] W. J. E. Beek, M. M. Wienk, and R. A. J. Janssen, "Efficient hybrid solar cells from zinc oxide nanoparticles and a conjugated polymer," *Adv. Mater.*, vol. 16, no. 12, pp. 1009–1013, 2004.
- [270] A. J. Haring, S. R. Ahrenholtz, and A. J. Morris, "Rethinking band bending at the p3Ht-tio<sub>2</sub> interface," *ACS Appl. Mater. Interfaces*, vol. 6, no. 6, pp. 4394–4401, 2014.
- [271] A. C. Arango, L. R. Johnson, V. N. Bliznyuk, Z. Schlesinger, S. A. Carter, and H.-H. Hörhold, "Efficient titanium oxide/conjugated polymer photovoltaics for solar energy conversion," *Adv. Mater.*, vol. 12, no. 22, pp. 1689–1692, 2000.
- [272] M. A. Niedermeier, M. Rawolle, P. Lellig, V. Körstgens, E. M. Herzig, A. Buffet, S. V. Roth, J. S. Gutmann, T. Fröschl, N. Hüsing, and P. Müller-Buschbaum, "Low-temperature sol-gel synthesis of nanostructured polymer/titania hybrid films based on custom-made poly(3-Alkoxy thiophene)," *ChemPhysChem*, vol. 14, no. 3, pp. 597–602, 2013.
- [273] V. Körstgens, S. Pröller, T. Buchmann, D. Moseguí González, L. Song, Y. Yao, W. Wang, J. Werhahn, G. Santoro, H. Roth, S. V. Iglev, R. Kienberger, and P. Müller-Buschbaum, "Laser-ablated titania nanoparticles for aqueous processed hybrid solar cells," *Nanoscale*, vol. 7, no. 7, pp. 2900–2904, 2015.
- [274] J. Boucl, P. Ravirajan, and J. Nelson, "Hybrid polymer-metal oxide thin films for photovoltaic applications," *J. Mater. Chem.*, vol. 17, no. 30, pp. 3141–3153, 2007.

- [275] S. Neyshadt, J. P. Jahnke, R. J. Messinger, A. Rawal, T. Segal Peretz, D. Huppert, B. F. Chmelka, and G. L. Frey, "Understanding and controlling organic–inorganic interfaces in mesostructured hybrid photovoltaic materials," *J. Am. Chem. Soc.*, vol. 133, no. 26, pp. 10119–10133, 2011.
- [276] J. Zhang, Q. Xu, Z. Feng, M. Li, and C. Li, "Importance of the relationship between surface phases and photocatalytic activity of  $\text{tio}_2$ ," *Angew. Chem.*, vol. 120, no. 9, pp. 1790–1793, 2008.
- [277] S. Liu, J. Yu, and M. Jaroniec, "Anatase  $\text{tio}_2$  with dominant high-energy 001 facets: Synthesis, properties, and applications," *Chem. Mater.*, vol. 23, no. 18, pp. 4085–4093, 2011.
- [278] P. Kohn, S. Pathak, M. Stefik, C. Ducati, U. Wiesner, U. Steiner, and S. Guldin, "Low temperature crystallisation of mesoporous  $\text{tio}_2$ ," *Nanoscale*, vol. 5, no. 21, pp. 10518–10524, 2013.
- [279] P. D. Cozzoli, A. Kornowski, and H. Weller, "Low-temperature synthesis of soluble and processable organic-capped anatase  $\text{tio}_2$  Nanorods," *J. Am. Chem. Soc.*, vol. 125, no. 47, pp. 14539–14548, 2003.
- [280] M. Tasbihi, U. L. Štangar, U. Černigoj, and K. Kogej, "Low-temperature synthesis and characterization of anatase  $\text{tio}_2$  powders from inorganic precursors," *Photochem. Photobiol. Sci.*, vol. 8, no. 5, p. 719, 2009.
- [281] Z. Lai, F. Peng, Y. Wang, H. Wang, H. Yu, P. Liu, and H. Zhao, "Low temperature solvothermal synthesis of anatase  $\text{tio}_2$  single crystals with wholly 100 and 001 faceted surfaces," *J. Mater. Chem.*, vol. 22, no. 45, pp. 23906–23912, 2012.
- [282] G. Zhang, S. Finefrock, D. Liang, G. G. Yadav, H. Yang, H. Fang, and Y. Wu, "Semiconductor nanostructure-based photovoltaic solar cells," *Nanoscale*, vol. 3, no. 6, p. 2430, 2011.
- [283] S. S. Williams, M. J. Hampton, V. Gowrishankar, I.-K. Ding, J. L. Templeton, E. T. Samulski, J. M. DeSimone, and M. D. McGehee, "Nanostructured titania-polymer photovoltaic devices made using pfpe-based nanomolding techniques," *Chem. Mater.*, vol. 20, no. 16, pp. 5229–5234, 2008.
- [284] W.-Q. Wu, H.-L. Feng, H.-S. Rao, Y.-F. Xu, D.-B. Kuang, and C.-Y. Su, "Maximizing omnidirectional light harvesting in metal oxide hyperbranched array architectures," *Nat. Commun.*, vol. 5, p. 3968, 2014.

- [285] S. H. Hwang, D. H. Shin, J. Yun, C. Kim, M. Choi, and J. Jang, "SiO<sub>2</sub>/TiO<sub>2</sub> Hollow nanoparticles decorated with Ag nanoparticles: Enhanced visible light absorption and improved light scattering in dye-sensitized solar cells," *Chem. Eur. J.*, vol. 20, no. 15, pp. 4439–4446, 2014.
- [286] S. Lou, X. Guo, T. Fan, and D. Zhang, "Butterflies: inspiration for solar cells and sunlight water-splitting catalysts," *Energy Environ. Sci.*, vol. 5, no. 11, pp. 9195–9216, 2012.
- [287] I. S. Cho, Z. Chen, A. J. Forman, D. R. Kim, P. M. Rao, T. F. Jaramillo, and X. Zheng, "Branched TiO<sub>2</sub> Nanorods for photoelectrochemical hydrogen production," *Nano Lett.*, vol. 11, no. 11, pp. 4978–4984, 2011.
- [288] M. Gao, L. Zhu, W. L. Ong, J. Wang, and G. W. Ho, "Structural design of TiO<sub>2</sub>-based photocatalyst for H<sub>2</sub> production and degradation applications," *Catal. Sci. Technol.*, vol. 5, no. 10, pp. 4703–4726, 2015.
- [289] P. Yang, A. H. Rizvi, B. Messer, B. F. Chmelka, G. M. Whitesides, and G. D. Stucky, "Patterning porous oxides within microchannel networks," *Adv. Mater.*, vol. 13, no. 6, pp. 427–431, 2001.
- [290] T. P. Chou, Q. Zhang, G. E. Fryxell, and G. Z. Cao, "Hierarchically structured ZnO film for dye-sensitized solar cells with enhanced energy conversion efficiency," *Adv. Mater.*, vol. 19, no. 18, pp. 2588–2592, 2007.
- [291] P. Yang, T. Deng, D. Zhao, P. Feng, D. Pine, B. F. Chmelka, G. M. Whitesides, and G. D. Stucky, "Hierarchically ordered oxides," *Science*, vol. 282, no. 5397, pp. 2244–2246, 1998.
- [292] M. A. Niedermeier, I. Groß, and P. Müller-Buschbaum, "Structuring of titania thin films on different length scales via combining block copolymer assisted sol-gel templating with wet-imprinting," *J. Mater. Chem. A*, vol. 1, no. 43, p. 13399, 2013.
- [293] I.-K. Ding, J. Zhu, W. Cai, S.-J. Moon, N. Cai, P. Wang, S. M. Zakeeruddin, M. Grätzel, M. L. Brongersma, Y. Cui, and M. D. McGehee, "Plasmonic dye-sensitized solar cells," *Adv. Energy Mater.*, vol. 1, no. 1, pp. 52–57, 2010.
- [294] R. Ganesan, J. Dumond, M. S. M. Saifullah, S. H. Lim, H. Hussain, and H. Y. Low, "Direct patterning of TiO<sub>2</sub> using step-and-flash imprint lithography," *ACS Nano*, vol. 6, no. 2, pp. 1494–1502, 2012.
- [295] W. Jiang, H. Liu, L. Yin, and Y. Ding, "Fabrication of well-arrayed plasmonic mesoporous TiO<sub>2</sub>/Ag films for dye-sensitized solar cells by multiple-step nanoimprint lithography," *J. Mater. Chem. A*, vol. 1, no. 21, pp. 6433–6440, 2013.

- [296] L. Persano, A. Camposeo, F. Di Benedetto, R. Stabile, A. M. Laera, E. Piscopiello, L. Tapfer, and D. Pisignano, "Cds-polymer nanocomposites and light-emitting fibers by in situ electron-beam synthesis and lithography," *Adv. Mater.*, vol. 24, no. 39, pp. 5320–5326, 2012.
- [297] M. J. Hampton, S. S. Williams, Z. Zhou, J. Nunes, D.-H. Ko, J. L. Templeton, E. T. Samulski, and J. M. DeSimone, "The patterning of sub-500 nm inorganic oxide structures," *Adv. Mater.*, vol. 20, no. 14, pp. 2667–2673, 2008.
- [298] S. S. Dinachali, M. S. M. Saifullah, R. Ganesan, E. S. Thian, and C. He, "A universal scheme for patterning of oxides via thermal nanoimprint lithography," *Adv. Funct. Mater.*, vol. 23, no. 17, pp. 2201–2211, 2012.
- [299] M. Moxey, A. Johnson, O. El-Zubir, M. Cartron, S. S. Dinachali, C. N. Hunter, M. S. M. Saifullah, K. S. L. Chong, and G. J. Leggett, "Fabrication of self-cleaning, reusable titania templates for nanometer and micrometer scale protein patterning," *ACS Nano*, vol. 9, no. 6, pp. 6262–6270, 2015.
- [300] S. S. Dinachali, J. Dumond, M. S. M. Saifullah, K. K. Ansah-Antwi, R. Ganesan, E. S. Thian, and C. He, "Large area, facile oxide nanofabrication via step-and-flash imprint lithography of metal-organic hybrid resins," *ACS Appl. Mater. Interfaces*, vol. 5, no. 24, pp. 13113–13123, 2013.
- [301] J. Yao, A.-P. Le, M. V. Schulmerich, J. Maria, T.-W. Lee, S. K. Gray, R. Bhargava, J. A. Rogers, and R. G. Nuzzo, "Soft embossing of nanoscale optical and plasmonic structures in glass," *ACS Nano*, vol. 5, no. 7, pp. 5763–5774, 2011.
- [302] V. C. Sundar, H.-J. Eisler, T. Deng, Y. Chan, E. L. Thomas, and M. G. Bawendi, "Soft-lithographically embossed, multilayered distributed-feedback nanocrystal lasers," *Adv. Mater.*, vol. 16, no. 23-24, pp. 2137–2141, 2004.
- [303] F. Todescato, I. Fortunati, S. Gardin, E. Garbin, E. Collini, R. Bozio, J. J. Jasieniak, G. Della Giustina, G. Brusatin, S. Toffanin, and et al., "Soft-lithographed up-converted distributed feedback visible lasers based on cdse-cdzns-zns quantum dots," *Adv. Funct. Mater.*, vol. 22, no. 2, pp. 337–344, 2011.
- [304] Y. J. He, J. F. Peng, W. Chu, Y. Z. Li, and D. G. Tong, "Black mesoporous anatase tio<sub>2</sub> nanoleaves: a high capacity and high rate anode for aqueous al-ion batteries," *J. Mater. Chem. A*, vol. 2, no. 6, pp. 1721–1731, 2014.
- [305] K. V. Bineesh, D.-K. Kim, and D.-W. Park, "Synthesis and characterization of zirconium-doped mesoporous nano-crystalline tio<sub>2</sub>," *Nanoscale*, vol. 2, no. 7, pp. 1222–1228, 2010.

- [306] X. Chen, X. Wang, and X. Fu, "Hierarchical macro/mesoporous  $\text{TiO}_2/\text{SiO}_2$  and  $\text{TiO}_2/\text{ZrO}_2$  nanocomposites for environmental photocatalysis," *Energy Environ. Sci.*, vol. 2, no. 8, pp. 872–877, 2009.
- [307] P. Şen, C. Hirel, C. Andraud, C. Aronica, Y. Bretonnière, A. Mohammed, H. Ågren, B. Minaev, V. Minaeva, G. Baryshnikov, H.-H. Lee, J. Duboisset, and M. Lindgren, "Fluorescence and ftir spectra analysis of trans-a2B2-Substituted di- and tetraphenyl porphyrins," *Materials*, vol. 3, no. 8, pp. 4446–4475, 2010.
- [308] N. Gondaliya, D. K. Kanchan, P. Sharma, and P. Joge, "Structural and conductivity studies of poly(ethylene oxide)-silver triflate polymer electrolyte system," *Mater. Sci. Appl.*, vol. 02, no. 11, pp. 1639–1643, 2011.
- [309] A. T. Heitsch, R. N. Patel, B. W. Goodfellow, D.-M. Smilgies, and B. A. Korgel, "GISaxs characterization of order in hexagonal monolayers of fept nanocrystals," *J. Phys. Chem. C*, vol. 114, no. 34, pp. 14427–14432, 2010.
- [310] X. Wei, W. Gu, W. Chen, X. Shen, F. Liu, J. W. Strzalka, Z. Jiang, and T. P. Russell, "Disorder-to-order transitions induced by alkyne/azide click chemistry in diblock copolymer thin films," *Soft Matter*, vol. 8, no. 19, p. 5273, 2012.
- [311] W. Wang, *Nanostructure-performance relationship in polymer-based solar cells*. PhD thesis, TECHNISCHE UNIVERSITÄT MÜNCHEN, 2016.
- [312] R. Meier, C. Birkenstock, C. M. Palumbiny, and P. Müller-Buschbaum, "Efficiency-improved organic solar cells based on plasticizer assisted soft embossed pedot:pss layers," *Phys. Chem. Chem. Phys.*, vol. 14, no. 43, pp. 15088–15098, 2012.

# List of publications

## Publications related to the dissertation

- L. Song, W. Wang, V. Körstgens, D. Moseguí González, Y. Yao, N. K. Minar, J. M. Feckl, K. Peters, T. Bein, D. Fattakhova-Rohlfing, G. Santoro, S. V. Roth, Stephan P. Müller-Buschbaum, “Spray Deposition of Titania Films with Incorporated Crystalline Nanoparticles for All-Solid-State Dye-Sensitized Solar Cells Using P3HT”, *Adv. Funct. Mater.*, vol. 26, pp. 1498–1506, 2016.
- L. Song, A. Abdelsamie, C. J. Schaffer, V. Körstgens, W. Wang, T. Wang, E. D. Indari, T. Fröschl, N. Hüsing, T. Haeberle, P. Lugli, S. Bernstorff, P. Müller-Buschbaum, “A Low Temperature Route toward Hierarchically Structured Titania Films for Thin Hybrid Solar Cells”, *Adv. Funct. Mater.*, vol. 26, pp. 7084–7093, 2016.
- L. Song, W. Wang, S. Pröller, D. Moseguí González, J. Schlipf, C. J. Schaffer, K. Peters, E. M. Herzig, S. Bernstorff, T. Bein, D. Fattakhova-Rohlfing, P. Müller-Buschbaum, “In Situ Study of Degradation in P3HT-titania Based Solid-state Dye-sensitized Solar Cells”, *ACS Energy Lett.*, vol. 2, pp. 991–997, 2017.
- L. Song, W. Wang, V. Körstgens, D. Moseguí González, F. C. Löhner, C. J. Schaffer, J. Schlipf, P. Zhang, K. Peters, Th. Bein, D. Fattakhova-Rohlfing, S. V. Roth, P. Müller-Buschbaum, “In situ study of spray deposited titania films for scalable fabrication of solid-state dye-sensitized solar cells”, *Adv. Energy Mater.*, 2017, submitted for review.

## Further publications

- D. Moseguí González, C. J. Schaffer, S. Pröller, J. Schlipf, L. Song, S. Bernstorff, E. M. Herzig, P. Müller-Buschbaum, “Co-dependence between crystalline and photovoltage evolutions in P3HT:PCBM solar cells probed with in-operando GIWAXS”, *ACS Appl. Mater. Interfaces*, vol. 9, pp. 3282–3287, 2017.

- L. Oesinghaus, J. Schlipf, N. Giesbrecht, Y. Hu, L. Song, T. Bein, P. Docampo, P. Müller-Buschbaum, “Towards tailored film morphologies: The origin of crystal orientation in hybrid perovskite thin films”, *Adv. Mater. Interfaces*, vol. 3, pp.1600403, 2016.
- D. Moseguí González, V. Körstgens, Y. Yao, L. Song, G. Santoro, S. V. Roth, P. Müller-Buschbaum, “Improved power conversion efficiency of P3HT:PCBM organic solar cells by strong spin-orbit-coupling-induced delayed fluorescence”, *Adv. Energy Mater.*, vol. 5, pp. 1401770, 2015.
- W. Wang, C. J. Schaffer, L. Song, V. Körstgens, S. Pröller, E. Dwi Indari, T. Wang, A. Abdelsamie, S. Bernstorff, P. Müller-Buschbaum, “In-operando morphology investigation of inverted bulk heterojunction organic solar cells by GISAXS”, *J. Mater. Chem. A*, vol. 3, pp. 8324–84331, 2015.
- V. Körstgens, S. Pröller, T. Buchmann, D. Moseguí González, L. Song, Y. Yao, W. Wang, J. Werhahn, G. Santoro, S. V. Roth, H. Iglev, R. Kienberger, P. Müller-Buschbaum, “Laser-ablated titania nanoparticles for aqueous processed hybrid solar cells”, *Nanoscale*, vol. 7, pp. 2900–2904, 2015.

## Scientific reports

- L. Song, A. Abdelsamie, C. J. Schaffer, V. Körstgens, W. Wang, T. Wang, E. D. Indari, T. Fröschl, N. Hüsing, T. Haeberle, P. Lugli, S. Bernstorff, P. Müller-Buschbaum, “A low temperature route towards hierarchically structured titania films for thin hybrid solar cells”, *Elettra and FERMI lightsources*, 2017.
- L. Song, A. Abdelsamie, C. J. Schaffer, V. Körstgens, W. Wang, T. Wang, E. D. Indari, T. Fröschl, N. Hüsing, T. Haeberle, P. Lugli, S. Bernstorff, P. Müller-Buschbaum, “A low temperature route towards hierarchically structured titania films for thin hybrid solar cells”, *Lehrstuhl für Funktionelle Materialien, Annual Report*, 2016.
- L. Song, W. Wang, V. Körstgens, D. Moseguí González, Y. Yao, N. K. Minar, J. M. Feckl, K. Peters, T. Bein, D. Fattakhova-Rohlfing, G. Santoro, S. V. Roth, P. Müller-Buschbaum, “Spray deposition of titania films with incorporated crystalline nanoparticles”, *Lehrstuhl für Funktionelle Materialien, Annual Report*, 2015.
- L. Song, T. Wang, A. Abdelsamie, V. Körstgens, C. J. Schaffer, S. Bernstorff, P. Müller-Buschbaum, “Low temperature synthesis and structuring of mesoporous titania films”, *Lehrstuhl für Funktionelle Materialien, Annual Report*, 2014.



- L. Song, M. A. Niedermeier, P. Müller-Buschbaum, “Low temperature route to porous titania nanostructures by block-copolymer assisted sol-gel method”, *Lehrstuhl für Funktionelle Materialien, Annual Report*, 2013.
- L. Song, M. A. Niedermeier, P. Müller-Buschbaum, “Fabrication of sponge-like titania nanostructures by sol-gel synthesis with different structure-directing agents ”, *Lehrstuhl für Funktionelle Materialien, Annual Report*, 2012.

## Conference talks

- L. Song, A. Abdelsamie, C. J. Schaffer, V. Körstgens, W. Wang, T. Wang, E. D. In-dari, T. Fröschl, N. Hüsing, T. Haeberle, P. Lugli, S. Bernstorff, P. Müller-Buschbaum, “A low temperature route towards hierarchically structured titania films for thin hybrid solar cells”, *International Conference on Composites/Nano Engineering (ICCE-24)*, Haikou (China), July 2016.
- L. Song, J. Schlipf, B. Su, “Hybrid Perovskite Photovoltaics”, *E13 Polymer Physics Summer School*, Obertauern (Austria), June 2016.
- L. Song, A. Abdelsamie, C. J. Schaffer, V. Körstgens, W. Wang, T. Wang, E. D. In-dari, T. Fröschl, N. Hüsing, T. Haeberle, P. Lugli, S. Bernstorff, P. Müller-Buschbaum, “A low temperature route towards hierarchically structured titania films for thin hybrid solar cells”, *DPG-Frühjahrstagung*, Regensburg (Germany), March 2016.
- L. Song, M. Philipp, N. Saxena, C. M. Palumbiny, M. Haese-Seiller, J.-F. Moulin, N. Hüsing, N. K. Minar, D. Fattakhova-Rohlfing, P. Müller-Buschbaum, “Films with hierarchical porosity assembled from ultra-small titania nanoparticles”, *JCNS-Workshop “Neutron Scattering on Nano-Structured Soft Matter”*, Tutzing (Germany), October 2015.
- L. Song, W. Wang, V. Körstgens, D. Moseguí González, Y. Yao, N. K. Minar, J. M. Feckl, K. Peters, T. Bein, D. Fattakhova-Rohlfing, G. Santoro, S. V. Roth, P. Müller-Buschbaum, “Spray deposition of titania films with incorporated crystalline nanoparticles”, *DPG-Frühjahrstagung*, Berlin (Germany), March 2015.
- L. Song, “Hybrid solar cells TiO<sub>2</sub>/conducting polymer system”, *E13 Polymer Physics Summer School*, Obertauern (Austria), June 2014.

## Conference poster presentations

- L. Song, A. Abdelsamie, C. J. Schaffer, V. Körstgens, W. Wang, T. Wang, E. D. Indari, T. Fröschl, N. Hüsing, T. Haeberle, P. Lugli, S. Bernstorff, P. Müller-Buschbaum, “A low temperature route towards hierarchically structured titania films for thin hybrid solar cells”, *6th Colloquium of the Munich School of Engineering*, Garching (Germany), July 2016.
- L. Song, W. Wang, V. Körstgens, D. Moseguí González, Y. Yao, N. K. Minar, J. M. Feckl, K. Peters, T. Bein, D. Fattakhova-Rohlfing, S. V. Roth, P. Müller-Buschbaum, “Spray Deposition of Titania Films with Incorporated Crystalline Nanoparticles for All-Solid-State Dye-Sensitized Solar Cells”, *5th International SolTech Conference in Munich*, Munich (Germany), April 2016.
- L. Song, W. Wang, V. Körstgens, D. Moseguí González, Y. Yao, N. K. Minar, J. M. Feckl, T. Bein, D. Fattakhova-Rohlfing, S. V. Roth, P. Müller-Buschbaum, “Spray Deposition of Titania Films with Incorporated Crystalline Nanoparticles for Solid-State Dye-Sensitized Solar Cells”, *5th Colloquium of the Munich School of Engineering*, Garching (Germany), July 2015.
- L. Song, W. Wang, V. Körstgens, D. Moseguí González, Y. Yao, N. K. Minar, J. M. Feckl, T. Bein, D. Fattakhova-Rohlfing, G. Santoro, S. V. Roth, P. Müller-Buschbaum, “Spray Deposition of Titania Films with Introduction of Crystalline Nanoparticles for Solid-State Dye-Sensitized Solar Cells”, *4th International Solar Technologies Go Hybrid-Workshop*, Kloster Banz (Germany), March 2015.
- L. Song, M. A. Niedermeier, V. Körstgens, D. Magerl, B. Su, S. Bernstorff, P. Müller-Buschbaum, “Synthesis of porous  $\text{TiO}_2$  nanostructures by the sol-gel method”, *4th Colloquium of the Munich School of Engineering*, Garching (Germany), July 2014.
- L. Song, M. A. Niedermeier, V. Körstgens, D. Magerl, B. Su, S. Bernstorff, P. Müller-Buschbaum, “Synthesis of porous  $\text{TiO}_2$  nanostructures by the sol-gel method”, *DPG-Frühjahrstagung*, Berlin (Germany), April 2014.
- L. Song, M. A. Niedermeier, P. Müller-Buschbaum, “Fabrication of sponge-like titania nanostructures by the combination of sol-gel synthesis”, *GISAXS 2013*, Hamburg (Germany), October 2013.
- L. Song, M. A. Niedermeier, P. Müller-Buschbaum, “Fabrication of sponge-like titania nanostructures by the combination of sol-gel synthesis”, *3rd Colloquium of the Munich School of Engineering*, Garching (Germany), July 2013.

- 
- L. Song, M. A. Niedermeier, P. Müller-Buschbaum, “Fabrication of sponge-like titania nanostructures by the combination of sol-gel synthesis” *DPG-Frühjahrstagung*, Regensburg (Germany), March 2013.



# Acknowledgments

To begin with, I am grateful to my supervisor Prof. Dr. Peter Müller-Buschbaum for the opportunity to work in the field of titania-based photovoltaics. He provides a good experimental and working environment as well as helpful advice and guidance throughout my whole Ph.D. period. His solid knowledge and expertise are a strong support for me to overcome all challenges in my scientific research. Besides scientific support, his trust, encouragement and patience always raise my spirits to keep on my Ph.D. studies. Thanks very much for him to help me to bolster my confidence in scientific research. Furthermore, the experience of beamtimes and conferences will be a precious treasure in my future life, thanks go to him again.

The China Scholarship Council (CSC) is gratefully acknowledged for funding. Its financial support liberate me from economic worry about my living expense during the Ph.D. period.

Many thanks to Dr. Martin Niedermeier for his infinite patience to help me get started in my Ph.D. studies. Also, "my" master students Amr Abdelsamie and Tianyi Wang must not be forgotten. Their excellent work constitute a critical part of my research. I enjoy the time working with them and hope they will have a bright future.

I will not accomplish my research without the aid of my dear colleagues. In no specific order, I want to thank Dr. Volker Körstgens, Dr. Ezzeldin Metwalli Ali, Dr. Eva M. Herzig, Dr. Martine Philipp, Dr. Weijia Wang, Dr. Qi Zhong, Dr. Monika Rawolle, Dr. Martin Niedermeier, Dr. Kuhu Sarkar, Dr. Shuai Guo, Dr. Claudia M. Palumbiny, Dr. Christoph Schaffer, Daniel Moseguí González, Bo Su, Dr. Yuan Yao, Franziska Löhrer, Nitin Saxena, Lorenz Bießmann, Johannes Schlipf, Senlin Xia, David Magerl, Nuri Hohn, Stephan Pröller, Lucas Kreuzer, Tobias Widmann, Dan Yang, Kun Wang. Within their helps over numerous experiments, data analysis and extensive discussions, I am able to push my research forward. Particularly, many thanks go to the colleagues involved in the beamtimes with me. Without their efforts, I would not obtain reasonable experimental results. Besides the scientific research, I really enjoy the friendly working atmosphere built up by all people from Lehrstuhl für Funktionelle Materialien. Non-scientific activities in our chair such as summer and winter hikes, summer BBQs, Christmas parties, beer-festive

trips bring me countless moments of joy throughout my whole Ph.D. period. Thanks to the people who I have not yet mentioned: Prof. Dr. Christine M. Papadakis, Dr. Anatoly Berezkin, Dr. Konstantinos Raftopoulos, Xiaohan Zhang, Bart-Jan Niebuur, Natalya Vishnevetskaya, Florian Jung, Jenny Lebert, Mihael Čorić, Oliver Filonik, Wei Chen, Wei Cao, Sebastian Grott, Shambhavi Pratap, Marion Waletzki, Carola Kappauf, Susanna Fink. Furthermore, I greatly appreciate the wedding gift for Weijia and me.

The support from experienced beamline scientists and technicians is a guarantee for the success of all beamtimes. Many thanks for their guidance, help and patience. I would like to thank Prof. Dr. Stephan V. Roth, Dr. Gonzalo Santoro, Dr. Shun Yu, Dr. Peng Zhang, Dr. Sarathlal Koyiloth Vayalil (P03/DESY), Dr. Sigrid Bernstorff (Elettra), Dr. Zhonghua Wu and Dr. Guang Mo (BSRF). Besides beamline scientists, many thanks to Prof. Dr. Alexander W. Holleitner and Peter Weiser from WSI, who provide me the access to SEM measurements.

I am cordially thank some external research groups with which I have fruitful collaborations. Many thanks to Norma K. Minar, Kristina Peters, Thomas Bein, Dina Fattakhova-Rohlfing (Ludwig-Maximilians-Universität München), Thomas Fröschl, Nicola Hüsing (Universität Salzburg), Tobias Haeberle and Paolo Lugli (Technische Universität München).

I am sincerely grateful to Dr. Volker Körstgens, Nuri Hohn, Franziska Löhner, Nitin Saxena, Johannes Schlipf, Daniel Moseguí González, Lorenz Bießmann, Tobias Widmann and Lucas Kreuzer for proof reading of the present thesis. All corrections are valuable for the improvement of my thesis.

I would like to thank our secretaries Marion Waletzki, Carola Kappauf and Susanna Fink. They offer me great helps on my administration, visa extension, trips, purchases and reimbursements. In addition, many thanks to Dr. Volker Körstgens and Nitin Saxena, who can always be found when I have problems regarding German translation. With respect to the life outside of work, I would like to thank Dr. Martin Niedermeier, Dr. Kuhu Sarkar, Dr. Shuai Guo, Dr. Claudia M. Palumbiny, Dr. Christoph Schaffer, Senlin Xia, Franziska Löhner, Mihael Čorić, Daniel Moseguí González, Johannes Schlipf to invite me to their private activities.

Finally, a big thank-you goes to my family. My wife, parents, parents-in-law and sister always give me unconditional support whenever I need. My family is the warmest harbor, where I always feel happy, reliable and at ease. Particularly, I want to thank my fabulous wife Dr. Weijia Wang for her company throughout my whole Ph.D. study as well as for her enormous endorsement in my work and personal life.